

Precision measurements and search for axion-like particles in final states with a Z boson and a photon in pp collisions at $\sqrt{s} = 13 \text{ TeV}$ with the ATLAS detector

Dissertation
zur Erlangung des Doktorgrades
an der Fakultät für Mathematik, Informatik und Naturwissenschaften
Fachbereich Physik
der Universität Hamburg

vorgelegt von
Vincent Goumarre

Hamburg

2023

Gutachter/innen der Dissertation:	Dr. Sarah Heim Prof. Dr. Elisabetta Gallo
Zusammensetzung der Prüfungskommission:	Prof. Dr. Sven-Olaf Moch Dr. Sarah Heim Prof. Dr. Elisabetta Gallo Prof. Dr. Gudrid Moortgat-Pick Dr Christian Sander
Vorsitzende/r der Prüfungskommission:	Prof. Dr. Sven-Olaf Moch
Datum der Disputation:	06.07.2023
Vorsitzender des Fach-Promotionsausschusses PHYSIK:	Prof. Dr. Günter H. W. Sigl
Leiter des Fachbereichs PHYSIK:	Prof. Dr. Wolfgang J. Parak
Dekan der Fakultät MIN:	Prof. Dr.-Ing. Norbert Ritter

Abstract

Precision measurements of Standard Model processes are a fundamental part of experimental particle physics. Diboson channels at the Large Hadron Collider (LHC) are interesting processes for precision measurements since the relatively high cross-sections and low background contamination allow for small uncertainties. This thesis presents differential cross-section measurements of the production of a Z boson and a photon ($Z\gamma$) in association with hadronic jets, using the full 139 fb^{-1} dataset of $\sqrt{s} = 13 \text{ TeV}$ proton–proton collisions collected by the ATLAS detector during Run 2 of the LHC. Distributions are measured using events in which the Z boson decays leptonically and the photon comes from initial-state radiation. Measurements are made in observables sensitive to the hard scattering of the event and others which probe additional soft and collinear radiation. Different Standard Model predictions are compared with the unfolded measurements and good agreement is seen. Measurements of $Z\gamma$ differential cross sections by the ATLAS collaboration are also interpreted in a search for low mass off-shell axion-like particles (ALPs). In the absence of signal, constraints are set on ALPs couplings to Z bosons and photons assuming gluon–gluon fusion production. The constraints are compared to those from other experiments and cosmological observations.

Zusammenfassung

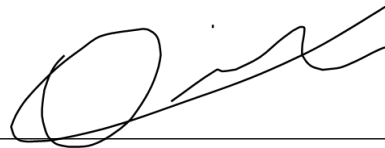
Präzisionsmessungen von Standardmodellprozessen sind ein grundlegender Bestandteil der experimentellen Teilchenphysik. Diboson-Produktionskanäle am Large Hadron Collider (LHC) sind interessante Prozesse für Präzisionsmessungen, da die relativ hohen Wirkungsquerschnitte und die geringe Hintergrundkontamination kleine Unsicherheiten zulassen. Diese Arbeit präsentiert differentielle Wirkungsquerschnittsmessungen der Produktion eines Z -Bosons und eines Photons ($Z\gamma$) in Verbindung mit hadronischen Jets unter Verwendung des vollständigen 139 fb^{-1} -Datensatzes von $\sqrt{s} = 13 \text{ TeV}$ Proton-Proton Kollisionen, die vom ATLAS-Detektor während des LHC Run 2 erfasst wurden. Verteilungen werden anhand von Ereignissen gemessen, in denen das Z -Boson leptonisch zerfällt und das Photon durch Abstrahlung im Anfangszustand entsteht. Messungen werden in Observablen durchgeführt, die die harte Streuung des Ereignisses testen, und in anderen, die zusätzliche weiche und kollineare Strahlung untersuchen. Unterschiedliche Standardmodellvorhersagen werden mit den entfalteten Messungen verglichen und es wird eine gute Übereinstimmung festgestellt. Messungen von differentiellen Wirkungsquerschnitten von $Z\gamma$ durch die ATLAS-Kollaboration werden auch bei der Suche nach off-shell Axion-ähnlichen Teilchen (ALPs) interpretiert. In Abwesenheit eines Signals werden Ausschlussgrenzen auf die ALPs-Kopplungen an Z -Bosonen und Photonen bestimmt, wobei eine Gluon-Gluon-Fusionsproduktion angenommen wird. Die Einschränkungen werden mit denen aus anderen Experimenten und kosmologischen Beobachtungen verglichen.

Declaration on oath

Hiermit erkläre ich an Eides statt, dass ich die vorliegende Dissertationsschrift selbst verfasst und keine anderen als die angegebenen Quellen und Hilfsmittel benutzt habe.

I hereby declare upon oath that I have written the present dissertation independently and have not used further resources and aids than those stated in the dissertation.

Hamburg, 11.05.2023

A handwritten signature in black ink, consisting of a large, stylized 'O' followed by several loops and a long horizontal stroke extending to the right.

Signature of the doctoral student

Acknowledgements

I would like to start by thanking three people who supervised me and have been important for my work. First and foremost, Dr. Sarah Heim for the time she spent helping me, explaining what I did not understand, and bringing corrections to my work during the whole PhD. She also made sure that I felt comfortable during my stay in Hamburg. Then, Dr. Lorenzo Rossini who supervised me during the $Z\gamma$ +jets project. More than a good guide in the project, he also became a friend. Finally, I would also like to thank Dr. Stefan Richter, who trusted me for writing a whole new software. He has been an incredible help for improving my coding skills and my French.

I would also thank the whole axion-like particles team, especially Sonia Carra, Sarah Heim, Federico Meloni and Beate Heinemann. Their help and support is one of the main reasons of the joy I had to work on this project.

This thesis would not have been possible without all the people who reviewed and corrected it: Sarah, Lorenzo, Trine, Sonia, Stephen and Stefan. Thank you to all of them.

I would also like to thank all the ATLAS DESY group members which made me feel welcome from the first day and have always been very responsive when I had an issue. In particular, I would like to thank the people who made me feel home when I just arrived in Hamburg: Alessandro B., Alessandro G., Eloisa, Emily, Fang-Ying, Hamish, Jordi, Judith and Nils.

During my stay in Hamburg, I never lived alone. This means that some people had to endure me this whole time. They have always been kind and helpful and I want to thank them for that: Fang-Ying, Lily and Karl, and Trine.

I would also like to thank particularly Dr. Trine "sødhjerte" Poulsen, an ex-physicist, new eco-scientist. I loved spending the two last years in Hamburg with her and I am delighted to follow her in a new adventure in Denmark. During my whole life, I never expected that German courses could be so rewarding.

I would also like to thank my friends, that I did not see often, but I have been delighted to meet when I was back in France: Alice, Anaïs, Antoine, Baptiste, Benjamin, Cécile, Coraline, Elise, Laura, Marc, Paul and Solène. They have been a precious source of distraction when going out was not really an option. The vacations and weekends with them are fantastic and I always look forward to the next one.

Last but not least, I would like to thank my family. Je n'ai pas souvent été très présent ces dernières années. Et pourtant, vous avez toujours été là pour m'accueillir quand, enfin, je daignais rentrer, ou simplement pour parler quand j'en avais besoin. Papa, maman, j'ai été fier d'être témoin de votre mariage et j'espère que les prochaines années seront toujours aussi heureuses. Marie, ne change rien, t'es la meilleure petite sœur. Théo, tu as aussi ta place dans cette famille.

Finally, and because I hate stories where everything ends well, I would like to make a "unacknowledgment". For the thing that annoyed me the most during my PhD, which forced me to

cancel my vacations, and have been a pain professionally and in my personal life. It did not make things easy and I consider the achievement of this thesis as a revenge against it: COVID-19.

Contents

1	Introduction	1
2	Standard Model and Beyond	3
2.1	The Standard Model of Particle Physics	3
2.1.1	Quantum Field Theory	3
2.1.2	Feynman diagrams	4
2.1.3	Particle Content of the Standard Model	6
2.1.4	Diboson processes	11
2.2	Problems with the Standard Model	13
2.3	Axions and axion-like particles	15
2.3.1	Axions	16
2.3.2	Axion-like particles	18
2.3.3	Off-shell ALPs	19
2.4	Monte-Carlo generators	21
2.4.1	Parton distribution functions	22
2.4.2	Hard process and Sudakov logarithms	22
2.4.3	Parton showers, hadronization and detector simulation	23
3	The LHC and the ATLAS experiment	25
3.1	The Large Hadron Collider	25
3.1.1	Design	25
3.1.2	Energy	27
3.1.3	Luminosity	28
3.1.4	LHC Runs	29
3.2	The ATLAS detector	31
3.2.1	Inner detector	33
3.2.2	Calorimeters	35
3.2.3	Muon spectrometer	38
3.2.4	Trigger and Data Acquisition	40
4	Object reconstruction and identification in ATLAS	43
4.1	Electrons	44
4.1.1	Reconstruction	44
4.1.2	Energy calibration	46
4.1.3	Identification	46
4.1.4	Identification efficiency measurements	47
4.1.5	Isolation	49
4.2	Photons	50
4.3	Muons	52
4.4	Jets	53
4.4.1	Particle flow algorithm	53
4.4.2	Jet reconstruction and anti- k_r algorithm	55

4.4.3	Pileup suppression	57
4.4.4	Jet calibration	58
5	$Z\gamma$ + jets study in the ATLAS detector	60
5.1	Context and motivations	60
5.2	Samples	61
5.3	Event selection	63
5.3.1	Object definition	63
5.3.2	Signal region definition	64
5.3.3	Observables	65
5.4	Background estimation	67
5.4.1	Z + jets estimate	68
5.4.2	Other sources of background	76
5.4.3	$e\mu\gamma$ control region	79
5.5	Unfolding	81
5.6	Uncertainties	83
5.7	Results	85
5.7.1	Data/SM	85
5.7.2	Unfolded results	92
6	Search for axion-like particles	96
6.1	$Z\gamma$ and WW measurements	96
6.2	ALPs production cross-section	98
6.3	Signal predictions	99
6.4	Likelihood fit	100
6.5	Results	102
6.6	Discussion	104
7	Conclusion	106
A	Spontaneous symmetry breaking	107
B	Kinematic parameters	109
C	Sanity checks on the correlation factor	111
C.1	Using data in non-isolated control region	111
C.2	Using events failing the track isolation	112
C.3	Using other generators	113
D	Additional plots for the $Z\gamma$ + jets data/SM results	114
E	Additional plots for the unfolded $Z\gamma$ + jets results	119
	Bibliography	123

1 | Introduction

The composition of matter is a question debated for millennia [1]. Only at the beginning of the 20th century, the existence of atoms was proven, with the study of the Brownian motion, first theoretically by Albert Einstein in 1905 [2] and then experimentally by Jean Perrin in 1909 [3]. But a few years prior to the acceptance of atoms as the basic component of the universe, Joseph J. Thomson discovered a particle much lighter than an atom [4], the first elementary particle: the electron.

During the 20th century, many other particles and families of particles were discovered in parallel with the development of Quantum Mechanics and Quantum Field Theory, the theories describing the physical properties at atomic and subatomic scales. All the discovered particles were included in a model describing their properties and interactions: the Standard Model of particle physics. This model found its last missing piece in 2012 with the discovery of the Higgs boson at the LHC [5, 6].

Although complete, the Standard Model exhibits some issues such as the matter-antimatter asymmetry, the muon anomalous magnetic dipole moment, the neutron lifetime, the strong CP problem and, in particular, the fact that it does not contain a Dark Matter candidate. According to astronomical measurements, Dark Matter is responsible for about 84 % of the mass of the universe [7]. In other words, everything described in the Standard Model accounts for only one sixth of the matter in the universe. To solve the issues of the Standard Model, several theories Beyond Standard Model have been developed. Among them, the axions are Dark Matter candidates intended to solve the strong CP problem.

To tackle the questions surrounding Dark Matter, different experiments have been built. Among them, accelerators are designed to collide particles and search for phenomena unexpected in the Standard Model. The Large Hadron Collider (LHC), built in 2008, is the most powerful collider ever built, with a center of mass energy of 13.6 TeV achieved in 2022.

A Toroidal LHC ApparatuS, more commonly known as ATLAS, is, along with CMS (Compact Muon Solenoid), one of the two general purpose experiments of the LHC. Among other contributions to particle physics, the ATLAS and CMS experiments discovered the Higgs boson [5, 6]. Other goals include the precise measurements of SM processes and the search for Dark Matter.

In ATLAS, billions of collisions happen every second. In the search for deviations, the data is compared to the Standard Model expectation, often in the form of simulated events. The precision of the simulation is a crucial aspect when searching for new phenomena, like Dark Matter signatures.

This thesis will focus on two aspects of searches for Dark Matter using the ATLAS detector: the search itself as well as the precision measurement of a Standard Model process with the same final state, which is not only a background to the search, but which can be used to improve event simulation in general. To do so, the effort has been turned toward the diboson process $pp \rightarrow Z(\rightarrow \ell\ell)\gamma$ using 139 fb^{-1} of data recorded by the ATLAS detector between 2015 and 2018

(LHC Run 2). This process is interesting to study for several reasons. First, it has low statistical uncertainties due to the relatively large cross-section and a small background contamination. Events with hadronic jets are studied, which can be used to improve QCD modelling, thus improving the Standard Model predictions. Moreover, using measurements of the $\ell\ell\gamma$ final state, strong limits can be set on the production of particles not described by the Standard Model. We constrain the production of axion-like particles.

This thesis is divided in five parts:

- Section 2 is an introduction to the theory of particle physics. This includes an overview of the Standard Model with a close look at the diboson processes that will be discussed later in the thesis. This first part also contains details on axions and axion-like particles, and on the MC generators.
- In Section 3, the Large Hadron Collider and the ATLAS detector are introduced.
- Section 4 contains more details about how particles are reconstructed in ATLAS, with focus on electrons.
- Section 5 describes the measurement of the diboson process $pp \rightarrow Z(\rightarrow \ell\ell)\gamma$ with focus on the jets content of the events.
- Finally, Section 6 presents how limits are set on the properties of off-shell axion-like particles, using the results of a previous $Z(\rightarrow \ell\ell)\gamma$ measurement.

2 | Standard Model and Beyond

Particle physics is the study of elementary particles, the most fundamental components of matter known so far. To describe their behaviour, the current most accurate model is the Standard Model of particle physics (SM). The SM is a paradigm realisation of Quantum Field Theory (QFT), a theory that describes quantum objects at high energy.

However, results of different observations and internal problems to the model hint that the SM does not perfectly depict reality. To answer these issues, many extensions of the model have been proposed. This can go from adding just a few particles to the current model, to changing the fundamental laws of physics. These models are referred to as Beyond Standard Model (BSM) extensions, and, so far, no experiment could favour any of them.

This chapter introduces the theoretical tools needed to fully understand the physics processes in the rest of this thesis. First the SM is presented with a focus on diboson processes. The latter will be the center of attention of Section 5 and 6, where they will be studied. The next section, will introduce shortcomings of the SM, specifically different issues related to particle physics. An answer to some of these issues, namely axions and axion-like particles (ALPs), will then be described in detail. Finally, the main tool used by experimental physicists to compare theoretical to experimental data, the Monte-Carlo generators, will be presented.

2.1 The Standard Model of Particle Physics

As this thesis is about experimental observations, only essential features (from an experimentalist point of view) of SM and QFT will be presented. QFT will be first introduced with very basic notions to indicate how the SM is constructed. Then, Feynman diagrams will be presented as a powerful method to handle calculations intuitively. The particles of the SM and their corresponding properties will then be discussed. Ultimately, a class of processes happening in hadron colliders, referred to as diboson processes, will be presented.

2.1.1 Quantum Field Theory

QFT is a theory combining quantum mechanics and special relativity, to describe the high energy physics at the atomic/subatomic level [8, 9, 10]. To describe physics as observed in this universe, the model used in particle physics is the SM. Mathematically, this model takes the form of a lagrangian density (\mathcal{L}) which is a relation between the kinetic energy (\mathcal{T}) and the potential energy (\mathcal{U}):

$$\mathcal{L} = \mathcal{T} - \mathcal{U}. \quad (2.1)$$

Particles, for example electrons, are described as fields (noted ψ for fermions, ϕ for scalar particles, etc). The Lagrangian of a fermion is given as [11]¹:

$$\mathcal{L}_f = i\bar{\psi}\gamma^\mu\partial_\mu\psi - m_f\psi^\dagger\psi, \quad (2.2)$$

where m_f is the mass of the fermion and $\bar{\psi} = \psi^\dagger\gamma^0$ the hermitian adjoint of ψ (γ^0 is a Dirac matrix). Two different parts can be extracted from this equation: a dynamic part $i\bar{\psi}\gamma^\mu\partial_\mu\psi$ and a potential $m_f\psi^\dagger\psi$. The fact that the mass is a potential will be important to understand the Higgs mechanism [12, 13, 14].

A Lagrangian for fermions, such as Eq. (2.2), is not invariant under the local gauge transformation $\psi \rightarrow e^{iq\lambda(x)}\psi$ (where $\lambda(x)$ is an arbitrary function). Although the gauge transformation preserves the mass term, the kinematic term changes. To make the Lagrangian invariant, a field term must be added and must transform as $A_\mu \rightarrow A_\mu + \partial\lambda(x)$ under local gauge. The Lagrangian is written as:

$$\mathcal{L} = i\bar{\psi}\gamma^\mu\mathcal{D}_\mu\psi - m\psi^\dagger\psi - \frac{1}{4}F^{\mu\nu}F_{\mu\nu}, \quad (2.3)$$

with the covariant derivation $\mathcal{D}_\mu = \partial_\mu + iqA_\mu$ and the field tensor $F^{\mu\nu} = \partial^\mu A^\nu - \partial^\nu A^\mu$. In general, if a Lagrangian is not local gauge invariant, a field must be added to the covariant derivative, as well as its tensor [15].

The Lagrangian is then inserted in an equation to describe the behavior of the fields. This equation is the Euler-Lagrange equation:

$$\partial_\mu \left(\frac{\partial\mathcal{L}}{\partial(\partial_\mu\phi_i)} \right) = \frac{\partial\mathcal{L}}{\partial\phi_i}. \quad (2.4)$$

This equation is the equation of motion of the particles and gives the so-called Dirac equation for fermions [11], Klein-Gordon equation for spin-0 boson [16, 17] and Proca equation for spin-1 boson [18].

2.1.2 Feynman diagrams

Eq. (2.4) on the Lagrangian is generally not used by experimental particle physicists and another tool is preferred: Feynman diagrams. Feynman calculus is a method to treat QFT as a perturbation theory, analogous to a series expansion [19, 20]. The rules for Feynman diagrams are a schematic method to use the Feynman calculus, with rules derived from the Lagrangian of the particles considered.

To understand the use of Feynman diagrams, one has to know the form of the cross-section when two particles (p_1, p_2) collide to create n particles ($p_3\dots p_n$). This relation is known as the Fermi's golden rule and reads as [9]:

$$\sigma = \frac{S}{4\sqrt{(p_1 \cdot p_2)^2 - (m_1 m_2)^2}} \int |\mathcal{M}|^2 (2\pi)^4 \delta(p_1 + p_2 - \sum_{j=3}^n p_j) \prod_{j=3}^n 2\pi \delta(p_j^2 - m^2) \theta(E_j) \frac{d^4 p_j}{(2\pi)^4}, \quad (2.5)$$

where S is a statistical factor (depending on the number of identical particles), $\delta(x)$ is the Dirac delta function (1 if $x = 0$ and 0 otherwise) and $\theta(x)$ is the Heaviside step function (1 if $x > 0$

1. In this thesis, the natural units are used: $c = \hbar = 1$

and 0 otherwise). \mathcal{M} is a matrix element that depends on the dynamics of the process while the rest of the equation addresses the kinematics. Feynman diagrams are a recipe to compute this matrix element \mathcal{M} .

Feynman diagrams for the Bhabha process $e^-e^+ \rightarrow e^-e^+$ are shown in Fig. 2.1. The diagram is read along the horizontal axis from left to right, as this represents the flow of time (particles on the left are scattering, creating the outgoing particles on the right), whilst the vertical axis represents distances. The Feynman diagram representing the s-channel reads as "an electron and a positron annihilate to create a photon, which in turn decays to give an electron-positron pair", while the t-channel reads as "the deflection of an electron and a positron trajectory by the exchange of a photon".

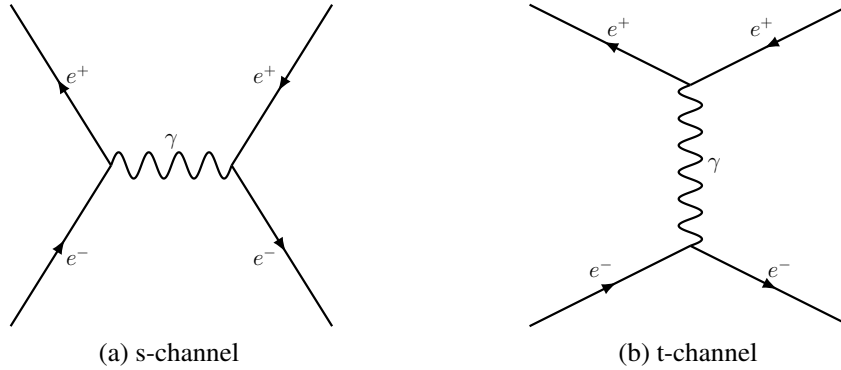


Figure 2.1: Example of Feynman diagrams for the process $e^-e^+ \rightarrow e^-e^+$. The sum of both diagram forms the leading order matrix element in α_{EM} .

Feynman diagrams are representations of mathematical expressions used to compute the matrix element \mathcal{M} presented earlier. The list of possible vertices is model dependent, and the goal is to find all the conceivable combinations that dictate the possible paths in which a predefined initial state transforms to a final state. The matrix \mathcal{M} is then the sum of all the Feynman diagram contributions for a given initial and final state. When squaring the matrix element, as required in Eq. (2.5), interference terms appear between the different Feynman diagrams.

At first sight, this might seem laborious since there would often be an infinite amount of possibilities. However, each vertex introduces a factor $\sqrt{\alpha}$, referred to as the coupling constant. For the EM interaction for example, the coupling constant is the fine structure constant $\alpha_{\text{EM}} = 1/137$ [21]. This means that the more vertices in a given diagram, the smaller the contribution of said diagram to \mathcal{M} .

Diagrams represent terms of a series expansion on the coupling constants. As the fine structure constant is small ($\alpha_{\text{EM}} \ll 1$), the contributions from diagrams with many vertices can be neglected. This is an interesting feature of Feynman calculus. However, this reasoning might be wrong if the coupling constant is such as $\alpha \sim 1$. This problem is often encountered when computing strong interactions, for example ($\alpha_s(M_Z) = 0.12$ [21]).

Coming back to the Bhabha scattering, Fig. 2.1 shows all the diagrams with a coefficient $\mathcal{O}(\alpha_{\text{EM}})$ which are called leading order (LO). Meanwhile, Fig. 2.2 contains a few diagrams contributing at $\mathcal{O}(\alpha_{\text{EM}}^2)$, called next-to-leading order (NLO), while further contributions can arise with $\mathcal{O}(\alpha_{\text{EM}}^3)$ at next-to-next-to-leading order (NNLO), etc.

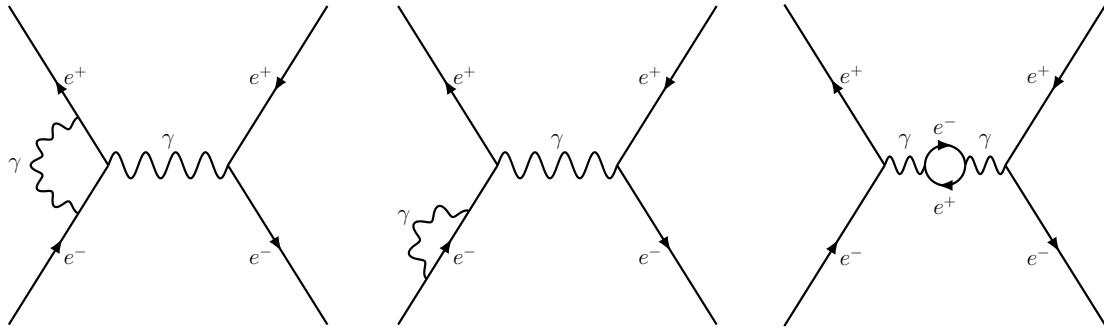


Figure 2.2: Feynman diagrams representing some of the second order contributions to the process $e^- + e^+ \rightarrow e^- + e^+$.

It should be noted that an internal particle (neither incoming or outgoing) in a Feynman diagram is so called "virtual". This means that its mass can be very different to the particle physical mass. In that case, the particle is said "off-shell", as opposed to "on-shell". However, experimentally, properties related to the virtual particles are expected to be visible. For example, an s-channel as shown in Fig. 2.1 is susceptible to exhibit a resonance on the outgoing electron-positron system invariant mass corresponding to the mass of the virtual particle (in this case, the virtual particle is a photon so the resonance would be at $m_{e^+e^-} = 0$).

2.1.3 Particle Content of the Standard Model

Now that the main principles of Feynman diagrams are introduced, the main focus of this section is to introduce the different particles and their possible modes of interaction. For elementary particle physics, the answer is given by the Standard Model, represented in Fig. 2.3.

The SM particles can be split in two categories based on their spin: fermions and bosons. In the following, particles of the SM will be discussed in more details. Their properties and their discovery will be addressed, and the Feynman diagrams will be introduced when discussing the bosons.

Fermions

Fermions are half-integer spin particles (all SM fermions have a spin-1/2). This property requires that they must respect Pauli's exclusion principle, which states that two fermions can not be in a simultaneous state of same spin and spatial location. That notion will be important when physics Beyond Standard Model (BSM) will be addressed, since it imposes that Dark Matter particles, if they are fermions, must have a minimal mass. The different fermions of the SM are presented below. All fermion types come in three generations in the SM.

Charged leptons (ℓ) Until now, some of the electron properties were discussed. In fact, the electron is one of the charged leptons. This category is defined as the fermions which are not sensitive to strong interaction and carry an electric charge. The electron, is the lightest charged lepton, making it very abundant. It is a key constituent of atoms, and plays a major role in

Standard Model of Elementary Particles

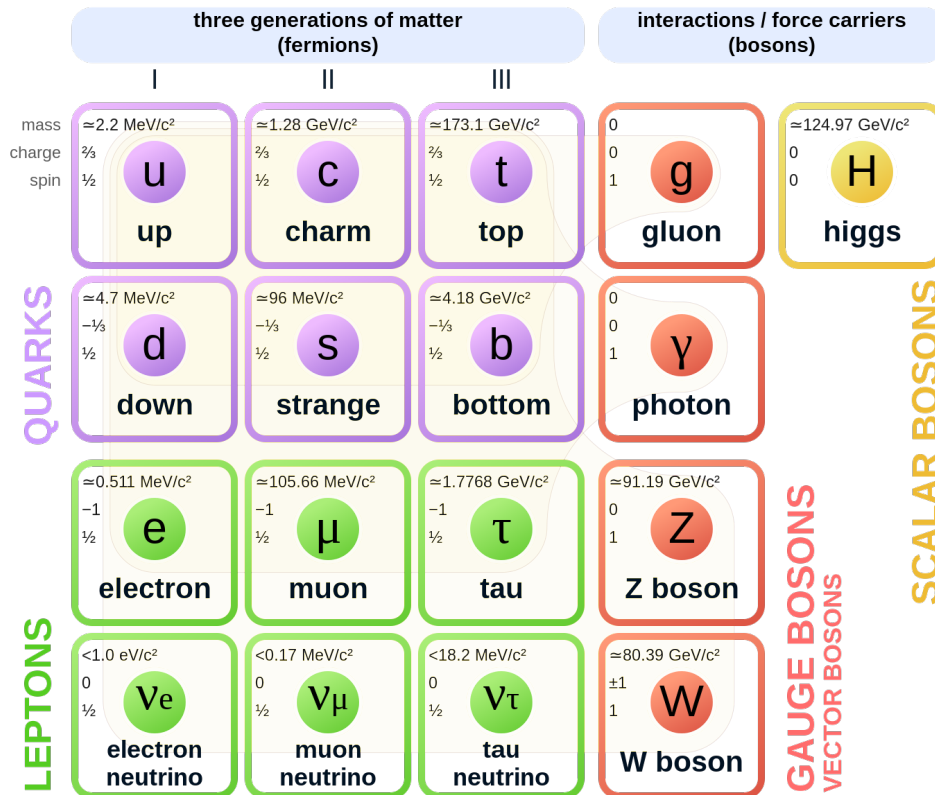


Figure 2.3: SM particles with mass, charge and spin properties. Figure taken from Ref. [22].

chemical reactions and electricity. It is thus not surprising that it was the first fundamental particle to have been discovered (in the 19th century [4]). As electrons are abundant and easily accessible, their properties can be measured with precision. They are a relatively light particle (compared to the other SM particles) with $m_e = 511 \text{ keV}$ and carry an electric charge of -1 . But the electron is not the only charged lepton. In 1936, the study of cosmic radiation revealed the existence of a particle about 200 times more massive than the electron, the muon (μ) [23, 24]. In fact the muon has the same properties as the electrons except for its mass. One of the production processes for this particle is the collision of highly energetic cosmic rays with atoms of the atmosphere. The explanation on why such a particle does not exist in abundance on earth is that muons are unstable. After a lifetime of $2.2 \mu\text{s}$, the muon decays into an electron (and neutrinos). The third charged lepton in the SM is the tau (τ). Its lifetime is only 0.3 ps , which explains why there is no "atmospheric tau". It was therefore discovered in 1975 in the Stanford Linear Accelerator Center [25]. Its mass is in the GeV range and it can decay either in a leptonic way (muon or electron), or into hadrons (involving quarks). The three particles introduced, electron, muon and tau, have the same properties with the exception of their masses, meaning that the vertices in the Feynman diagrams will obey the same rules. Such particles obeying this principle are said to be in different generations.

Neutral leptons (ν) The neutral leptons in the SM are called neutrinos (ν). They are only sensitive to the weak interaction, which makes them hard to detect. They were already proposed

in 1930 by Wolfgang Pauli to explain nuclear beta decays [26]. If the decay of a neutron into a proton released only an electron ($n \rightarrow p + e^-$), then the electron energy would have been fixed. Experimentally, the electron spectrum corresponds to a three-body decay. The third particle is a neutral massless particle: the neutrino ($n \rightarrow p + e^- + \bar{\nu}$). The first direct observation of a neutrino was done in 1956, thanks to a reaction $\bar{\nu} + p \rightarrow n + e^+$ occurring in water [27]. In 1962, it was experimentally demonstrated that neutrinos coming from the pion decays were different from neutrinos coming from beta decays [28]. This indicated that there was actually two different kinds of neutrinos: the electron neutrino (ν_e), and the muon neutrino (ν_μ). After the discovery of the tau lepton, the tau neutrino (ν_τ) was expected to be a third neutrino flavour and experimental confirmation was established in 2000 [29]. Meanwhile, an issue appeared in the amount of neutrinos coming from the sun, where they were about 3 times less abundant than the expectation [30, 31]. This discrepancy, called the solar neutrino problem, was later solved by the discovery of the neutrino oscillation [32, 33]. The neutrino oscillation is a change of neutrino flavour over time. Although neutrinos were initially thought to be massless, the flavour oscillation could only be explained by the presence of distinct masses between the neutrino generations, allowing mixing between the mass and the interaction eigenstates. Until now, this mass has never been measured but direct measurements estimated it to be smaller than 1 eV [34]. This value is close to what is expected by cosmological observations [7, 35]. Because neutrinos interact only via the weak interaction, this has consequences on their helicity. This notion will be introduced when discussing parity violation in the paragraph dedicated to the W and Z boson.

Quarks (q) Until 1974, many particles had been detected, creating a "subnuclear zoo" [36]. Some of them were bosons, called mesons (pions for example), and others were fermions, called baryons (such as neutrons and protons). Mesons and baryons are combined under the term hadrons. Attempts were made to classify them, for example Gell-Mann in 1961 with the Eightfold Way which gave some interesting predictions [37]. In this effort, Gell-Mann and Zweig proposed the quark model in 1964 [38, 39, 40]. In this model, mesons and baryons were not elementary particles but made from three different quarks (up, down and strange). Although the model was consistent with the observed mesons (made of a quark-antiquark pair $q\bar{q}$) and baryons (made of three quarks qqq) properties, it was not accepted at the time. The main issue was that no such particle had ever been observed. This phenomenon is now known as colour confinement (see explanations in the gluon paragraph). Some later experiments showed that protons were composite particles [41, 42] but it was not before the "November Revolution" in 1974 that the notion of quarks was fully accepted. At that time, the J/ψ particle was discovered [43, 44] and the quark model was extended to include a fourth quark: the charm quark [45]. In 1977 [46] and 1995 [47, 48], two more quarks were added to the standard model: the bottom and top quarks. The mass of the 6 quarks are ranging from MeV to hundreds of GeV. Quarks have fractional electric charge, with value $+2/3$ for up (u), charm (c) and top (t), and $-1/3$ for down (d), strange (s) and bottom (b). The difference between quarks and leptons is that they are sensitive to the strong interaction.

Bosons

Bosons are particles with an integer spin, thus not sensitive to the Pauli's exclusion principle. In the SM, bosons are the particles responsible for mediating particle interactions. For example, the electromagnetic force is due to the exchange of photons between two charged particles.

The SM introduces bosons for three of the four forces through the $SU(3) \times SU(2) \times U(1)$: strong (gluons), weak (Z and W bosons) and electromagnetic (photons). Gravity does not have a corresponding particle in the SM, but its is negligible at the energy range reached by particle accelerators. Along with the bosons already mentioned, the SM proposes another particle to explain the mass of particle: the Higgs boson.

Photons (γ) The question of whether light is made out of particles or waves was contested until the beginning of the 20th century. The problem favoured the wave paradigm in the middle of the 19th century with the development of electromagnetic theory. In 1900 and 1905 Plank [49] and Einstein [50], respectively, restored the particle paradigm, stating that the light had both properties. The particle of light was named the photon. The photon is the carrier of the electromagnetic interaction and its properties are studied in a theory called quantum electrodynamics (QED). Photons couple to particles with an electric charge, meaning that they directly interact with fermions (except neutrinos) and W bosons. They are massless spin-1 particles. The Feynman interaction linked to photons is given in Fig. 2.4.

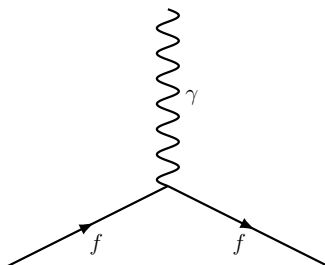


Figure 2.4: Vertex between photons and charged fermions (vertices involving W bosons are shown in Fig. 2.5).

Z bosons and W bosons As QED is a theory explaining the electromagnetic interaction, theorists in the 1950s and 1960s tried to develop a theory to explain the mechanism behind beta decays. In 1967, a unified theory of the electromagnetic and weak interaction, called electroweak theory, was released [51]. This could explain beta decay by the mediation of a massive spin-1 gauge boson: the W boson. The main difficulty in the process was that gauge bosons are expected to be massless, however the W boson is massive. Current measurements of its mass give $m_W = 80.4 \text{ GeV}$ [21]. The answer to that problem is the introduction of spontaneous symmetry breaking, called the Higgs mechanism, explained in Appendix A. One of the main achievements of the theory was the prediction of a new spin-1 boson: the Z boson ($m_Z = 91.2 \text{ GeV}$). On the contrary to the W boson which is a charged particle, the Z boson is zero charge. The Feynman vertices of the W and Z bosons are available in Fig. 2.5. The weak interaction has two distinct features that makes it unique: quark flavour non-conservation and parity violation. The quark flavour non-conservation is unique to the W boson. When a W boson decays, the quarks need not be a quark-antiquark pair of the same flavour (this would violate the charge conservation). Moreover, the generations of quarks are mixed by the so-called CKM matrix [52, 53], meaning that, for example, a W boson can decay in a pair $s\bar{u}$. Parity symmetry breaking is another peculiarity of the weak interaction. To understand the notion of parity, let's consider an ultra-relativistic fermion, meaning that it has a speed close to the speed of light ($\gamma \gg 1$). When the spin is projected onto the direction of propagation, there are two possibilities: either it is in the same direction or it is in the opposite direction. If it is in the same direction,

the particle is said to be right-handed, while it is left-handed otherwise. Suppose a negative pion (a light spin-0 meson, made out of a quark-antiquark pair $d\bar{u}$) decays into a muon and an antineutrino $\pi^- \rightarrow \mu + \bar{\nu}_\mu$. If parity symmetry was respected, the statistical distribution of this process would end up with half of the final state being a left-handed muon and a right-handed antineutrino, and half being a right-handed muon with a left-handed antineutrino. Experimentally though, only the case where the left-handed muon is observed [54, 55]. This indicates that parity is violated in weak interactions. Neutrinos interact only by the weak interaction, and they only exist as left-handed neutrinos and right-handed antineutrinos in nature.

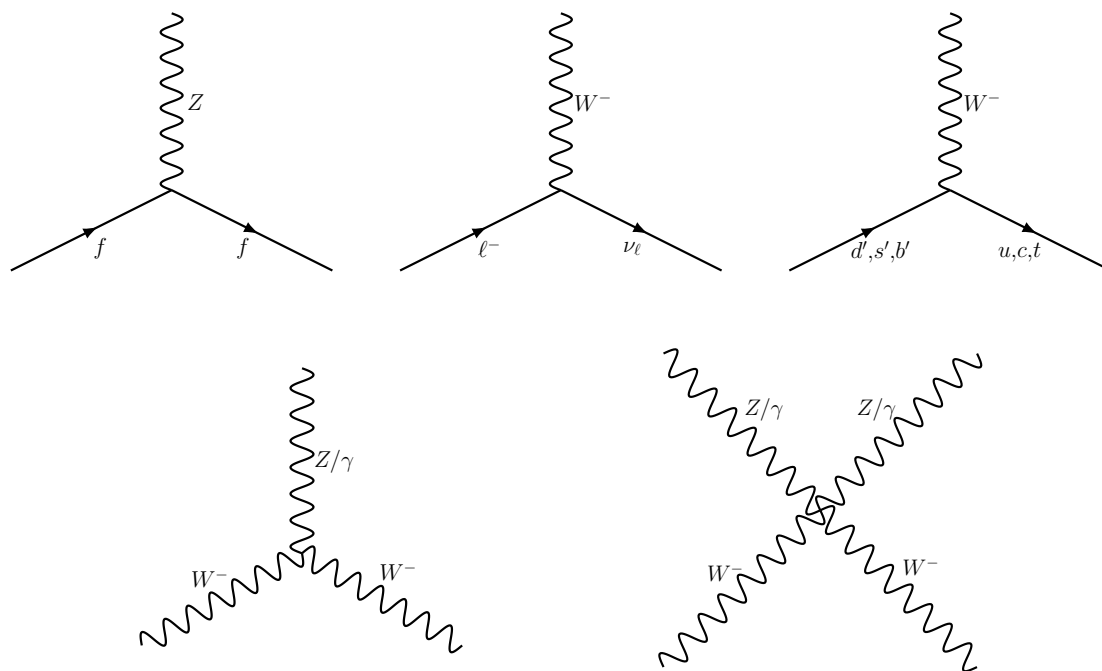


Figure 2.5: Vertices between Z and W bosons and other particles.

Gluons (g) In the atomic model, the repulsive force imposed by the electric charge of the protons should make all nuclei (except hydrogen) unstable. As gravity is not strong enough at that scale to compensate, a new force should be present in order to keep the nucleus from decaying. This need for a strong force is strengthened by the quark model which explains why quarks bind to form protons, neutrons and other hadrons. The particle responsible for the strong interaction has been discovered in 1978 at DESY and given the name gluon [56]. Like photons, gluons are massless, chargeless and have spin-1. The charge associated to the strong interaction is called colour. Quarks are the only fermions to have a colour property. Gluons also carry two colours simultaneously, making them interact with themselves. The Feynman diagrams linked to the vertices involving gluons are shown in Fig. 2.6. Hadrons do not have a colour charge since they are either made of three quarks of a different colours (baryons) or a quark-antiquark pair made of a colour and its anticolour counterpart (mesons). The fact that gluons carry colours is important to explain the colour confinement. Because they can interact with themselves, the strength of the interaction increases at low energy, i.e. large distances. This implies that quarks trying to escape hadrons endure an increasing force. It can happen that the force is so strong that the energy is released by the creation of new quarks creating several new hadrons. Therefore,

quarks and gluons can not be detected as independent particles, but always remain in bound states.

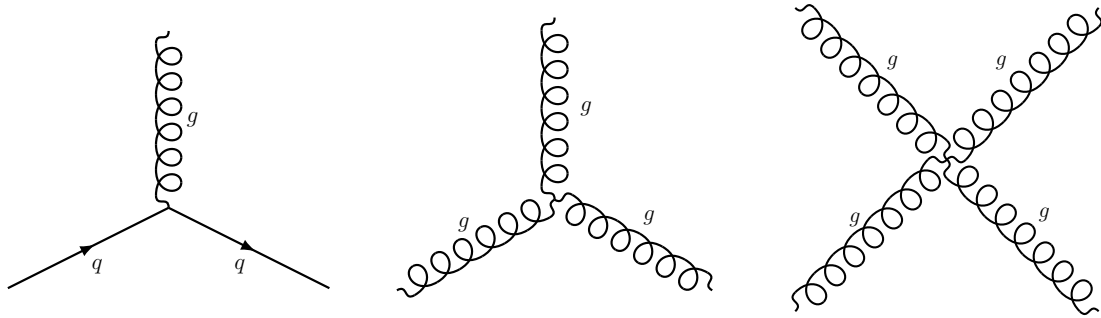


Figure 2.6: Vertices between gluons and other particles.

Higgs bosons (H) As stated earlier in this chapter, gauge symmetries imply the existence of a field corresponding to a massless boson (for example in Eq. (2.3)). W and Z bosons are gauge bosons yet they have a mass, which should violate the associated gauge symmetry. To answer this contradiction, several theorists proposed a mechanism in 1964 called the Higgs mechanism [12, 13, 14]. Its principle relies on the concept of spontaneous symmetry breaking induced by a potential whose minimum has multiple local minimal degeneracies. A summary of this process can be found in Appendix A. The Higgs mechanism applied to the electroweak $SU(2) \times U(1)$ symmetry gives masses to the W and Z boson. Moreover, the physical W boson, Z boson and photon are all coming from a mixing of the four initial fields (3 from $SU(2)$ and 1 from $U(1)$). In this process, the photon does not acquire a mass. The Higgs boson (H) was discovered in 2012 at the LHC [5, 6]. They are chargeless, spin-0 bosons. They interact with every massive particle, including themselves, as they have a measured mass $m_H \approx 125$ GeV. The interactions are summarized in Fig. 2.7.

2.1.4 Diboson processes

Diboson processes are a class of processes in which the final state consists of two electroweak bosons. Examples of mechanisms leading to diboson outcomes are given in Fig. 2.8. In accelerator searches, a W and Z boson are only detected indirectly by the product of their decays. This leads to a wide range of final states, resulting in multiple possibilities to study them.

Many diboson processes were already studied at the Tevatron [57] and LEP colliders [58], and are still studied nowadays at the LHC. Here is a non-exhaustive list of channels scrutinised by the ATLAS detector:

- $W(\rightarrow \ell\nu)W(\rightarrow \ell\nu)$ [59, 60], with the presence of jet(s) [61, 62], or created by the process $\gamma\gamma \rightarrow WW$ [63],
- $Z(\rightarrow \ell\ell)Z(\rightarrow \ell\ell)$ and $Z(\rightarrow \ell\ell)Z(\rightarrow \nu\nu)$ [64, 65, 66, 67],
- $W(\rightarrow \ell\nu)Z(\rightarrow \ell\ell)$ [68, 69, 70],
- $Z(\rightarrow \ell\ell/\nu\nu/qq)\gamma$ [71, 72, 73, 74],

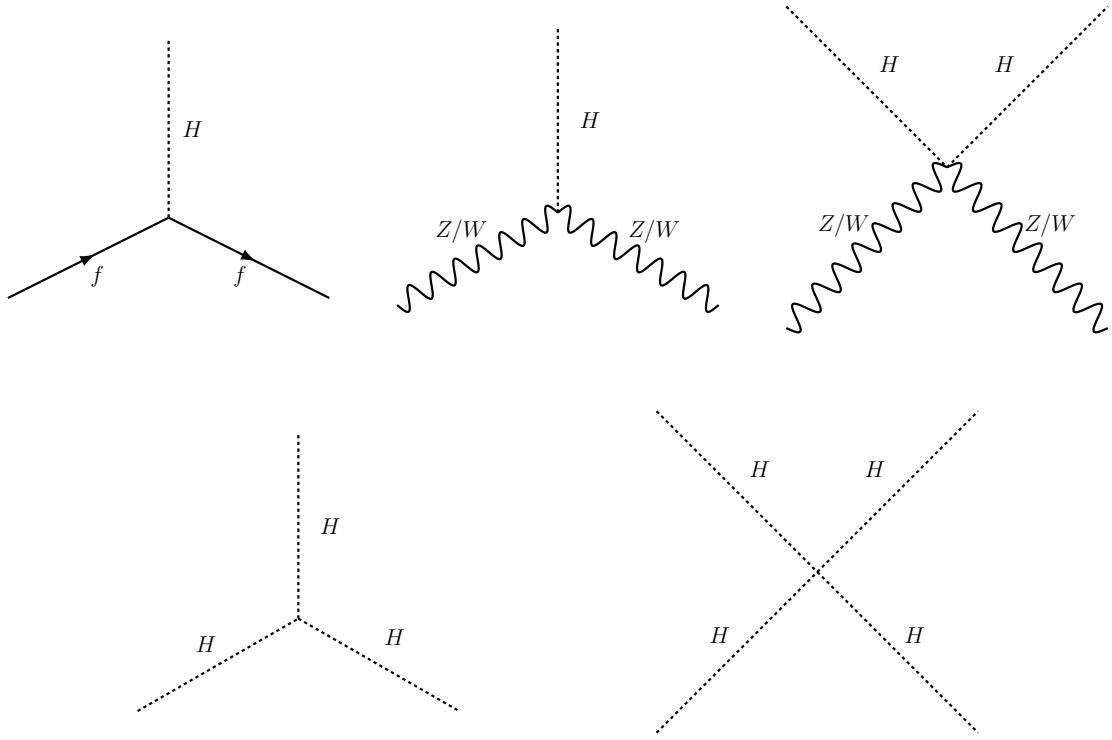


Figure 2.7: Vertices between the Higgs boson and other particles.

- $W(\rightarrow \ell\nu)W(\rightarrow qq)$ and $W(\rightarrow \ell\nu)Z(\rightarrow qq)$ [75].

The diboson processes are often studied with leptonic decays since they have low backgrounds and large number of events. Fig. 2.9 shows the cross-section of several processes, among which the WW , WZ and ZZ have a relatively high value with low experimental uncertainties. The precision of the measurements are often better than the state-of-art perturbative QFT calculations, as shown by Fig. 2.10. In that case, data can be used to improve the SM computations, as a complement to the single boson channels. These processes are therefore naturally good candles to estimate the SM parameters, both in the electroweak and QCD sectors.

An example of this precision is the discrepancy between data and SM prediction for the WW channel during the 2012 data taking at LHC [77]. An excess of data was both detected by CMS [78] and ATLAS [79] compared to the estimated NLO SM process (enhanced with the $gg \rightarrow WW$). The issue was solved by calculating the WW process up to NNLO to have a more precise prediction [80].

The diboson channels can also be used to search for BSM phenomena. For example, many measurements also estimate the anomalous triple and quartic gauge coupling (aTGC and aQGC respectively). An example can be taken from the ZZ channel [81] that can probe the ZZZ and $ZZ\gamma$ couplings. The SM contribution is very small for these couplings, mainly due to an intermediate state with a fermion loop ($Z \rightarrow \text{fermion loop} \rightarrow ZZ$). In BSM (for example supersymmetry), additional particles might contribute to the loop, hence increasing the triple gauge coupling [82]. The detection of an aTGC would be a clue of new underlying physics.

Using diboson processes to probe new particles has already been successfully used. In 2012, the Higgs boson was discovered by looking at different diboson channels such as the ZZ , WW and

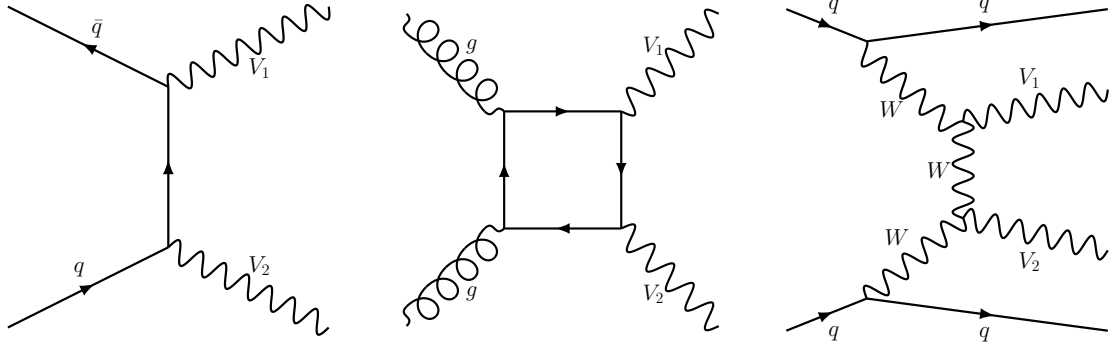


Figure 2.8: Examples of Feynman diagrams involved in diboson processes. The labels V_1 and V_2 denote two electroweak gauge bosons respecting the allowed couplings given in Section 2.1.3.

mostly $\gamma\gamma$ [5, 6]. The Feynman diagrams with the highest contributions for these channels are given in Fig. 2.11. The ZZ and $\gamma\gamma$ channels are still used today to set the tightest constraints on the Higgs boson mass [83, 84], with an estimate of $m_H = (125.25 \pm 0.17) \text{ GeV}$ [21]. The main backgrounds of the Higgs boson searches, as well as searches for new diboson resonances, are non-resonant diboson production. This emphasizes the need to have a good model for the diboson production.

Before the Higgs boson discovery, speculations were done on its mass. The $W^+W^- \rightarrow W^+W^-$ process helped to give an upper limit to the Higgs mass. Without contribution of the Higgs boson to the channel, the cross-section would be infinite [85]. This divergence is cancelled by the Higgs boson, and calculation of the cross-section led to a limit $m_H < 1 \text{ TeV}$.

2.2 Problems with the Standard Model

As was stated previously, only 3 of the 4 fundamental forces are introduced at the particle level: gravity, is not included in the SM. In general, this is not a problem for collider physics since the force of gravity would be negligible compared to any other. But when it comes to astrophysics, this might lead to a mismodelling of some phenomena. Close to a massive object, such as a black hole, or in the first moments after the big-bang, the gravitational force is sufficiently high that it is comparable to the other forces. In that case, gravity can not be neglected anymore. There are attempts to create new theories including gravity at the microscopic level, such as string theory [86] and quantum loop gravity [87].

The hierarchy problem tackles the issue of the Higgs mass. Theoretically, the mass of the Higgs boson would be much greater than the one experimentally observed [88]. The reason is that fermions and bosons loops impose large corrections to the mass via the Higgs boson propagator. However, fermions and bosons contributions are opposite: fermions contribute positively and bosons negatively. In absence of any relation between fermions and bosons in the SM, the Higgs mass is expected to be infinite. The presence of a new symmetry was proposed to explain the hierarchy problem. The Higgs boson mass might be fixed by introducing a whole new set of particles with properties linked to the SM particles. Such models are called Supersymmetry. The idea is that new bosons are associated to each SM fermion and new

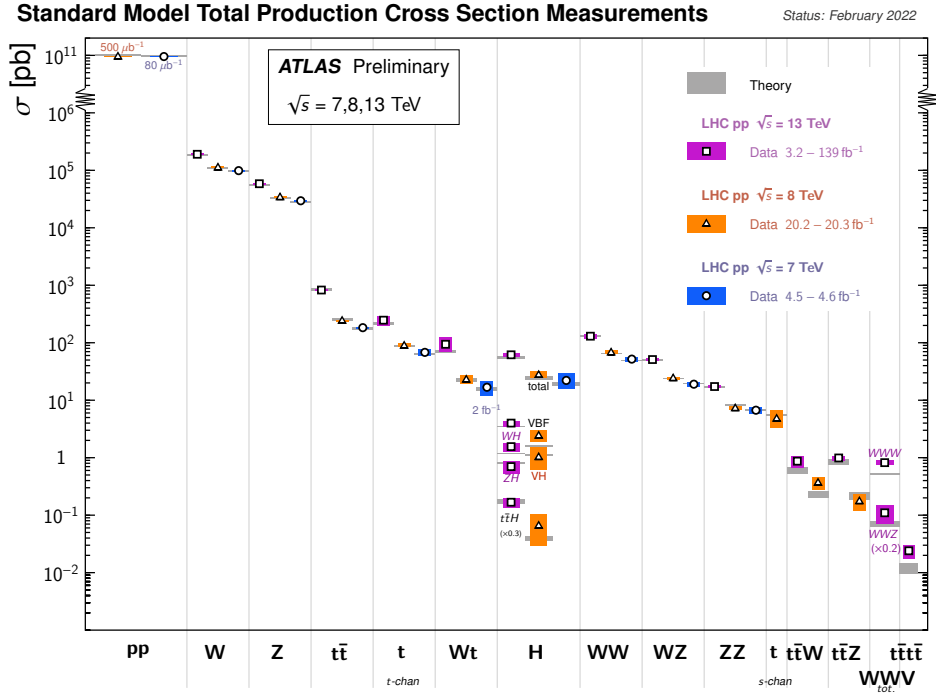


Figure 2.9: Cross-section of different processes of the SM as measured at the ATLAS detector. Figure taken from Ref. [76].

fermions to each SM boson. This implies that the content of elementary particles is more than doubled. Interestingly, supersymmetry would also be a prerequisite for string theory.

Experimentally, the most compelling evidence of the presence of new physics comes from astrophysics and cosmology. By looking at the velocity of objects in and around galaxies, they were shown to rotate faster than what would have been expected [89]. This led to the conclusion that galaxies are filled with a mass from an unknown origin: Dark Matter (DM). The presence of such material gives hints on some properties of hypothetical particles. For example, their low interaction with light (only via gravitational lensing) implies that they have no electric charge. The fact that they are still present billions of years after the formation of galaxies implies that they are (relatively) stable.

When it comes to general relativity, another mystery is the presence of so called dark energy. In 1998, first evidence emerged that the expansion of the universe is accelerating [90, 91]. Today, the main model for cosmology is the so called Λ -CDM [21], that refers to both dark energy (Λ) and cold Dark Matter (CDM). The issue is knowing the origin of dark energy. Quantum vacuum energy, a feature of QFT, has been proposed as an explanation. However, when calculations are made, the force created by such a phenomenon should be several orders of magnitude bigger than what is observed [92].

Recently, in 2022, new results seemed to show that the magnetic dipole moment of the muon might be underestimated by the SM [93]. This new result hints that there are some BSM processes. It is interesting to make a few remarks on this discovery. First, the significance of the observation, 4.5σ , does not satisfy the requirements of a discovery in particle physics (5σ). Moreover, theoretical calculations lead to conflicting results that can reduce the significance of the divergences [94], as shown in Fig. 2.12. The main difference between the diverse calculations is the treatment of the QCD contribution to the muon magnetic dipole moment. It is therefore

Diboson Cross Section Measurements

Status: February 2022

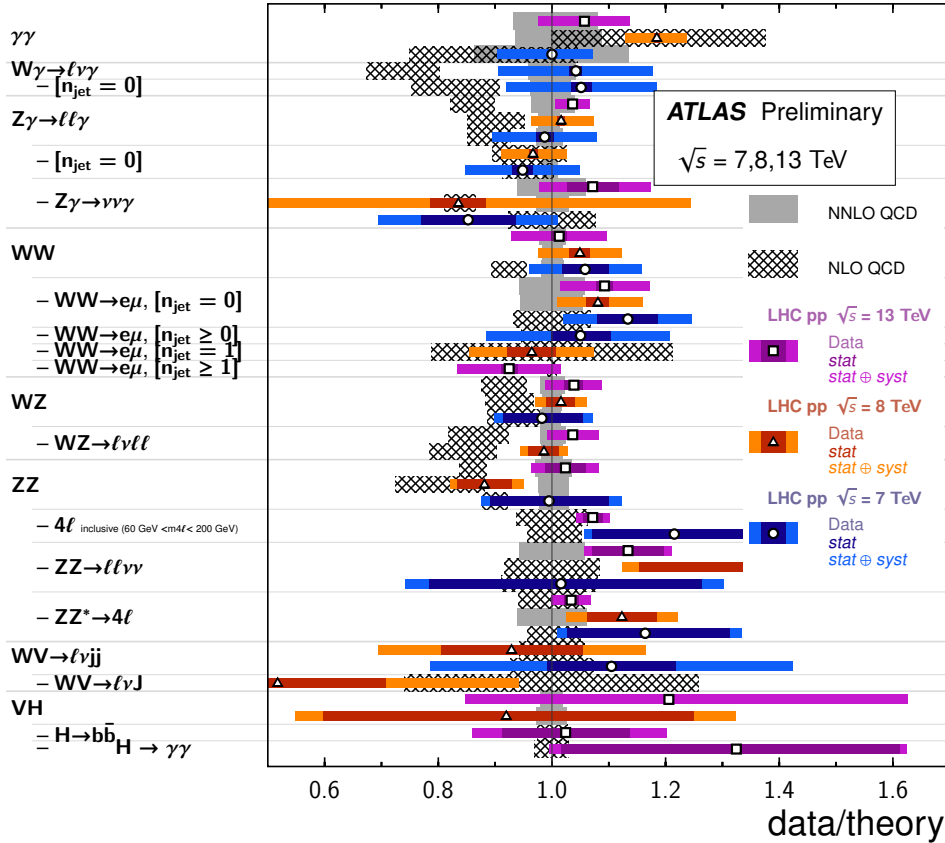


Figure 2.10: Comparison of the theoretical and measured cross-sections for the diboson processes measured at the ATLAS detector. Figure taken from Ref. [76].

not yet well understood if the anomalous magnetic dipole moment of the muon is indeed due to new physics processes or simply calculation issues.

Another conflict between experimental results and theory comes from strong CP violation. An account of this concern is given in the next section. The solution to said problem could also solve the issue of DM by introducing a new particle, the axion.

2.3 Axions and axion-like particles

Axions are hypothetical particles thought to explain the observation of strong CP symmetry conservation. Axions are spin-0 chargeless bosons which are DM candidates. Axion-like particles (ALPs) have a broader definition, even though the main characteristics remain the same. In this section, the main concepts surrounding axions will be introduced. Their hypothetical properties will be provided, before enlarging the scope and introducing ALPs. These concepts will be useful for Section 6, where the ALPs properties in a specific scenario are being constrained through the measurement of diboson cross-sections.

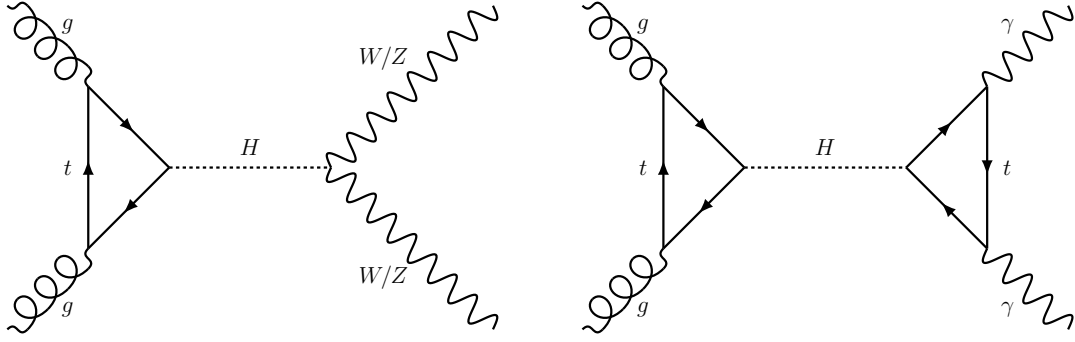


Figure 2.11: Feynman diagrams showing the Higgs boson production and decay processes that played a leading role in the Higgs boson discovery.

2.3.1 Axions

As stated previously, axions arise from the so-called strong CP problem, that is introduced hereafter. The QCD Lagrangian can include a CP violation term, also called Θ -term, as shown below [21, 98]:

$$\mathcal{L}_\Theta = -\bar{\Theta} \frac{\alpha_s}{8\pi} G_{\mu\nu}^a \tilde{G}^{\mu\nu,a}, \quad (2.6)$$

where $\bar{\Theta}$ is a free parameter in the SM, α_s the strong coupling constant, G the colour field strength defined as $\tilde{G}^{\mu\nu,a} = \varepsilon^{\mu\nu\lambda\rho} G_{\lambda\rho}^a$ (with ε the antisymmetric matrix with $\varepsilon^{0123} = 1$) and the term a is a sum over the colours.

As the parameter $\bar{\Theta}$ denotes an angle, its range is $-\pi < \bar{\Theta} < \pi$, and the expected value is in the order of $\bar{\Theta} \sim \mathcal{O}(1)$. Experimentally, the measurement of the neutron electric dipole moment set an upper bound of $|\bar{\Theta}| \lesssim 10^{-10}$ [99, 100].

This means that the CP violating term in QCD is experimentally heavily suppressed. Two phenomena can explain the previous. The first one would be a coincidence. The term $\bar{\Theta}$ can take any value so it is possible that, somehow, it is very low. Another explanation, more satisfactory from a theoretical point of view, is that the conservation of CP in the strong interaction is due to a new symmetry. This symmetry is called the Peccei-Quinn (PQ) symmetry and is noted $U(1)_{PQ}$ [101, 102].

The presence of a new symmetry introduces a new particle, the axion. It is a spin-0 boson which couples to the gluons with a term:

$$\mathcal{L}_a = \frac{a}{f_a} \frac{\alpha_s}{8\pi} G_{\mu\nu}^a \tilde{G}^{\mu\nu,a}, \quad (2.7)$$

where f_a is the decay constant. Combining Eq. (2.6) and (2.7), the CP violating term becomes:

$$\mathcal{L} = \left(\frac{a}{f_a} - \bar{\Theta} \right) \frac{\alpha_s}{8\pi} G_{\mu\nu}^a \tilde{G}^{\mu\nu,a}. \quad (2.8)$$

This lagrangian is at the ground state for the value $\langle a \rangle = f_a \bar{\Theta}$, meaning that there is a spontaneous symmetry breaking. This involves that the axion acquires a mass, that is given by:

$$m_a = 5.7 \times \left(\frac{10^9 \text{ GeV}}{f_a} \right) \text{ meV}. \quad (2.9)$$

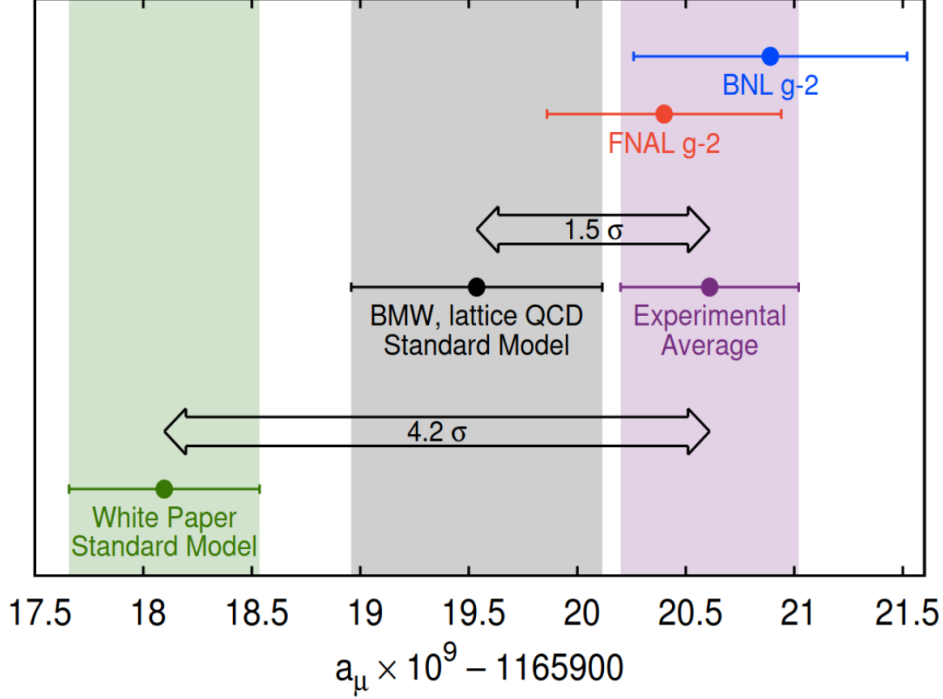


Figure 2.12: Results for the muon anomalous magnetic dipole moment ($a_\mu = (g_\mu - 2)/2$). Experimental data are from Brookhaven E821 experiment (BNL) [95] and Fermilab E989 (FNAL) [93], and computation from Muon g-2 Theory Initiative (white paper) [96] and the Budapest-Marseille-Wuppertal Collaboration (BMW) [94]. Figure taken from Ref. [97].

For axions, the constraint of the QCD strong CP conservation imposes that all the properties of the particle depends only on the decay constant f_a . The coupling of axions with gauge bosons implies the interaction Lagrangian [103]:

$$\mathcal{L} = \frac{g_{agg}}{4} aG\tilde{G} + \frac{g_{aWW}}{4} aW\tilde{W} + \frac{g_{aZZ}}{4} aZ\tilde{Z} + \frac{g_{a\gamma\gamma}}{4} aF\tilde{F} + \frac{g_{aZ\gamma}}{4} aF\tilde{Z}, \quad (2.10)$$

where the different coupling constants are [103, 104]:

$$g_{agg} = -\frac{1}{2\pi f_a} \alpha_s, \quad (2.11)$$

$$g_{aWW} = -\frac{1}{2\pi f_a} \frac{\alpha_{EM}}{\sin^2(\theta_W)} \left(\frac{L}{N} - 0.75 \right), \quad (2.12)$$

$$g_{aZZ} = -\frac{1}{2\pi f_a} \frac{\alpha_{EM}}{\sin^2(\theta_W) \cos^2(\theta_W)} \left(\frac{Z}{N} - 0.52 \right), \quad (2.13)$$

$$g_{a\gamma\gamma} = \frac{1}{2\pi f_a} \alpha_{EM} \left(\frac{E}{N} - 1.92 \right), \quad (2.14)$$

$$g_{aZ\gamma} = -\frac{1}{2\pi f_a} \frac{\alpha_{EM}}{\sin(\theta_W) \cos(\theta_W)} \left(\frac{2R}{N} - 0.74 \right). \quad (2.15)$$

The constants E , L , Z , R and N are coefficients which are model dependent. For example, the two main models are the so called DFSZ [105, 106] and KSVZ [107, 108] giving the values $E/N = 8/3$ and $E/N = 0$ respectively [109]. In practice, the value of E/N can take many different values depending on the considered model.

For a QCD axion, all the properties are given depending on a single parameter f_a (or m_a) in a given model. This is due to the strong CP conservation that imposes constraints on the mass and coupling constants. But a larger class of bosons which share some of the axions properties, but do not solve the strong CP violation issue, can be defined: axion-like particles.

2.3.2 Axion-like particles

An axion-like particle (ALP) is a spin-0 boson that arises from a PQ symmetry but without cancelling the strong CP violation term. The removal of this constraint implies that the mass, the couplings, and the decay constant are independent [21, 110]. This allows for a larger phase-space to be explored.

Even though the phase-space is multi-dimensional, all the couplings are not completely independent. Due to the mixing implied by the Higgs mechanism, the couplings between the different electroweak bosons must obey the following relation [103]:

$$g_{aZZ} = - \left(\cos^2(\theta_W) + \frac{\sin^4(\theta_W)}{\cos^2(\theta_W)} \right) g_{aWW} + \frac{\cos^3(\theta_W)}{\sin(\theta_W)} g_{aZ\gamma} + \left(1 + \cos^2(\theta_W) + \frac{\sin^4(\theta_W)}{\cos^2(\theta_W)} \right) g_{a\gamma\gamma}. \quad (2.16)$$

This equation comes from the Higgs mixing mechanism of the gauge couplings.

The existence of ALPs is partly motivated by their possible presence in string theory [110]. Moreover, ALPs could be DM candidates. This statement does not depend on the mass of the ALPs. This is due to the fact that they are bosons, thus are exempt from the Pauli exclusion principle. For fermions, the amount of DM in the universe imposes DM candidates to have a certain mass, since two fermions can not be in the same state. This is not true for bosons, e.g. ALPs, although cosmological models might impose limits.

If axions or ALPs existed, one might wonder how it can be detected. State of art constraints set on the axions can be found in Ref. [109], and the different techniques will be summarized here. Strong constraints on the ALPs existence are set by astrophysical sources. For example, if DM was actually made of ALPs, its mass and coupling to matter would have an influence on the inflation phase [111] and the cosmic microwave background [112]. Thus, data from cosmological observations can help constrain the axion mass. As ALPs would interact with photons, its properties would influence other observations such as stellar evolution [113], or light polarisation in the vicinity of black holes [114].

Along with astrophysical observations, laboratory experiments have been carried out on the axions. This involves some axion specific experiments, which aim at transforming axions to detectable photons. At DESY, several such project are being built [115] such as ALPS II [116], babyIAXO [117, 118] and MADMAX [119, 120]. In all the listed experiments, ALPs are expected to be detected by transforming them into a photon by using intense magnetic fields.

Apart from experiments specifically designed to detect ALPs, accelerators also look for them, along with many other BSM particles. A summary of the different searches for ALPs at the LHC can be found in Ref. [121]. The search focuses mainly on four directions: the resonance in the $\gamma\gamma \rightarrow \text{ALP} \rightarrow \gamma\gamma$ process [122, 123], the Higgs boson decay into ALPs [124, 125, 126], the mono-X signatures where the ALPs are invisible and hinted via missing energy [127, 128, 129], and the fixed-target (or beam dump) experiments studying at pion decays [130]. However, these studies generally work on ALPs with relatively high masses (in the order of GeV to several

hundreds of GeV). This range is incompatible with the sub-eV limits on QCD axions (see Fig. 2.13). A new technique for probing ALPs down to very low masses has recently been developed [131] and will be described extensively in Section 6.

Since there is only one free parameter, QCD axions are much easier to constrain than ALPs. Limits set experimentally on the mass of the axions are shown in Fig. 2.13. In general, ALPs boundaries are represented in 2D plots where the abscissa represents the mass and the ordinate is a coupling constant. A representation of the limits set on the photon coupling constant by astrophysical, laboratory and accelerator experiments are shown in Fig. 2.14.

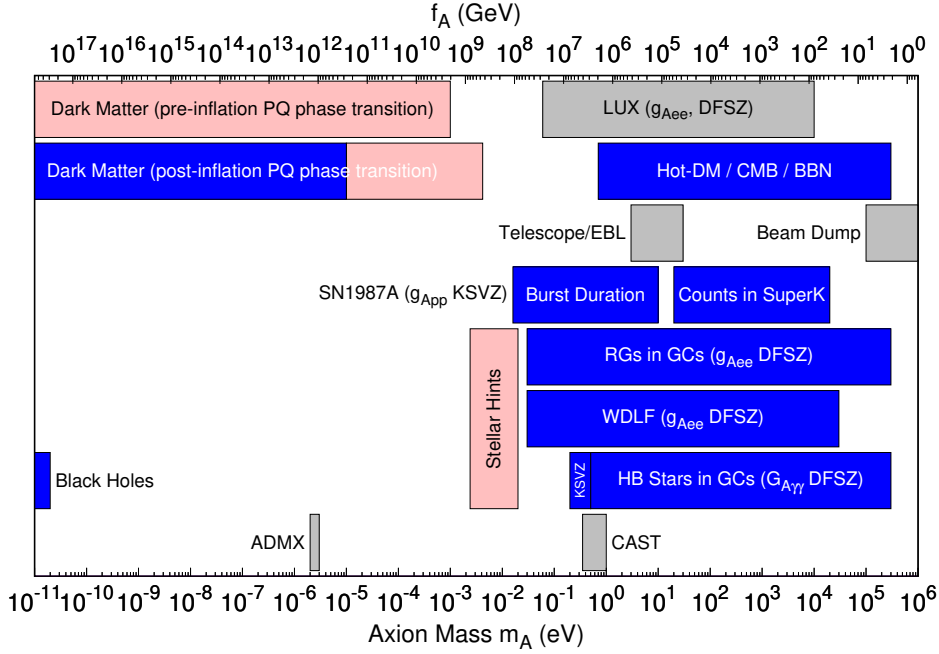


Figure 2.13: Exclusion ranges on the QCD axion mass, as of 2018. The blue and grey areas correspond to exclusions set by astrophysical observation and axion experiments respectively. The pink areas correspond to allowed regions where axions might explain experimental findings. Figure taken from Ref. [132].

2.3.3 Off-shell ALPs

This part focuses on the off-shell production of ALPs, where the energy scale of the collision between two particles is typically much higher than the mass of the ALPs and much lower than the decay constant f_a . Mathematically, this is expressed by:

$$m_a^2 \ll \hat{s} \ll f_a^2. \quad (2.17)$$

Fig. 2.13 shows that astrophysical constraints force the QCD axions to have a low mass, in the sub-eV range (corresponding to a decay constant $f_a > 10^3$ TeV). In the LHC, this mass scale would fit the requirements in Eq. (2.17) since the typical $\sqrt{\hat{s}}$ range is around 10^2 GeV.

When satisfying the condition in Eq. (2.17), an effective field theory [131] associated to the ALP vertices can be built that has the following Lagrangian:

$$\delta\mathcal{L}_{eff} \supset c_{\tilde{G}}\mathcal{O}_{\tilde{G}} + c_{\tilde{B}}\mathcal{O}_{\tilde{B}} + c_{\tilde{W}}\mathcal{O}_{\tilde{W}} + c_{a\Phi}\mathcal{O}_{a\Phi}, \quad (2.18)$$

where θ_W is the Weinberg angle. Eq. (2.22) will be important in Section 6.5 to relate the limits set with the $Z\gamma$, WW [134], $\gamma\gamma$ and ZZ channels [131]. The term $c_{a\Phi}\mathcal{O}_{a\Phi}$ in Eq. (2.18), after symmetry breaking, becomes the coupling of the axions with the quarks and leptons.

2.4 Monte-Carlo generators

MC generators help to simulate the complexity of collisions, starting from Feynman diagrams and ending with a complete event as seen by the detector. For that, the simulation is divided into several levels, defined below:

- Parton level: The simulation is done with free quarks and gluons, and some of the unstable particles (for example Z bosons or W bosons) have not decayed.
- Particle/hadron level: The quarks and gluons are confined into hadrons and the unstable particles have decayed. This level actually describes the "true" particles before they hit a particle detector. In the rest of this work, this stage is called "truth level".
- Detector/reconstruction level: The truth level is passed through a simulation of the detector to have results that can be compared to the data. This stage is also called "reco level".

Progression through the levels makes the simulation closer to what happens in data.

An example of the complexity of a process is shown in Fig. 2.15. In addition to the hard process (Feynman diagram of the signal event), three main properties must be taken into account in the simulation of a process: the parton distribution function (PDF), the parton showers (PS) and the hadronisation. PS and hadronisation can be computed separately from the hard process thanks to the QCD factorization theorem, which states that hard and soft scales can be treated separately [135].

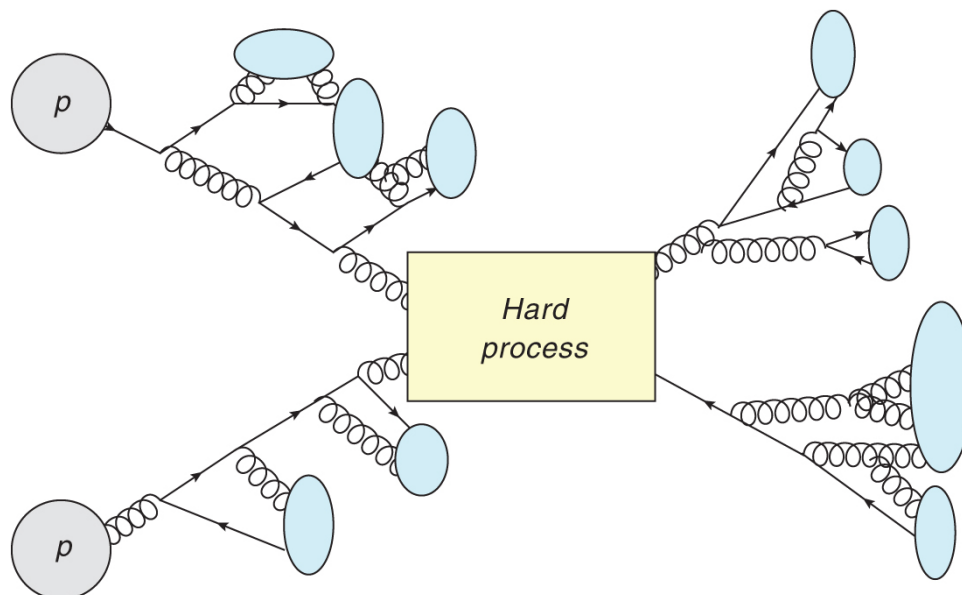


Figure 2.15: Representation of a process happening in MC simulations. Figure taken from Ref. [136].

2.4.1 Parton distribution functions

The PDF is an important notion for the colliding protons, on the left side of Fig. 2.15. The PDF encodes the properties of the partons (quark or gluon) emerging from the proton (or any hadron used for collision). As protons are composite particles, each constituent carries a fraction of the total momentum. This momentum fraction, noted x_i , ranges from 0 (the parton has no energy) to 1 (the parton carries the whole proton energy). The total cross-section of two colliding protons (1 and 2) has the form:

$$\sigma = \sum_{i,j \in \{q,\bar{q},g\}} \int_0^1 dx_1 \int_0^1 dx_2 f_i(x_1) f_j(x_2) \hat{\sigma}_{ij}, \quad (2.23)$$

where the PDF $f_i(x)$ is the probability to find a particle of type i with a momentum fraction x inside the proton.

The PDF depends on the energy scale of the system q^2 . At low energy, the proton can be approximated as two up quarks and a down quark, but this picture becomes incorrect at high energies. At energies close to the LHC, gluons produce many quark-antiquark pairs. This phenomena must be taken into account when modelling the PDF, as shown in Fig. 2.16.

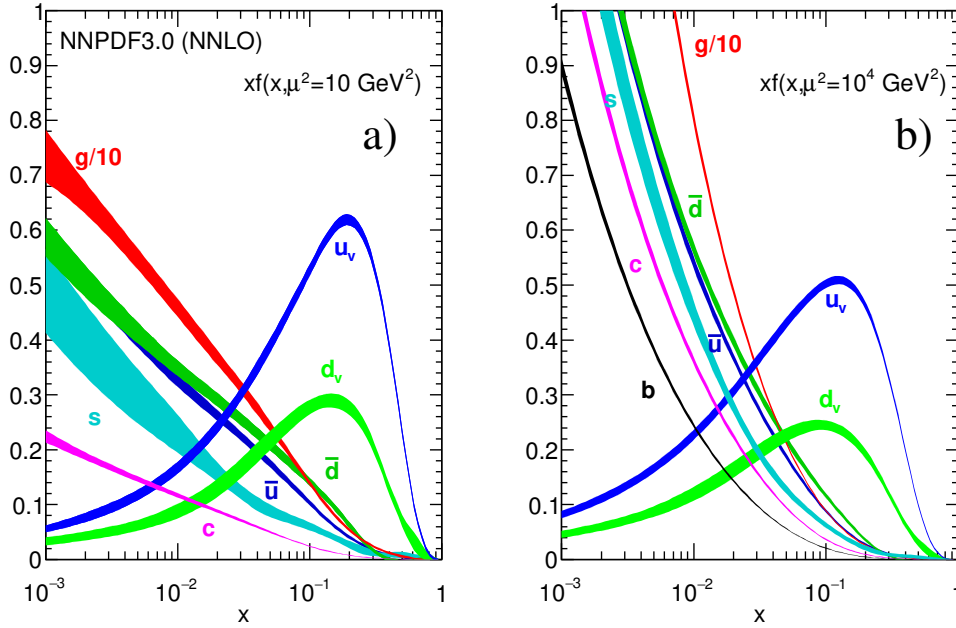


Figure 2.16: PDF for quarks and gluons in protons at different energy scales. Figure taken from Ref. [137].

MC simulations use PDF sets to obtain the momentum of initial state partons. This is an important part of the generator since it is a major source of uncertainty [138]. Results from different experiments are used to adjust the parameters of the PDF sets.

2.4.2 Hard process and Sudakov logarithms

The hard process is computed with matrix elements from the Feynman diagram prescription. This is therefore a fixed-order computation in α_s . For example, MATRIX proposes computations up to NNLO [139]. Recently, some channels have experimental data with sufficiently

small uncertainties, that the electroweak correction of some QED related processes can not be neglected.

Such computation also contains diagrams including outgoing partons. Using matrix elements with external partons and that are parton showered can lead to a double counting of some diagrams. To overcome this issue, some generators combine both methods. This step is commonly called "merging". This is done to improve the precision on parton properties: the PS models soft parton activity whilst the matrix element models hard jet activity.

One of the challenges of fixed order computation using matrix elements is to take into account the Sudakov logarithms. The Sudakov logarithms are well-known in the field of QCD and appear in the form:

$$\alpha_s(\mu)^n \ln^m \frac{\mu}{\mu_0}, \quad (2.24)$$

where μ and μ_0 are different scales, n the order of computation and $m \leq 2n$.

Such factors appear in many QCD computations, for example, in the running coupling constant calculation [140]. This feature of fixed-order calculations on α_s (at NⁿLO) results in problematic logarithms. A perturbative expansion is done with fixed-order terms and relies on the fact that the coupling constant is small ($\alpha_s(M_Z) \approx 0.12$ can be considered $\ll 1$), but also that the coefficients remain reasonable. The logarithm can reach high values and therefore, dominate the series.

To account for this issue, the computation can be done around the logarithms. This process is called resummation. In that case, the calculation is called "leading logarithm" (LL) if the expansion is done around the \ln^m term, next-to-leading logarithm (NLL) for \ln^{m-1} , etc. Often, the QCD calculations are implemented in MC generators with a certain order of α_s and logarithm, referred to as NⁿLO+N^mLL.

2.4.3 Parton showers, hadronization and detector simulation

The PS approach is used to mimic the soft emission of QCD related particles. They extend the fixed order computation, and complete the same target as the resummation approach on that respect. The PS approach used is based on the probability for a parton to emit particles. The computation relies on the virtuality of an emitted parton which differentiates hard and soft processes:

$$q^2 = z(1-z)\theta^2 E^2, \quad (2.25)$$

where E is the emitted parton energy, θ the angle of emission and z the energy fraction carried by the emitted parton.

The probability that there is no resolvable parton shower between two virtualities Q and Q_0 is given as a Sudakov form factor:

$$\Delta_i(Q^2, Q_0^2) \sim \exp \left\{ -C_F \frac{\alpha_s}{2\pi} \ln^2 \frac{Q^2}{Q_0^2} \right\}. \quad (2.26)$$

Here, the cutoff Q_0 is chosen to avoid divergences and corresponds to the inability of the detector to detect a particle with too low momentum or small angle of emission.

Following the hard matrix element and soft-collinear PS sub-processes, the remaining partons must be hadronised. This is due to strong confinement, in which a free quark or gluon can not

exist alone (the colour charge must be zero). There are mainly two procedures used to achieve that: the Lund string model [141] and the cluster hadronisation [142].

At this point, the process is at the truth level. To compare the simulations to the experimental data, a simulation of the detector is needed. Some softwares are specially designed for that purpose, such as GEANT4 [143] which includes the ATLAS detector.

Many other subtleties are added in the MC simulations, such as the intrinsic transverse momentum carried by the partons in the hadrons, pileup, or multiple partonic interactions involving several partons of two colliding hadrons. However, the main procedure described previously consists of using the PDF of the colliding particles, computing the hard process, proceeding to the PS, hadronizing and simulating the detector response.

3 | The LHC and the ATLAS experiment

3.1 The Large Hadron Collider

3.1.1 Design

The Large Hadron Collider (LHC) is a particle accelerator based at CERN (Centre Européen pour la Recherche Nucléaire), located at the border between France and Switzerland in the region of Geneva [144]¹. With a circumference of 26.7 km, it is the largest collider ever built [21]. As the name indicates, the LHC accelerates and collides hadrons, mainly protons, but also heavy-ion nuclei such as xenon (Xe) and lead (Pb)².

The LHC was built in the former tunnel of the Large Electron-Positron Collider (LEP, 1989-2000). The goal of the LHC compared to LEP, was to achieve higher energies. The aim was to discover the Higgs boson and, potentially, to find hints of theories Beyond Standard Model.

The architecture of the LEP tunnel was a constraint for the design of the LHC and its maximum energy for two reasons. First, the tunnel consists of 8 sections each corresponding to an arc followed by a long straight line. This pattern was adapted for electrons, whose acceleration in the straight lines compensated the energy loss by synchrotron radiation, expressed as:

$$\frac{dE}{dt} \propto \frac{E^4}{m^4 r^2} \quad (3.1)$$

with r being the curvature radius of the accelerator. However, hadrons are more massive, implying that synchrotron radiation is reduced and less curvature (or stronger magnetic fields) are needed to deflect their trajectory. Second, due to the limited space available in the tunnel, a two-bore magnet design (shown in Fig. 3.1) is hosting the two opposing direction beams of hadrons.

To follow the LHC curvature, 1232 main dipole magnets are placed to bend the particle's trajectory. In addition, quadrupoles are used to keep the particles in a beam (they tend to repel each other due to the electric charge), and sextupoles, octupoles and decapoles act as correctors to the trajectory. All the magnets are made of niobium-titanium (NbTi) cables cooled down to 2 K to reach a superconducting regime. This allows the magnets to reach a magnetic field up to 8 T. Each of the straight lines contains 16 radiofrequency (RF) cavities (8 for each beam direction) responsible for the particles acceleration. The RF cavities deliver an electric field oscillating at around 400 MHz and are able to accelerate the particles up to 16 MeV per LHC lap.

Besides the LHC, many other, mostly older accelerators are located and used at CERN, mainly to accelerate protons prior to entering the LHC. A diagram representing the CERN accelerator complex is shown in Fig. 3.2, and the different steps of the proton acceleration are described in

1. Section 3.1 is mainly based on information found in Ref. [144], unless another reference is given.

2. The rest of the thesis only focuses on the case of the proton-proton (pp) collisions



Figure 3.1: Picture of the LHC with a 3D cutaway artist's impression. The proton beams are accelerated in opposite directions along the red lines. Figure taken from Ref. [145].

this paragraph. First, protons are produced by stripping the electrons from a hydrogen gas using an electric field. The protons are then sent to a linear accelerator (Linac 2 until 2020, replaced by the Linac 4 afterward). At the exit of this first accelerator, protons have reached an energy of 50 MeV and enter the Proton Synchrotron Booster. They are boosted up to 1.4 GeV before being injected in the Proton Synchrotron which accelerates them to 25 GeV. The Super Proton Synchrotron is the last step for protons before entering the LHC with an energy of 450 GeV and reaching the final energy of 6.8 TeV.

It takes time for protons to fly through the whole accelerator complex. The time between the end of a physics run and the beginning of the next run is called turnaround and is measured to be 6 h to 7 h on average during the period 2015-2018 [147]. Different processes contribute to the turnaround (acceleration, stabilisation, faults,...), including the injection and ramp up. The injection is the time for the protons to fill the LHC, and lasts about 70 min. Once in the LHC, protons are ramped up to reach their maximal energy requiring a further 20 min [148]. Thereafter (and after ensuring to have a stable beam), the turnaround is over and the physics run can start. This lasts around 8 h before the protons remaining in the beams are dumped.

During a physics run, protons collide at four different points on the ring, called interaction points (IPs). They host the four main detectors, where the experiments are carried out:

- ATLAS on IP1: general-purpose detector.
- CMS on IP5: general-purpose detector.
- ALICE on IP2: detector focused on heavy-ion physics.
- LHCb on IP8: detector focused on b -quark physics.

Smaller experiments are placed around the IPs to search for physics for which larger detectors are not adapted. For example, FASER [149] and SND@LHC [150] are experiments placed in the forward region (close to the beam line) of IP1, and look for neutrinos and weakly interacting

The CERN accelerator complex Complexe des accélérateurs du CERN

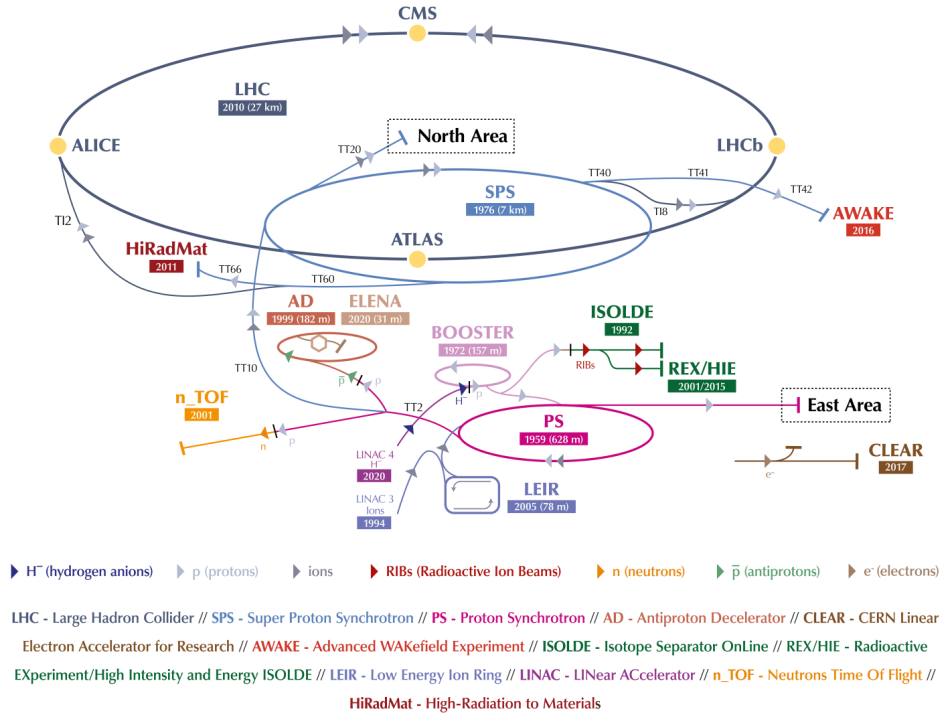


Figure 3.2: CERN accelerator complex. Figure taken from Ref. [146].

BSM particles. Also in the forward region of the IP1 lies the LHCf experiment [151], studying the neutral pions and neutrons to have a better understanding of cosmic rays. In the IP5 forward region, the TOTEM experiment [152] measures the proton cross-section and aims at collecting data to have a better understanding of the proton structure. Finally, the MoEDAL [153] experiment, placed at IP8, searches for BSM particles such as magnetic monopoles, dyons, or other exotic particles.

3.1.2 Energy

As stated, the LHC is a 26.7 km circumference ring which can accelerate, as of 2023, protons up to an energy of 6.8 TeV. These two properties are tightly linked, since the radius of curvature r of a particle's trajectory depends on the momentum p of the particle ($p = \sqrt{E^2 - m^2}$) and the dipole magnetic field B used to bend the beam:

$$r = \frac{p}{qB}, \quad (3.2)$$

where q is the magnitude of the charge of the particle. Therefore, it is not surprising that the LHC being the largest particle collider, is also the one accelerating protons to the highest energy.

The great energy applied to particles by the LHC is optimized by the use of two opposing direction beams. This leads to a center-of-mass energy, which is simply the sum of the energy of a particle in each beam:

$$\sqrt{s} = 2E, \quad (3.3)$$

where E is the energy of one particle (see Appendix B for an proof of this formula).

At the LHC, in 2022, the proton–proton collisions have a center-of-mass energy of $\sqrt{s_{pp}} = 13.6$ TeV. We can compare this value with a fixed-target experiment, where the proton would hit a target at rest in the laboratory frame. If a proton accelerated at $E = 6.8$ TeV was colliding a fixed target, the center-of-mass energy would be $\sqrt{s_{fix}} \approx 0.11$ TeV. For heavy-ion nucleus, during Run 2, the center-of-mass energy per nucleon pair is $\sqrt{s_{NN}} = 5.02$ TeV for Pb–Pb collisions [147], and $\sqrt{s_{NN}} = 5.44$ TeV for Xe–Xe collisions [154].

Although the energy reached 13.6 TeV in 2022, this thesis analyzed data collected during Run 2 only (period 2015-2018), with an energy $\sqrt{s_{pp}} = 13$ TeV (see Section 3.1.4).

3.1.3 Luminosity

Along with the energy, the amount of collisions is also an important quantity. Indeed, the precision of an analysis is related to the number of events, which in turn is proportional to the quantity of collisions occurring in the IP. This principle is critical for rarer processes, but is also important for precision measurements.

In a collider, the rate of events for a process is related to the instantaneous luminosity L as follows:

$$\frac{dN}{dt} = \sigma \times L, \quad (3.4)$$

where dN/dt is the number of event per unit of time and σ the cross-section for the process. The luminosity is often expressed in $\text{cm}^{-2} \text{s}^{-1}$. In an analysis, the total number of events N is given by:

$$N = \sigma \times \int L(t) dt. \quad (3.5)$$

$\int L(t) dt$ is called the integrated luminosity and is usually expressed in barn ($1 \text{ b} = 1 \times 10^{-28} \text{ m}^2$).

The instantaneous luminosity is expressed as:

$$L = \frac{N_b^2 n_b f_{rev} \gamma_r}{4\pi \epsilon_n \beta^*} F, \quad (3.6)$$

where $f_{rev} \approx 11$ kHz is the revolution frequency of protons and $\gamma_r = E/m$ (≈ 6900 for protons accelerated at 6.5 TeV) is the relativistic gamma factor. The other parameters are introduced below, and their values can be found in Table 3.1.

In the LHC, protons are not accelerated one by one but in bunches, which are packs of around $N_b \approx 1 \times 10^{11}$ protons (N_b is the number of particles per bunch). These bunches are separated from each other by a minimum of about 25 ns, with around $n_b \approx 2500$ bunches to fly at the same time in the beam pipe (n_b is the number of bunches per beam).

Due to the quadrupole magnets, protons oscillate around the beam center. This phenomenon is called betatron oscillations. In first approximation, this oscillation is sinusoidal. Therefore, the trajectory of protons can be drawn as an ellipse in the $(x, dx/dz)$ plane. The ellipse has then an area $\pi \epsilon$ which defines the transverse emittance ϵ , and a beta function β defined as $x_{max} = \sqrt{\epsilon \beta}$ where x_{max} is the maximum deviation from the beam center [155].

When the bunches are colliding, they can not collide completely head on. There is still an angle θ_c between the two beams, as shown in Fig. 3.3 which introduces a reduction factor [21]:

$$F = \left(1 + \left(\frac{\sigma_z}{\sigma^*} \tan \frac{\theta_c}{2} \right)^2 \right)^{-1/2}, \quad (3.7)$$

with σ_z the root mean square (RMS) bunch length and σ^* the transverse RMS beam size.

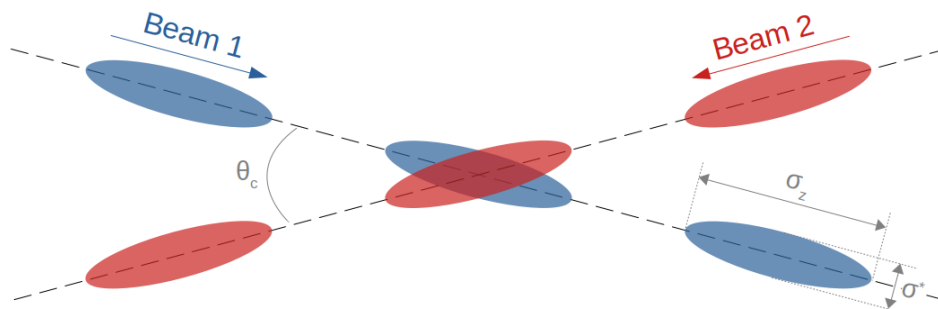


Figure 3.3: Schematic beam collision geometry at the LHC.

Another relevant parameter to mention in relation to luminosity is the number of interaction per bunch crossing μ . This number is given by the formula below:

$$\mu = \frac{L\sigma_{inel}}{n_b f_{rev}}, \quad (3.8)$$

where σ_{inel} is the pp inelastic cross-section ($\sigma_{inel} = 80$ mb). On average, when two bunches were crossing at the LHC between 2015 and 2018, more than 30 proton–proton interactions occurred, as shown in Fig. 3.4.

Out of all the collision occurring during a bunch crossing, only one might results in particles with enough energy to be of interest. The other collisions lead to a source of background called in-time pileup. When a particular final state is studied, some particles might be interpreted as being part of the process while actually coming from a different collision. This notion is a challenge for analyses at the LHC because it affects the measurement by adding an additional energy contribution. Pileup can also have different sources like another particle hitting the same detector before the electronics integration time (out-of-time pileup), particles in the LHC cavern hitting the detector (cavern background), protons interacting with the beam pipe (beam-halo events) or protons interacting with residual gas in the beam pipe (beam gas events) [157].

3.1.4 LHC Runs

LHC data are separated in "runs" which are periods of data taking. Runs are separated by shutdowns (LS for Long Shutdown) where the LHC and the detectors can be upgraded and renovated. Fig. 3.5 shows the schedule for the LHC and HL-LHC. The details of the different runs are discussed below.

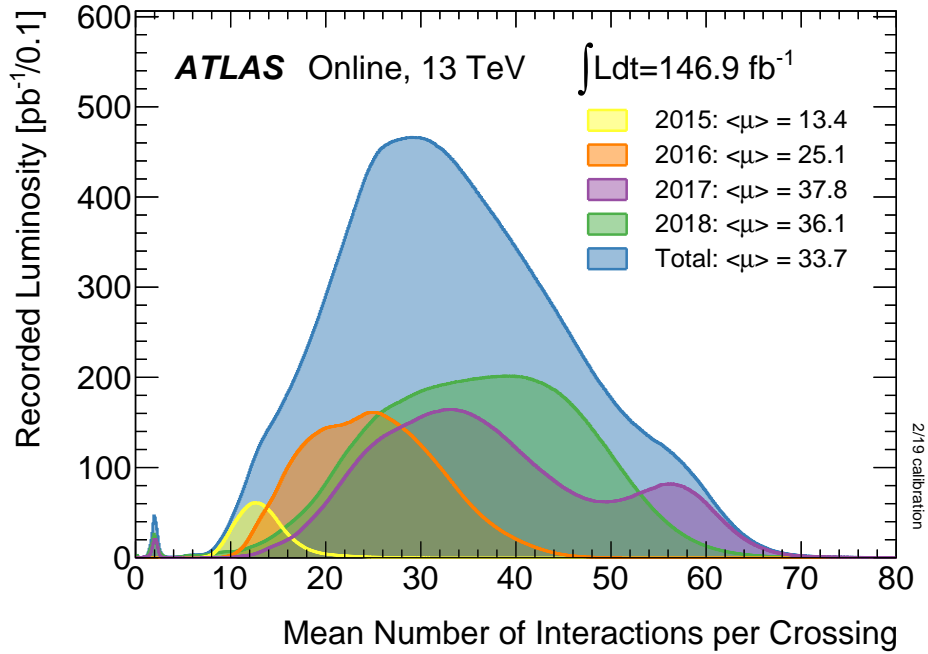


Figure 3.4: Mean number of interaction per crossing recorded during Run 2 for proton–proton collisions. Figure taken from Ref. [156].

Run 1, 2 and 3

Run 1 occurred during the period 2010–2012 and its greatest achievement was the discovery of the Higgs boson announced in July 2012. The center-of-mass energy of the collisions was $\sqrt{s} = 7 \text{ TeV}$ to 8 TeV and the integrated delivered luminosity on IP1/5 (ATLAS/CMS) was about 29 fb^{-1} [159, 160]. The choice to accelerate the beam no higher than 8 TeV was done because of defective pieces in the interconnections between LHC magnets. This issue was solved during the long shutdown 1 (LS1) occurring between 2013 and 2015 [161].

Run 2 took place in the period 2015–2018 with an energy increased to $\sqrt{s} = 13 \text{ TeV}$. The integrated delivered luminosity by the LHC was around 160 fb^{-1} , which means that the amount of data during that run was much greater than in Run 1 [162, 163]. However, the delivered luminosity is greater than the recorded luminosity by the ATLAS detector which was 147 fb^{-1} for Run 2. The difference is due to problems on the detector or time for ramping up the voltage of the tracking systems (occurs once the beam has been declared stable). In the rest of this thesis, the luminosity for Run 2 will be given as 139 fb^{-1} . This corresponds to the luminosity of events "good for physics", which passed a data quality requirement. This data quality is based mainly on the absence of defects in the detector that would impair the data-taking process [164]. However, within a data taking period, the conditions are not entirely homogeneous, with some differences depending on the year or even moment of physics run. Table 3.1 highlights the main parameters of Run 2 for each year. Fig. 3.4 shows the distribution over the mean number of interaction per crossing recorded.

Run 3 started in spring 2022 and is expected to go on until 2025 and to reach an integrated luminosity of 200 fb^{-1} to 250 fb^{-1} . The center-of-mass energy is slightly higher than Run 2, achieving a value of $\sqrt{s} = 13.6 \text{ TeV}$ [165].

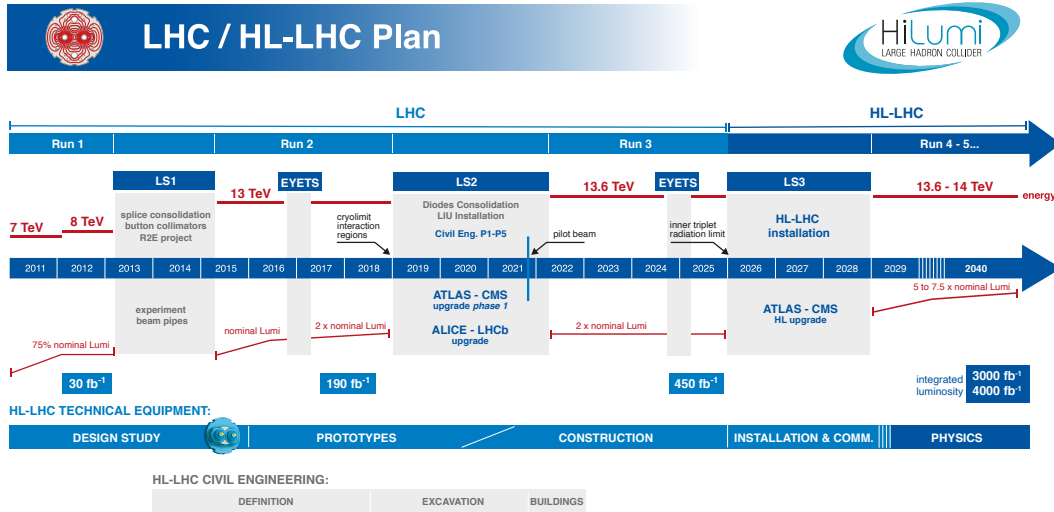


Figure 3.5: Schedule of the LHC runs, as expected in February 2022. Figure taken from Ref. [158].

Parameter	2015	2016	2017	2018
Proton energy (TeV)	6.5	6.5	6.5	6.5
Peak Luminosity L ($10^{34} \text{ cm}^{-2} \text{ s}^{-1}$)	0.5	1.4	2.1	2.1
Integrated Luminosity (fb^{-1})	4.2	39.7	50.6	66
Number particles per bunch N_b (10^{11})	1.0–1.25	1.0–1.25	1.0–1.25	1.0–1.25
Number bunch per beam n_b	2244	2220	2556	2556
Emittance ϵ_n (μm)	3.5	2.2	2.2	1.9
Beta function at collision point β^* (cm)	80	40	40–30	30–25
Turnaround time (h)	6–7	7.1	6.2	6.0

Table 3.1: Parameters of the LHC beam during Run 2. Data taken from Ref. [147].

High-Luminosity LHC

The High-Luminosity LHC (HL-LHC) is a project mainly aiming at increasing the luminosity of the LHC from 2029 to 2038. This will be preceded by a 3 years period of shutdown (2026–2028) where the LHC and the detectors will be upgraded. The luminosity is expected to reach an instantaneous value of $5 \times 10^{34} \text{ cm}^{-2} \text{ s}^{-1}$ to $7.5 \times 10^{34} \text{ cm}^{-2} \text{ s}^{-1}$ and to achieve an integrated average of 300 fb^{-1} per year, meaning that there would be twice as much data each year as collected in the full Run 2. This will result in a mean number of interactions per crossing around $\langle \mu \rangle = 140$. Furthermore, the center-of-mass energy should increase to $\sqrt{s} = 14 \text{ TeV}$ [166].

3.2 The ATLAS detector

The ATLAS detector is located around the interaction point 1 and is one of the two general purpose experiments at the LHC, along with CMS. ATLAS is a cylindrical detector around

the beam line, measuring 25 m in diameter and 44 m in length. These dimensions make it the biggest detector at CERN [167]³.

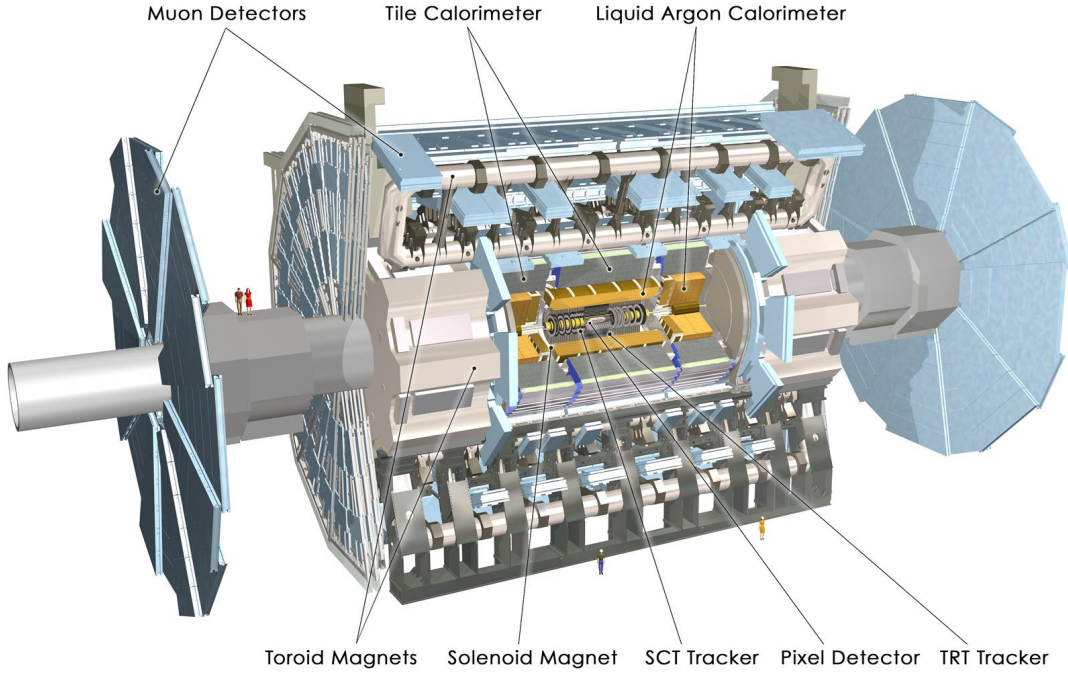


Figure 3.6: Cutaway view of the ATLAS detector with the different constituting elements. Figure taken from Ref. [168].

To describe the detector properties or the path of a particle in it, the coordinate system must be defined. In ATLAS, the x -axis is horizontal and pointing toward the center of the LHC, the y -axis is vertical and pointing upward, the z -axis is in the direction of the beam, and the origin is at the nominal collision point. It is however often more convenient to use coordinates focused on angles where the azimuthal angle ϕ is defined as the angle around the beam axis (angle from the x -axis of the projection on the transverse plan) and the polar angle θ is the angle from the beam axis.

However, we can often find other coordinate systems to replace the polar angle by a more physics oriented coordinate, the rapidity, defined as

$$y = \frac{1}{2} \ln \frac{E + p_z}{E - p_z}, \quad (3.9)$$

with E the energy of the particle(s) and p_z the projection of the momentum on the z -axis. For ultra-relativistic particles ($E \gg m$), rapidity is equivalent to pseudorapidity defined as

$$\eta = -\ln \tan(\theta/2). \quad (3.10)$$

The latter is widely used to describe the ATLAS detector. Finally, a pseudorapidity-azimuthal angle between two points can be defined as

$$\Delta R = \sqrt{\Delta\eta^2 + \Delta\phi^2}. \quad (3.11)$$

³ Section 3.2 is mainly based on information found in Ref. [167], unless another reference is given.

The ATLAS detector is made of three main layers, nested around the beamline. From the inside out, there is:

- The Inner Detector (ID) which purpose is to measure precisely the tracks of the charged particles in a 2 T magnetic field.
- The calorimeters which are stopping and measuring the energy of electrons, photons and hadrons.
- The muon spectrometer which is measuring the energy and momentum of the muons, deflected in a magnetic field.

The different parts of the detector are shown in Fig. 3.6. Each sub-detector is separated in two regions called barrel and end-cap. The barrel section are co-axial cylindrical layers located in the low pseudorapidity (called central) region. End-caps is a term used to describe the disk layers in high pseudorapidity (called forward) regions. The magnetic field in the ATLAS detector is created by four sets of magnets: a solenoid surrounding the ID and a toroid in the muon spectrometer and two other toroids at the end-cap. More details on the design of the different parts of the detector is presented hereafter.

3.2.1 Inner detector

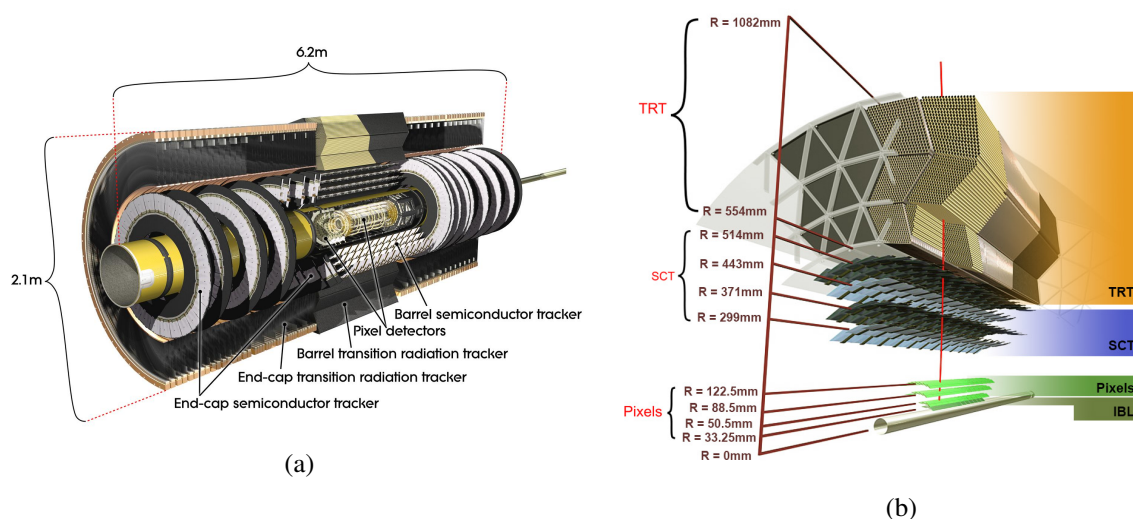


Figure 3.7: Schematic view of the inner detector and its different constituents. Figure (a) shows a compact version while figure (b) exhibits the different layers. Figure taken from Ref. [169, 170].

The ID is the part of the ATLAS detector closest to the beam line. Because it is innermost, the resolution of the instrument is essential to separate the more than 1000 particles flying after each bunch crossing (every 25 ns), find the collision locations (vertices) and identify particles. Charged particles going through the ID are detected and their momentum measured if it is greater than 0.5 GeV. To allow for momentum measurement, the whole ID is immersed in a 2 T magnetic field created by a central solenoid to deflect the charged particles. The momentum

measurement is precise for low momentum particles but the uncertainty grows with the transverse momentum:

$$\sigma \left(\frac{1}{p_T} \right) \cdot p_T = 0.036\% \cdot p_T \oplus 1.3\%, \quad (3.12)$$

where $\sigma(1/p_T)$ is the resolution and p_T is expressed in GeV [171].

The ID is composed of three different sub-detectors: silicon pixel trackers, semiconductor trackers (SCT) and transition radiation tracker (TRT). A detailed view of the ID can be found in Fig. 3.7.

The principle of the pixel detector and SCT is similar because they are both solid state semi-conductors. When a particle enters the material, it excites electrons and create an electron-hole pair. As a potential is applied at the end of the material, this pair creates an electric current. There are 4 layers of pixels and 4 layers of SCT in the barrel, with 3 layers of pixels and 9 layers of SCT in each end-cap.

The tracking detector is built in concentric cylinders in the barrel, and in disks perpendicular to the beam axis in the end-cap. It covers a range $|\eta| < 2.5$. The precision of the sensor detection is measured in terms of $R-\phi \times z$ where $R-\phi$ is the size in the plan perpendicular to the beam axis and z the size along the beam axis. For pixel detectors, this precision has a $R-\phi \times z$ value of $10 \times 115 \mu\text{m}^2$ while it is $17 \times 580 \mu\text{m}^2$ for the SCT. The pixel trackers and SCTs have respectively 80.4 and 6.3 million readout channels, which ensure a good measurement precision.

During the shutdown of the LHC in 2013-2014 (LS1), the pixel detector was repaired [172]. Moreover, a new layer, called Insertable Barrel Layer (IBL) [173], was included between the beam pipe and the innermost layer of pixels. This new detector was added to improve the tracking precision and robustness, which means that failure of individual pixel modules impact less the tracking performances. Moreover, the resolution for the IBL, spanning in the region $|\eta| < 3.03$, is better than the initial pixel detector, with an IBL pixel size of $R-\phi \times z$ of $50 \times 250 \mu\text{m}^2$ against $50 \times 400 \mu\text{m}^2$ for the pixels.

The TRT is the third and last set of trackers. It is composed of about 300000 straw tubes filled with a gas mixture of argon or xenon (Ar or Xe, 70 %), carbon dioxide (CO₂, 27 %) and dioxygen (O₂, 3 %). A high voltage current is applied between the cylinder walls and a central wire. When a particle goes through the gas, it creates a few ionizations of the gas. Due to the electric field, the electrons drift toward the center. During the drift, the electrons create a cascade, amplifying the signal by a coefficient 2.5×10^4 , called the gas gain. When the electrons arrive at the wire, they create a detectable electric current [174].

The TRT is primarily used for tracking but can also contribute to identify particles crossing it. When passing through the edge of the cylinder, particles with high energy emit X-rays photons called transition radiation photons. These photons are then absorbed by the gas mixture. The transition radiation is mainly emitted by particles with a relatively high Lorentz factor, typically $\gamma > 1000$. The amount of energy deposited in the TRT by the photons increase with the energy of the particle. Therefore, a threshold is set to separate hadrons (usually with a low γ) and electrons (usually with a high γ). During Run 1, the gas mixture contained xenon but was later replaced by argon for cost reason after the presence of leaks. This change induced a lower efficiency for the identification purpose due to a lower absorption of the transition radiation photons.

By design, the TRT is less precise in terms of spatial resolution than the precision tracking detector, and covers a more central region, up to $|\eta| < 2.0$, as shown in Fig. 3.8. Data is collected by about 351 000 readout channels. However, it has a better contribution to the momentum measurement due to a large number of measurements per track (around 36 hits) and longer particle tracks.

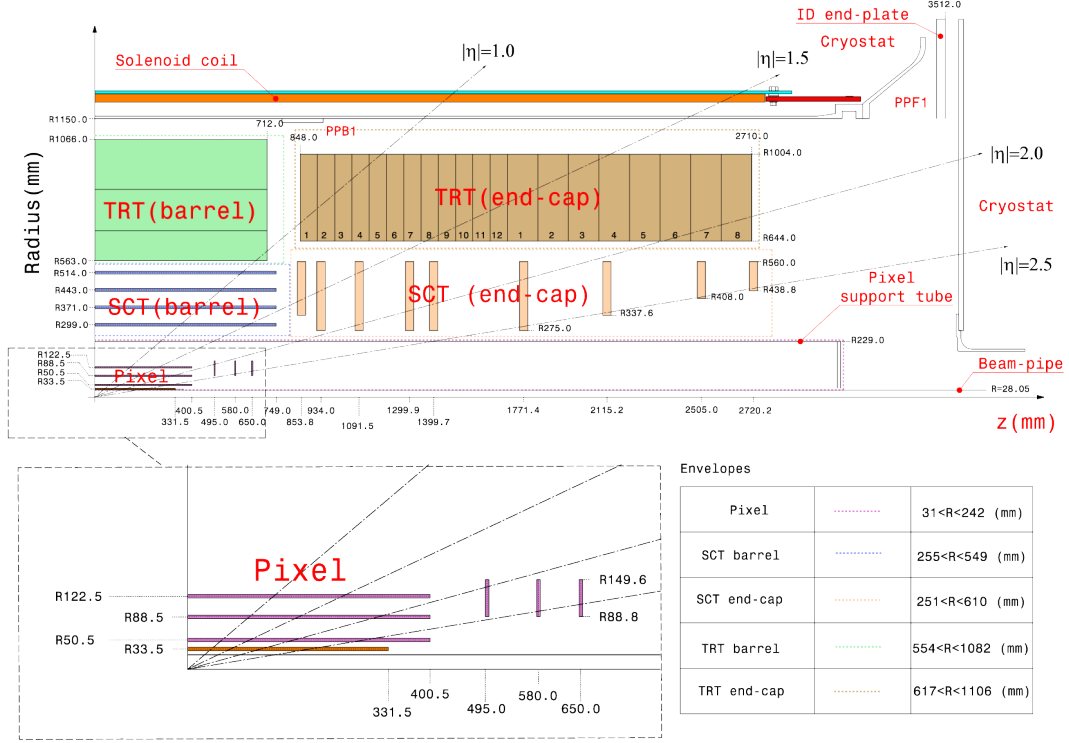


Figure 3.8: View of a quarter-section of the ID. Several pseudorapidity paths are represented. On the bottom plot, the orange detector represents the IBL. Figure taken from Ref. [172].

3.2.2 Calorimeters

The ATLAS calorimeters are based on the same operating principle: one passive medium responsible for creating showers of particles and one active medium that detects the particles induced in the shower [21]. The final goal of the calorimeters is to stop electrons, photons and hadrons and to measure their energy.

The resolution of the calorimeters on the energy measurement E is given by a general expression:

$$\frac{\sigma(E)}{E} = \frac{A}{\sqrt{E}} \oplus B \oplus \frac{C}{E}, \quad (3.13)$$

where A is the sampling term (in $\% \text{ GeV}^{1/2}$), B the constant term (in $\%$) and C the noise term (in $\% \text{ GeV}$) [171]. The constants depend on the type of particle and the design considered. However, it can be deduced that, on the contrary to the ID, the relative energy resolution generally increases for particles at high energy.

The ATLAS calorimeters cover a space of $|\eta| < 4.9$, including forward regions which are not covered by the ID. As shown in Fig. 3.9, the calorimeters are separated in two parts with different

purposes: the electromagnetic calorimeter and the hadronic calorimeter. The following sections introduce the different parts of the detectors and their main characteristics.

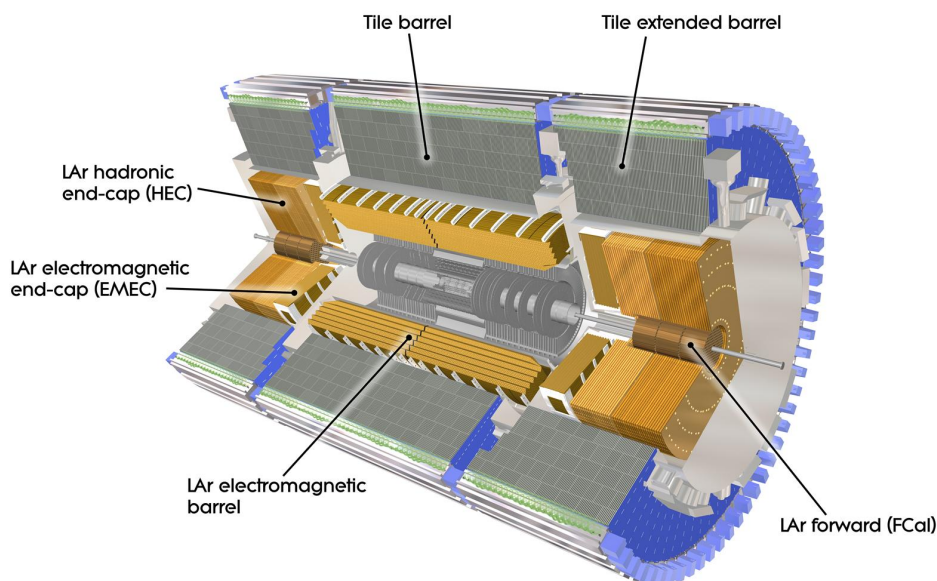


Figure 3.9: Schematic cutaway view of the calorimeters. Figure taken from Ref. [175].

Electromagnetic calorimeter

The liquid-argon (LAr) electromagnetic calorimeter aims primarily at measuring electrons and photons. It is composed of a cylindrical barrel ($|\eta| < 1.475$) and two wheel-shaped end-caps ($1.375 < |\eta| < 3.2$). For the parts where $|\eta|$ matches the ID range, the electromagnetic calorimeter has a fine granularity in order to measure precisely the properties of the electrons and photons properties, identify them and reject the background. For the rest of the calorimeter, a coarser granularity is sufficient for hadron reconstruction and missing transverse energy measurement.

Although the EM calorimeter covers the whole $|\eta| < 3.2$ phase-space, its response is not uniform. Indeed, the shift between the barrel and the end-cap regions contains a so called "transition region", comprised between $1.37 < |\eta| < 1.52$. The energy resolution in this region is generally deteriorated compared to the rest of the measurements in the calorimeter, due to a large amount of material in front of the calorimeters (cables for the ID, power supplies for the barrel, . . .).

As shown in Fig. 3.10, the detector is made in an accordion shape to preserve a complete symmetry in the whole transverse plane. The EM calorimeter is made of two main materials: the lead absorber (passive) and the LAr gap (active). The role of the lead is to create an electromagnetic shower, occurring when high energy photons and charged particles fly through the material. The LAr is ionized by particles passing through it and the subsequent free electrons then drift toward the high voltage kaptons [176]. To remain liquid, the argon is cooled down to 88.5 K.

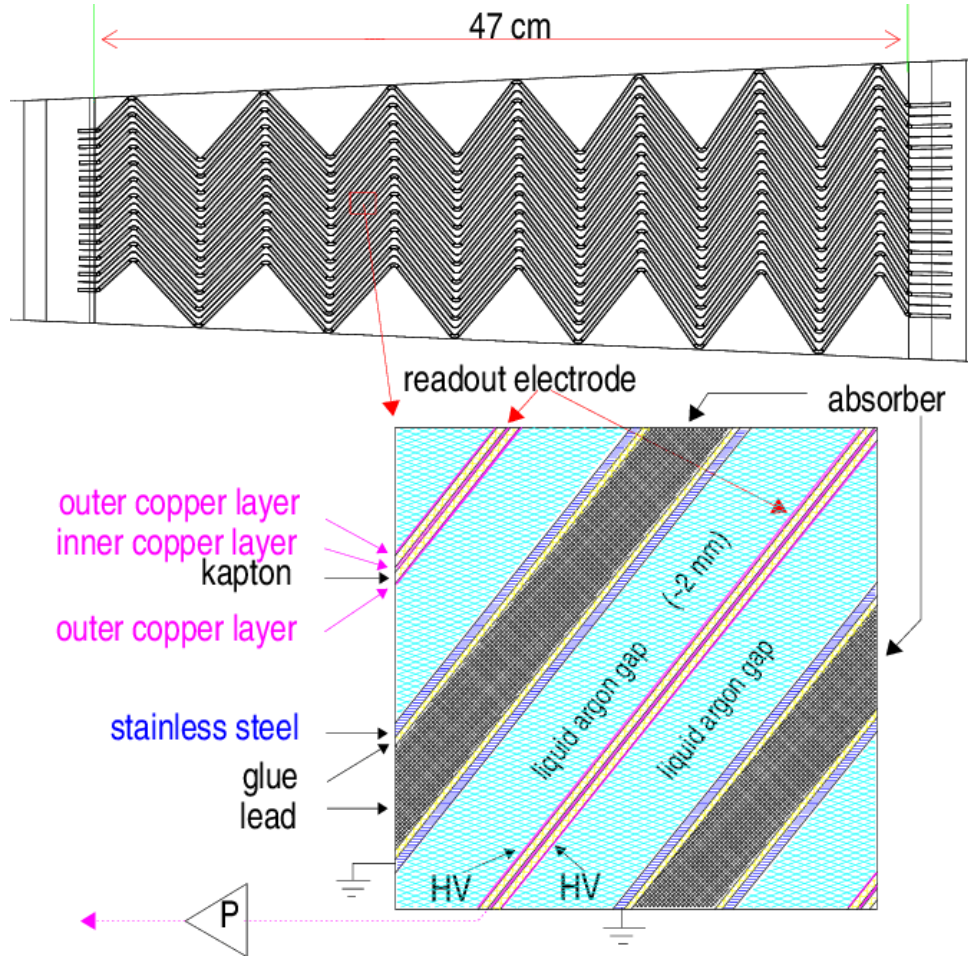


Figure 3.10: Schematic view of the LAr calorimeters. The top figure displays the accordion shape of the barrel calorimeter. The bottom figure is a zoom showing the different elements composing the calorimeter. Figure taken from Ref. [176].

For $|\eta| < 1.8$, a presampler detector located ahead of the electromagnetic calorimeter helps to correct for the energy lost by the particles before entering the calorimeter. This consists of 1.1 cm (0.5 cm) of LAr in the barrel (end-cap).

The electromagnetic calorimeter's thickness can be expressed as unit of radiation length (X_0), defined as the mean distance over which the electron energy is divided by a factor e (Euler's number) due to Bremsstrahlung effect [21]. In the case of ATLAS, the thickness of the electromagnetic calorimeter is greater than $22X_0$, both in the barrel and in the end-cap.

Hadronic calorimeters

The hadronic calorimeters have the purpose to measure the energy of hadrons passing through the detector. The main difference of the hadronic calorimeters compared to the EM ones lies in the interaction in the passive medium being inelastic strong interactions. The good resolution is induced by a thickness equivalent to about 10 interaction lengths of active calorimeter, defined as the mean distance before an inelastic interaction occurs between the particle and the detector. The interaction length of the calorimeters over the whole pseudorapidity range can be observed in Fig. 3.11.

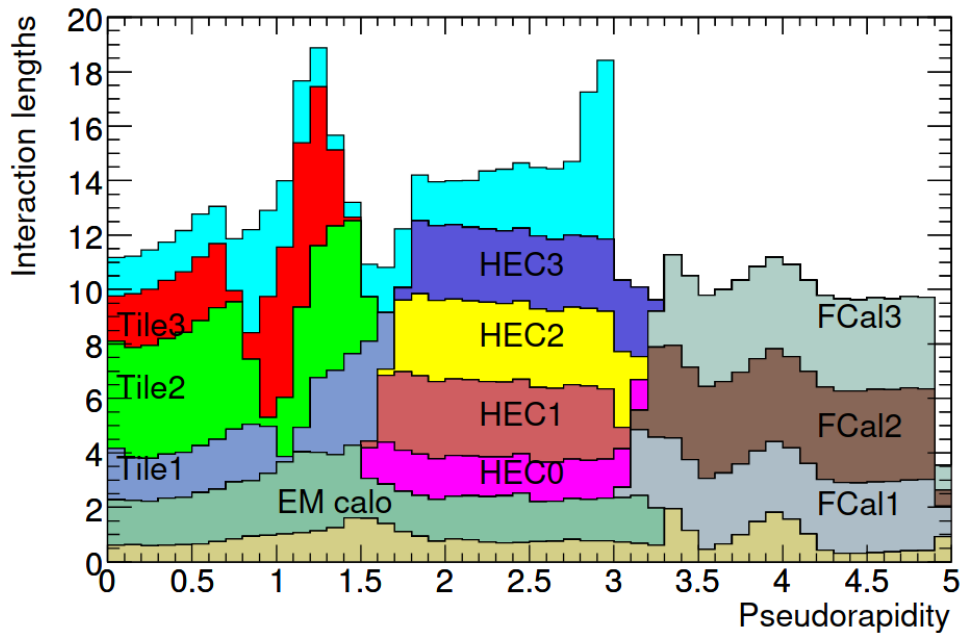


Figure 3.11: Amount of material in the calorimeter (in unit of interaction length) as a function of the pseudorapidity. The beige part at the bottom represents the amount of material in front of the calorimeters and the light blue part on the top depicts the material before the muon spectrometer. Figure taken from Ref. [167].

There are three pieces to the hadronic calorimeters:

Tile calorimeter The tile calorimeter is composed of a barrel ($|\eta| < 1$) and two extended barrels ($0.8 < |\eta| < 1.7$). This detector is made out of steel absorbers (passive) and polystyrene scintillating tiles (active) combined with photomultipliers, in a design shown in Fig. 3.12. When a particle flies across the scintillator, light is emitted and the photomultiplier converts the luminous signal to an electric signal and increase it until it becomes readable. There are three layers of tiles for a total thickness of 9.7 interaction lengths.

LAr hadronic end-cap calorimeter Also named HEC, this calorimeter is assembled on two independent wheels in each end-cap making particles go through 4 layers if they cross an end-cap. These wheels contain 32 modules shaped as wedges and span in the range $1.5 < |\eta| < 3.2$. This calorimeter uses liquid-argon as active medium (as the name indicates), while the passive medium is made from copper plate absorbers.

LAr forward calorimeter The forward calorimeter (FCal) is a calorimeter for very high pseudorapidity particles ($3.1 < |\eta| < 4.9$). There are three modules in total: one made out of copper for the EM measurements and two out of tungsten for hadronic energy measurements.

3.2.3 Muon spectrometer

The muon spectrometer is built to detect muons, whose penetration power allow them to cross completely the calorimeters, conserving most of their energy. The goal of the spectrometer is to measure their momentum. To do so, a strong magnetic field is created by toroid magnets (for $|\eta| < 1.4$) and end-cap magnets (for $1.6 < |\eta| < 2.7$) to deflect the particles' trajectory. The

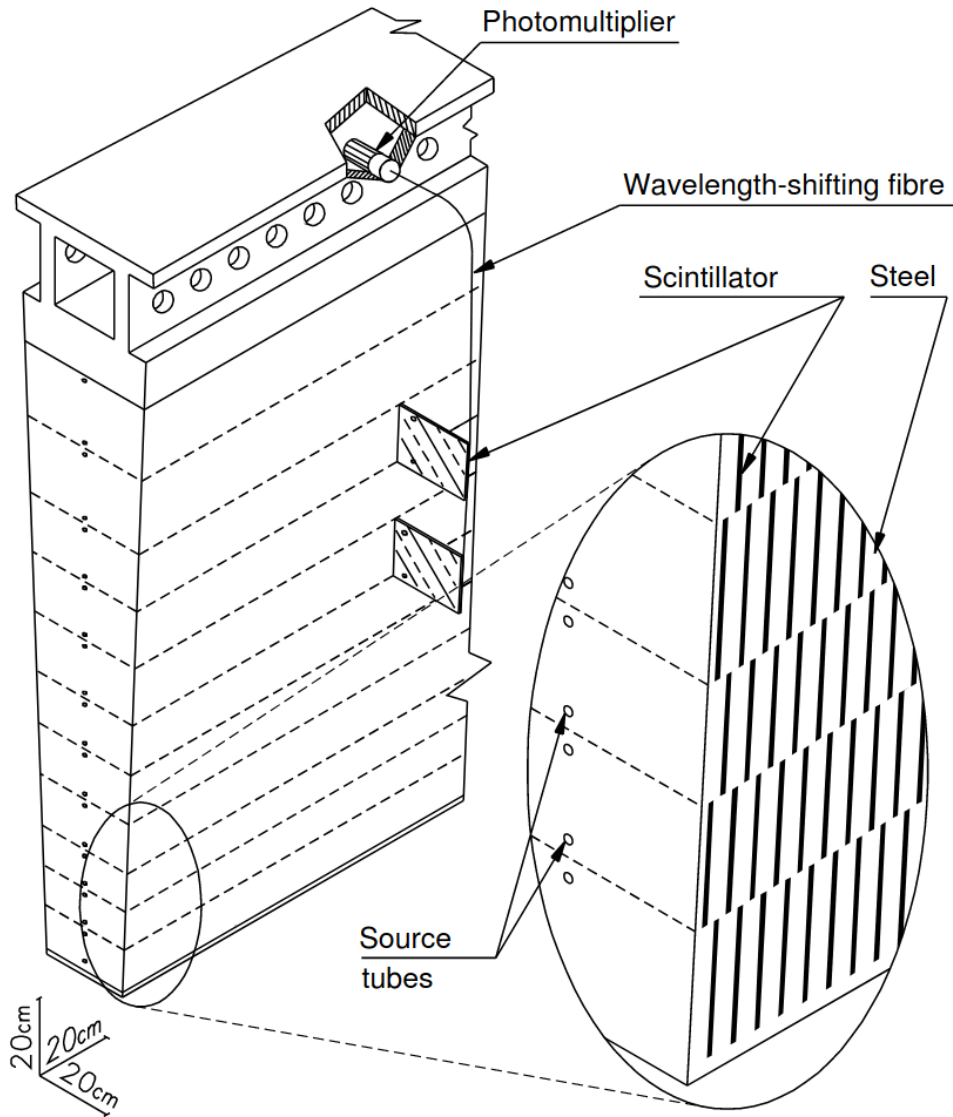


Figure 3.12: Schematic view of the tile calorimeter with its components. Figure taken from Ref. [167].

bending power can be expressed as an integral over a line of the magnetic field ($\int B d\ell$) and is measured to be in the range 1 Tm to 7.5 Tm.

The detectors of the spectrometer are built in three layers of Monitored Drift Tubes (MDT) in the central region ($|\eta| < 2.7$). For high pseudorapidity ($2.0 < |\eta| < 2.7$), Cathode Strip Chambers (CSC) with a higher granularity is used to handle higher background rates. Similarly to the TRT, both MDT and CSC are made of a gaseous argon and carbon dioxide mixtures which ionize when a high-energy particle flies through it. The electrons created then drift toward an anode wire, thus creating an electric current.

A trigger system is also used to identify bunch-crossings, have a transverse momentum threshold and measure muons coordinates. This system uses Resistive Plate Chambers (RPC) in the barrel and Thin Gap Chambers (TGC) in the end-caps. A detailed view of the muon spectrometer constituents can be found on Fig. 3.13.

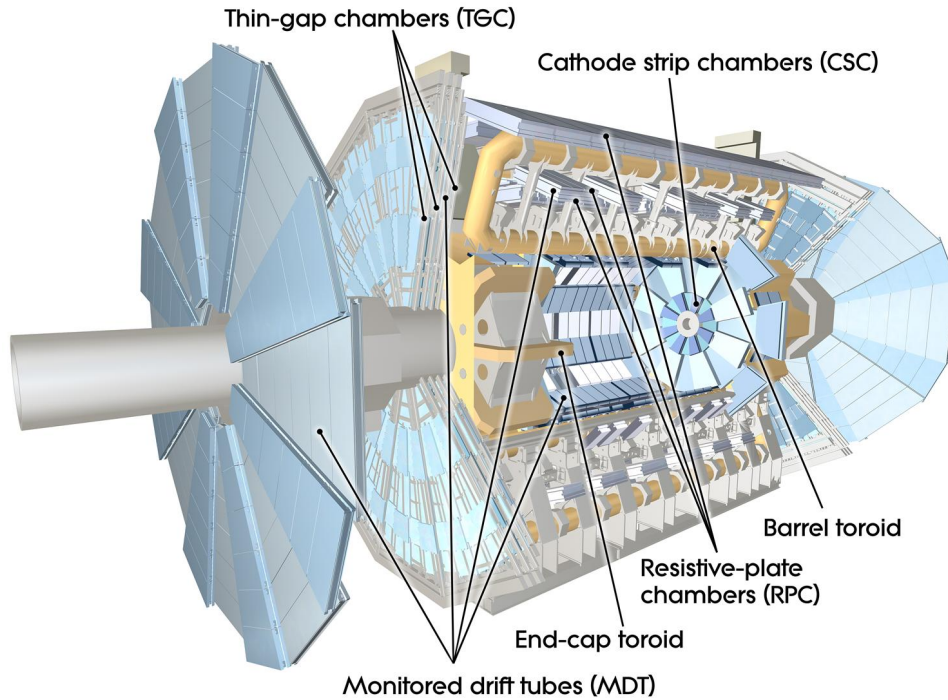


Figure 3.13: Schematic cutaway view of the muon spectrometer. Figure taken from Ref. [177].

3.2.4 Trigger and Data Acquisition

The Trigger and Data Acquisition (TDAQ) is the system able to read events and select the most interesting ones for physics analysis. This is an essential element for storing collision data in ATLAS. With an average 1×10^9 collision per second, the amount of data directly coming from the detector is colossal: around 60 TB/s. To avoid wasting computer resources by storing irrelevant events and detector outputs, the TDAQ selects the most useful events thanks to two different levels: Level-1 (L1) and High-Level Trigger (HLT) [178]. Fig. 3.14 shows the structure of the trigger hardware and software for the ATLAS detector.

The heart of the L1 trigger system is the Central Trigger Processor (CTP). It applies the trigger selections and a dead-time after each selected events to minimize out-of-time pileup contributions.

To apply the triggers, the information coming from the detectors must be processed. For the calorimeter information, this is achieved by the level-1 calorimeter (L1Calo) trigger. The data coming from the calorimeters are digitised and calibrated in the preprocessor. They are then sent to the Cluster Processor (CP) which identifies the electrons, photons and tau candidates, and to the Jet/Energy-sum Processor (JEP) identifying jet candidates, as well as producing the total and missing energy information. In parallel, the level-1 muon (L1Muon) trigger introduce a similar treatment on data coming from the muon spectrometer. This helps to identify muons, both in the barrel and end-cap regions.

The L1Calo algorithm identifies particles by building towers of energy, i.e. the sum of the transverse energy deposited in an element of $\Delta\eta \times \Delta\phi$. L1Calo and L1Muon can apply a threshold on the measured energies to define regions of interest (RoIs), defined as interesting η and ϕ coordinates. Information from L1Calo and L1Muon are then combined in the level-1

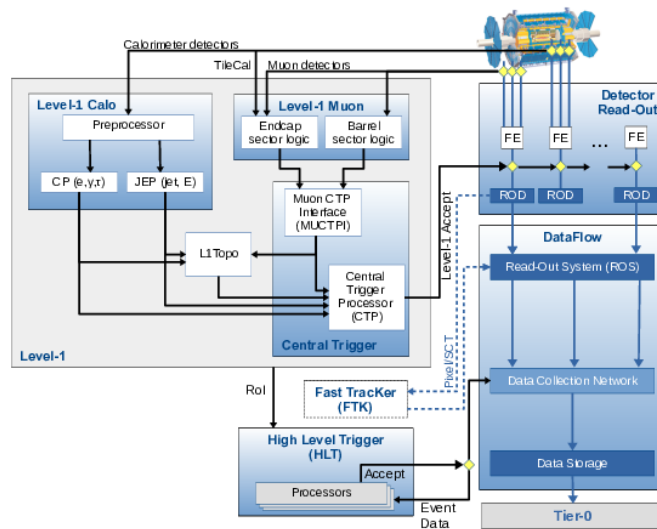


Figure 3.14: The ATLAS TDAQ system. Figure taken from Ref. [179].

topological (L1Topo) trigger. Quantities are calculated more precisely before they reach the CTP and pass the L1 trigger selection.

The whole L1 trigger allows to decrease the data rate from an input (collision) frequency of 40 MHz down to 100 kHz. When passing a L1 trigger, the data from all the detectors along with the RoIs detected by L1 are read out by the Front-End (FE) detector electronics. An initial processing and formatting is done by ReadOut Drivers (RODs). The data are then stored on the ReadOut System (ROS) until processed by the HLT step.

In the HLT, most reconstruction processes have two steps. The first stage is a fast calculation and allows to reject a majority of events. The second part is slower and contains a more precise reconstruction. When an event passes the HLT, the data is stored before the offline reconstruction. The word "offline" here corresponds to treatment done after being stored at the Tier-0 facility, as opposed to "online" services that run during real-time data taking. During Run 2, events were selected by the HLT with a frequency of 1.2 kHz on average, corresponding to a data storage of 1.2 GB s^{-1} .

Triggers have been considerably upgraded since the start of the LHC, particularly after Run 2 [180]. These upgrades were made in anticipation of the increase in luminosity during Run 3 compared to Run 1 and 2. The main improvements have been made for L1, by allowing it to extract more information from the detectors. This was possible by enhancing the accessible granularity and range of the calorimeters [181], improving the algorithms for jet selection and pileup corrections, and benefiting from the construction of the New Small Wheel in the muon spectrometer's end-cap [182].

The HLT selection is performed following a so called "menu" which corresponds to the algorithms to be executed and the requirements to be applied. The trigger menus are separated in different categories:

Typical offline selection	L1 [GeV]	HLT [GeV]
Single isolated μ , $p_T > 27$ GeV	20	26 (i)
Single isolated tight e , $p_T > 27$ GeV	22 (i)	26 (i)
Single μ , $p_T > 52$ GeV	20	50
Single e , $p_T > 61$ GeV	22 (i)	60
Single τ , $p_T > 170$ GeV	100	160

Table 3.2: Main ATLAS single lepton triggers used for 2018 data taking period. The sign (i) denotes an online isolation requirement and the numbers are the transverse momenta thresholds. Data taken from Ref. [183].

- primary triggers for physics analysis
- support triggers for efficiency and performance measurements
- alternative triggers for alternative reconstruction algorithm (e.g. experimental or new triggers)
- backup triggers for tighter selections
- calibration triggers for calibration, storing very small events

Part of the single leptons trigger menu for 2018 data taking is given in Table 3.2. The name of the triggers give information about the trigger selections occurring. For example, `e26_lhtight_nod0_ivarloose`, requires electron (e) with $p_T > 26$ GeV (26), a tight identification likelihood (`lhtight`) that does not take the impact parameter d_0 and significance $|d_0/\sigma(d_0)|$ into account (`nod0`), and a loose isolation requirement in a variable cone size (`ivarloose`). As the name has only lower case letters, the selections are done at HLT level. In the case of capital letter, this indicates a L1 selection requirement. The notions of isolation and likelihood refer to reconstruction and identification properties and are described in Section 4.

4 | Object reconstruction and identification in ATLAS

When a collision occurs between two protons at IP1, the outgoing particles fly through the ATLAS detector, leaving electrical signals in the detector cells. Relevant information about the particles properties (i.e. mass, flavour, charge, energy, creation point, . . .) are essential to retrieve from the signal, in order to have a reliable understanding of the underlying physics occurring in the collision. The set of procedures used for extracting information from detector signals is called reconstruction.

Reconstruction and identification of particles exploit the different properties of the sub-components of the detector. Information on the location of interaction of a particle can be extracted to assess its nature, as shown in Fig. 4.1. Each sub-detector has a specific functionality, and the reconstruction of physics objects relies on the combination of different parts of the detector.

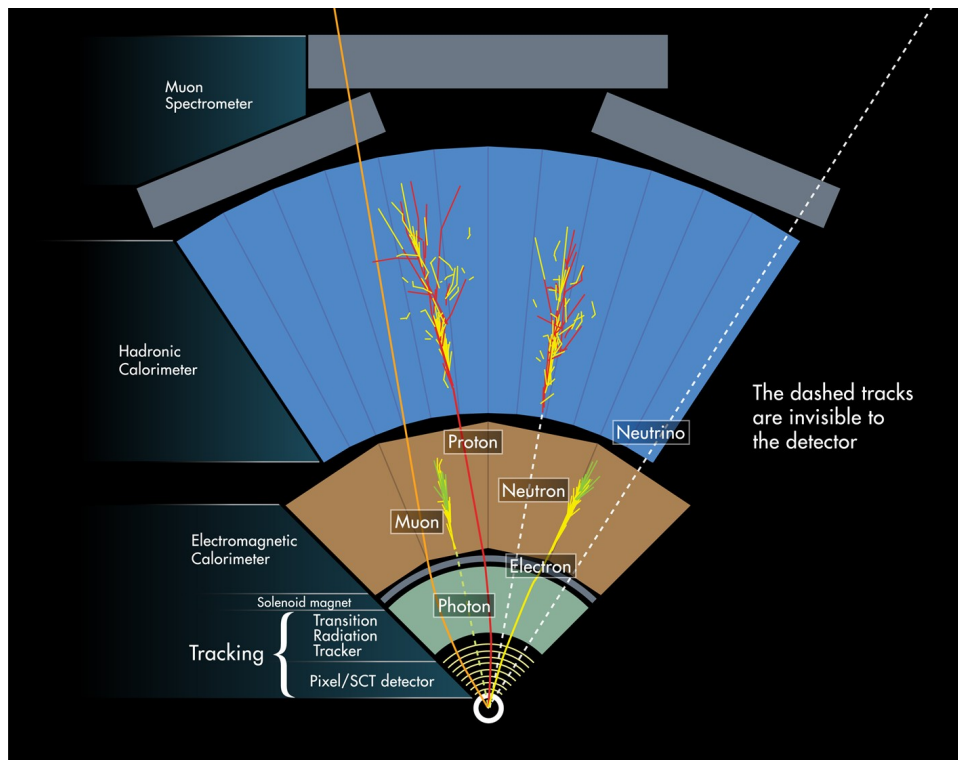


Figure 4.1: Drawing of the interaction of particles with the ATLAS detector. Dotted lines are used for particles leaving no trace. Figure taken from Ref. [184].

The tracking detector is sensitive to charged particles. This means that electrons, muons and charged hadrons (protons, pions, . . .) leave a series of hits in the different ID layers, that can later be reconstructed into a track. The EM calorimeter stops photons and electrons while the hadronic calorimeter stops hadrons, and both calorimeters measure the energy of the particles. Muons are detected by the whole detector, including the muon spectrometer located on the outer part of the detector. Moreover, the magnetic fields applied in the ID and in the muon spectrometer bend the trajectories of the charged particles, which allows to measure their momentum.

The reconstruction and identification of particles is much more complex than considering the parts of the detector where there is a signal. Difficulty arises due to, for example, misidentification of a particle mimicking a different particle, decay of particles in the detector, missing hits on the path of a particle, and other sources that may create an ambiguity in the particle reconstruction and identification. The following sections aim at giving more details on the detection of different types of particles that are later used in the $Z\gamma$ +jets (see Section 5) and ALPs (see Section 6) analyses: electrons, photons, muons and jets.

4.1 Electrons

Electrons are charged leptons that are relatively light compared to other particles in the SM ($m_e \approx 511 \text{ keV}$ [21]). As illustrated in Fig. 4.2, they leave a track in the ID because they are charged, and are stopped by the EM calorimeter due to their low penetrative power (induced by the small mass). Both the track and the calorimeter measurements are used to reconstruct and identify electrons.

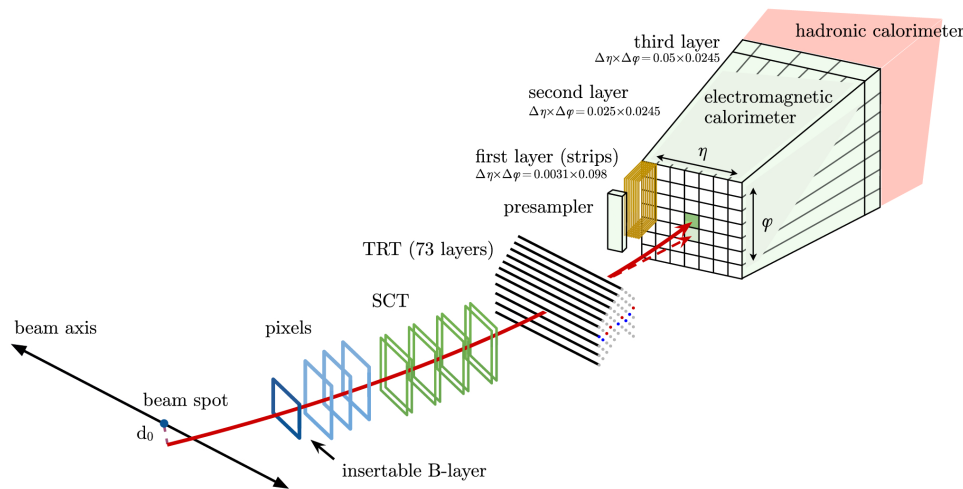


Figure 4.2: Schematic path of an electron through the ATLAS ID and EM calorimeter. Figure taken from Ref. [185].

4.1.1 Reconstruction

Reconstruction of an electron uses both the ID and the EM calorimeter information. The reconstruction is done in three main steps: topo-cluster reconstruction from the energy deposits in the calorimeters, track reconstruction from the ID hits and matching with a topo-cluster, and supercluster reconstruction combining the two aforementioned topo-cluster and track [186]¹.

Topo-cluster reconstruction Topo-clusters are dynamic and variable-size clusters constructed from the energy deposited by particles in the EM and hadronic calorimeters. In the ATLAS detector, the so called ‘4-2-0’ topo-cluster reconstruction is used. The first step for

1. Section 4.1 is mainly based on information found in Ref. [186], unless another reference is given.

reconstructing a topo-cluster is to build proto-cluster seeds defined by $|\zeta_{cell}^{EM}| \geq 4$, where the significance of a calorimeter cell ζ_{cell}^{EM} is defined by:

$$\zeta_{cell}^{EM} = \frac{E_{cell}^{EM}}{\sigma_{cell}^{EM}}, \quad (4.1)$$

with E_{cell}^{EM} the cell energy as measured with the response of the EM calorimeter and σ_{cell}^{EM} the expected cell noise (taking into account the electric noise and pileup contribution).

All neighbouring cells with $|\zeta_{cell}^{EM}| \geq 2$ are then added to the proto-cluster. The algorithm then includes in the cluster any neighbouring cells passing the same significance and repeats the operation until all neighbours have $|\zeta_{cell}^{EM}| < 2$. Finally, all adjacent cells with $|\zeta_{cell}^{EM}| \geq 0$ are also included in the cluster.

These steps make a cluster of cells with $|\zeta_{cell}^{EM}| \geq 4$, $|\zeta_{cell}^{EM}| \geq 2$ and $|\zeta_{cell}^{EM}| \geq 0$, hence the name '4-2-0' topo-cluster. If two proto-clusters share the same $|\zeta_{cell}^{EM}| \geq 2$ cell, they are merged as one cluster. However, proto-clusters are split if they have several local maxima, defined as cells with $E_{cell}^{EM} > 500\text{MeV}$.

To be considered when reconstructing electrons and photons, clusters must satisfy criteria on the energy deposited in the EM calorimeter $E_{cluster}^{EM} > 400\text{MeV}$, and the EM fraction $f_{EM} = E_{cluster}^{EM}/E_{cluster} > 0.5$ with $E_{cluster}$ the total energy of the cluster deposited in the EM and hadronic calorimeters.

Track reconstruction Tracks are reconstructed following a pattern recognition algorithm [187]. Its goal is to link the hits left by particles in the ID to build tracks, starting from the silicon detector (pixel and SCT) and then extending to the TRT [185]. The pattern recognition is then improved by allowing energy loss in material around RoIs, defined as fixed size calorimeter clusters compatible with EM showers. Once the pattern reconstruction occurred, tracks are fitted to improve the estimates on the track properties.

Tracks are then extrapolated to the second layer of the EM calorimeter and matched with the topo-cluster's barycentre of constituent cells in that second layer. One of the matching criteria is the coherence between the topo-cluster energy and the track momentum, meaning that the track momentum must be measured precisely. To achieve a better accuracy, the electron or photon candidate tracks are refitted with a dedicated Gaussian Sum Fitter algorithm [188] to account for loss of energy induced by Bremsstrahlung radiation. Tracks and topo-clusters are then matched by their angular distance, hence $|\Delta\eta| < 0.05$ and $-0.10 < q(\phi_{track} - \phi_{cluster}) < 0.05$, where q is the reconstructed charge, η_{track} and ϕ_{track} are the coordinates of the track extrapolated to the second layer of the calorimeter, and $\eta_{cluster}$ and $\phi_{cluster}$ are the topo-cluster barycentre coordinates. If there are several tracks matching a cluster, the reconstruction procedure selects one of the tracks based on the value of ΔR and the number of hits in the ID.

In the case of a photon, the interaction with material in the ID can provoke the creation of an electron-positron pair. Although the particles detected are electrons, the object is identified as "converted photon" (not "electron"). This case is examined in Section 4.2.

Supercluster reconstruction A supercluster consists of a seed cluster and potential satellites. Satellites are included in order to account for EM showers (Bremsstrahlung radiation or topo-cluster splitting) resulting from interactions of an electron with the detector material. To build an electron supercluster, topo-clusters are ranked by decreasing transverse energy.

Going in order, the topo-cluster becomes an electron supercluster seed if it has $E_T > 1$ GeV and is matched to a track with at least 4 silicon hits.

From this seed, possible satellite clusters are searched. Clusters are considered satellites of an electron seed cluster if they are encompassed in a window $\Delta\eta \times \Delta\phi = 0.075 \times 0.125$ around the seed-cluster barycentre (which correspond to 3×5 cells in the second layer of the EM calorimeter). Moreover, if a cluster is within $\Delta\eta \times \Delta\phi = 0.125 \times 0.300$ around an electron seed and share the same best-matched track, it is also considered as a satellite. If a topo-cluster is a satellite, it can not become a seed or the satellite of another seed.

Finally, tracks are matched to superclusters. The matching criteria between superclusters and tracks are the same as the criteria applied previously between topo-clusters and tracks.

A supercluster associated with a track constitutes the analysis-level electron. However, as electrons and photons are reconstructed independently, it is possible that the identification fails to tell if the cluster is an electron or a photon. This ambiguity results in the creation of both an electron and a photon objects marked as ambiguous.

4.1.2 Energy calibration

Calibration is an essential step to be able to compare the MC results and data. When particles go through the detector, the measured momentum (or energy) can contain alterations compared to the "true" momentum for different reasons (detector efficiency and non-uniformity, energy loss in passive material, etc). This leads to differences in the values of momentum between MC at truth level, MC at reco level and data. Therefore, calibration is applied so that these three values are matching as much as possible. To do so, both the MC at reco level and the data are calibrated to get their momentum as close to each others as possible, as well as to the truth level simulation.

For electrons and photons, the calibration occurs following the steps described below [189]:

- The energy resolution of the particle is optimized using the EM shower shape properties. This stage uses the same algorithm for the data and simulation.
- Data are corrected to account for differences in responses in the layers of the EM calorimeter.
- Correction for non-uniformities are then applied to data, taking into account boundaries between calorimeter modules and non-uniformities in the detector voltage.
- The data overall energy scale is then adjusted, as well as the MC energy resolution. This is done by computing the difference between data and simulation results in a sample of $Z \rightarrow ee$.

4.1.3 Identification

In addition to the reconstructed analysis-level particles, analyses often use more selective criteria on the identification and isolation of the particles. This selection removes more misidentified particles than well identified ones, hence improving the signal to noise ratio. The process leading

to the electron identification is discussed in this section, while details on the electron isolation can be found in Section 4.1.5.

It is possible that other particles fake the electron behaviour and are interpreted as electrons. This background is mainly due to hadronic jets, converted photons, and electrons coming from heavy-flavour hadron decays (non-prompt electrons). To remove the background contribution, further criteria are applied on different variables related to track, longitudinal and lateral development of EM shower, and spatial compatibility of track and cluster. For example, the track requirements include conditions on the transverse impact parameter d_0 , the smallest distance transverse to the beam line between the track and the interaction point. This set of criteria is called identification.

The electron identification is based on a likelihood discriminant defined as:

$$d_L = \frac{L_S}{L_S + L_B}, \quad (4.2)$$

with $L_{S(B)}$ is the likelihood for an electron to be a prompt signal (resp. background). This likelihood is computed by the following formula:

$$L_{S(B)}(\mathbf{x}) = \prod_{i=1}^n P_{S(B),i}(x_i), \quad (4.3)$$

where $P_{S(B),i}(x_i)$ is the probability density function (pdf) value of the signal (resp. background) for the criteria i at value x_i . The signal pdf values are derived from data, using the tag-and-probe method. More details on this method can be found in Section 4.1.4.

There are three main electron identification working points for Run 2: Loose, Medium and Tight. They all require a minimum value on d_L and additional requirements which are adjusted for each of the 9 bins used in $|\eta|$ and 12 bins in E_T , using simulated events. The criteria are chosen so that electrons passing the Tight working point also pass Medium, and the ones passing Medium also pass Loose.

4.1.4 Identification efficiency measurements

As explained in Section 4.1.3, the rejection of objects misidentified as electrons by the identification criteria also implies the rejection of some prompt electrons. This means that the MC simulations must remove electrons during the identification phase with the same probability as in data. This is done by measuring the identification efficiency, which is a crucial step to ensure that data and MC predictions can be accurately compared [190]².

The identification efficiency is defined, for all working points, as the number of electrons passing the identification (*id*) criteria divided by the number of all the reconstructed electrons:

$$\epsilon_{id} = \frac{N_{pass\ id}}{N_{reco}}. \quad (4.4)$$

The application of the ratio between the data and MC efficiency (as a function of η and p_T) to simulations, allows MC results to match the results in data.

2. Section 4.1.4 is mainly based on information found in Ref. [190], unless another reference is given.

The number of reconstructed electrons is estimated with the so called *tag-and-probe* method [185, 190]. It consists in taking, at low energy ($p_T^{probe} < 20\text{ GeV}$), the $J/\Psi \rightarrow ee$ resonance, and at high energy ($p_T^{probe} > 15\text{ GeV}$), the $Z \rightarrow ee$ resonance. Two electrons are chosen so that one electron has to pass very strict requirements to be as certain as feasible that it is indeed an electron (called "tag"), while the second one is unbiased (called "probe") and only has the identification criteria applied if it is in the numerator of Eq. (4.4). Fig. 4.3 gives a graphical representation of the method.

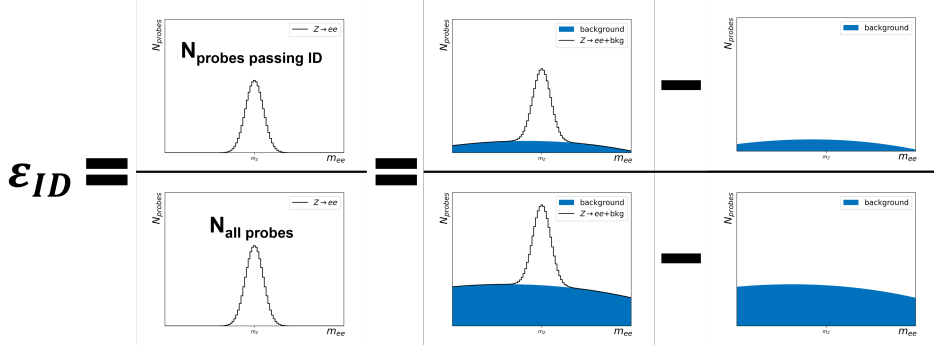


Figure 4.3: Schematic representation of the Z_{mass} efficiency measurement method, including background rejection.

It is worth mentioning that the tag-and-probe method is exclusive neither to the identification efficiency measurements, nor the electrons. Indeed, it is also applied for reconstruction, isolation [185] and trigger [191] efficiency measurements, and for objects as diverse as muons [192], taus and t -quarks [193]. For simplicity, the remainder of this section focuses only on the $Z \rightarrow ee$ decay. The non-electron background in numerator and denominator is determined with two methods, Z_{mass} and Z_{iso} , which are then combined to give a single result. The methods are briefly outlined below (details are available in Ref. [190]).

Z_{mass} method

Fig. 4.4 shows the data/MC distribution of the dilepton system (m_{ee}) for the $Z \rightarrow ee$ events in the tag-and-probe region in a bin of η and p_T . The background shape is estimated using a sample in which probes fail the identification criteria. This sample still contains some remaining signal, which is subtracted using MC simulation. The estimate is then normalised to the side bands of the Z resonance peak ($m_{ee} \ll 91.2\text{ GeV}$ and $m_{ee} \gg 91.2\text{ GeV}$). After this, the Z resonance peak remains and the number of $Z \rightarrow ee$ events can be deduced.

Z_{iso} method

The Z_{iso} method uses the transverse energy in a cone $\Delta R = 0.3$ around the probe. The idea is that signal electrons have a low amount of surrounding particles while misidentified jets are poorly isolated. This can be seen in MC simulations, as plotted in Fig. 4.5. The regions $E_T^{cone0.3}/25\text{ GeV} < 0.5$ (good isolation, dominated by signal) and $E_T^{cone0.3}/25\text{ GeV} > 0.5$ (bad isolation, dominated by background) are used to fit the amount of signal and background respectively.

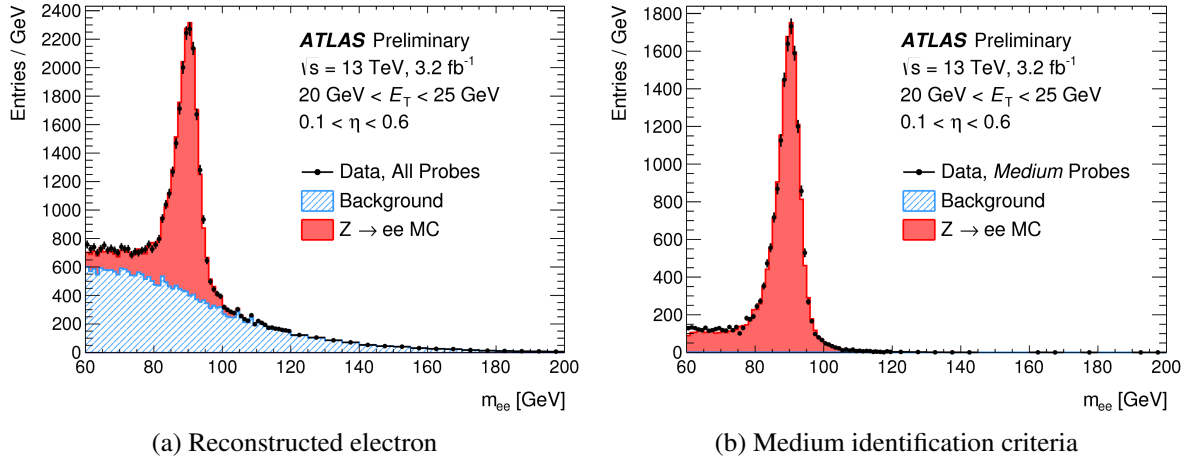


Figure 4.4: Example of the Z_{mass} method applied to the 2015 data at $20 \text{ GeV} < p_T^{probe} < 25 \text{ GeV}$ and $0.10 < \eta_{probe} < 0.60$. To compute the identification efficiency for the Medium criteria, the amount of $Z \rightarrow ee$ events in Fig. (b) is divided by the amount in Fig. (a). The MC results are given here as an illustration. Figure taken from Ref. [190].

Results

The efficiencies of the electron identification measured in Run 2 data are shown in Fig. 4.6. As the transverse momentum and pseudorapidity of the electron are two factors (among others) affecting the efficiency, the results are given as a function of these observables. The efficiency is decreasing from the Loose to the Tight working point. Loose has an efficiency mainly above 90 %, Medium between 80 % to 90 % and Tight between 70 % to 85 %. On the pseudorapidity distribution, we can identify some structural features where the efficiency fluctuates. For example, the transition region between the EM calorimeter and endcap at $1.37 < |\eta| < 1.52$ leads to a decrease of the efficiency.

4.1.5 Isolation

Isolation is a notion linked to the energy deposited around a particle. The more a particle is surrounded by objects, the less it is isolated. There are two possible isolation types: the calorimeter isolation and the track isolation.

The calorimeter isolation is defined as the amount of energy deposited in a cone around the electron cluster. To compute it, the size of the cone must be defined as a radius $\Delta R = XX/100$. For electrons, the only cone size used in ATLAS for the working points is $\Delta R = 0.2$ ($XX = 20$). The energy deposited around the cluster is therefore the raw energy in the cone corrected for the energy of the cluster itself and the pileup. This can be expressed as:

$$E_T^{coneXX} = E_{T,raw}^{isolXX} - E_{T,core} - E_{T,leakage}(E_T, \eta, \Delta R) - E_{T,pileup}(\eta, \Delta R), \quad (4.5)$$

where

- E_T^{coneXX} is the calorimeter isolation variable
- $E_{T,raw}^{isolXX}$ is the raw calorimeter isolation defined as the sum of transverse energy of positive energy topo-clusters whose barycentre lies inside the cone

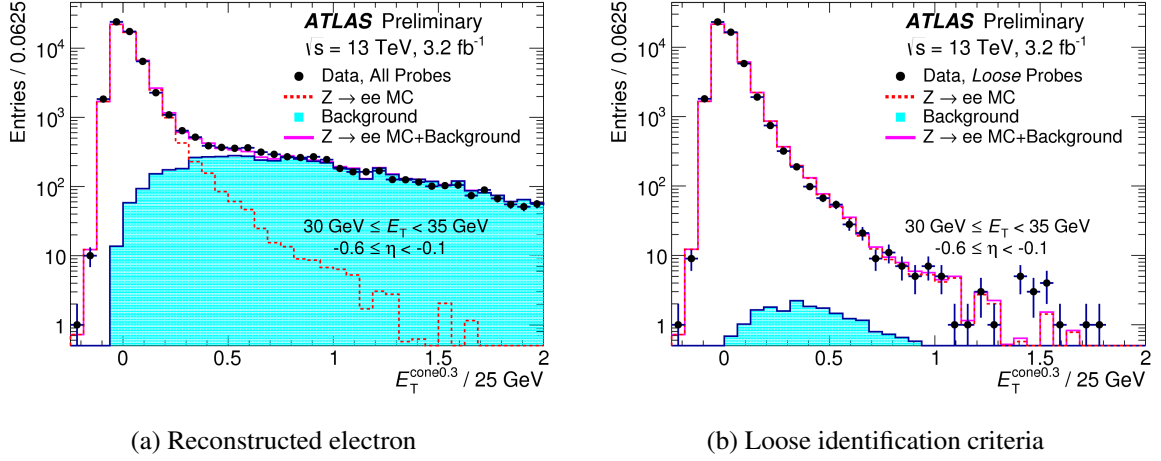


Figure 4.5: Example of the Z_{iso} method applied to the 2015 data at $30 \text{ GeV} < p_T^{probe} < 35 \text{ GeV}$ and $-0.6 < \eta_{probe} < -0.1$. To compute the identification efficiency for the Loose criteria, the amount of $Z \rightarrow ee$ events in Fig. (b) is divided by the amount in Fig. (a). Figure taken from Ref. [190].

- $E_{T,core}$ is the EM energy in a range $\Delta\eta \times \Delta\phi = 0.125 \times 0.175$ around the electron cluster barycentre
- $E_{T,leakage}$ is the leakage energy of the electron cluster out of the window defined for $E_{T,core}$
- $E_{T,pileup}$ is the correction for the pileup energy contribution to the isolation cone.

The track isolation is the sum of all the transverse momenta of the tracks within a defined cone, except for the track of the electron under study. Only tracks passing a few quality criteria ($p_T > 1 \text{ GeV}$, $|\eta| < 2.5$, more than 7 silicon hits) and sharing at least one silicon hit with the electron are considered. The track isolation within a cone $\Delta R = XX/100$ is noted p_T^{coneXX} . However, this definition is not adapted to electron(s) coming from a boosted particle decays, where the other products can be spatially close to the electron. This leads to the creation of a track isolation with variable cone size $p_T^{varconeXX}$ defined in a radius:

$$\Delta R = \min\left(\frac{10}{p_T[\text{GeV}]}, \Delta R_{max}\right), \quad (4.6)$$

where $\Delta R_{max} = XX/100$ is the maximum cone size.

Isolation working points are defined by applying conditions on the calorimeter and the track isolations. For example, the criteria applied for the FCLoose isolation on electrons are:

$$E_T^{cone20}/p_T < 20, \quad p_T^{varcone20}/p_T < 0.15. \quad (4.7)$$

4.2 Photons

Photons are treated analogously to electrons due to their similar properties in the EM calorimeter. Although some photons, called unconverted, do not leave any track in the ID (as photons are chargeless), others, called converted, create an electron-positron pair when entering the detector material, increasing the photon resemblance to an electron. Because the reconstruction,

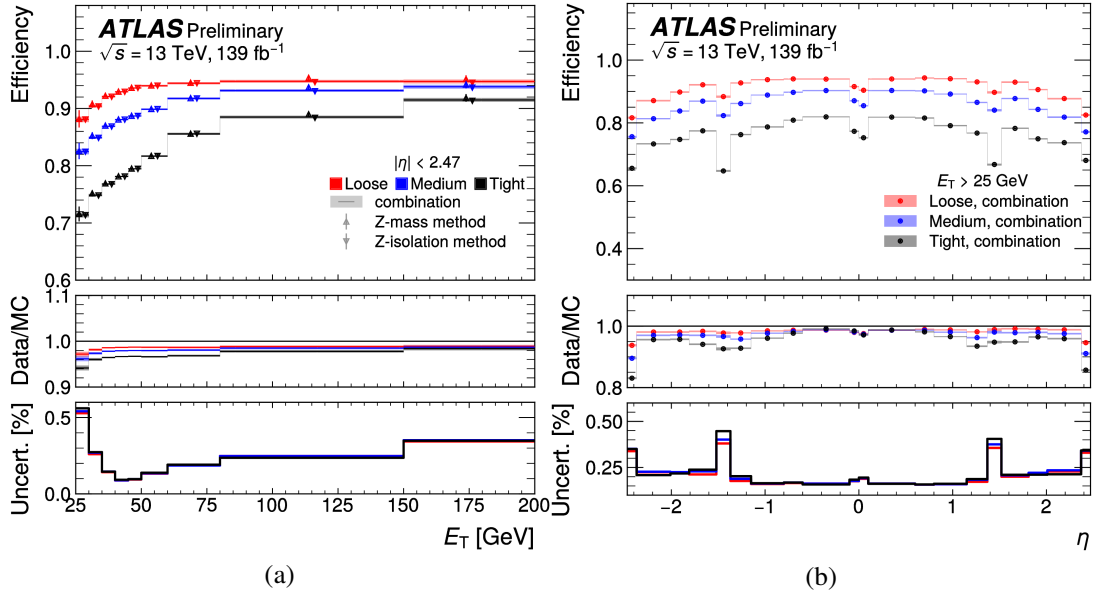


Figure 4.6: Efficiency measurement for the Loose, Medium and Tight working points with the full Run 2 data along (a) transverse momentum and (b) pseudorapidity. The MC results are given here as an illustration. Figure taken from Ref. [194].

identification and isolation processes are similar to the electron procedure as described in Section 4.1, only the main differences applying to photons are listed below [186]³.

Reconstruction During the topo-cluster reconstruction, the process is the same as for the electrons.

The main difference with electrons arises for converted photons. When a photon converts, it results in two tracks with opposite charges, corresponding to the electron-positron pair, and consistent with an initial massless particle. In that case, the conversion vertex is reconstructed. It is also possible that there is only one track, for example, because the two tracks are so close that it only creates one track. In that case, a conversion vertex can also be reconstructed, provided that the track passes stricter requirements than in the double track case with no hit in the innermost ID layers. The conversion vertices and the topo-cluster are then matched in terms of $|\Delta\eta|$ and $|\Delta\phi|$.

During the supercluster reconstruction, a photon seed must satisfy $E_T > 1.5$ GeV without condition on track or conversion vertex. As for the electron, clusters in a window $\Delta\eta \times \Delta\phi = 0.075 \times 0.125$ centered on the seed cluster barycentre are considered as satellites. Moreover, a cluster is considered a satellite if its best-matched track is part of the conversion vertex of the seed cluster.

The photon energy calibration is analogous to electrons and is described in Section 4.1.2.

Identification As for electrons, the photon identification criteria applied in analyses are used to select prompt photons and reject misidentified particles, like hadronic jets or π^0 decaying into

3. Section 4.2 is mainly based on information found in Ref. [186], unless another reference is given.

photons. On the contrary to electrons, whose selection is done using a likelihood function, the photon identification uses a cut-based selection, meaning that if a criteria on one of the variables fails, the photon fails the selection.

There are two identification working points in total: Loose and Tight. As for electrons, Tight is a subset of Loose. Although converted and unconverted photons have different shower shapes, only the Tight identification is performed differently for both cases.

Isolation The photon isolation is performed both with cones $\Delta R = 0.2$ and $\Delta R = 0.4$ ($XX = 20$ and $XX = 40$) around the photon cluster barycentre. There are two recommended isolation working points using the calorimeter and track isolation variables (FixedCutLoose and FixedCutTight), and one using the calorimeter isolation variable only (FixedCutTightCaloOnly). For example, FixedCutLoose requires the following criteria:

$$E_T^{cone20} < 0.065E_T, \quad p_T^{cone20}/E_T < 0.05. \quad (4.8)$$

4.3 Muons

Muons are leptons, like electrons, and therefore don't interact strongly. In the LHC energy ranges, muons are minimum ionising particles, meaning that they do not interact a lot with matter. Muons can therefore fly through the calorimeters, and reach the muon spectrometer in the outer part of the detector. The muon spectrometer is thus a central element in the muon reconstruction methods, along with the ID. Calorimeters only play a secondary role, mainly by estimating the energy loss of the particle.

There are five different reconstruction methods for muons [192]⁴:

1. Combined (CB): muon spectrometer and ID tracks are matched and the energy loss in calorimeters is taken into account.
2. Inside-out combined (IO): The ID track is extrapolated to the muon spectrometer and three aligned muon spectrometer hits must be found along the extrapolation. The energy loss in the calorimeter is taken into account during the track fitting. This method is useful for regions of the detector where the muon spectrometer has a low coverage, and for low- p_T muons which can not make it through the whole muon spectrometer.
3. Muon spectrometer extrapolated (ME): The muon spectrometer track can not be matched to an ID track and therefore is extrapolated to the beamline. This is for example used for muons having a trajectory outside of the ID range ($|\eta| > 2.5$).
4. Segment-tagged (ST): The ID track is extrapolated to the muon spectrometer where it has to match tightly at least on segment. The muons properties are entirely deduced from the ID track.
5. Calorimeter-tagged (CT): The ID track is extrapolated to the calorimeter where the signature of a minimum-ionising particle is searched. The ID track characteristics are used for the muons properties.

4. Section 4.3 is mainly based on information found in Ref. [192], unless another reference is given.

The calibration parameters are extracted mainly by comparing CB muons between data and MC simulation results [195]. The corrections are applied to the simulated muon transverse momenta, both on the scale and the resolution (correction on the resolution is called smearing). The calibration is done to take into account the mismodelling in the magnetic field and in the energy loss due to materials before the muon spectrometers. The smearing is applied to include inhomogeneities in the magnetic field and detector features such as spatial resolution and misalignment.

Once reconstructed, like electrons and photons, muons are then identified thanks to various criteria. These criteria concern the number of hits in the ID and muon spectrometer, the fit properties, as well as the compatibility of the different measurements in the detector. This leads to three working points (Loose, Medium and Tight, all subset of the previous one) depending on how well criteria are passed. For example, the Medium working point is accepting CB and IO muons at $|\eta| < 2.5$ and ME muons at $|\eta| > 2.7$, with further criteria applied on the hits, and the charge over momentum ratio compatibility between ID and muon spectrometer. In addition to the three working points already stated, two working points are added for specific phase-space regions: High- p_T for $p_T > 100 \text{ GeV}$ and Low- p_T for $p_T < 18 \text{ GeV}$.

Isolation criteria can also be applied in analyses to remove non-prompt muons created in heavy-flavour hadron decays. Similarly to electrons and photons, these working points are based on the ratio between the energy in a cone around a muon and the muon energy. This value can be taken in ID, calorimeters or both, depending on the desired level of isolation. However, when both are used, the charged particle contributions would be double-counted, due to their interaction both in the ID and calorimeters. Therefore, a particle flow algorithm (see Section 4.4) is applied to preserve only the neutral particles contribution in the calorimeter. For example, the isolation working point PflowLoose_FixedRadIso is defined as:

$$\begin{aligned} p_T^{\text{varcone30}} + 0.4 \cdot E_T^{\text{neflow20}} &< 0.16 \cdot p_T^\mu, & \text{if } p_T^\mu < 50 \text{ GeV} \\ p_T^{\text{cone20}} + 0.4 \cdot E_T^{\text{neflow20}} &< 0.16 \cdot p_T^\mu, & \text{if } p_T^\mu > 50 \text{ GeV} \end{aligned} \quad (4.9)$$

where $p_T^{\text{varcone30}}$ and p_T^{cone20} are the transverse momentum of all the ID tracks surrounding the muon (as defined in Section 4.1), E_T^{neflow20} is the transverse energy of the neutral particles surrounding the muon as measured by the calorimeters, and 0.4 is a correction factor for the muon energy deposited and the pileup effects.

4.4 Jets

Jets are collimated sprays of energetic hadrons [196] originating from a quark or a gluon. As no stable state can have a colour charge, partons create a chain of reactions leading to a stream of particles. This phenomenon is called hadronization. Particles created by this process can either have an electric charge or be neutral and therefore do not always leave a track in the ID. However, even if some do not leave tracks, they reach the EM and hadronic calorimeters where their energy can be measured.

4.4.1 Particle flow algorithm

The jets used in this thesis are reconstructed with a particle flow algorithm [197]. The algorithm is based on the idea that the momentum resolution in the tracker of a low-energy charged particle

(constituent of a jet) is better than its energy resolution in the calorimeter. As a consequence, the ID measurements are preferred over the calorimeters for charged particles. There are also other advantages of using the tracker, such as a better angular resolution, detection of low transverse momentum charged particles which never reach the calorimeters because they are trapped in the magnetic field, and the reconstruction of the originating vertex.

Neutral particles can only be measured by the calorimeter. Therefore, the calorimeter must be used for measurements of the properties of neutral particles while the tracker is used for charged particles. However, the calorimeter also collects the energy of charged particles, that is then subtracted, so that it is not double counted by the calorimeter and the tracker. On the other hand, the energy of neutral particles is kept since they are not measured in the ID. The particle flow algorithm works using several steps detailed below.

Topo-cluster reconstruction The topo-cluster reconstruction is done in the EM and hadronic calorimeters following the ‘4-2-0’ method, as described in Section 4.1.1.

Track selection The selection on the tracks used in the particle flow algorithm is strict. The preselected tracks must have at least 9 silicon hits and no missing hit in the pixel detector, where it is expected. Moreover, tracks must be within $|\eta| < 2.5$ and their transverse momentum in the range $0.5 \text{ GeV} < p_T < 40 \text{ GeV}$. The latter is chosen to keep a decent computing time (no improvement in jet resolution under 0.5 GeV) and remove high momentum jets which are often not isolated enough.

Matching tracks to topo-clusters Once tracks and topo-cluster are reconstructed, they must be matched. First, the energy measured in clusters must match the momentum measured in the tracker $E^{clus}/p^{trk} > 0.1$. Then, the topo-cluster that is the closest to the track is considered as the matching one. To compute the distance of a track to a topo-cluster, the metric $\Delta R'$ is used:

$$\Delta R' = \sqrt{\left(\frac{\Delta\phi}{\sigma_\phi}\right)^2 + \left(\frac{\Delta\eta}{\sigma_\eta}\right)^2} \quad (4.10)$$

where σ_ϕ and σ_η are the angular topo-cluster widths. If there is no topo-cluster in a radius $\Delta R' < 1.64$, it is assumed that the track is not associated to any topo-cluster.

Expected deposited energy To subtract the right amount of energy in the calorimeter corresponding to the charged particles, it is crucial to be able to convert the track momentum into calorimeter energy. To do so, an expectation value $\langle E_{ref}^{clus}/p_{ref}^{trk} \rangle$ is determined using MC single-particles sample. On average, the energy deposited in the calorimeter by a particle with a track momentum p^{trk} is given by:

$$\langle E_{dep} \rangle = p^{trk} \langle E_{ref}^{clus}/p_{ref}^{trk} \rangle \quad (4.11)$$

Recovering split showers A particle can deposit its energy in several clusters, and it is thus important to know how much of its energy lies in the cluster(s) considered. To differentiate the case of a distribution of energy in a single or multiple topo-clusters, the following discriminant is introduced:

$$S(E^{clus}) = \frac{E^{clus} - \langle E_{dep} \rangle}{\sigma(E_{dep})} \quad (4.12)$$

where $\sigma(E_{dep})$ is the spread of the expected energy.

In the case where $S(E^{clus}) < -1$, a split shower recovery procedure is initiated, consisting in matching all topo-clusters in a radius $\Delta R = 0.2$ to the track.

Cell-by-cell subtraction When a topo-cluster is associated to a track (charged particle), the energy in the calorimeter is subtracted since it is already measured in the track.

If the energy in a topo-cluster is smaller than $\langle E_{dep} \rangle$, the whole topo-cluster is removed. If $E^{clus} > \langle E_{dep} \rangle$ the energy is removed layer by layer, in concentric circles centered on the layer of highest energy density (LHED) until the energy removed matches $\langle E_{dep} \rangle$.

The LHED is defined as the layer where the rate of increase in energy density is the highest. The energy density for the cell j in the layer i is given as

$$\rho_{ij} = \frac{E_{ij}}{V_{ij}}, \quad (4.13)$$

with V_{ij} the volume of the cell in radiation lengths. Then, the cells are weighted (w_{ij}) depending on the proximity to the track position. The weighted average density for the layer i is given by

$$\langle \rho' \rangle_i = \sum_j w_{ij} \rho_{ij}. \quad (4.14)$$

Ultimately, the rate of increase is

$$\Delta \rho'_i = \frac{\langle \rho' \rangle_i - \langle \rho' \rangle_{i-1}}{d_i - d_{i-1}}, \quad (4.15)$$

with d_i is the depth of layer i in interaction lengths. The LHED is defined as the layer where $\Delta \rho'_i$ is maximal.

Remnant removal After the cell subtraction, it is possible that some of the energy deposited by a charged particle remains, due to shower fluctuations. This last step removes the rest of the topo-cluster if the energy remaining is less than $1.5\sigma(E_{dep})$.

4.4.2 Jet reconstruction and anti- k_t algorithm

After the particle flow algorithm, jets are reconstructed using the anti- k_t algorithm [198] on the surviving topo-clusters. The anti- k_t is a jet clustering algorithm belonging to the family of soft-resilient algorithms. This kind of algorithms construct jets with regular boundaries, which allows a simplified calibration and elimination of pileup. Soft-resilient algorithms are opposed to soft-adaptable algorithms (e.g. SIScone [199]), with irregular boundaries, more suited for the branching nature of QCD interactions.

The anti- k_t algorithm works by adding together topo-clusters based on a distance defined as:

$$d_{ij} = \min(k_{ti}^{2p}, k_{tj}^{2p}) \frac{\Delta_{ij}^2}{R^2}, \quad (4.16)$$

$$d_{iB} = k_{ti}^{2p}, \quad (4.17)$$

where k_t is the transverse momentum, i and j denote entities (in our case, topo-clusters), B the LHC proton beam, $\Delta_{ij}^2 = (y_i - y_j)^2 + (\phi_i - \phi_j)^2$, R a radius parameter to be set and p a parameter to be set. These formulas are used for a range of algorithms depending on the value

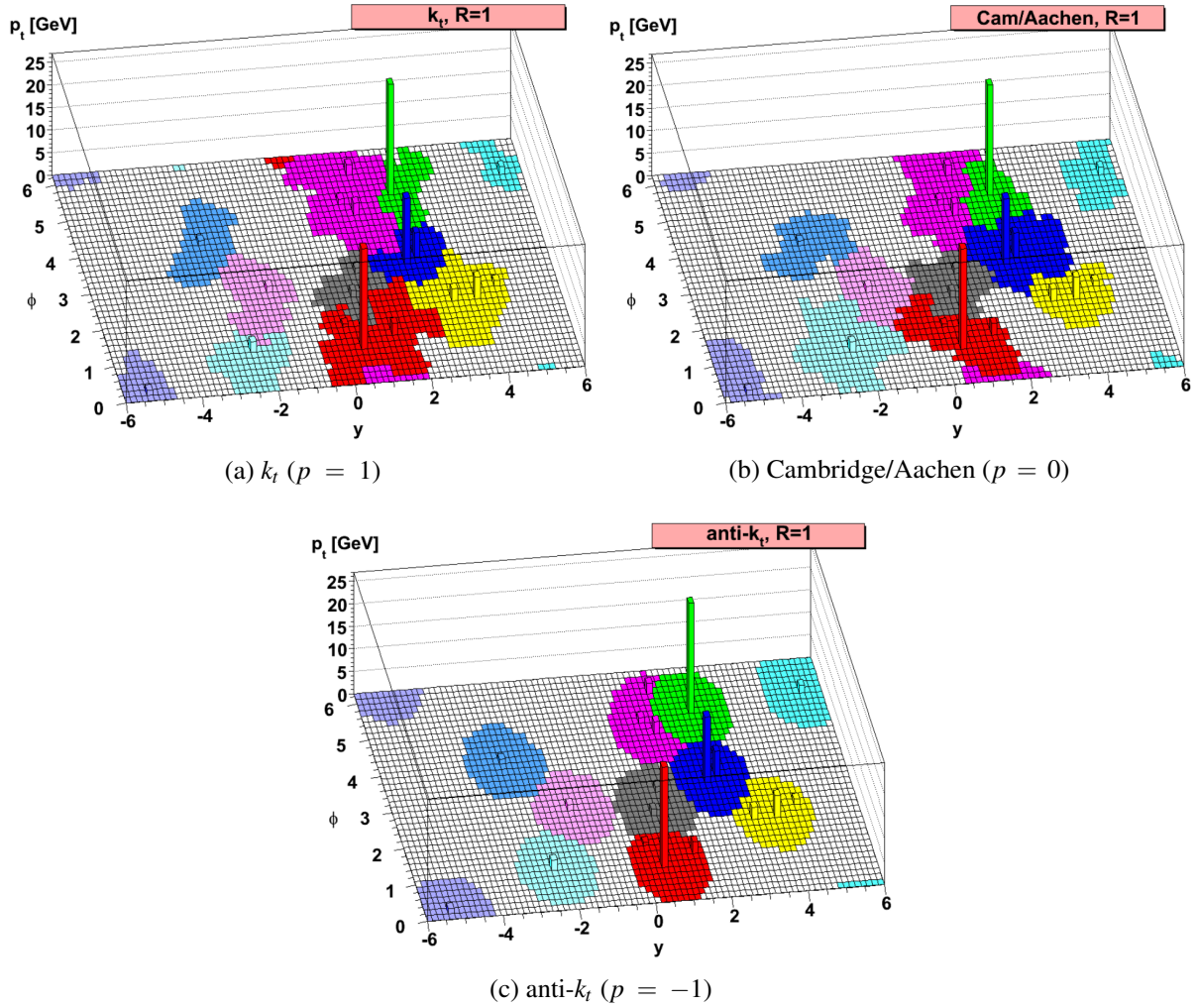


Figure 4.7: Resulting jets areas obtained with different clustering algorithms for MC generated jets. Figure taken from Ref. [198].

of p . For example, $p = 1$ corresponds to the inclusive k_t algorithm while $p = 0$ is the inclusive Cambridge/Aachen algorithm. The anti- k_t algorithm uses $p = -1$. The differences between the various jet clustering algorithms are visualized in Fig. 4.7.

The clustering algorithm acts by taking the smallest of all distances between topo-clusters. If it is a distance of type d_{ij} , then the i and j topo-clusters are combined. If it is of type d_{iB} the topo-cluster i is removed from the list of entities that can be clustered.

In the anti- k_t algorithm, the negative value of p favours the hardest particle such that $\min(k_{ti}^{2p}, k_{tj}^{2p}) = 1/k_{t,hardest}^2$. This means that all soft topo-cluster in a radius R around a hard one is merged with the latter. This leads to almost circular clusters of radius R around hard topo-clusters, as shown in Fig. 4.7. In the case of two hard jets, three cases can be distinguished. Either they are separated by more than $2R$ in which case they don't interfere with each other. Or they are closer than R and they merge. Finally, they can be at a distance between R and $2R$, which means that their disks should overlap so each cluster is delimited by a boundary b following $\Delta_{1b}/k_{t1} = \Delta_{2b}/k_{t2}$.

In Section 5, jets are created by the anti- k_t algorithm with parameter $R = 0.4$. The input entities are the topo-clusters (surviving the energy subtraction) with tracks matching $|z_0 \sin \theta| < 2$ mm,

with z_0 the longitudinal impact parameter (impact parameter projected on the beam line), or without a track.

4.4.3 Pileup suppression

To remove most of the pileup jets, a pileup suppression technique called Jet Vertex Tagger (JVT) [200] is implemented. The JVT is based on two variables: corrJVF and R_{p_T} . These variables are derived from the pileup jet subtraction used during Run 1 called Jet Vertex Fraction (JVF). The JVF was used during Run 1 but its efficiency depended on the number of vertices. With the increase of the luminosity for Run 2, the efficiency would have decreased and it has been decided to change toward a corrected JVF. The corrected JVF is defined as:

$$\text{corrJVF} = \frac{\sum_m p_{T,m}^{\text{track}}(\text{PV}_0)}{\sum_l p_{T,l}^{\text{track}}(\text{PV}_0) + \frac{p_T^{\text{PU}}}{k \cdot n_{\text{track}}^{\text{PU}}}} \quad (4.18)$$

where $p_{T,l}^{\text{track}}(\text{PV}_n)$ is the transverse momentum of the track l associated with the jet originating from the vertex n (with $n = 0$ being the hard-scatter vertex), $k = 0.01$ a constant and $n_{\text{track}}^{\text{PU}}$ the number of pileup tracks per event. The term $p_T^{\text{PU}} = \sum_{n \geq 1} \sum_l p_{T,l}^{\text{track}}(\text{PV}_n)$ is the scalar sum of all tracks momentum coming from pileup vertices. The $k \cdot n_{\text{track}}^{\text{PU}}$ factor prevents the denominator of the corrJVF to increase when the number of interaction increases, thus creating a relatively stable efficiency, independent of the amount of primary vertices. The corrJVF variable is usually low for pileup jets and high for hard-scatter jets, as shown in Fig. 4.8.

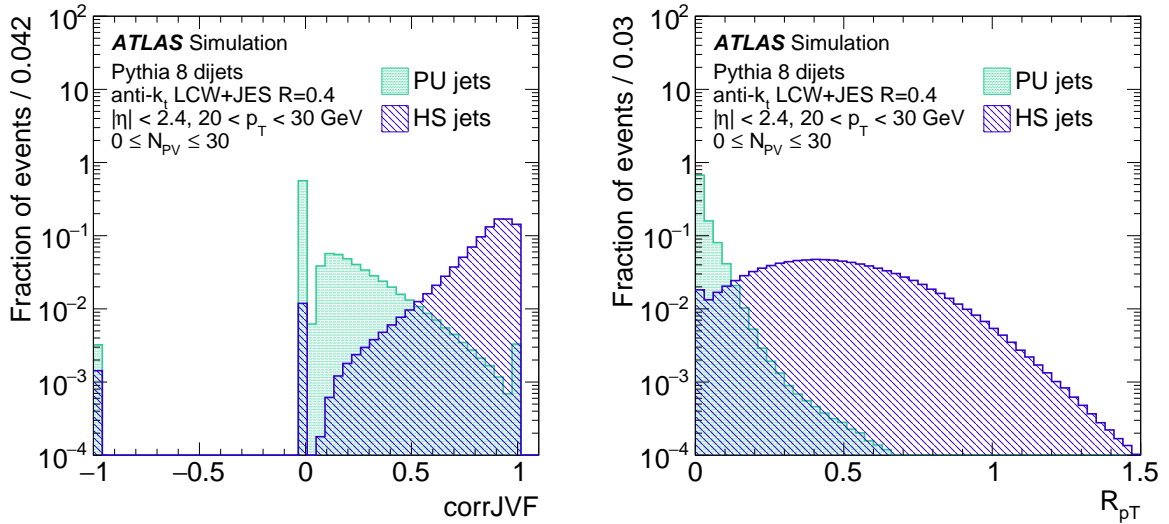


Figure 4.8: Distribution of corrJVF (left) and R_{p_T} (right) for pileup (PU) and hard-scatter (HS) jets with $20 \text{ GeV} < p_T < 30 \text{ GeV}$. Figure taken from Ref. [200].

In addition, another variable has been introduced relying only on hard-scatter observables:

$$R_{p_T} = \frac{\sum_k p_{T,k}^{\text{track}}(\text{PV}_0)}{p_T^{\text{jet}}} \quad (4.19)$$

where p_T^{jet} is the jet transverse momentum. This value is usually lower for pileup jets than for hard-scatter jets, as shown in Fig. 4.8.

The JVT works by distributing the simulated jets on a 2D $\text{corrJVF} \times R_{p_T}$ plane. For any jet, the probability to be a hard-scatter jet is computed by the rate of hard-scatter jets in its surrounding. The surrounding is defined as a local neighbourhood of the 100 closest jets using a Euclidean metric in the $\text{corrJVF} \times R_{p_T}$ space. Then a minimum value is set on the JVT, depending on the working point desired. For example, for jets within $|\eta| < 2.4$ and $20\text{GeV} < p_T < 120\text{GeV}$, the Medium working point is defined as:

$$\text{JVT} > 0.59 \quad (4.20)$$

4.4.4 Jet calibration

The jet calibration [201] is applied both on data and MC simulations to account for different effects which affect the measured transverse momentum, the pseudorapidity or the resolution. To account for these phenomena, both simulation- and data-based calibrations are implemented.

The simulation-based calibrations are applied in three different steps: pileup corrections, jet energy scale (MCJES) and η calibrations and global sequential calibration (GSC). The main idea is to correct the reco transverse momentum by taking into account the jet area A , the number of primary vertices N_{PV} and the mean number of interactions per bunch crossing μ :

$$p_T^{\text{corr}} = p_T^{\text{reco}} - \rho \times A - \alpha \times (N_{\text{PV}} - 1) - \beta \times \mu, \quad (4.21)$$

where p_T^{reco} is the reconstructed jet transverse momentum before correction (matched to a truth jet), ρ the median p_T density $\rho = \langle p_T/A \rangle$, and α and β are coefficient determined by MC. The coefficients are set for each bin of p_T^{true} and $|\eta_{\text{det}}|$ (pseudorapidity pointing from the geometric center of the detector) independently.

Then, the MCJES consists in compensating the calorimeter and reconstruction biases, including the calorimeter response and loss of energy in the passive material, as well as biases in the η reconstruction. To do so, the jet energy is corrected so that the jet energy response \mathcal{R} , defined as the mean of a gaussian fit on the $E^{\text{reco}}/E^{\text{true}}$ ratio, is close to 1. This response is computed in bins of E^{reco} and η_{det} and the correction is applied to reconstructed jets. Moreover, due to the calorimeter geometry, there is a bias concerning the η reconstruction. This is solved by introducing a correction on the difference between η_{reco} and η_{true} , depending on η_{det} and E^{reco} of the jets.

The previous corrections are applied on jets, independently of their features. However, jets have different properties depending on the flavour of their initiating parton, energy distribution, etc. By reducing the effects of the dependencies on jet measurements, a better resolution can be obtained. To do so, the GSC procedure is performed, where jets response are corrected based on their properties, such as the fraction of energy in the different parts of the calorimeters, the number of tracks and their width, etc. This correction, which does not change the value of the response but their resolution, is applied both on data and MC reconstructed jets.

Finally, once the detector level MC jets match closely to the truth jets, data and MC reco jets have still some remaining discrepancies. To fix this, a so called "in situ" calibration is applied. This calibration is applied to data so that it matches the MC reco (and therefore MC truth)

predictions. The in situ calibration is done in three steps all based on the same general principle. The idea is to use a well calibrated reference object counteracting the jet, in order to measure the response defined as the ratio between the transverse momentum of the jet and the reference:

$$\mathcal{R}_{in\ situ} = \frac{p_T^{\text{jet}}}{p_T^{\text{ref}}}. \quad (4.22)$$

A more robust method is used to mitigate the effect of mismodelling of additional radiative jets by using the double ratio c define as:

$$c = \frac{\mathcal{R}_{in\ situ}^{\text{data}}}{\mathcal{R}_{in\ situ}^{\text{MC}}}. \quad (4.23)$$

In ATLAS, the in situ method is carried in three steps: η intercalibration, low- p_T and high- p_T jets calibration. The η intercalibration is done to correct the energy scale of the forward jets ($0.8 < |\eta_{\text{det}}| < 4.5$). To do so, dijet events with one jet in the central region (reference object) and the other jet in the forward region are used. For low- p_T jets, Z/γ +jet events are considered with the Z or γ being the reference. This calibration is done only for low- p_T since the statistic is lacking for recoil jets associated to Z/γ above a few hundreds of GeV. For high- p_T jets, a multijet balance (MJB) technique is used where a high- p_T jet is balanced against several low- p_T jets, taken as references. Combining the Z/γ +jet and MJB calibration offers the possibility to calibrate the jet scale on the whole energy range.

5 | $Z\gamma$ + jets study in the ATLAS detector

This chapter presents the analysis of the $pp \rightarrow Z\gamma$ + jets process with the ATLAS Run 2 dataset. The $Z\gamma$ + jets study is, as of April 2023, accepted for publication and can be found prepublished in Ref. [202] and in the form of a conference note in Ref. [203]. The goal is to study the production of jets associated with the process. Details on the motivations for the study of jets in the $Z\gamma$ + jets process are introduced in Section 5.1. An introduction to the data and simulated samples, as well as a brief description of the MC generators used, is given in Section 5.2. Section 5.3 presents the objects selected, as well as the variables chosen in the analysis. The different sources of background faking the $Z\gamma$ signal and the methods to compute them are introduced in Section 5.4. The unfolding method used to migrate from reconstruction to truth level is explained in Section 5.5. Introduction to the uncertainty sources and presentation of the results of the analysis are done in Section 5.6 and Section 5.7 respectively.

5.1 Context and motivations

The production of $Z\gamma$ is an interesting channel to study the electroweak sector for several reasons. The first is that it has a relatively high cross-section compared to other diboson processes (around 530 fb for the process given in Fig. 5.1 [72]), thus leading to a large amount of data (around 70 000 events for an integrated luminosity of 139 fb^{-1}). This allows to make precise measurements of SM properties, and also to test for BSM phenomena. The characteristics of diboson processes are discussed in Section 2.1.4.

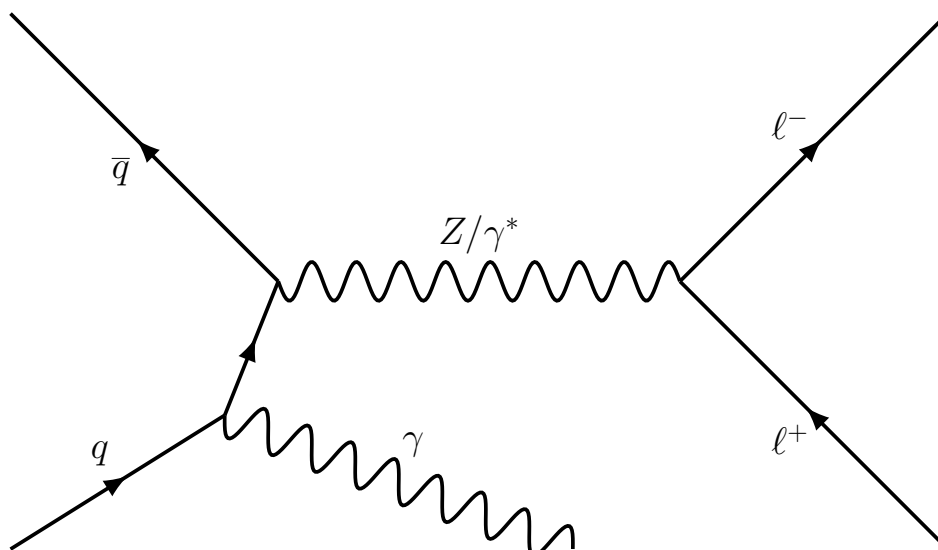


Figure 5.1: Feynman diagram of the ISR $pp \rightarrow Z\gamma$ process where the Z boson decays leptonically, studied in the $Z\gamma$ + jets analysis.

The $Z\gamma$ channel is also a source of background for other processes such as the Higgs boson decay $H \rightarrow Z\gamma$ [204]. A good understanding of the $Z\gamma$ process could help reduce uncertainties in

Period	2015	2016-2018
Trigger	e24_lhmedium_L1EM20VH e60_lhmedium e120_lhloose mu20_iloose_L1MU15 mu50	e26_lhtight_nod0_ivarloose e60_lhmedium_nod0 e140_lhloose_nod0 mu26_ivarmedium mu50

Table 5.1: List of single lepton triggers used in the $Z\gamma$ +jets analysis. Details on the trigger naming schemes are available in Section 3.2.4.

the corresponding searches and future measurements. Moreover, the $Z\gamma$ channel can indirectly be used in other searches for new Higgs bosons in the ZZ decay channel, where the $Z\gamma$ process can be used as a mean to estimate the $pp \rightarrow ZZ$ background [205].

The $Z\gamma$ differential cross-section distributions have already been measured by ATLAS with the Run 1 dataset at collision center-of-mass energies $\sqrt{s} = 7\text{ TeV}$ [206] and $\sqrt{s} = 8\text{ TeV}$ [207], and even with the whole Run 2 dataset at $\sqrt{s} = 13\text{ TeV}$ [72].

The previous analyses were inclusive in jet activity, while this new iteration focuses on the jet activity and QCD modelling. Precise knowledge of QCD phenomena is needed to search for Dark Matter (DM) since the data are evaluated by comparing them to simulated samples using QCD properties. Lower uncertainties on the MC therefore cause bigger significance in the case of a deviation with the data, or stronger constraints in the case of an agreement between data and MC simulations.

More precisely, calculations of QCD processes performed with matrix elements, PS, or resummation, as discussed in Section 2.4.3, are dominated by Sudakov logarithms. The Sudakov logarithms are terms in $\alpha_s^n \ln^k(p_T/m)$ for the order n in QCD, where p_T is the transverse momentum and m the mass of the system. Among other things, the goal of this new $Z\gamma$ +jets analysis is to measure observables that are potentially sensitive to the way the calculations deal with the Sudakov logarithms. Comparing MC results with the data can test the quality of modelling of the PS and resummation.

5.2 Samples

The analysis uses the data collected by the ATLAS detector during Run 2 (running period 2015-2018). This corresponds to an integrated luminosity of 139 fb^{-1} . Events are chosen so that they pass at least one of the single lepton triggers listed in Table 5.1. The rest of the selection is explained in Section 5.3.2 after the object definitions in Section 5.3.1.

For the $Z\gamma$ signal simulation, the MC generator Sherpa 2.2.11 [208] is used, unless otherwise specified, for example in the Z +jets and pileup estimates, as well as the data unfolding.

To compare the measurements with different signal predictions, several generators are used: Sherpa 2.2.11, Sherpa 2.2.4, MadGraph5 [209], MiNNLO_{PS} [210, 211] and MATRIX [139]. A summary of the main features of the generators is given in Table 5.2 and is described in more details below.

Generator	QCD accuracy	PDF	Parton shower
Sherpa 2.2.11	0,1j@NLO+2,3j@LO	NNPDF3.0NNLO	Sherpa 2.2.11
Sherpa 2.2.4	0,1,2,3j@LO	NNPDF3.0NNLO	Sherpa 2.2.4
MadGraph5	0,1j@NLO	NNPDF3.0NLO_as_0118	Pythia8.212
POWHEG	NNLO	NNPDF3.0NNLO	MiNNLO _{PS}
MATRIX	NNLO	CT14NNLO	MadGraph5

Table 5.2: $Z\gamma$ signal samples for comparison with the unfolded data distributions. For MATRIX, MadGraph5 is used as a parton-particle correction and not as PS.

As stated previously, Sherpa 2.2.11 is used for the unfolding process, the data-driven background estimates and as comparison to the data. It generates samples by calculating the matrix elements at NLO accuracy in QCD with up to one additional parton and at LO with up to three additional partons. Concerning the electroweak processes, the generator is limited to the order α_{EW}^2 . To simulate the PDF, the set NNPDF3.0NNLO [138] is used. In addition, Frixione isolation [212] is applied to the photon, requiring the following parameters: $\delta_0 = 0.1$, $\varepsilon = 0.1$, and $n = 2$. The photon is also required to be $p_T^\gamma < 7 \text{ GeV}$. Once the matrices are generated, the NLO and LO diagrams are merged with MEPS@LO [213] which also performs the parton shower.

Sherpa 2.2.4 generates matrix elements at LO in QCD with up to three additional partons, and α_{EW}^2 . Otherwise, this version of Sherpa uses essentially the same parameters as Sherpa 2.2.11.

For the MadGraph5 sample, matrix elements are computed at NLO with up to one additional parton. The PDF used in this generator is the NNPDF3.0NLO_as_0118 set. To generate the subsequent parton showers, the generator is interfaced with Pythia8 [214].

MiNNLO_{PS} is not a generator by itself, but rather an approach. The generator behind this prediction is POWHEG at NNLO using the NNPDF3.0NNLO PDF set with the same Frixione isolation parameters as for Sherpa 2.2.11. The MiNNLO_{PS} approach consists in merging the NNLO matrix elements with parton showers by including the spin correlation, interference and off-shell effects.

Finally, the MATRIX generator is used to make fixed-order calculations at NNLO. The PDF set used is CT14NNLO and the Frixione isolations are analogous to what was required in Sherpa 2.2.11. Since MATRIX only delivers results at parton level while the measurement is done at particle level, a correction is applied to "dress" the lepton. This means that leptons are corrected for collinear photon radiation by adding to their four-momenta, the four-momenta of photons not coming from hadronic decay and within $\Delta R < 0.1$. A parton to particle correction is also applied to take into account the hadronization that are not included in MATRIX. This correction is derived using MadGraph5 and Pythia8.

The backgrounds are detailed in Section 5.4. They are estimated with different generators, as shown in Table 5.3.

Process	Generator	QCD accuracy	PDF	Parton shower
$Z + \text{jets}$	POWHEG	NLO	CT10NLO	Pythia8.186
$t\bar{t}\gamma, tW\gamma$	MadGraph5	LO	NNPDF2.3LO	Pythia8.212
ZZ, WZ	Sherpa 2.2.2	0,1j@NLO+2,3j@LO	NNPDF3.0NNLO	Sherpa 2.2.2
$WZ\gamma, WW\gamma$	Sherpa 2.2.11	NLO+1,2j@LO	NNPDF3.0NNLO	Sherpa 2.2.11
EWK $V\gamma$	MadGraph5	LO	NNPDF3.0LO	Pythia8.240

Table 5.3: Generators and details of the background samples.

Object	Electrons	Muons	Photons
Kinematics	$p_T > 25 \text{ GeV}$ $ \eta < 2.47$ (excl. $1.37 < \eta < 1.52$)	$p_T > 25 \text{ GeV}$ $ \eta < 2.5$	$p_T > 30 \text{ GeV}$ $ \eta < 2.37$ (excl. $1.37 < \eta < 1.52$)
Identification	Medium	Medium	Tight
Isolation	FCLoose	PflowLoose_FixedRadIso	FixedCutLoose
Impact parameter	$ d_0/\sigma(d_0) < 5$ $ z_0 \sin \theta < 0.5 \text{ mm}$	$ d_0/\sigma(d_0) < 3$ $ z_0 \sin \theta < 0.5 \text{ mm}$	-

Object	Jets
Algorithm	anti- k_t ($R = 0.4$, PFlow)
Kinematics	$p_T > 30 \text{ GeV}$ if $ \eta < 2.5$ $p_T > 50 \text{ GeV}$ if $2.5 < \eta < 4.4$
Pileup mitigation	JVT Medium for $p_T < 120 \text{ GeV}$ and $ \eta < 2.5$

Table 5.4: Object definition for the $Z\gamma + \text{jets}$ analysis. The different parameters are explained in Section 4.

5.3 Event selection

5.3.1 Object definition

For the events passing the triggers, selections are applied to define the different objects used in the analysis. A summary of the object definition can be found in Table 5.4.

An electron is required to have a transverse momentum $p_T > 25 \text{ GeV}$ and a pseudorapidity $|\eta| < 2.47$. However, it should not be in the EM calorimeter transition region located at $1.37 < |\eta| < 1.52$. The required identification is Medium (defined in Section 4.1.3) and the isolation must pass the FCLoose criteria (defined in Eq. (4.7)). The transversal impact parameter d_0 is required to have a significance $|d_0/\sigma(d_0)| < 5$ and the longitudinal impact parameter z_0 must satisfy $|z_0 \sin \theta| < 0.5 \text{ mm}$.

A muon is required to be central with $|\eta| < 2.5$ and have a transverse momentum $p_T > 25 \text{ GeV}$. The identification must be Medium (defined in Section 4.3) and the isolation PflowLoose_FixedRadIso (defined in Eq. (4.9)). Like electrons, requirements are applied on the vertex position, imposing $|d_0/\sigma(d_0)| < 3$ and $|z_0 \sin \theta| < 0.5 \text{ mm}$.

Photons are expected to have $p_T > 30\text{ GeV}$ and $|\eta| < 2.37$, excluding the transition region $1.37 < |\eta| < 1.52$. They must be Tight identified (defined in Section 4.2) and FixedCutLoose isolated (defined in Eq. (4.8)).

The jets are reconstructed using the particle flow algorithm and clustered with the anti- k_r algorithm and a radius parameter of $R = 0.4$ (see Section 4.4). Jets are then defined depending on if they are central or forward. In the central region $|\eta| < 2.5$, the momentum requirement is set to $p_T > 30\text{ GeV}$, while it is increased to $p_T > 50\text{ GeV}$ for the forward region $2.5 < |\eta| < 4.4$. The use of a step function allows to keep many jets while rejecting the pile-up as much as possible. Finally, the pileup is suppressed using the Medium working point of the JVT (defined in Eq. (4.20)).

In addition to the aforementioned isolation requirements for each object, further selections are done on the close-by objects to avoid overlaps and make sure that the selected objects are well-defined. The selections are done in the following order:

1. Jets are removed if they are within $\Delta R < 0.4$ of a photon or $\Delta R < 0.2$ of an electron.
2. Electrons and muons are removed if they are within $\Delta R < 0.4$ of a jet.
3. Photons are removed if they are within $\Delta R < 0.4$ of an electron or a muon.
4. Electrons are removed if they are within $\Delta R < 0.2$ of a muon.

5.3.2 Signal region definition

After the objects have been defined, a set of requirements can be applied on them. This selection is optimized to remove most of the background while trying to keep the desired signal events (here, the ISR $Z(\rightarrow \ell\ell)\gamma$ events).

Events must have at least two opposite sign and same flavour charged leptons (taus are not considered). This means that they are required to have either an electron-positron pair (e^-e^+), or a muon-antimuon pair ($\mu^-\mu^+$). Moreover, the lepton with the highest transverse momentum (called leading lepton) must have a minimum transverse momentum of 30 GeV to ensure a high trigger efficiency. The mass of the dilepton system $m_{\ell\ell}$ is required to pass $m_{\ell\ell} > 40\text{ GeV}$ to avoid low-mass resonances (e.g. J/Ψ) and off-shell photons γ^* .

Along with leptons, events are required to contain at least one photon. The two leptons and the photon must pass a requirement as follows:

$$m_{\ell\ell} + m_{\ell\ell\gamma} > 182\text{ GeV}. \quad (5.1)$$

This choice is explained by the rejection of the final state radiation (FSR) process shown in Fig. 5.2. As seen in Fig. 5.3, most of the events are concentrated in two zones: $m_{\ell\ell} = 91\text{ GeV}$ and $m_{\ell\ell\gamma} = 91\text{ GeV}$. In the first case, the photon comes from ISR and it is likely that $m_{\ell\ell} \sim m_Z$ and $m_{\ell\ell\gamma} > m_Z$. If the FSR occurs, then $m_{\ell\ell\gamma} \sim m_Z$ and $m_{\ell\ell} < m_Z$. To differentiate both cases, the selection is chosen to be a diagonal between the two ridges, thus rejecting the FSR case.

The selection implies that only a small part of the whole set of events detected by ATLAS is studied. This phase-space is called "signal region" (SR). In addition to the SR, another region called "control region" (CR) is defined to check that the different background sources, simulated or data-driven, describe correctly the data for the observables considered in the analysis, without unblinding data. Here, unblinding is the process of looking at the data/SM comparison plots.

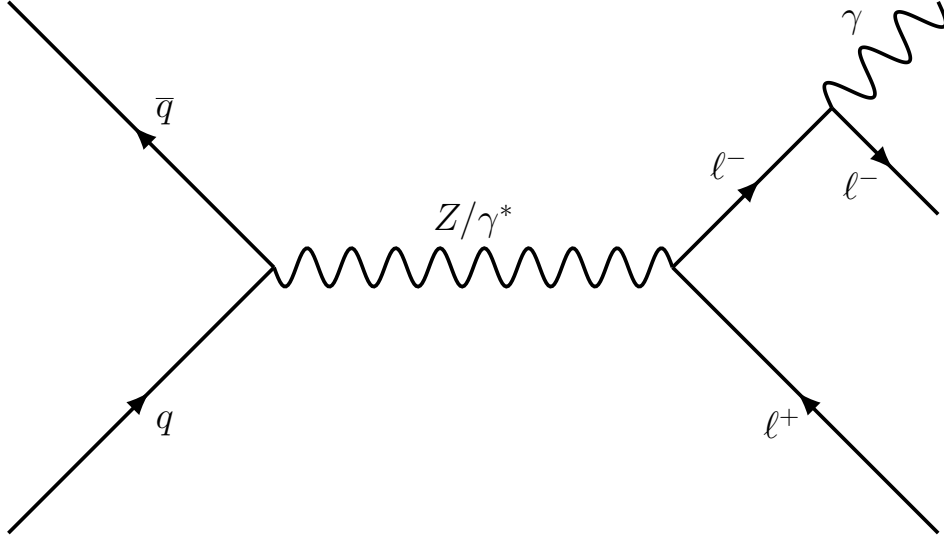


Figure 5.2: Feynman diagram of the FSR $Z\gamma$ process.

Unblinding before establishing the method to estimate the background sources could have led to a source of bias.

In this analysis, the CR has the same characteristics as the signal region, except that the leptons are chosen to have different flavours: a positron-muon ($e^+\mu^-$) or electron-antimuon ($e^-\mu^+$) pair. This region is also called the $e\mu\gamma$ region.

5.3.3 Observables

The goal of this analysis is to study the jet behaviour. This leads to the choice of observables shown in Table 5.5 and 5.6, which are either sensitive to QCD radiation or describe the process in itself. The latter are called "hard variables" because they represent the hard scale process and are non-zero at LO. For example, p_T^γ , $p_T^{\ell\ell}$ and $m_{\ell\ell\gamma}$ are hard scale variables, meaning that these are non-zero at LO and represent the scale of the process. On the contrary, variables which are sensitive to additional QCD emission are called "resolution variables", and are non-zero with increasing jet activity. Examples of these variables are jet variables (p_T^{jet} , $m_{\ell\ell\gamma j}, \dots$) but also $p_T^{\ell\ell\gamma}$, $p_T^{\ell\ell} - p_T^\gamma$, etc.

The analysis is focused on 14 one-dimensional (1D) observables. In addition, four observables already analyzed in Ref. [72] are used as control variables, in particular to develop the background estimate methods. The 1D observables used and their descriptions are given in Table 5.5.

In addition to the 1D observables, 3 observables are given following a two-dimensional (2D) distribution. They are chosen to be one hard variable and one resolution variables. The resolution variable is measured precisely (with many bins) while the hard variable is split coarsely. The 2D observables are given in Table 5.6. One can remark that the $p_T^{\ell\ell\gamma}$ is given as a hard variable in the 2D distribution while listed as a resolution variable when looked at as a 1D distribution. This is because the $p_T^{\ell\ell\gamma} \times p_T^{\ell\ell\gamma j}$ distribution studies the behaviour of the subleading jet. In that case, the system of interest is not $\ell\ell\gamma$ anymore but rather $\ell\ell\gamma j$, making the $p_T^{\ell\ell\gamma}$ be non-zero.

Type	Name	Description
Hard variables	p_T^γ *	Transverse momentum of the photon
	$m_{\ell\ell\gamma}$ *	Invariant mass of the dilepton-photon system
	H_T	Scalar sum of the transverse momentum of all visible objects (leptons, photons, jets)
	$p_T^\gamma/\sqrt{H_T}$	Ratio between the transverse momentum of the photon and the square root of H_T
	$\Delta R(\ell, \ell)$	Pseudorapidity-azimuthal angle between the two leptons (see definition in Eq. (3.11))
	$p_T^{\ell\ell}$	Transverse momentum of the dilepton system
	$p_T^{\ell\ell} + p_T^\gamma$	sum of the transverse momentum of the dilepton system and the photon
Resolution variables	$p_T^{\ell\ell\gamma}$ *	Transverse momentum of the dilepton-photon system
	$p_T^{\ell\ell\gamma}/m_{\ell\ell\gamma}$ *	Ratio of the transverse momentum of the dilepton-photon system and its invariant mass
	$p_T^{\ell\ell} - p_T^\gamma$	Difference between the transverse momentum of the dilepton system and of the photon
	N_{jets}	Number of jets
	p_T^{jet1}	Transverse momentum of the leading jet (if $N_{\text{jets}} \geq 1$)
	$p_T^{\ell\ell\gamma j}$	Transverse momentum of the dilepton-photon-leading jet system (if $N_{\text{jets}} \geq 1$)
	$m_{\ell\ell\gamma j}$	Invariant mass of the dilepton-photon-leading jet system (if $N_{\text{jets}} \geq 1$)
	$\Delta\phi(\text{Jet}, \gamma)$	Azimuthal angle between the leading jet and the photon (if $N_{\text{jets}} \geq 1$)
	p_T^{jet2}	Transverse momentum of the subleading jet (if $N_{\text{jets}} \geq 2$)
	$p_T^{\text{jet2}}/p_T^{\text{jet1}}$	Ratio between the transverse momentum of the subleading and leading jets (if $N_{\text{jets}} \geq 2$)
m_{jj}	Invariant mass of the dijet system (if $N_{\text{jets}} \geq 2$)	

Table 5.5: List of the 1D distributions considered in the study. The asterisk (*) denotes the variables already measured in Ref. [72] which are used only as a control variables.

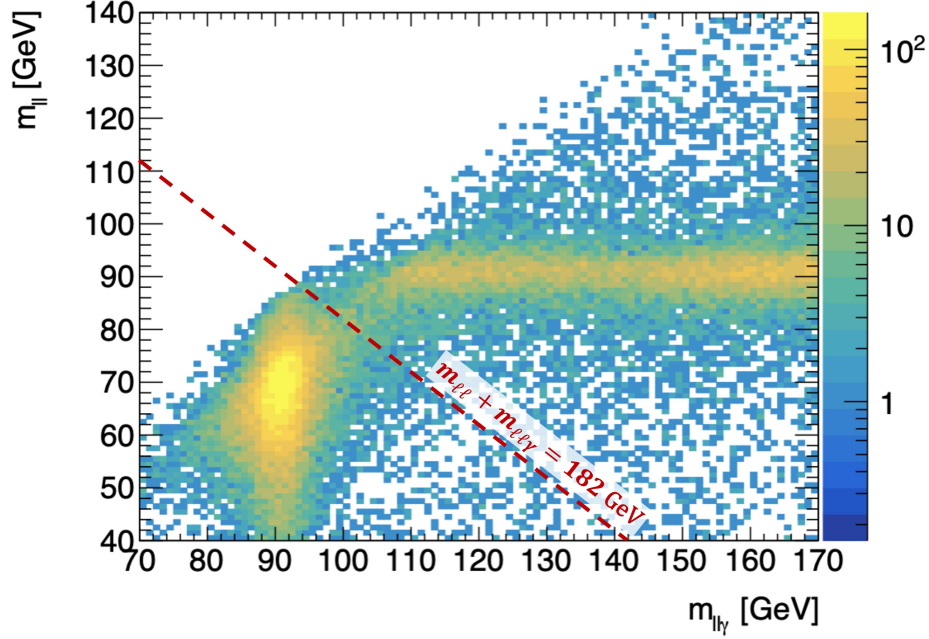


Figure 5.3: Distribution of the $Z(\rightarrow \ell\ell)\gamma$ events on the $m_{\ell\ell} \times m_{\ell\ell\gamma}$ plane. The red line represents the boundary $m_{\ell\ell} + m_{\ell\ell\gamma} = 182 \text{ GeV}$ dividing the the event failing (below) and passing (above) the selection criteria.

Hard variable	Resolution variables
$m_{\ell\ell\gamma}$	$p_T^{\ell\ell\gamma} / m_{\ell\ell\gamma}$
$p_T^{\ell\ell} + p_T^{\gamma}$	$p_T^{\ell\ell} - p_T^{\gamma}$
$p_T^{\ell\ell\gamma}$	$p_T^{\ell\ell\gamma j}$

Table 5.6: List of the 2D distributions considered in the study.

5.4 Background estimation

Data events selected by the requirements presented in Section 5.3 include $Z(\rightarrow \ell\ell)\gamma$ events, but also events from other background processes. These backgrounds have several origins: processes with the same final state (2 leptons and one photon), pileup contributions and misidentification of particles. The selection applied reduces the background but does not completely remove it.

For each observable, the background estimates are added together and subtracted from the data distribution. This step is crucial for comparing the measurements with different signal estimations, as well as to perform further interpretation, such as testing a DM candidate model. In the $Z(\rightarrow \ell\ell)\gamma$ process, the main sources of background are, by order of importance, Z + jets, pileup photons, $t\bar{t}\gamma$, multiboson production, production of $Z\gamma$ by electroweak processes and $tW\gamma$. In this section, the different background sources and their estimations are explained, with a focus on the Z + jets process. After the description of the background, the $e\mu\gamma$ control region will be introduced to check the validity of the estimates.

5.4.1 Z + jets estimate

The Z + jets process is the most important source of background along with the pileup photon contribution. These two sources are not independent since part of the Z + jets events contain pileup jets. The Z + jets contributions enter the SR when a jet is misidentified as a photon (see Fig. 5.4). This background is estimated using a data-driven sideband method.

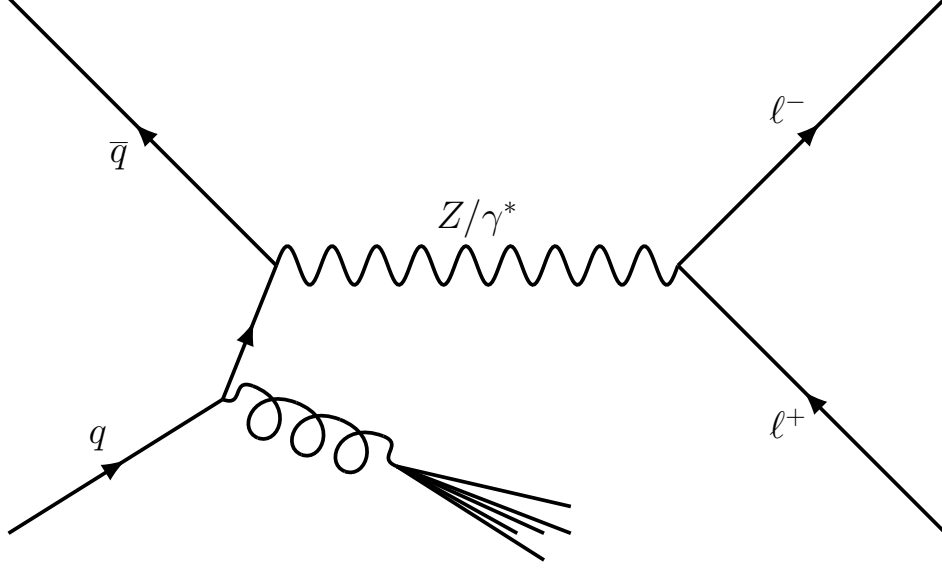


Figure 5.4: Example of Feynman diagram for the Z + jets process. In the $Z\gamma$ + jets analysis, it can happen that the jets are misidentified as a photon.

Sideband method

The Z + jets contribution is an important source of background, for which the MC modelling of the isolation and identification of the fake photon is limited. Therefore, the estimate is done using a data-driven method called a two-dimensional sideband method. This method is based on the division of the data and MC events in 4 regions, called A, B, C and D, based on passing or failing the identification and isolation criteria. The goal of this procedure is to define the Z + jets estimate in the SR (region A) from the parameters in the control regions (regions B, C and D) by a cross product:

$$N_{SR,A}^{Z+jets} = R \times \frac{N_{CR,B}^{Z+jets} N_{CR,C}^{Z+jets}}{N_{CR,D}^{Z+jets}}, \quad (5.2)$$

where R is a correction factor called "correlation factor" and the different N_X^{Z+jets} can be deduced from

$$N_X^{data} = N_X^{sig} + N_X^{bkg} + N_X^{Z+jets}, \quad N_X^{sig} = c_X N_A^{sig}, \quad (5.3)$$

with c_X a leakage parameter. The advantage of the division in 4 regions is that quantities originating from MC simulations (N^{Z+jets} and N^{sig}) can be redefined to be fractions (R and c_X). This removes some of the systematic errors introduced by a mismodelling of the simulations.

To enter the sideband method, events are expected to pass all the selections of the signal region, except for the photon identification and calorimeter isolation ($E_T^{cone20} < 0.065 p_T^\gamma$). The regions

are then defined depending on whether the photon passes or fails the isolation and identification criteria (see Fig. 5.5):

- Region A: It corresponds to the SR, where the photon is identified as Tight and isolated ($E_T^{cone20} < 0.065p_T^\gamma$).
- Region B: The photon is identified as Tight but fails the calorimeter isolation criteria ($E_T^{cone20} > 0.065p_T^\gamma + E_{\text{gap}}$).
- Region C: The photon fails the Tight identification but passes the isolation criteria ($E_T^{cone20} < 0.065p_T^\gamma$).
- Region D: The photon fails both the Tight identification and the isolation criteria ($E_T^{cone20} > 0.065p_T^\gamma + E_{\text{gap}}$).

To ensure a good quality in the data and simulations, all photons must pass a Tight identification where some criteria are loosened. Such working points are called LoosePrime. In this analysis, the chosen identification is LoosePrime4, where most of the requirements on the cluster in the first layer of the EM calorimeter are removed (w_{s3} , f_{side} , ΔE_s and E_{ratio} in Ref. [186]). The choice of the LoosePrime working point has consequences on the $Z + \text{jets}$ estimate and is therefore a source of systematic uncertainties.

The isolation gap E_{gap} for regions B and D is introduced to reduce the amount of $Z\gamma$ signal events in the region B and D. Here, it is chosen to be $E_{\text{gap}} = 2 \text{ GeV}$. As for the LoosePrime choice, this decision involves a systematic uncertainty that will be discussed later in this section.

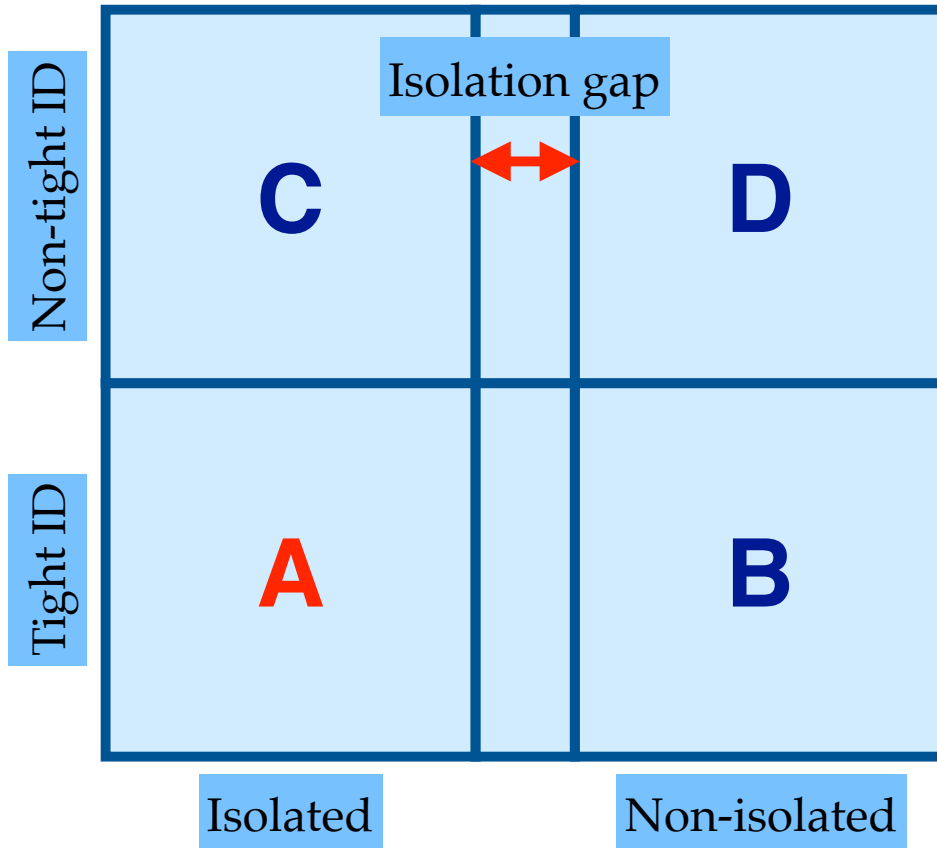


Figure 5.5: Representation of the different regions in the sideband method.

The correlation between the different regions on the $Z + \text{jets}$ estimates is taken into account by the correlation factor R defined as:

$$R = \frac{N_A^{Z+\text{jets}} \cdot N_D^{Z+\text{jets}}}{N_B^{Z+\text{jets}} \cdot N_C^{Z+\text{jets}}}, \quad (5.4)$$

where $N_X^{Z+\text{jets}}$ is the amount of $Z + \text{jets}$ events from MC simulation in the region X . This correlation is expected to be 1 if the four regions were completely uncorrelated, while MC simulations actually give a result $R > 1$ (precise results will be shown later), implying a correlation between the identification and isolation criteria.

The contamination of $Z\gamma$ events in the CR is accounted by the signal leakage factors, noted c_X , representing the relative amount of $Z\gamma$ signal events ending up in the different regions B, C and D:

$$c_B = \frac{N_B^{\text{sig}}}{N_A^{\text{sig}}}, \quad c_C = \frac{N_C^{\text{sig}}}{N_A^{\text{sig}}}, \quad c_D = \frac{N_D^{\text{sig}}}{N_A^{\text{sig}}}, \quad (5.5)$$

where N_X^{sig} denotes the number of $Z\gamma$ signal events in the region X .

The data-driven estimate of the signal events can be described by:

$$\begin{aligned} N^{\text{sig}} &= N_A^{\text{data}} - N_A^{\text{bkg}} - N_A^{Z+\text{jets}} \\ &= N_A^{\text{data}} - N_A^{\text{bkg}} - R \frac{\left[\left(N_B^{\text{data}} - N_B^{\text{bkg}} \right) - c_B N^{\text{sig}} \right] \left[\left(N_C^{\text{data}} - N_C^{\text{bkg}} \right) - c_C N^{\text{sig}} \right]}{\left(N_D^{\text{data}} - N_D^{\text{bkg}} \right) - c_D N^{\text{sig}}}, \end{aligned} \quad (5.6)$$

where N^{sig} is the number of data-driven signal events, N_X^{data} is the total amount of data as measured by ATLAS and passing the criteria for the region X , and N_X^{bkg} the amount of background other than $Z + \text{jets}$ contribution in the region X . The equation on N^{sig} forms a degree two polynomial whose positive root it given by:

$$N^{\text{sig}} = \frac{-b + \sqrt{b^2 - 4ac}}{2a}, \quad (5.7)$$

with

$$\begin{cases} a &= R c_C c_B - c_D, \\ b &= \left(N_D^{\text{data}} - N_D^{\text{bkg}} \right) + c_D \left(N_A^{\text{data}} - N_A^{\text{bkg}} \right) - R \left[c_C \left(N_B^{\text{data}} - N_B^{\text{bkg}} \right) + c_B \left(N_C^{\text{data}} - N_C^{\text{bkg}} \right) \right], \\ c &= R \left(N_B^{\text{data}} - N_B^{\text{bkg}} \right) \left(N_C^{\text{data}} - N_C^{\text{bkg}} \right) - \left(N_A^{\text{data}} - N_A^{\text{bkg}} \right) \left(N_D^{\text{data}} - N_D^{\text{bkg}} \right). \end{cases} \quad (5.8)$$

The data-driven signal estimate is used to deduce the purity P defined as the ratio between the signal events by the signal and $Z + \text{jets}$ events:

$$P = \frac{N^{\text{sig}}}{N_A^{\text{data}} - N_A^{\text{bkg}}} \quad (5.9)$$

Finally, from the purity, the data-driven estimate of the $Z + \text{jets}$ events is given by:

$$N^{Z+\text{jets}} = \left(N_A^{\text{data}} - N_A^{\text{bkg}} \right) \cdot (1 - P). \quad (5.10)$$

There are therefore three main steps in the computation of the $Z + \text{jets}$ estimates: correlation factor estimate by MC, purity computation and $Z + \text{jets}$ calculation. The following section focuses on the different ways to carry out the computation of these three quantities.

Strategies for the correlation factor and purity calculations

The computation shown in the previous section can be done in various ways, leading to different estimates of the Z + jets background. For example, the computation can be done either on the whole yield or for each bin of each observable. Several strategies had been investigated, and a summary of their strength and weaknesses can be found below.

Bin-by-bin Intuitively, the most accurate way to proceed would be to compute all components of the Z + jets estimate in each bin of each observable. An example for the transverse momentum of the photon p_T^γ is given in Fig. 5.6. However, in many bins, the lack of events (mainly in the B, C and D regions) create large statistical fluctuations and uncertainties, meaning that the Z + jets estimate is not reliable.

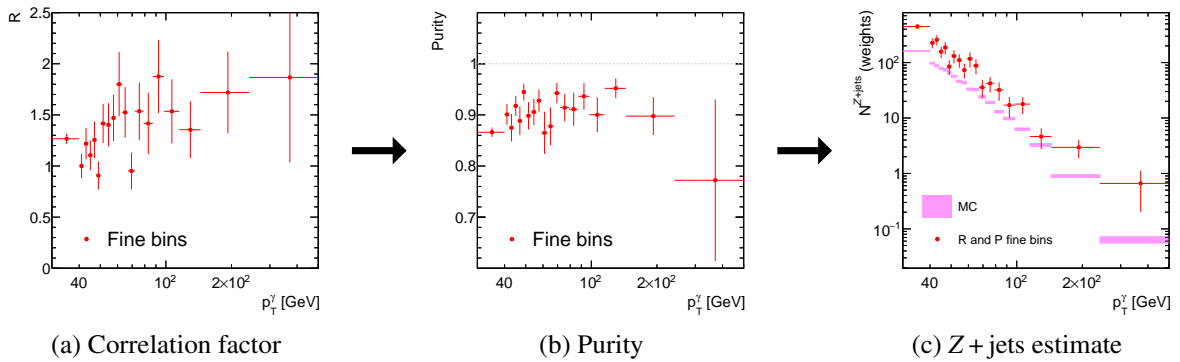


Figure 5.6: Steps for the bin-by-bin method for the Z + jets estimate.

Fit function One solution could be the use of fit function on either or both the correlation factor and purity, as shown in Fig. 5.7. This has the advantage of smoothing the statistical uncertainties and keeping the overall trend. This fit function could be applied either on the correlation factor, on the purity, or both. However, the use of this technique was dropped due to the large amount of observable implying many fit functions to tune. Moreover, the functions were chosen depending on the trend of the observable and lacked a theoretical motivation.

Inclusive To avoid any problem of statistics, the whole yield can be used to compute the Z + jets. This would mean that the correlation factor or the purity would be computed inclusively, and then the result would be broken down in each bin and the Z + jets yield would be computed bin-by-bin. A schematic presentation is available on Fig. 5.8. The main issue with this method is that all information on the shape of the correlation factor or purity, which is not flat in most distributions, would be lost. This method was used to compute the purity in Ref. [72].

Larger bins A solution to keep both the general shapes of the distributions and have more statistics is to have larger bins than previously considered for either or both of the correlation factor and purity, as shown in Fig. 5.9. By combining several bins, there are more events in large bins and thus less statistical fluctuations. Moreover, the new binning can be chosen to have the least possible impact on the shape of the distribution, thus avoiding artificial behaviour.

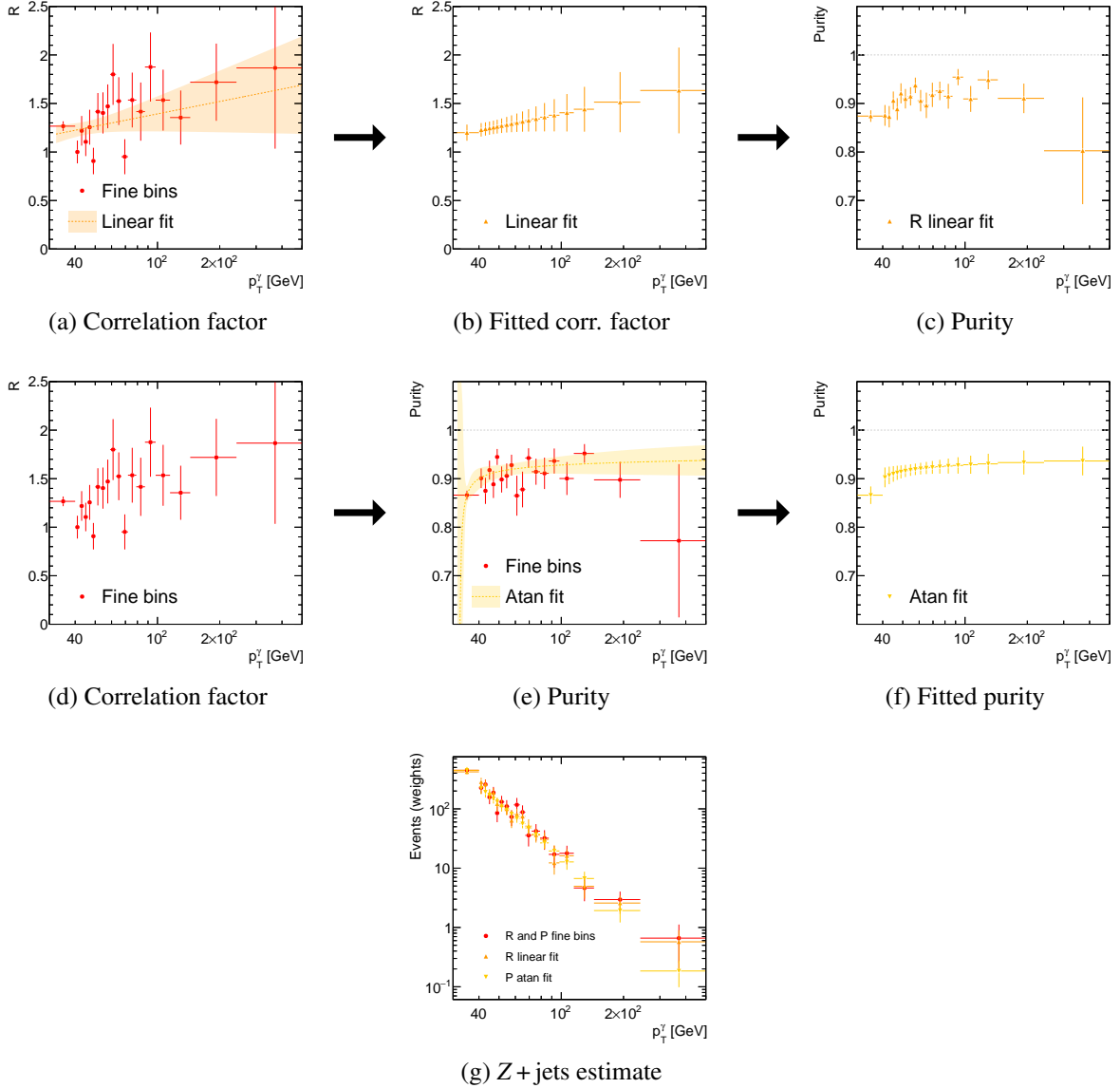


Figure 5.7: Steps for the fit function method applied to the correlation factor (top) and purity (middle) for the Z + jets estimate (bottom).

Considering the previous techniques, the one retained is the "larger bins" computation for the correlation factor and purity. From now on, the binning as defined for the result plots is called "fine bins" while the ones used for the computation of the purity are called "large bins".

Uncertainties

The uncertainties on the estimated Z + jets yields come from different sources: statistics, background, choice of MC generator and choice of the working points. These sources are briefly described in the next paragraphs.

First, the statistical uncertainty comes from both the data and MC simulations. Although the binning of the different variables has been optimised to have around 2% statistical uncertainty on the expected data in the SR, the use of 4 different regions on all MC and data values makes

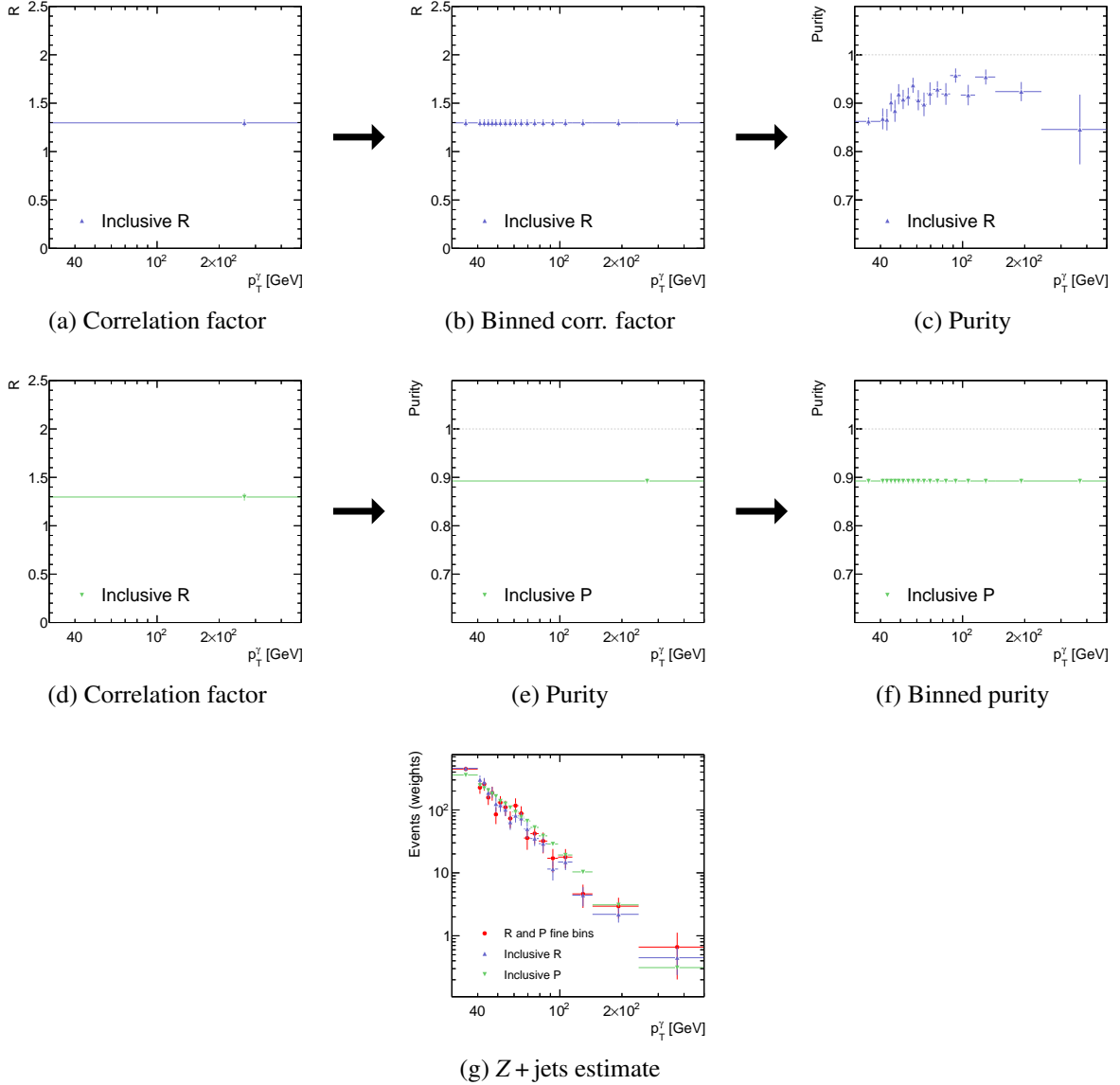


Figure 5.8: Steps for the inclusive method applied to the correlation factor (top) and purity (middle) for the Z + jets estimate (bottom).

the statistical uncertainty much larger. However, as explained previously, the use of larger bins to compute the purity decreases this uncertainty.

In addition to the statistical uncertainty, there is an uncertainty on the cross-section of the background and $Z\gamma$ processes simulated by MC. This source of systematic uncertainties is called the background uncertainty (see Section 5.6 for details on the background uncertainties). This uncertainty is propagated through the whole Z + jets computation (Eq. (5.4) to (5.10)).

Then, the results of the ABCD method also depends on the chosen MC generator for the signal. Therefore, as an alternative sample, the $Z\gamma$ process estimate from MadGraph is used and the difference with the Sherpa estimate of the signal leakage parameter gives the uncertainty:

$$\delta_{generator}^2 = [c_X(\text{MadGraph}) - c_X(\text{Sherpa})]^2. \quad (5.11)$$

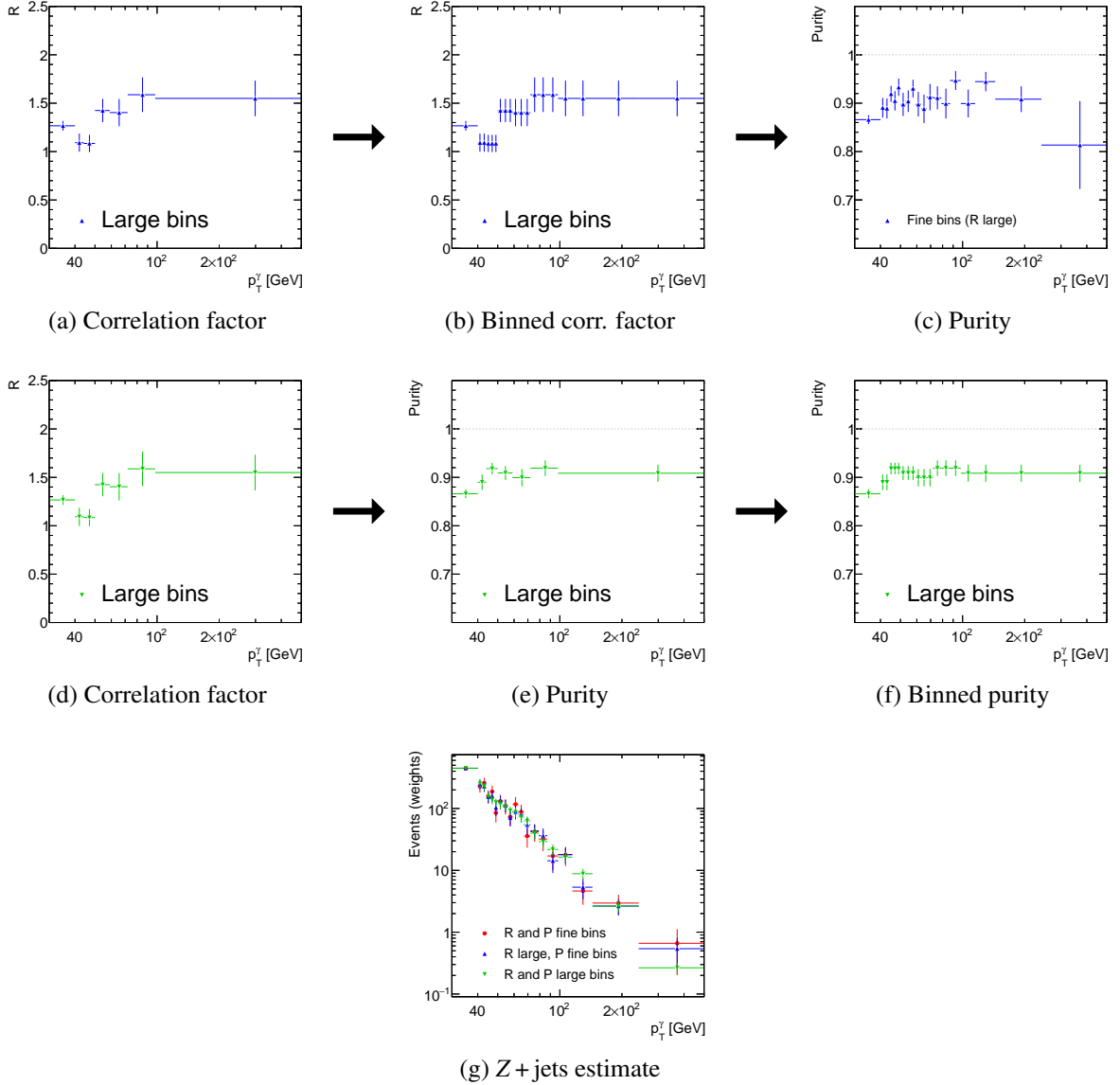


Figure 5.9: Steps for the larger bins method applied to the correlation factor (top) and purity (middle) for the Z + jets estimate (bottom).

Finally, as discussed when introducing the sideband method, the choice of the working points for the anti-tight (LoosePrime4) and non-isolated ($E_{\text{gap}} = 2 \text{ GeV}$) regions impact the results of the correlation factor. Therefore, the difference with other working points are taken as uncertainties. For the anti-tight, the so called LoosePrime3 (LoosePrime4 including the E_{ratio} requirement) and LoosePrime5 (LoosePrime4 without requirement on the w_{stot} , see Ref. [186]) working points are considered. Concerning the gap energy, the values 1 GeV and 3 GeV are used to derive the uncertainties. For each parameter, the uncertainty in each bin is given by:

$$\delta_{\text{wp}}^2 = [R(\text{wp}_1) - R(\text{wp}_{\text{ref}})]^2 + [R(\text{wp}_2) - R(\text{wp}_{\text{ref}})]^2, \quad (5.12)$$

with $\text{wp}_{1,2}$ the working points considered for the uncertainties.

To summarize, the sources of uncertainties are:

Statistics Number of events per region.

Anti-tight Isolation gap	LoosePrime4 2 GeV
R	1.30 \pm 0.04 (stat.) \pm 0.23 (syst)
$c_B (\times 10^{-3})$	13.4 \pm 0.1 (stat.) \pm 2.1 (syst)
$c_C (\times 10^{-3})$	56.1 \pm 0.2 (stat.) \pm 0.2 (syst)
$c_D (\times 10^{-3})$	1.9 \pm 0.0 (stat.) \pm 0.2 (syst)
$N_A^{\text{data}} - N_A^{\text{bkg}}$	90891 \pm 311 (stat.) \pm 566 (syst)
$N_B^{\text{data}} - N_B^{\text{bkg}}$	3542 \pm 60 (stat.) \pm 9 (syst)
$N_C^{\text{data}} - N_C^{\text{bkg}}$	15811 \pm 127 (stat.) \pm 3 (syst)
$N_D^{\text{data}} - N_D^{\text{bkg}}$	3823 \pm 62 (stat.) \pm 2 (syst)
N^{sig}	81117 \pm 574 (stat.) \pm 2269 (syst)
P	0.89 \pm 0.01 (stat.) \pm 0.02 (syst)
$N^{Z+\text{jets}}$	9773 \pm 465 (stat.) \pm 2159 (syst)

Table 5.7: Values and uncertainties of the different variables contributing to the sideband method for the inclusive Z + jets yield estimate. The first lines show the working points considered for the study. In the second part, the intermediate numbers derived from the MC simulation and data are given. Finally, the third part gives the derived values of the different variables introduced in Eq. (5.8), (5.9) and (5.10).

Background Cross-section uncertainty of background processes, propagated in the computation.

Generator Uncertainty on the leakage parameters between different MC generators:

$$\delta_{generator}^2 = [c_X(\text{MadGraph}) - c_X(\text{Sherpa})]^2.$$

Anti-tight Uncertainty on the correlation factor depending on the anti-tight considered:

$$\delta_{anti-tight}^2 = [R(\text{LoosePrime5}) - R(\text{LoosePrime4})]^2 + [R(\text{LoosePrime3}) - R(\text{Looseprime4})]^2.$$

Isolation gap Uncertainty on the correlation factor depending on the isolation gap considered:

$$\delta_{E_{\text{gap}}}^2 = [R(E_{\text{gap}} = 3 \text{ GeV}) - R(E_{\text{gap}} = 2 \text{ GeV})]^2 + [R(E_{\text{gap}} = 1 \text{ GeV}) - R(E_{\text{gap}} = 2 \text{ GeV})]^2.$$

Results

For illustration, the result of the inclusive Z + jets estimate is given in Table 5.7, including the results of the different steps of the estimation. Different checks are done on the estimated value of the correlation factor and can be found in Appendix C. The results will also be analyzed in terms of differential cross-section for the different studied observables. This has consequences on the values for each bins, but also on the uncertainties. In general, each bin of a histogram has an uncertainty greater than shown in the table, due, in particular, to the smaller amount of available data.

$N^{Z+\text{jets}}$	9773	
Statistical unc.	465	(4.8 %)
Background unc.	382	(3.9 %)
Generator unc.	830	(8.5 %)
Iso. gap unc.	681	(7.0 %)
Anti-tight unc.	1931	(19.8 %)
Total uncertainty	2182	(22.3 %)

Table 5.8: Contribution of each source of uncertainties to the inclusive $Z + \text{jets}$ estimate.

The details of the uncertainty sources for the $N^{Z+\text{jets}}$ estimate are given in Table 5.8, again for the inclusive case for illustration. The main contribution to the total uncertainty is given by the choice of the anti-tight (LoosePrime4) selection. In comparison, the statistical uncertainty contribution is very low. However, the situation is somewhat different for the differential distributions. Since the binning reduces the available statistics the related uncertainty is increased. This phenomenon can be observed on Fig. 5.10, which shows that the contribution of the anti-tight uncertainty is not the main source of uncertainty in every bin, even though it remains important.

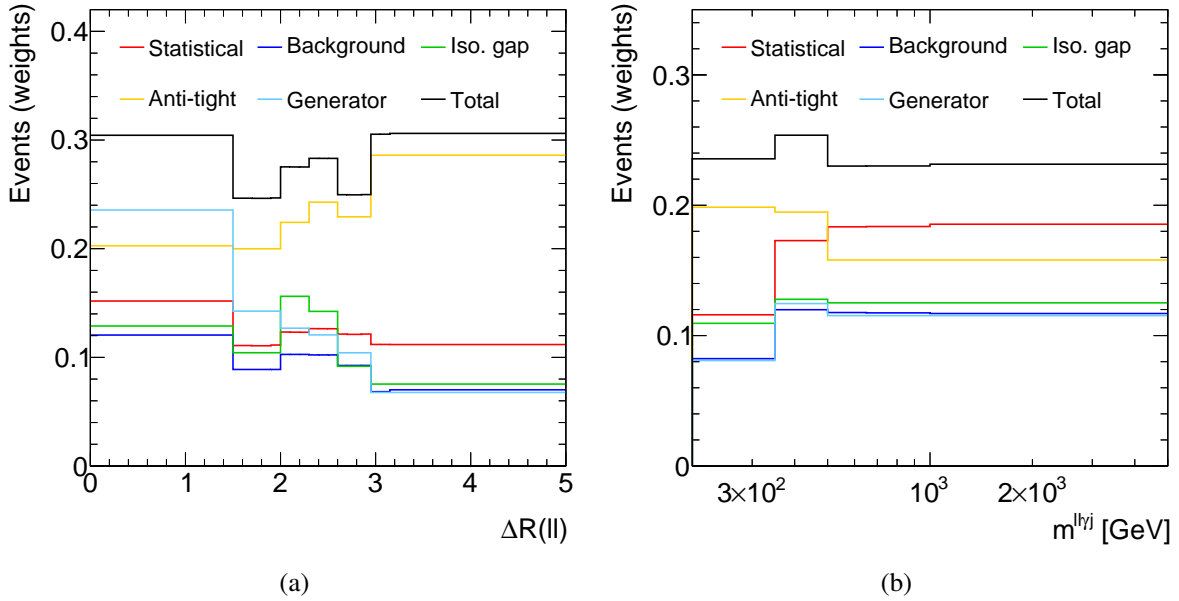


Figure 5.10: $Z + \text{jets}$ relative uncertainties by source for (a) $\Delta R(\ell, \ell)$ and (b) $m^{\ell\ell\gamma j}$. The distributions have been chosen to show histograms where the anti-tight uncertainty is not dominant in every bin.

5.4.2 Other sources of background

Pileup contribution

Besides the $Z + \text{jets}$ process, the pileup contribution is one of the two biggest sources of background. It emerges when the Z boson and the photon come from two different proton–proton collisions.

The pileup contribution is estimated by measuring the fraction of pileup events in data, given by:

$$f_{\text{PU}} = \frac{N_{\text{PU}}}{N_{\text{data}}}, \quad (5.13)$$

where N_{PU} is the number of pileup events and N_{data} the total amount of data.

As they come from different vertices, information on the longitudinal position of the reconstructed vertices of the photon (z_γ) and Z boson (also called z_{PV} for Primary Vertex) are used to evaluate the number of pileup events. The Z boson vertex is well reconstructed (leptons are detected by the trackers), while the photon vertex has a worse resolution. The difference Δz between these two values is given by:

$$\Delta z = z_\gamma - z_{\text{PV}}. \quad (5.14)$$

The photon vertex can only be reconstructed precisely if the photon is converted into an electron-positron pair (see Section 4.2 for a definition), because the two tracks resulting from the conversion can be used to define the vertex position. In our estimate, Eq. (5.13) is therefore computed using only data events with a converted photon. Fortunately, the pileup fraction computed from events with a converted photon is the same as the pileup fraction for all events as the probability that a photon converts is independent from its origin.

The region of low $|\Delta z|$ is dominated by single proton–proton collision events while the high $|\Delta z|$ region is enhanced in pileup events, as shown in Fig. 5.11. The latter is therefore a perfect phase-space to estimate the pileup fraction precisely. Data show that the pileup events are distributed along $|\Delta z|$ as a gaussian with a width $\sigma = 50 \text{ mm}$ [72]. Therefore, the region $|\Delta z| > 50 \text{ mm}$ is used to compute the pileup fraction. In this region, we have the equation:

$$N_{\text{PU}}^{|\Delta z| > 50 \text{ mm}} = N_{\text{data}}^{|\Delta z| > 50 \text{ mm}} - N_{\text{single } pp}^{|\Delta z| > 50 \text{ mm}} = N_{\text{PU}} \cdot P(|\Delta z| > 50 \text{ mm}), \quad (5.15)$$

where $P(|\Delta z| > 50 \text{ mm})$ is the probability for the pileup events to be in the region $|\Delta z| > 50 \text{ mm}$. Due to the gaussian shape of the pileup distribution along $|\Delta z|$, this probability has a value $P(|\Delta z| > 50 \text{ mm}) = 0.32$.

Merging Eq. (5.13) with Eq. (5.15), the pileup fraction can be computed as:

$$f_{\text{PU}} = \frac{N_{\text{data}}^{|\Delta z| > 50 \text{ mm}} - N_{\text{single } pp}^{|\Delta z| > 50 \text{ mm}}}{0.32 \cdot N_{\text{data}}}. \quad (5.16)$$

The computation of the pileup fraction is done in each bin for $p_T^\gamma \times N_{\text{jets}}$ (see Fig. 5.12). For each data event, the pileup weight is given as the pileup fraction corresponding to the p_T^γ and N_{jets} properties of the event. The "scale" of the pileup is obtained by adding the pileup weight of all the data events. To simulate the pileup background, samples with a Z boson and a photon are merged. The distribution obtained by this MC estimate is the "shape" of the pileup. The final step consists in rescaling the shape so that the integral is equal to the scale computed earlier.

The amount of jets is shown to be overestimated by the shape method due to jets coming both from the Z and photon sample. Suppressing the (recoil) jet associated to the photon mimics the JVT cut since most of the primary vertices correspond to Z events. A systematic uncertainty for variables involving jets is then derived by comparing the distributions obtained between the cases where the photon associated jets are removed and where they are not.

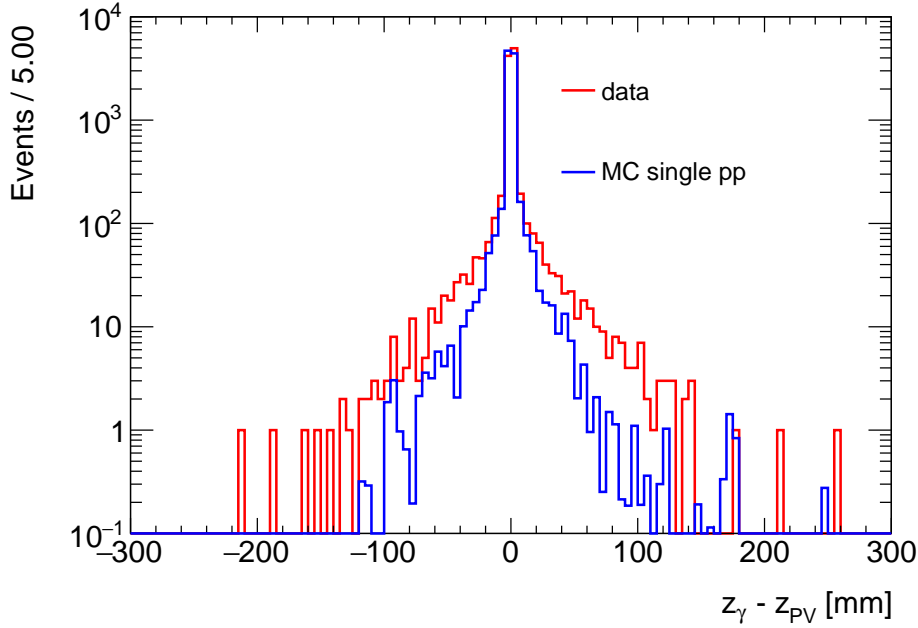


Figure 5.11: Distribution of Δz for data and for MC events where the Z boson and the photon are created in the same pp collision.

Pileup enhanced data samples can be used to assign uncertainties by imposing special requirements on the photon vertex. In this case, it is required that the photon vertex is closer to the second hardest vertex than to the primary one. In that way, the photon is much more likely to come from a different vertex, which means that the sample is enhanced in pileup events. The difference between the pileup shape estimate and the distribution from the pileup enhanced sample is taken as systematic uncertainty. It can be added that such a measure allows to measure the Δz distribution and check the gaussian assumption $P(|\Delta z| > 50 \text{ mm}) = 0.32$. This is done in Fig. 5.13 and the result is indeed $\sigma = 50 \text{ cm}$.

The pileup and Z + jets contributions are entangled due to the fact that some pileup jets can be interpreted as a photon, hence making the event contribute to both sources. It has been shown in Ref. [72] that the fraction of pileup events where the photon is actually a misidentified jets is $(46 \pm 7) \%$. Therefore, a coefficient 0.5 is applied to the pileup events to avoid double counting events in the estimates.

$t\bar{t}\gamma$, multiboson and $tW\gamma$

In the previous sections, the methods to estimate the Z + jets and pileup background contributions were discussed. The remaining background sources are estimated directly with MC simulations and are discussed here. Some example of Feynman diagrams mimicking the $Z\gamma$ signal are given in Fig. 5.14, and information about each source of background is given below.

- $t\bar{t}\gamma$: The $t\bar{t}\gamma$ process is the biggest source of background estimated with MC simulation. When decaying the t -quark can produce a charged lepton, a neutrino and jets. In the case where the two leptons from the two quarks have the same flavour, the $t\bar{t}\gamma$ would have the same final state as the $Z\gamma$ with two leptons, one photon and jets. The $t\bar{t}\gamma$ background MC results are multiplied with a coefficient of 1.44 to compensate for the fact that the

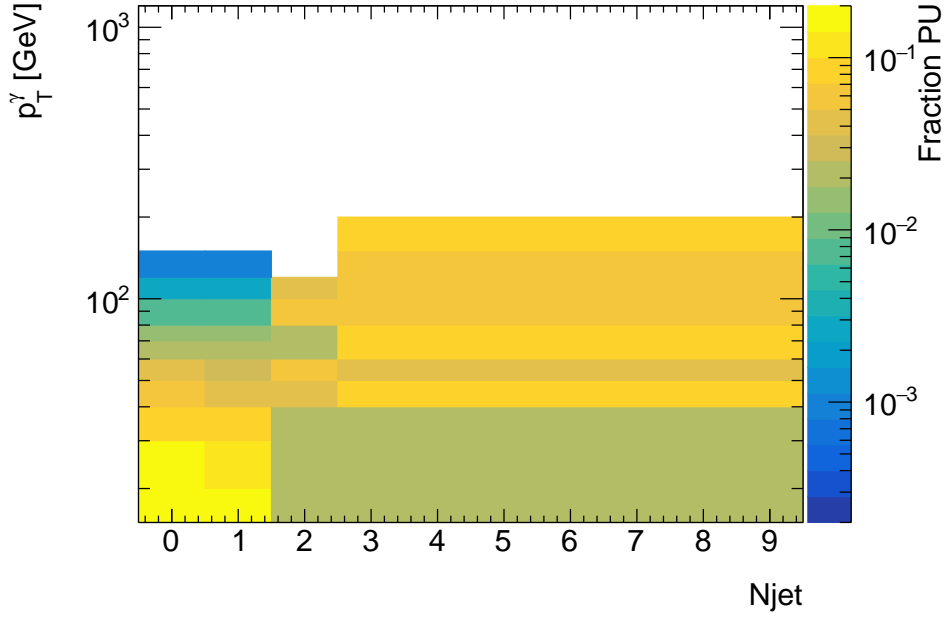


Figure 5.12: Pileup fraction as a function of the jet multiplicity and photon transverse momentum.

generation is done at LO only [215]. The agreement of the $t\bar{t}\gamma$ estimate and the data was tested in the $e\mu\gamma$ CR (see Section 5.4.3).

- ZZ and WZ : The ZZ and WZ contributions to the background are due to the leptonic decay of the W and Z bosons ($Z \rightarrow \ell\ell$ and $W \rightarrow \ell\nu$). As there is no veto for events with more than two leptons, if one of the leptons is misidentified as a photon, then the final state has two or three leptons and a (fake) photon.
- $WZ\gamma$ and $WW\gamma$: The $WZ\gamma$ is similar to the WZ process, except that the photon is not misidentified. The $WW\gamma$ process is a source of background when the two W bosons create a leptonic decay with same flavour leptons ($WW \rightarrow \ell\nu\ell\nu$). ZZ , WZ , $WZ\gamma$ and $WW\gamma$ are labeled "multiboson".
- $tW\gamma$: The $tW\gamma$ contains a t -quark that decays into a charged lepton, a neutrino and a jet while the W boson decays into a lepton and neutrino pair with the leptons having the same flavour.
- EWK $V\gamma$: The vector boson fusion contribution contains two quarks exchanging a W boson or Z boson resulting in two leptons and a photon. In itself, this process is a $Z\gamma$ process, even if the fact that the photon is not coming from an ISR makes it a small source of background in this analysis.

5.4.3 $e\mu\gamma$ control region

The $e\mu\gamma$ region is a region where the selection applied is identical to the signal region, except that the leptons are required to have different flavours: one electron and one muon. This region is interesting to check if the $t\bar{t}\gamma$ and jet faking photon background estimates model properly the data. This is possible by the absence of $Z\gamma$ signal, making the $t\bar{t}\gamma$ and Z + jets contribution

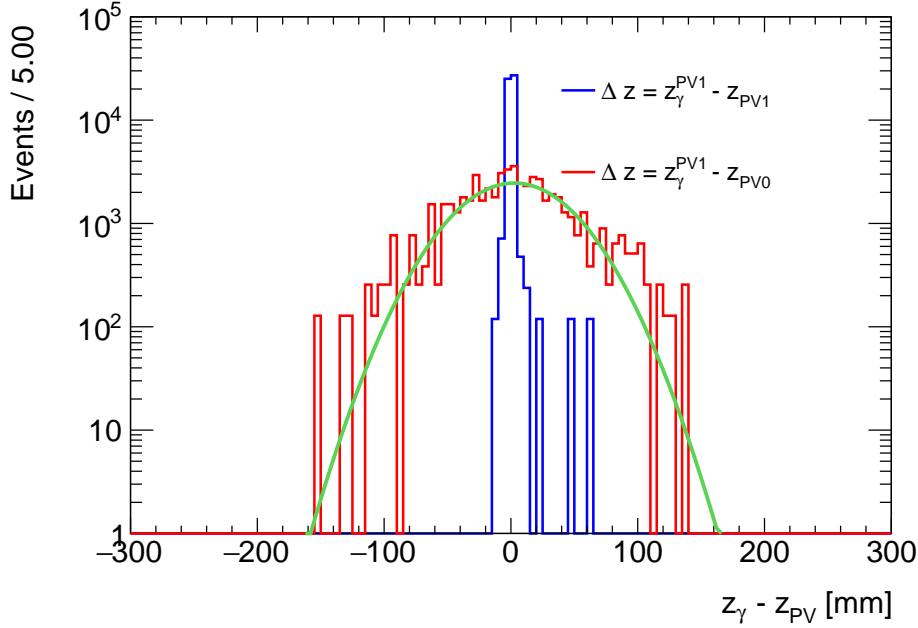


Figure 5.13: Data distribution of the difference between the z_γ (when the photon is requested to point toward the second highest p_T vertex) and the second highest p_T vertex called primary vertex (blue) or the highest p_T vertex (red). The green curve is a Gaussian fit of the red curve.

dominant. As it is a control region, observables that are blinded for the signal region during the analysis development can be studied in this phase-space.

The dominating process of the region is the $t\bar{t}\gamma$ production. Therefore, this region is a good place to test the biggest source of background estimated by MC only. In the $e\mu\gamma$ CR, the other contributions to the estimate are the $e\mu$ + fake photon, the ZZ , WZ and $\tau\tau\gamma$ processes. The latter is due to the decay of the τ into muons and electrons.

The estimate of fake photons is made in an analogous way as for the Z + jets estimate. By doing so, we can check that the method gives adequate results. Indeed, we can use the $t\bar{t}\gamma$ as signal in the $e\mu\gamma$ control region and the ZZ , WZ and $\tau\tau\gamma$ as background and apply the formulas used in Section 5.4.1. The main difference with the method described earlier is the use of a fixed correlation factor $R = 1.30 \pm 0.04$, referring to the value estimated in the signal region with statistical uncertainties.

The binnings of the distributions are also wider than the ones used in the SR due to the smaller statistics of the $e\mu\gamma$ region. Instead, the "large binning" as defined within the Z + jets method is used.

Fig. 5.15 shows the distributions of some variables in the CR. The uncertainties for these distributions are both statistical and cross-section uncertainties. The latter is computed as 30 % for all MC samples, except for the $t\bar{t}\gamma$ which is 15 % [215]. The background uncertainties are also propagated through the fake photon computation method. It results in an uncertainty of about 20 % on the $e\mu$ + fake photon contribution.

The distributions in the $e\mu\gamma$ region show that the SM estimate mostly matches the Run 2 data. However, a mismodelling can be seen in the low jet events, mainly in the N_{jets} observable. This

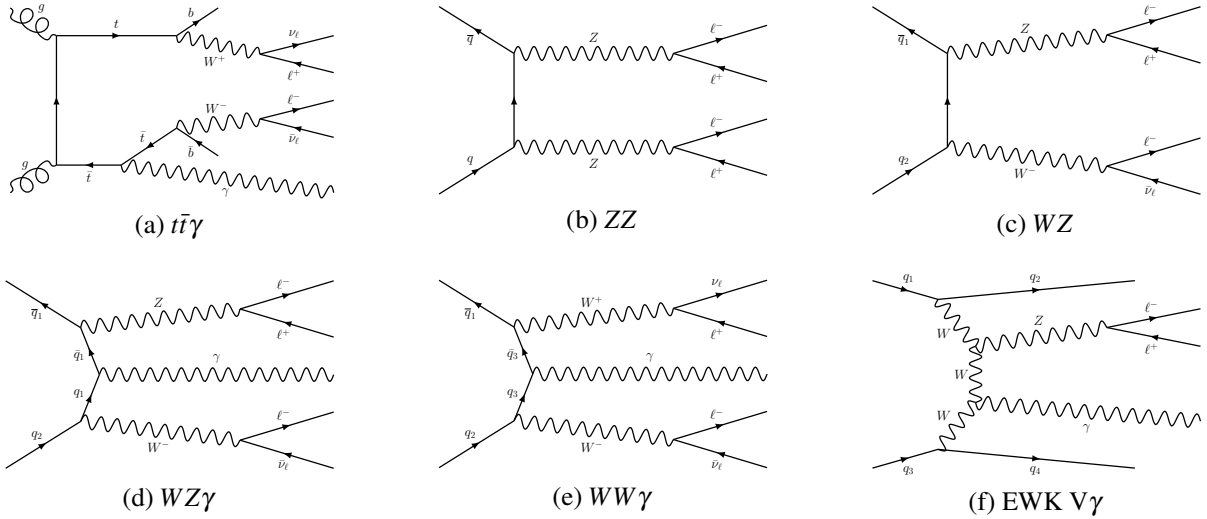


Figure 5.14: Example of Feynman diagrams showing background processes mimicking the signal $Z\gamma$ process.

discrepancy does however not dramatically affect the signal region since it is a small fraction of the $t\bar{t}\gamma$ events which, by itself, account for less than 5 % of the total SM estimate.

5.5 Unfolding

The data analysed in this study are based on the detection of particles in the ATLAS detector. The measured properties will thus contain features introduced by the detector. To be able to compare the data with theory predictions or measurements from several experiments, the influence of the detector should be minimized. Unfolding aims at removing as much detector dependency in the data as possible. It consists in transforming distributions at reconstruction (reco) level (see Section 2.4) to distributions at generator (truth) level.

There are several methods to unfold data, such as the bin-to-bin correction or the matrix inversion methods. Each of these options have some issues: assumption of the absence of correlation between bins, potentially large statistical fluctuations, bias introduced by MC simulations, etc. To mitigate the mentioned issues, in this analysis, the tool used to unfold is based on the Iterative Bayesian Unfolding (IBU) [216].

The IBU relies on the computation of the inverse of the migration matrix $P(E|C)$. To simplify, this matrix allows to go from the truth level to the reco level. The arguments in the probability are the bins of a truth distribution (C_i with $i = 1, 2, \dots, n_C$ for "cause") and the bins of a reco distribution (E_j with $j = 1, 2, \dots, n_E$ for "effect"). The migration denotes the probability that an event being in the bin i at truth level would be in the bin j at reco level. Fig. 5.16 shows an example of a migration matrix for the N_{jets} variable.

Inverting the migration matrix would allow to go from the detector level to the particle level. The inversion, in IBU, is done using the Bayes' theorem:

$$P(C_i|E_j) = \frac{P(E_j|C_i) P_0(C_i)}{\sum_{l=1}^{n_C} P(E_j|C_l) P_0(C_l)}, \quad (5.17)$$

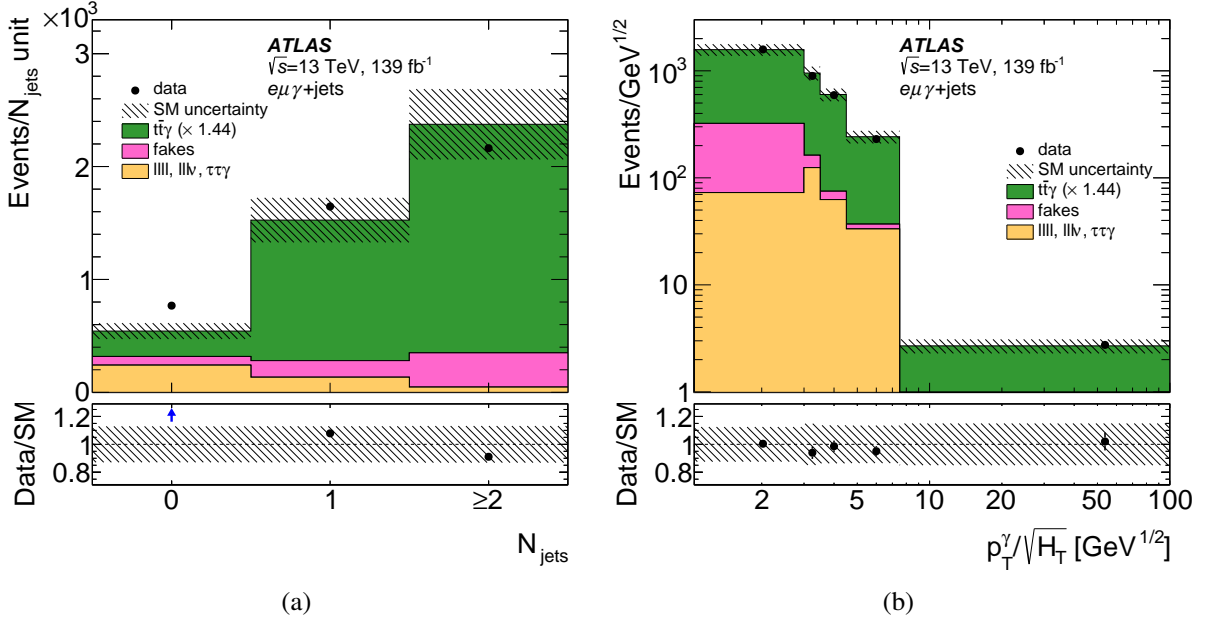


Figure 5.15: $e\mu\gamma$ measurements and estimates for the N_{jets} (a) and $p_T^\gamma/\sqrt{H_T}$ (b) distributions.

where the subscript 0 denotes the 0th iteration.

Eq. (5.17) and its usage rely on several variables that must be defined:

- The initial distribution of the reco events $n_0(E)$.
- The initial rate of events in the bin i (also called prior) at truth level $P_0(C_i)$ can be deduced from the truth MC simulations. In case this is not known, the default rate is set to $P_0(C_i) = 1/n_C$.
- The probability of an event in the bin i at truth level to lie in the bin j at reco level $P(E_j|C_i)$.

It is worth to mention that some other variables can be derived from the previous ones and are useful for the rest of the method. The efficiency is computed as $\epsilon_{0,i} = \sum_{j=1}^{n_E} P(E_j|C_i)$. It is smaller than 1 ($\epsilon_i \leq 1$) because some of the truth event can be outside of the SR. The total number of observed events is given by $N_{\text{obs}} = \sum_{j=1}^{n_E} n_0(E_j)$. Finally, the initial expected number of events $n_0(C_i)$ is defined as $n_0(C_i) = P_0(C_i)N_{\text{obs}}$.

Now that the initial state is introduced, Eq. (5.17) can be applied. This gives a first iteration of the IBU, indicated by the subscript 1. From there, the distribution of the events at truth level are given by:

$$n_1(C_i) = \frac{1}{\epsilon_{0,i}} \sum_{j=1}^{n_E} n_0(E_j)P(C_i|E_j), \quad (5.18)$$

$$P_1(C_i) = \frac{n_1(C_i)}{\sum_{i=1}^{n_C} n_1(C_i)}. \quad (5.19)$$

Other variables such as a new estimate of the amount of true events $N_{1,\text{true}} = \sum_{i=1}^{n_C} n_1(C_i)$ and the overall efficiency $\epsilon_1 = N_{\text{obs}}/N_{1,\text{true}}$ can also be defined.

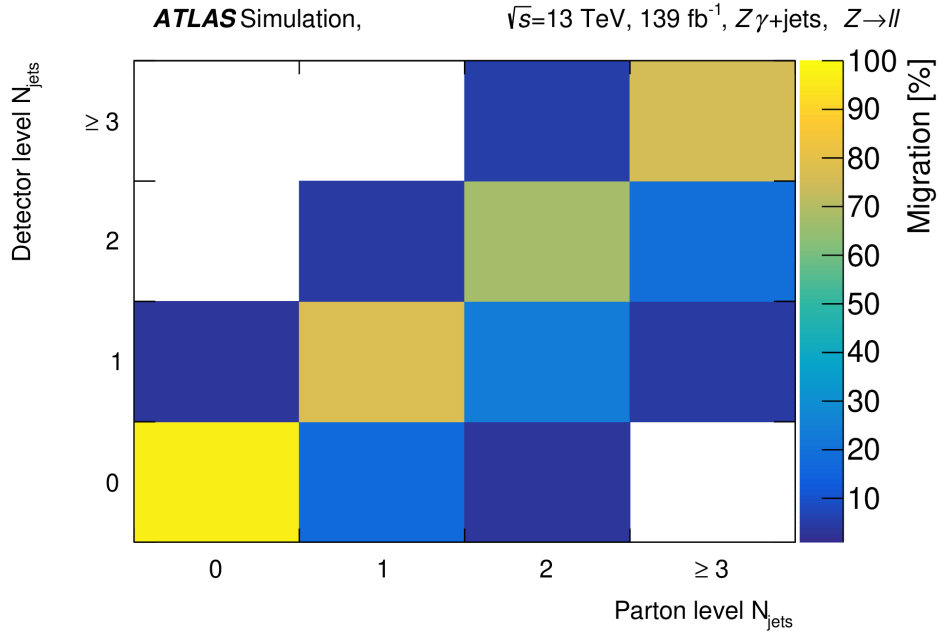


Figure 5.16: Example of a migration matrix where the truth level is on the abscissa and the reco on the ordinate. Figure taken from Ref. [203].

This process can be done iteratively, meaning that the parameters $n_1(C)$ and $P_1(C)$ can be used to compute $n_2(C)$ and $P_2(C)$, etc. The number of iterations is optimised based on the amount of bias introduced in the results. The bias comes from the fact that the different variables introduced for the unfolding algorithm, $P(E|C_i)$ and $P_0(C)$, are estimated with MC simulations. In this analysis, the migration matrix is evaluated with a Sherpa 2.2.11 $Z\gamma$ sample. The bias is computed by applying the unfolding procedure on a different MC sample: MadGraph5. The reco simulation is then unfolded with the Sherpa 2.2.11 migration matrix and compared to the MadGraph5 truth level. The ratio of the unfolded distribution and the truth one is the bias. From the computation of the bias, in the $Z\gamma+\text{jets}$ analysis, the chosen number of iteration is 2. The bias is responsible for a source of systematic uncertainty that will be discussed in Section 5.6.

5.6 Uncertainties

Uncertainties are a central part of any physics measurement. In the $Z\gamma+\text{jets}$ analysis, the uncertainties can be classified into four broad sources: statistical, experimental, theoretical and unfolding.

Statistical uncertainties Statistical uncertainties take into account the possible statistical fluctuations in the data and MC simulations. The behaviour of this uncertainty is such that the less data there is in a phase-space, the higher the relative uncertainty is. In fact, this analysis uses a Poisson distribution to evaluate the uncertainties. For each bin of each distribution, the statistical uncertainty is given as the quadratic sum of all event weights w_i ($w_i = 1$ for data) in the bin:

$$\Delta\sigma_{\text{stat}} = \sqrt{\sum_{\text{events}} w_i}. \quad (5.20)$$

Experimental uncertainties The experimental uncertainties are systematic uncertainties related to detector imperfections. This includes, for example, the finite energy resolution of the ATLAS detector, the calibration and the correction of the mismodelling of reconstruction effects in the simulation. This uncertainty affects the different reconstructed objects in different ways, since they are not reconstructed or calibrated identically.

Uncertainties on the energy (or momentum for muons) scale and resolution need to be considered for all particles. Moreover, electrons, muons and photons have uncertainties on the measured identification and isolation efficiencies. Electrons and muons have further uncertainties corresponding to the trigger efficiencies.

Jet energy scale and resolution uncertainties are due to different sources: detector modelling, statistical effects, flavour composition and jet flavour response. In addition to the jet energy scale and resolution uncertainties, jets also suffer from JVT efficiency uncertainties.

Finally, to take into account the luminosity measurement inaccuracy, 1.7 % uncertainty is applied [163].

Theoretical uncertainties The theoretical uncertainties are applied to the MC signal prediction to account for different phenomena, such as higher order contributions, PDF choice and uncertainties on the strong coupling constant.

The higher order contribution uncertainties are computed by varying the renormalization and factorization scale independently by a factor of two up and down. The highest variation in the cross-section is kept as an uncertainty.

Furthermore, an uncertainty is introduced to cover uncertainties on the cross-section of all the background processes estimated by MC. This is assigned by applying 30 % to all bins of all the MC background results, except for the $t\bar{t}\gamma$ where only 15 % is applied [215]. The latter corresponds to the factor difference between the LO and NLO cross-section. The background (or cross-section) uncertainties then propagate to the Z + jets estimate through the sideband method described in Section 5.4.1.

The nominal value of the signal is obtained by using the PDF set NNPDF30_nnlo_as_0118. The uncertainties are computed following the PDF4LHC recommendations [217]. Uncertainties on the strong interaction coupling α_s are set using a similar approach with NNPDF30_nnlo_as_0117 and NNPDF30_nnlo_as_0119 sets.

Unfolding uncertainties The unfolding procedure introduces uncertainties and must propagate the other sources of uncertainties. The uncertainties introduced by the unfolding itself are mainly due to the choice of sample used to extract the unfolding parameters. The uncertainty is computed using a data-driven closure test. This test consists in reweighting the MC signal at reco level with a smooth function (obtained by matching the signal distribution to data after background subtraction) and then unfold it. The difference with the nominal unfolding is taken as the uncertainty.

To propagate the systematic uncertainties, the MC estimates are used. To do so, the reco level MC sources of uncertainties are varied by $\pm 1\sigma$ and unfolded. The result is then compared to the nominal value and the difference is the uncertainty. Concerning the statistical uncertainties, the propagation is done using statistically-independent replicas of

the data or MC results. They are then unfolded and the root mean square of the replicas distribution is the unfolded statistical uncertainty.

The total uncertainty (statistical + systematics) on the inclusive SM prediction for the $Z\gamma$ + jets analysis is around 4%. However, as stated previously, the uncertainty is not homogeneous and can vary between bins and distributions. Table 5.9 shows, for the N_{jets} distribution as an example, that the statistical uncertainty is typically lower than the systematic one. This confirms the statement about the $Z\gamma$ measurement being a precision measurement thanks to the relatively large cross-section. Moreover, the systematics for most of the sources are relatively stable with the number of jets. The biggest dependency concerns the jet uncertainties due to the forward jet modelling and the pileup estimate.

N_{jets}	0	1	2	> 2
Source	Uncertainty [%]			
Electrons	1.0	0.9	0.8	0.8
Muons	0.3	0.3	0.3	0.4
Jets	1.7	1.7	4.5	8.8
Photons	1.4	1.3	1.3	1.2
Pileup	2.1	0.8	0.2	0.3
Background	1.8	1.8	3.0	4.4
MC statistical	0.1	0.2	0.3	0.4
Data statistical	0.8	1.5	1.8	1.9
Luminosity	1.7	1.7	1.7	1.7
Theory	0.6	0.2	1.4	1.0
Total	4.2	3.8	6.3	10.3

Table 5.9: Relative systematic uncertainties on the $Z\gamma$ + jets cross-section as a function of N_{jets} .

5.7 Results

5.7.1 Data/SM

The data/SM comparison refers to the juxtaposition of the measured data yields and the SM estimates. To do so, the estimated yields of all background sources and the signal estimated by MC are stacked and the sum is compared to data.

To account for the fact that the $Z\gamma$ signal is only generated at NLO in Sherpa 2.2.11, a factor 1.08 is applied to the signal estimate. This ratio has been computed to match the data and estimated SM yields. The estimate of each contribution to the total measured yield can be found in Table 5.10 and the reco level histograms for the different variables can be found in Fig. 5.17 to 5.20 and in Appendix D.

The systematic uncertainties shown in these figures and the table are only cross-section uncertainties on the MC background estimates, uncertainties discussed in Section 5.4 for the Z + jets and pileup estimates, and experimental uncertainties applied on the $Z\gamma$ signal estimate. The theory uncertainties (except background) which range between 5% to 10% are not included.

Source	$ee + \mu\mu$		
Signal ($\times 1.08$)	79389.8	± 56.5 (stat.)	± 2295.2 (syst.)
Z + jets	9773.5	± 465.1 (stat.)	± 2131.9 (syst.)
Pileup	2510.5	± 72.7 (stat.)	± 698.0 (syst.)
$t\bar{t}\gamma$ ($\times 1.44$)	3609.8	± 14.5 (stat.)	± 541.5 (syst.)
Multiboson	947.9	± 5.5 (stat.)	± 160.2 (syst.)
EWK $Z\gamma jj$	812.8	± 1.9 (stat.)	
$tW\gamma$	148.2	± 0.6 (stat.)	± 44.5 (syst.)
Total prediction	97192.5	± 474.4 (stat.)	± 3259.0 (syst.)
Data	96410	± 310.5 (stat.)	

Table 5.10: Estimated event yields and uncertainties for the $Z\gamma$ signal and the background processes, compared to the total yield measured in data. For $tW\gamma$, diboson and $t\bar{t}\gamma$ the background uncertainties are included. The Z + jets systematic uncertainties contain the propagation of the background uncertainties, the E_{gap} and anti-tight criteria, and the generator uncertainty. For the signal, the experimental uncertainties are considered. Yields are obtained using Sherpa 2.2.11 for the signal.

In most of the histograms, a good agreement between data and estimates can be observed. Small differences are observed in some histograms but these are covered by the theoretical uncertainties.

In particular, the variable N_{jets} does not have the same mismodelling as in the $e\mu\gamma$ control region, as shown in Fig. 5.20. As explained previously, the mismodelling of the jets in the $t\bar{t}\gamma$ samples does not highly affect the signal region since the $t\bar{t}\gamma$ contribution to the SM is small. The estimate in the signal region matches the data for the jet multiplicity.

Finally, some effects such as the overestimate at low $p_T^{\ell\ell\gamma}$ and underestimate at high $p_T^{\ell\ell\gamma}$ (see Fig. 5.17) were already observed during the previous $Z\gamma$ measurements [72].

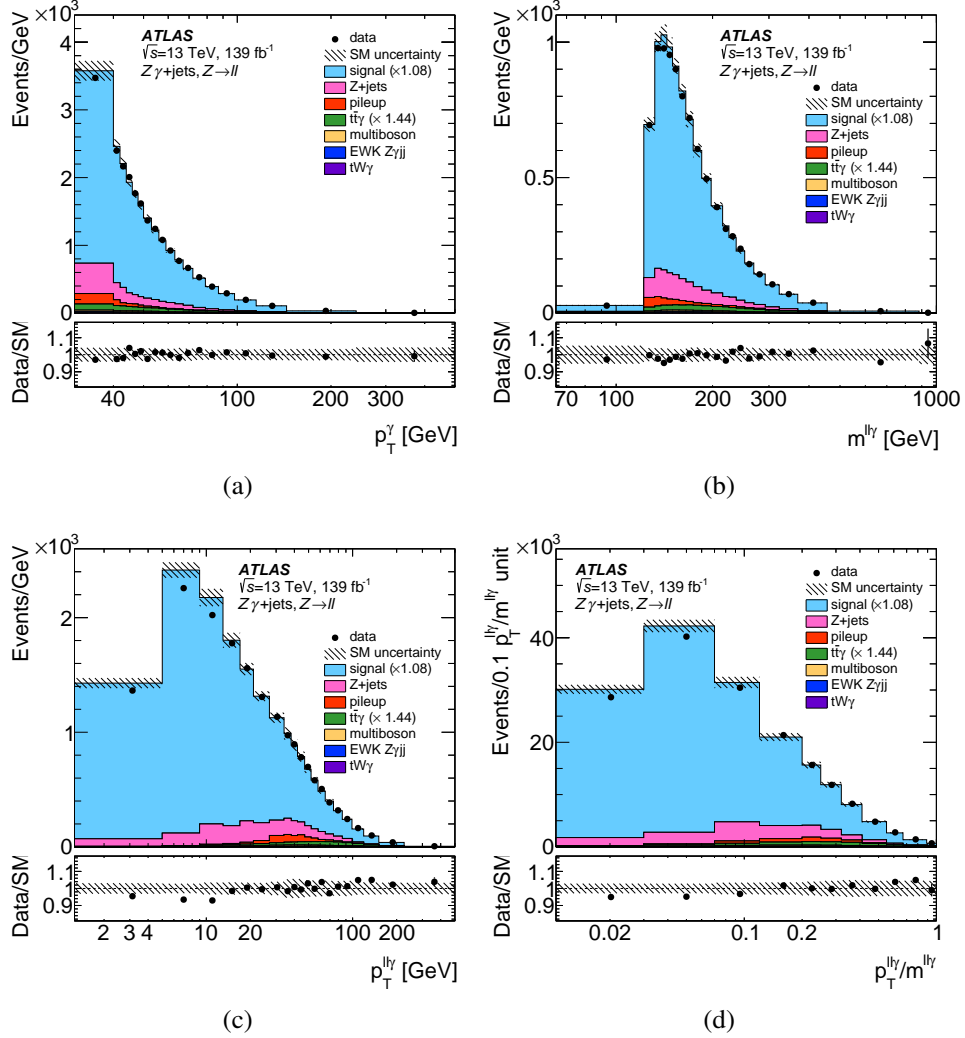


Figure 5.17: The measured p_T^γ (a), $m_{\ell\ell\gamma}$ (b), $p_T^{\ell\ell\gamma}$ (c), and $p_T^{\ell\ell\gamma}/m_{\ell\ell\gamma}$ (d) yield distributions (dots) in the signal region. The error bars (not visible for most points) represent the data statistical uncertainty. The MC simulation of the signal from Sherpa 2.2.11 (blue histograms) and the estimates of various backgrounds (coloured histograms) are also included. For $tW\gamma$, diboson and $t\bar{t}\gamma$ the background uncertainties are included. The Z +jets systematic uncertainties contain the propagation of the background uncertainties, the E_{gap} and anti-tight criteria, and the generator uncertainty. For the signal, the experimental uncertainties are considered. The lower part of each figure shows the ratio of the data to the expected total SM distribution. The hatched band represents the statistical and systematic uncertainties of the SM background yields added in quadrature.

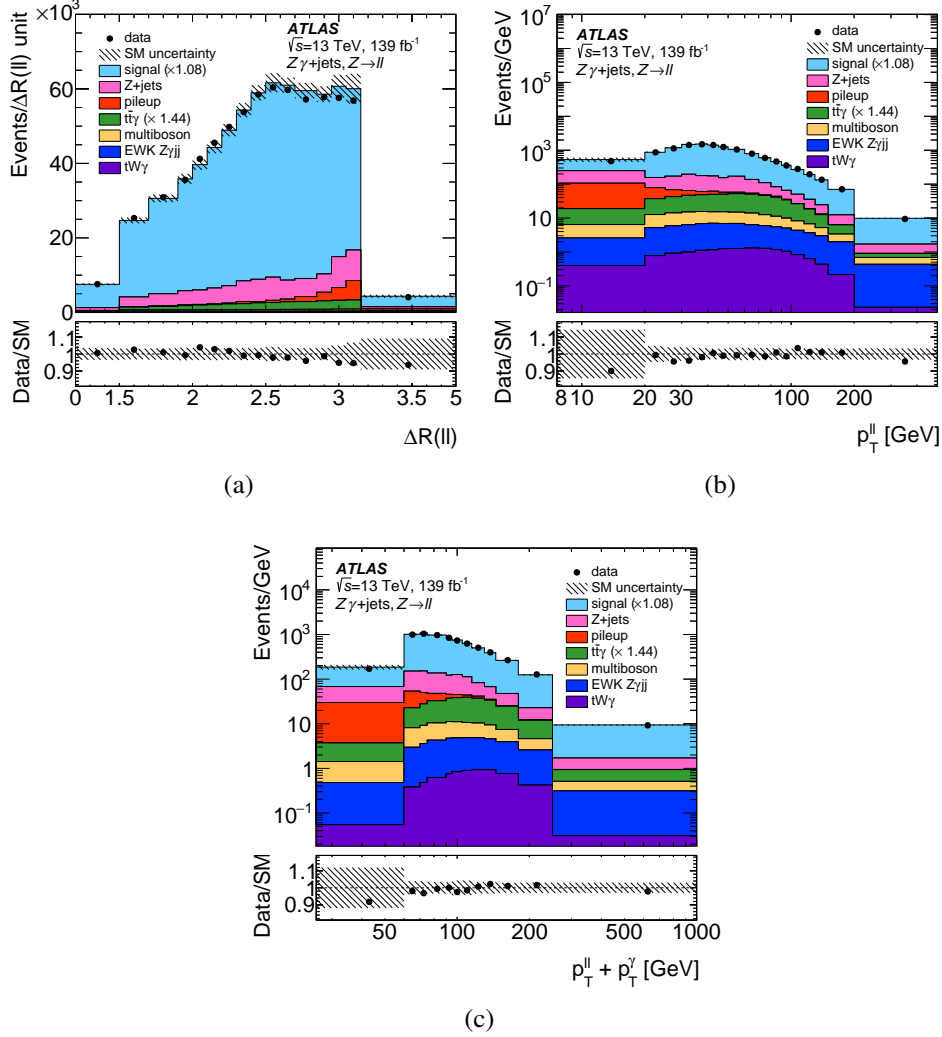


Figure 5.18: The measured $\Delta R(\ell, \ell)$ (a), $p_T^{\ell\ell}$ (b), and $p_T^{\ell\ell} + p_T^\gamma$ (c) yield distributions (dots) in the signal region. The error bars (not visible for most points) represent the data statistical uncertainty. The MC simulation of the signal from Sherpa 2.2.11 (blue histograms) and the estimates of various backgrounds (coloured histograms) are also included. For $tW\gamma$, diboson and $t\bar{t}\gamma$ the background uncertainties are included. The Z +jets systematic uncertainties contain the propagation of the background uncertainties, the E_{gap} and anti-tight criteria, and the generator uncertainty. For the signal, the experimental uncertainties are considered. The lower part of each figure shows the ratio of the data to the expected total SM distribution. The hatched band represents the statistical and systematic uncertainties of the SM background yields added in quadrature.

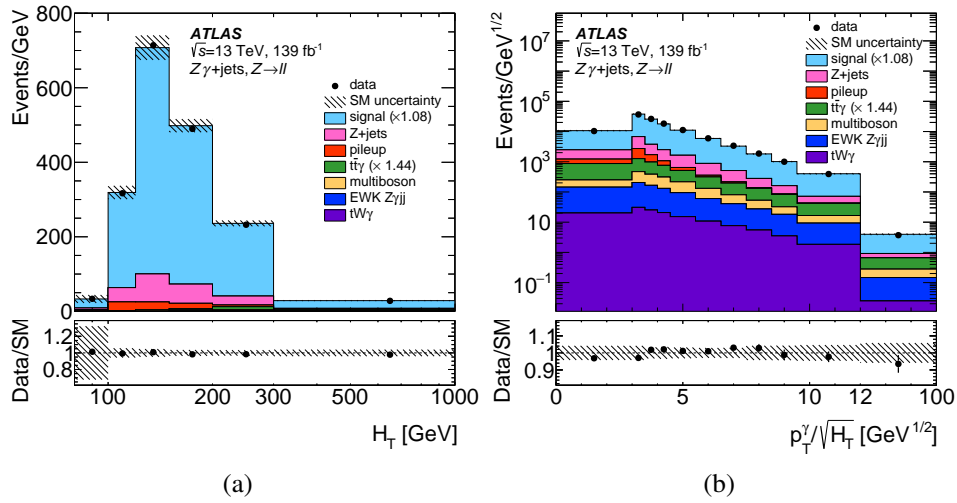


Figure 5.19: The measured H_T (a) and $p_T^\gamma/\sqrt{H_T}$ (b) yield distributions (dots) in the signal region. The error bars (not visible for most points) represent the data statistical uncertainty. The MC simulation of the signal from Sherpa 2.2.11 (blue histograms) and the estimates of various backgrounds (coloured histograms) are also included. For $tW\gamma$, diboson and $t\bar{t}\gamma$ the background uncertainties are included. The Z + jets systematic uncertainties contain the propagation of the background uncertainties, the E_{gap} and anti-tight criteria, and the generator uncertainty. For the signal, the experimental uncertainties are considered. The lower part of each figure shows the ratio of the data to the expected total SM distribution. The hatched band represents the statistical and systematic uncertainties of the SM background yields added in quadrature.

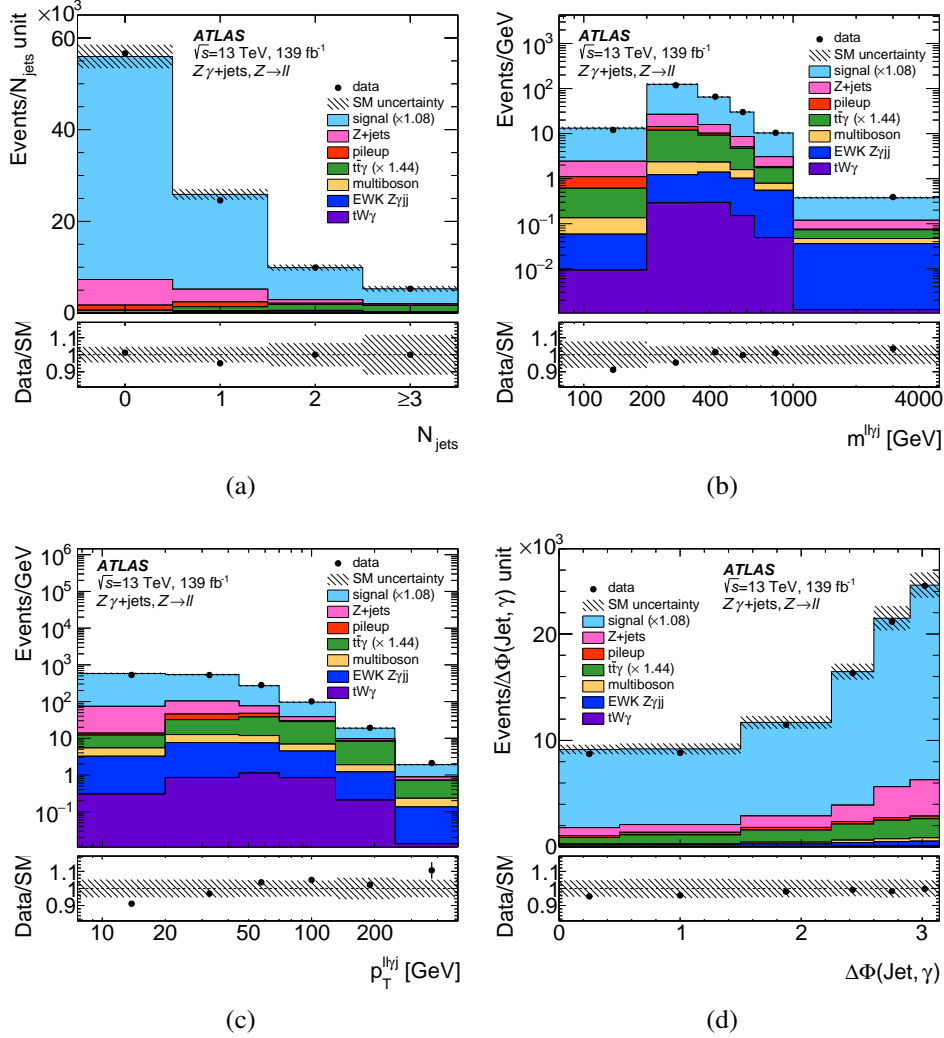


Figure 5.20: The measured N_{jets} (a), $m^{\ell\ell\gamma}$ (b), $p_T^{\ell\ell\gamma}$ (c), and $\Delta\phi(\text{Jet}, \gamma)$ (d) yield distributions (dots) in the signal region. The error bars (not visible for most points) represent the data statistical uncertainty. The MC simulation of the signal from Sherpa 2.2.11 (blue histograms) and the estimates of various backgrounds (coloured histograms) are also included. For $tW\gamma$, diboson and $t\bar{t}\gamma$ the background uncertainties are included. The Z + jets systematic uncertainties contain the propagation of the background uncertainties, the E_{gap} and anti-tight criteria, and the generator uncertainty. For the signal, the experimental uncertainties are considered. The lower part of each figure shows the ratio of the data to the expected total SM distribution. The hatched band represents the statistical and systematic uncertainties of the SM background yields added in quadrature.

Checking $Z(\rightarrow ee)\gamma$ and $Z(\rightarrow \mu\mu)\gamma$ channels separately The results presented above are given for the $Z(\rightarrow \ell\ell)\gamma$ channel. It was assumed until now that the SM estimates match the data in the $Z(\rightarrow ee)\gamma$ and $Z(\rightarrow \mu\mu)\gamma$ cases, just because the "sum" did. However, it is possible that there are badly modelled regions in both channels that cancel out when they are taken together.

The first thing to check is the inclusive cross-section, to see if the Z + jets results are consistent, as shown in Table 5.11. It can be seen that the total prediction matches the data both in the $Z(\rightarrow ee)\gamma$ and $Z(\rightarrow \mu\mu)\gamma$ channels. Then, the Z + jets contribution, calculated independently for the three channels, give consistent results, both for the nominal value and the uncertainties.

Another check that was carried out is the agreement between SM estimates and data in the distributions. Some histograms corresponding to the $Z(\rightarrow ee)\gamma$ and $Z(\rightarrow \mu\mu)\gamma$ channels are presented in Fig. 5.21 and, overall, the SM prediction is close to the collected data in both channels.

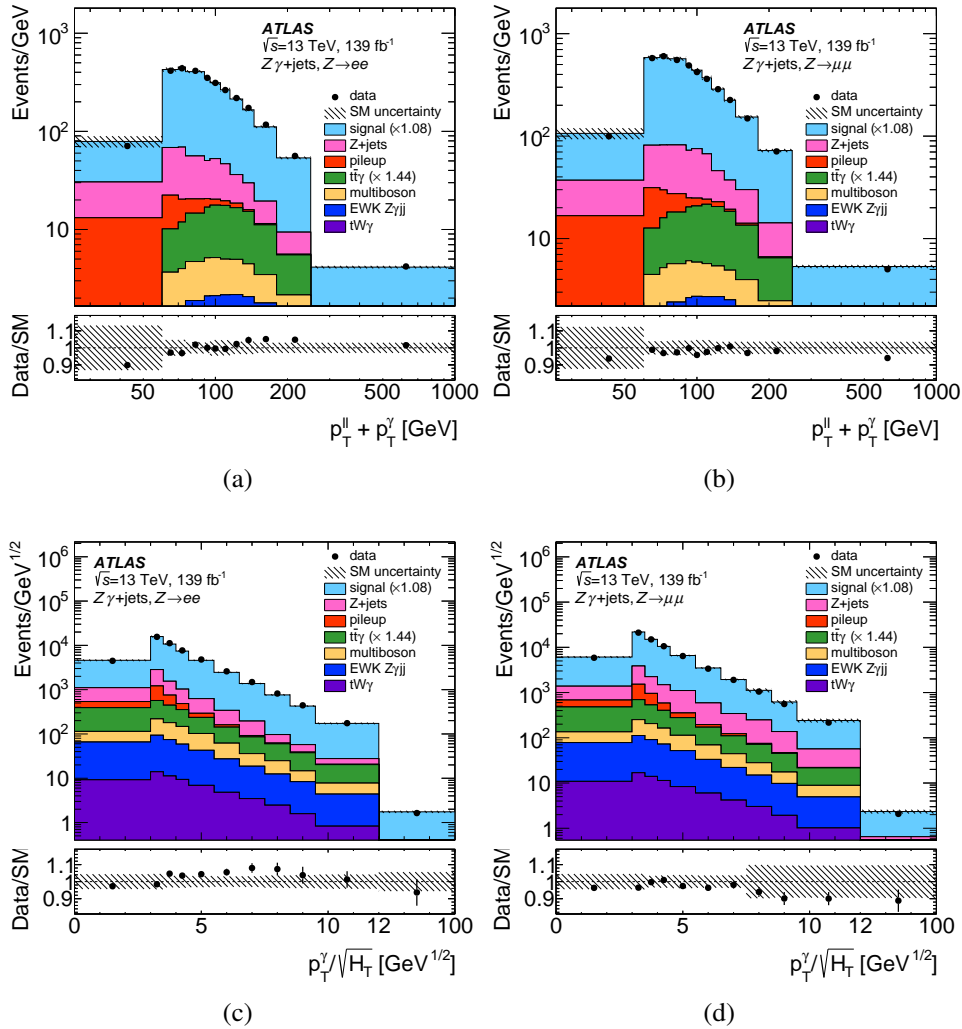


Figure 5.21: From top to bottom, the measured $p_T^{\ell\ell} + p_T^\gamma$ and $p_T^\gamma/\sqrt{H_T}$ distributions (dots) in the $Z(\rightarrow ee)\gamma$ channel on the left and the $Z(\rightarrow \mu\mu)\gamma$ channel on the right.

Source	$Z(\rightarrow \ell\ell)\gamma$	$Z(\rightarrow ee)\gamma$	$Z(\rightarrow \mu\mu)\gamma$
Signal ($\times 1.08$)	79389.8 \pm 56.5 \pm 2295.2	33487.7 \pm 36.4 \pm 967.5	45902.1 \pm 43.2 \pm 1334.5
Z + jets	9773.5 \pm 465.1 \pm 2131.9	4004.1 \pm 274.8 \pm 862.4	5883.6 \pm 406.9 \pm 1330.4
Pileup	2510.5 \pm 72.7 \pm 698.0	1067.1 \pm 47.0 \pm 367.5	1442.9 \pm 55.5 \pm 372.4
$t\bar{t}\gamma$ ($\times 1.44$)	3609.8 \pm 14.5 \pm 541.5	1616.1 \pm 9.7 \pm 242.4	1993.8 \pm 10.8 \pm 299.1
Multiboson	947.9 \pm 5.5 \pm 160.2	449.3 \pm 3.9 \pm 82.3	498.7 \pm 3.8 \pm 79.4
EWK $Z\gamma jj$	812.8 \pm 1.9	369.3 \pm 1.3	443.4 \pm 1.4
$tW\gamma$	148.2 \pm 0.6 \pm 44.5	67.4 \pm 0.4 \pm 20.2	80.8 \pm 0.4 \pm 24.2
Total prediction	97192.5 \pm 474.4 \pm 3259.0	41061.0 \pm 281.3 \pm 1371.5	56245.3 \pm 413.1 \pm 1945.7
Data	96410 \pm 310.5	41396 \pm 203.5	55014 \pm 234.6

Table 5.11: Estimated event yields and uncertainties for $Z(\rightarrow ee)\gamma$, $Z(\rightarrow \mu\mu)\gamma$ and $Z(\rightarrow \ell\ell)\gamma$, compared to the total yields measured in data. For $tW\gamma$, diboson and $t\bar{t}\gamma$ the background uncertainties are included. The Z + jets systematic uncertainties contain the propagation of the background uncertainties, the E_{gap} and anti-tight criteria, and the generator uncertainty. For the signal, the experimental uncertainties are considered. Yields are obtained using Sherpa 2.2.11 for the signal.

5.7.2 Unfolded results

As stated previously, unfolding allows the data to be compared to theory predictions, without the need to simulate the detector. The background predictions are subtracted from data and the unfolded results are compared to the $Z\gamma$ predictions.

The unfolded results are shown in Fig. 5.22 to Fig. 5.24 and in Appendix E. In general, Sherpa, MadGraph, MiNNLO_{PS} and MATRIX predictions all adequately describe the data. Sherpa tends to underestimate the total cross-section and this effect is greater for Sherpa 2.2.4 than Sherpa 2.2.11. Contrary to the detector level study, no correction is applied on the $Z\gamma$ signal sample generated by Sherpa 2.2.11.

All the studied generators tend to mismodel both H_T and $p_T^\gamma/\sqrt{H_T}$, shown in Fig. 5.23. They underestimate data at high H_T and low $p_T^\gamma/\sqrt{H_T}$. These two observables are the only ones where Sherpa 2.2.11 significantly mismodels the data. In the rest of the distributions, Sherpa 2.2.11 does not have significant deviations from the data, except for the slight underestimate discussed above.

The $p_T^{\ell\ell}$, $p_T^{\ell\ell} + p_T^\gamma$ and $\Delta R(\ell, \ell)$ in Fig. 5.22 distributions show how Sherpa 2.2.4 tends to underestimate the data. In particular, event yields at low jet multiplicities are underestimated, as shown in Fig. 5.24.

On the contrary, MadGraph5 underestimates the high jet multiplicity, as can be seen in Fig. 5.24. This generator also underestimates the high dijet mass and high $m_{\ell\ell\gamma j}$ (Fig. 5.24). On the contrary, the $\Delta\phi(\text{Jet}, \gamma)$ (Fig. 5.24) is overestimated at low values by MadGraph5 compared to the data.

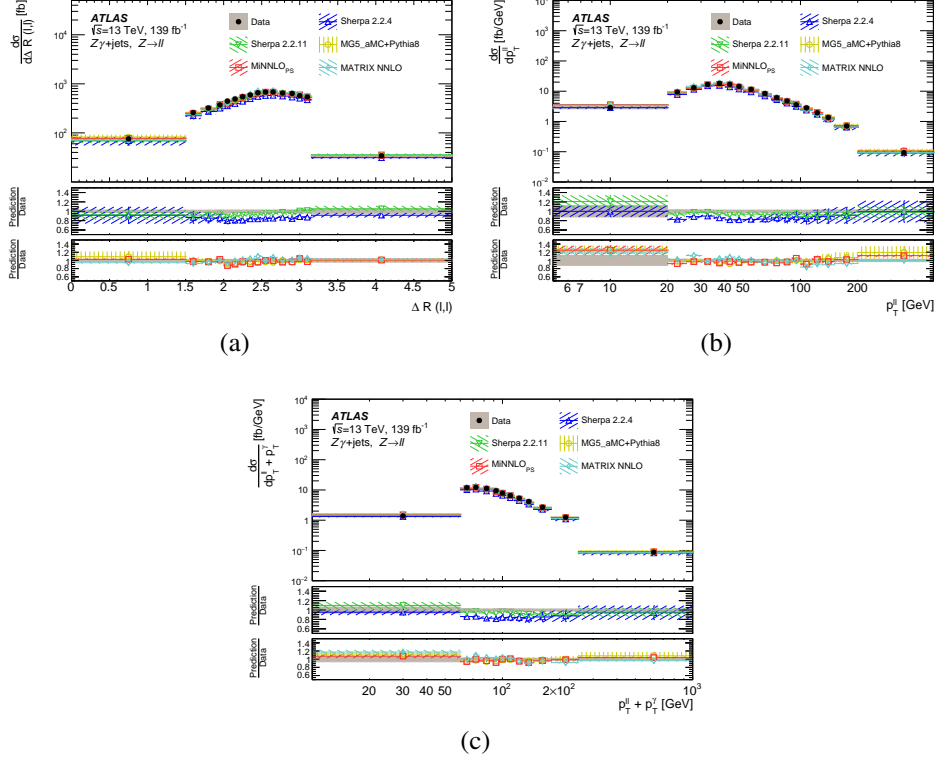


Figure 5.22: Measured differential cross-sections (black data points) as a function of the observables $\Delta R(\ell, \bar{\ell})$ (a), $p_T^{\ell\bar{\ell}}$ (b), and $p_T^{\ell\bar{\ell}} + p_T^{\gamma}$ (c). Error bars (not visible for most points) on the data points show the statistical uncertainty, while the grey area shows the total uncertainty in the unfolded result. SM predictions include: Sherpa 2.2.4, Sherpa 2.2.11, MadGraph5 (MG5_aMC+Pythia8 in the legend), MiNNLO_{PS}, and MATRIX. Dashed bands represent the statistical uncertainty and theoretical uncertainty on the signal predictions (PDF and scale variations). The bottom panels show the ratio of the SM prediction to the measured cross-sections.

Compared to the other generators, MATRIX computes the matrix elements without parton shower or resummation. This can be seen on the N_{jets} distribution (Fig. 5.24), where there is no event with more than 2 jets (and an overestimate of events with exactly 2 jets). The fixed order computation describes the data surprisingly well, also in resummation-sensitive regions such as $p_T^{\text{jet}2}/p_T^{\text{jet}1}$ (Fig. E.1). $\Delta\phi(\text{Jet}, \gamma)$ is however overestimated at high values, and $p_T^{\ell\bar{\ell}\gamma}$ is overestimated at low values and underestimated at high values (Fig. 5.24). The observable $p_T^{\ell\bar{\ell}\gamma}/m_{\ell\bar{\ell}\gamma}$ (Fig. E.4), sensitive to low- p_T jets, shows some mismodelling.

In this chapter, the methods and results of the analysis of the $Z\gamma$ +jets channel were presented. Overall, good agreement between the data and the SM prediction was observed, both for MC generator with PS and fixed order. Many lessons can be drawn from this analysis. The first point is that the statistical uncertainties of the measurements are relatively low compared to the systematic uncertainties. This means that more collected data wouldn't affect significantly the results. The excellent precision implies that the analysis can be used to improve theoretical models. For example, the focus on the jet related observables allows for a better check of the behaviour of the QCD related process in simulations (e.g. parton showers, hadronization, . . .).

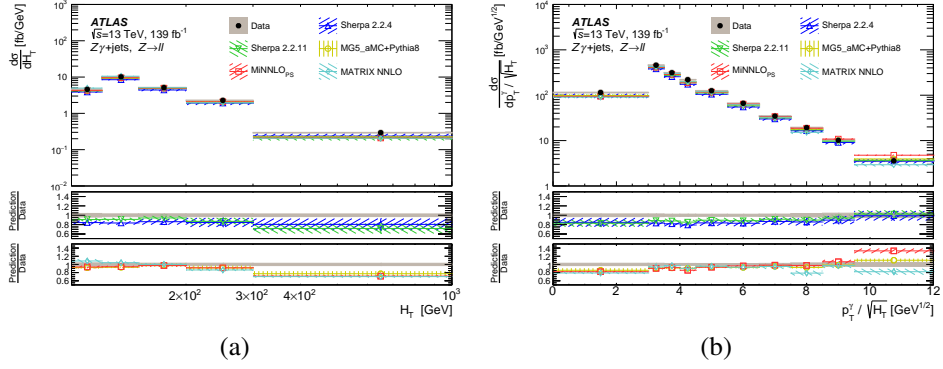


Figure 5.23: Measured differential cross-sections (black data points) as a function of the observables H_T (a) and $p_T^\gamma/\sqrt{H_T}$ (b). Error bars (not visible for most points) on the data points show the statistical uncertainty, while the grey area shows the total uncertainty in the unfolded result. SM predictions include: Sherpa 2.2.4, Sherpa 2.2.11, MadGraph5 (MG5_aMC+Pythia8 in the legend), MiNNLO_{PS}, and MATRIX. Dashed bands represent the statistical uncertainty and theoretical uncertainty on the signal predictions (PDF and scale variations). The bottom panels show the ratio of the SM prediction to the measured cross-sections.

Finally, the precision of the measures allows to set strong boundaries on the BSM processes, as will be demonstrated in the next chapter.

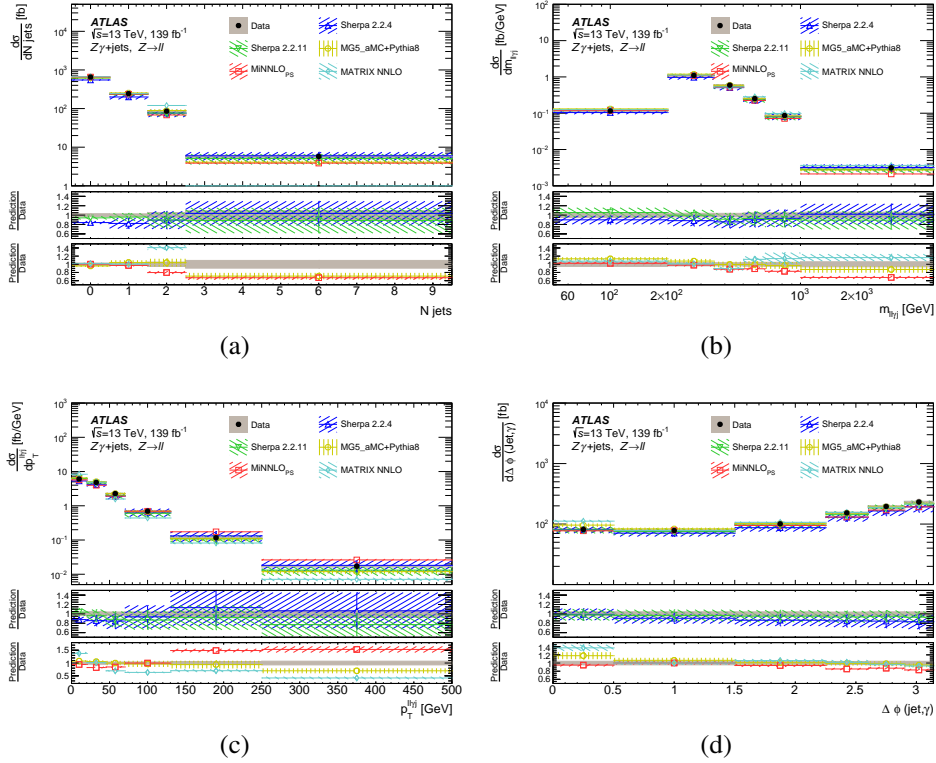


Figure 5.24: Measured differential cross-sections (black data points) as a function of the observables N_{jets} (a), $m_{\ell\ell\gamma j}$ (b), $p_T^{\ell\ell\gamma j}$ (c), and $\Delta\phi(\text{Jet}, \gamma)$ (d). Error bars (not visible for most points) on the data points show the statistical uncertainty, while the grey area shows the total uncertainty in the unfolded result. SM predictions include: Sherpa 2.2.4, Sherpa 2.2.11, MadGraph5 (MG5_aMC+Pythia8 in the legend), MiNNLO_{PS}, and MATRIX. Dashed bands represent the statistical uncertainty and theoretical uncertainty on the signal predictions (PDF and scale variations). The bottom panels show the ratio of the SM prediction to the measured cross-sections.

6 | Search for axion-like particles

In Section 5, a measurement of the $Z\gamma$ +jets process from the ATLAS detector dataset was presented. The comparison of the data with the SM predictions showed no sign of BSM physics and can be used to impose constraints on new physics models. The $Z\gamma$ process is interesting to set boundaries on BSM physics since the uncertainties are relatively low, thus allowing to set tight limits.

In this chapter, the $Z\gamma$ measurement from Ref. [72] is used to constrain a model with a DM candidate: ALPs. The method used to set boundaries on the ALPs model is directly inspired from Ref. [131] and the results were published in Ref. [134]. This is the first study of off-shell ALPs, whose properties are introduced in Section 2.3.3, performed using ATLAS, and the first such study in the chosen final states. In addition to the $Z\gamma$ channel, the WW channel [60, 62] was also examined using the same methods and tools. However, to give a concrete example of the search procedure, we will focus on the $Z\gamma$ process.

The method to search for off-shell ALPs is based on comparing the data with a MC estimate, built by the generation of a SM prediction and an ALP signal sample:

$$\sigma_{MC} = \sigma_{SM} + \mu\sigma_{ALP}. \quad (6.1)$$

Here, μ is the signal strength, σ_{SM} is the SM prediction and σ_{ALP} is the MC ALP prediction for a certain set of coupling constants. By constraining the signal strength μ thanks to a statistical evaluation, limits can be set on the coupling constants of the ALPs.

Section 6.1 explains the scope of the ATLAS measurements on which the search for off-shell ALPs is done and how the data and SM predictions are retrieved. An introduction to the ALPs cross-section in the off-shell approximation is given in Section 6.2. Section 6.3 presents how the off-shell ALPs signal is generated by MC. Section 6.4 introduces the statistical tool used to compare MC with the data in order to deduce a constraint on the coupling constants of the ALPs. Finally, the limits set on the ALP coupling constants will be presented in Section 6.5 and discussed in Section 6.6.

6.1 $Z\gamma$ and WW measurements

This off-shell ALP study relies on two diboson channels ($Z\gamma$ and WW) and three published measurements: $Z\gamma$ [72], $WW0j$ [60] and $WW1j$ [62]. The data, their uncertainties and the MC predictions were collected from the HEPData files corresponding to the unfolded measurements [218, 219, 220]. For the SM estimate of the diboson processes, a MATRIX computation at NNLO is used. Table 6.1 summarizes the fiducial phase-spaces used in the different measurements.

Due to the chronology of the studies, the analysis presented in Section 5 was not part of this search. Information relative to the $Z\gamma$ cross-section were extracted from Ref. [72]. This measurement is inclusive in jet activity, but otherwise has the same selection criteria as the

Variable	Selection criteria		
	$Z\gamma$	$WW0j$	$WW1j$
p_T^ℓ	$> 25, 30 \text{ GeV}$	$> 27 \text{ GeV}$	$> 27 \text{ GeV}$
$ \eta_\ell $	< 2.47	< 2.5	< 2.5
$m_{\ell\ell}$	$> 40 \text{ GeV}$	$> 55 \text{ GeV}$	$> 85 \text{ GeV}$
p_T^γ	$> 30 \text{ GeV}$	-	-
$ \eta_\gamma $	> 2.37	-	-
$\Delta R(\ell, \gamma)$	> 0.4	-	-
$m_{\ell\ell\gamma} + m_{\ell\ell}$	$> 182 \text{ GeV}$	-	-
$p_T^{\ell\ell}$	-	$> 30 \text{ GeV}$	-
E_T^{miss}	-	$> 20 \text{ GeV}$	-
p_T^{jet}	-	$< 35 \text{ GeV}$	$> 30 \text{ GeV}$

Table 6.1: Selection criteria defining the fiducial cross-section of the $Z\gamma$, $WW0j$ and $WW1j$ cross-section measurements. Data taken from Ref. [134].

$Z\gamma$ +jets analysis discussed above. The requirements are briefly summarized below. The measurement is made on the full Run 2 dataset corresponding to an integrated luminosity of 139 fb^{-1} . The object selection requires at least two same flavour opposite charge leptons (electrons or muons) and a photon. The leading lepton (with the highest transverse momentum) is required to have $p_T^{\text{lead } \ell} > 30 \text{ GeV}$ while the subleading lepton (with the second highest momentum) $p_T^{\text{sub-lead } \ell} > 25 \text{ GeV}$. Concerning the photon, the requirement on the transverse momentum is $p_T^\gamma > 30 \text{ GeV}$. A selection criteria is also placed on the dilepton and dilepton-photon system masses: $m_{\ell\ell} + m_{\ell\ell\gamma} > 182 \text{ GeV}$. There are 6 available observables: p_T^γ , $|\eta_\gamma|$, $m_{\ell\ell\gamma}$, $p_T^{\ell\ell\gamma}$, $p_T^{\ell\ell\gamma}/m_{\ell\ell\gamma}$ and $\Delta\phi(\ell\ell, \gamma)$.

The $WW0j$ measurement studies the data from the Run 2 collected from 2015 to 2016 corresponding to an integrated luminosity of 36.1 fb^{-1} . The $WW0j$ selection requires that the event has exactly 2 leptons with opposite flavour (an electron and a muon) and transverse momentum $p_T^\ell > 27 \text{ GeV}$. There are additional criteria on the missing transverse energy (due to neutrinos), dilepton transverse momentum and mass. A jet veto is also imposed, requiring that there is no jet with $p_T^{\text{jet}} > 35 \text{ GeV}$. The observables in the $WW0j$ study include $p_T^{\text{lead } \ell}$, $m_{e\mu}$, $p_T^{e\mu}$, $|y_{e\mu}|$, $\Delta\phi(e, \mu)$ and $|\cos(\theta^*)|^1$.

The $WW1j$ uses the full Run 2 data with an integrated luminosity of 139 fb^{-1} . The selection of events is very similar to the $WW0j$ analysis, except for the jets, dilepton and missing energy requirements. In the $WW1j$, at least one jet with $p_T^{\text{jet}} > 30 \text{ GeV}$ is required. The observables are the same as the $WW0j$ with the following additional ones: $p_T^{\text{sub-lead } \ell}$, $p_T^{\text{lead jet}}$, N_{jets} , H_T^2 , S_T^3 , $m_{T,e\mu}^4$.

1. $|\cos(\theta^*)| = \tanh[\Delta\eta(e, \mu)/2]$

2. scalar sum of all jet transverse momenta

3. scalar sum of all jet and lepton transverse momenta

4. $m_{T,e\mu} = \sqrt{(E_{T,e\mu} + E_T^{\text{miss}})^2 - (\vec{p}_{T,e\mu} + \vec{p}_T^{\text{miss}})^2}$, where $E_{T,e\mu} = \sqrt{|\vec{p}_{T,e\mu}|^2 + m_{e\mu}^2}$

6.2 ALPs production cross-section

The method of the off-shell ALPs search is to compare the data obtained by the ATLAS detector and available publicly as differential cross-section distributions, to the SM prediction with or without ALP signal. The ALP signal is, here, investigated as a mediator for the s-channel $gg \rightarrow \text{ALP} \rightarrow Z(\rightarrow \ell\ell)\gamma$ (Fig. 6.1).

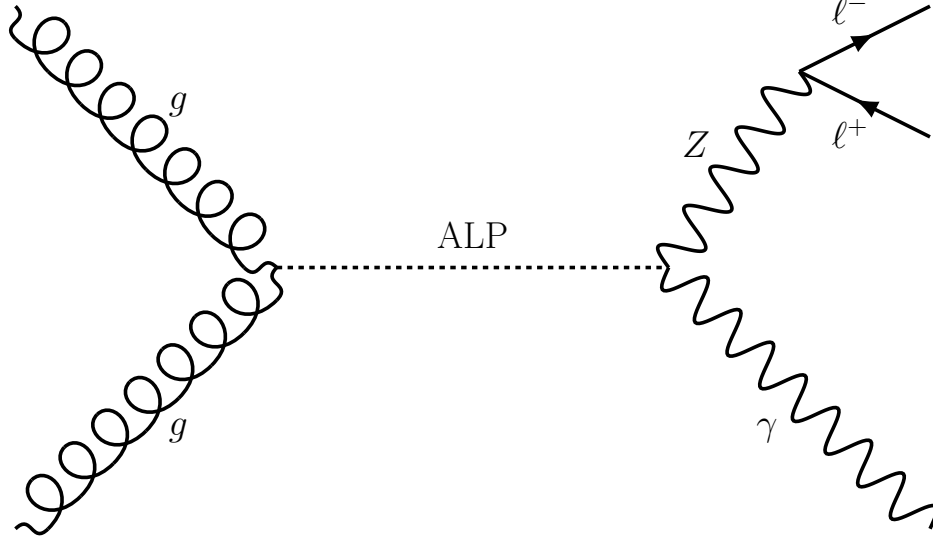


Figure 6.1: Feynman diagram of the off-shell ALP production in the $Z\gamma$ process.

In the scenario considered for this search, the ALPs is supposed to be off-shell:

$$m_a^2 \ll \hat{s} \ll f_a^2, \quad (6.2)$$

where m_a and f_a are the mass and the decay constant of the ALPs, and $\sqrt{\hat{s}}$ is the center-of-mass energy of the gluon–gluon system. The ALPs effective Lagrangian introduced in Section 2.3.3 implies a cross-section [131]:

$$\sigma_{Z\gamma} \propto g_{agg}^2 g_{aZ\gamma}^2 \hat{s}. \quad (6.3)$$

This cross-section has two interesting features. The first one is that it increases with \hat{s} . Typically, a standard model process such as a diboson production involves that the cross-section would be $\sigma_{SM} \propto 1/\sqrt{\hat{s}}$, which makes the search quite competitive with respect to other strategies. Fig. 6.2 illustrates this difference between the SM and ALP signal for MC simulations for the $m_{\ell\ell\gamma}$ observable ($\sim \sqrt{\hat{s}}$).

The second interesting feature of the ALP cross-section is that it is independent of m_a for a wide mass range. This is important for the MC generation of the ALPs signal since the shape would not be affected by the mass, as long as the relation $m_a \ll \sqrt{\hat{s}} \sim 100 \text{ GeV}$ holds. This can be tested by comparing distributions of different ALP masses, as shown in Fig. 6.3. Up to 10 to 100 GeV, all the distributions agree within uncertainties.

A Feynman diagram like Fig. 6.1 where the gluons are replaced by quarks is possible in the off-shell approximation. However, this contribution is negligible for equivalent $c_{\tilde{G}}$ and $c_{a\Phi}$. In fact, its impact is visible only if the parameter $c_{\tilde{G}}$ is about a thousand time smaller than $c_{a\Phi}$. This is shown in Fig. 6.4, where a constant quark–quark contribution can be seen for very low $c_{\tilde{G}}$ and the gluon–gluon contribution can be seen for high $c_{\tilde{G}}$ with a slope proportional to $c_{\tilde{G}}^2$ for diboson final states and $c_{\tilde{G}}^4$ for dijet final state ($c_{\tilde{G}}^2$ for $gg \rightarrow \text{ALP}$ and $c_{\tilde{G}}^2$ for $\text{ALP} \rightarrow gg$).

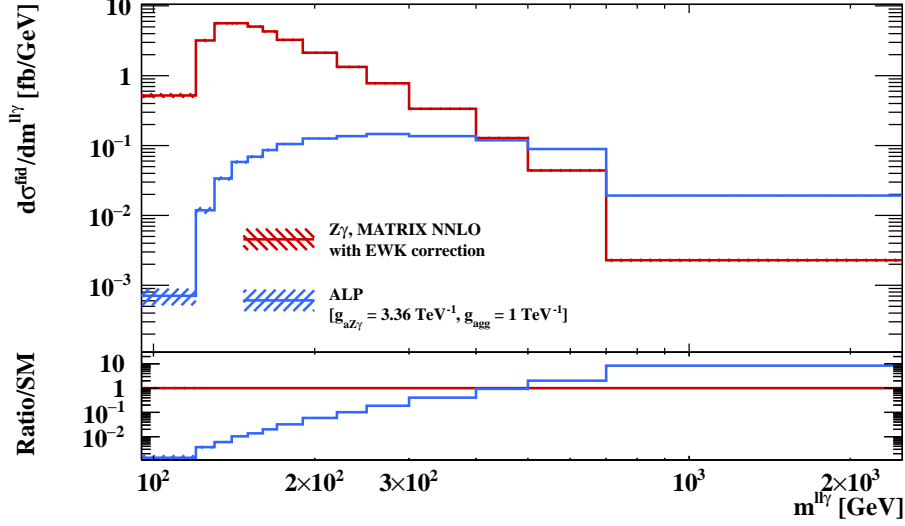


Figure 6.2: Differential cross-section for $m_{\ell\ell\gamma}$ for the SM (red) and the ALP signal (blue) generated by MadGraph5 with $g_{aZ\gamma} = 3.36 \text{ TeV}^{-1}$ and $g_{agg} = 1 \text{ TeV}^{-1}$. The bottom plot shows the ratio of the ALPs prediction with respect to the SM estimates, highlighting the different shape.

6.3 Signal predictions

The process $gg \rightarrow \text{ALP} \rightarrow Z\gamma$ is generated by MadGraph5 [209] using an Universal FeynRule Output (UFO) [221], corresponding to a set of rules encoding the behavior of the ALPs in the region considered. In general, the final state $\ell\ell\gamma$ can be affected by the $\gamma^*(\rightarrow \ell\ell)\gamma$ process. However, the event selection criteria allows to suppress this process, thus making it negligible. To generate the ALPs signal, a set of parameters has been chosen:

- $m_a = 1 \text{ MeV}$: the mass is irrelevant as long as $m_a^2 \ll \hat{s}$.
- $f_a = 1 \text{ TeV}$: it could be argued that the condition $\hat{s} \ll f_a$ might not be satisfied in some events (including high-energy binning of the p_T^γ , $m_{\ell\ell\gamma}$ and $p_T^{\ell\ell\gamma}$ observables). However, Fig. 6.5 shows the comparison of different values of f_a which have been tested for the UFO considered and no difference has been found in the shape of the distribution even for relatively low f_a . This parameter does not change the physics but just the coupling constants, and the value of 1 TeV is thus chosen for simplicity.
- $c_{\tilde{G}} = 0.25$: chosen for simplicity in the computation, so that $g_{agg} = 1 \text{ TeV}^{-1}$
- $c_{\tilde{W}} = 1$ and $c_{\tilde{B}} = 0$: the associated coupling constant is $g_{aZ\gamma} = 3.36 \text{ TeV}^{-1}$. The choice to have $c_{\tilde{W}} \neq c_{\tilde{B}}$ was needed to have $g_{aZ\gamma} \neq 0$.
- $c_{a\Phi} = 1$: the $qq \rightarrow \text{ALP}$ contribution is negligible and this variable does not play any role as long as $c_{a\Phi} \sim c_{\tilde{G}}$.

Once the ALP events are generated by MadGraph5, criteria from the event selection of $Z\gamma$ Ref. [72], $WW0j$ [60] and $WW1j$ [62] are applied to the samples by RIVET 3.1.2 [222]. This software contains official routines for the ATLAS analyses selections. The cross-section of the ALP signal for the $Z\gamma$ channel with the parameters used for the generation is $\sigma_{\text{ALP}}^{\text{gen}} = 99.3 \text{ fb}$.

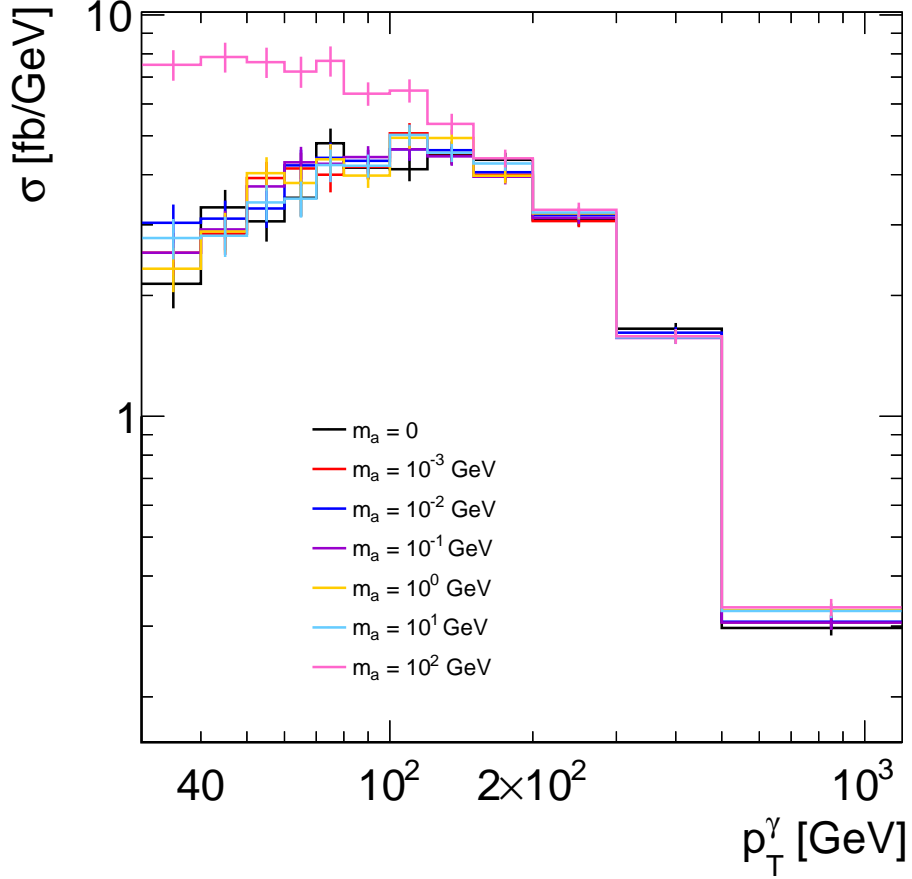


Figure 6.3: Distribution of the observable p_T^γ for the ALPs signal (with statistical uncertainties), for different values of the ALP mass.

6.4 Likelihood fit

The statistical interpretation of the results is performed using the "EFT Fitter for UNfolded measurements" (EFTfun) software developed by the ATLAS collaboration. The likelihood used for this search takes into account the uncertainties properties. This means that uncertainties are treated differently if they are correlated or uncorrelated. The likelihood for a distribution is computed as a function of the Mahalanobis distance [223]:

$$L(\mu) = \frac{1}{\sqrt{(2\pi)^k |C|}} \exp\left(-\frac{1}{2} (\vec{\sigma}_{\text{data}} - \vec{\sigma}_{MC}(\mu))^T C^{-1} (\vec{\sigma}_{\text{data}} - \vec{\sigma}_{MC}(\mu))\right), \quad (6.4)$$

with $\vec{\sigma}$ being the vector representing the bins of a distribution, k the dimension of this vector, and C the covariance matrix. The likelihood formula is used to compute the confidence level on the variable μ by [224]:

$$1 - CL_\mu = \int_{-2\ln[L(\mu)/L_{\max}]}^{\infty} \frac{1}{\sqrt{2\pi t_\mu}} e^{-t_\mu/2} dt_\mu, \quad (6.5)$$

where L_{\max} is the maximum likelihood, typically when $\mu \approx 0$ if there is no BSM signal. In BSM search, the confidence level to reach is $CL_\mu = 95\%$ and is associated to the variable called $\mu_{95\%}$.

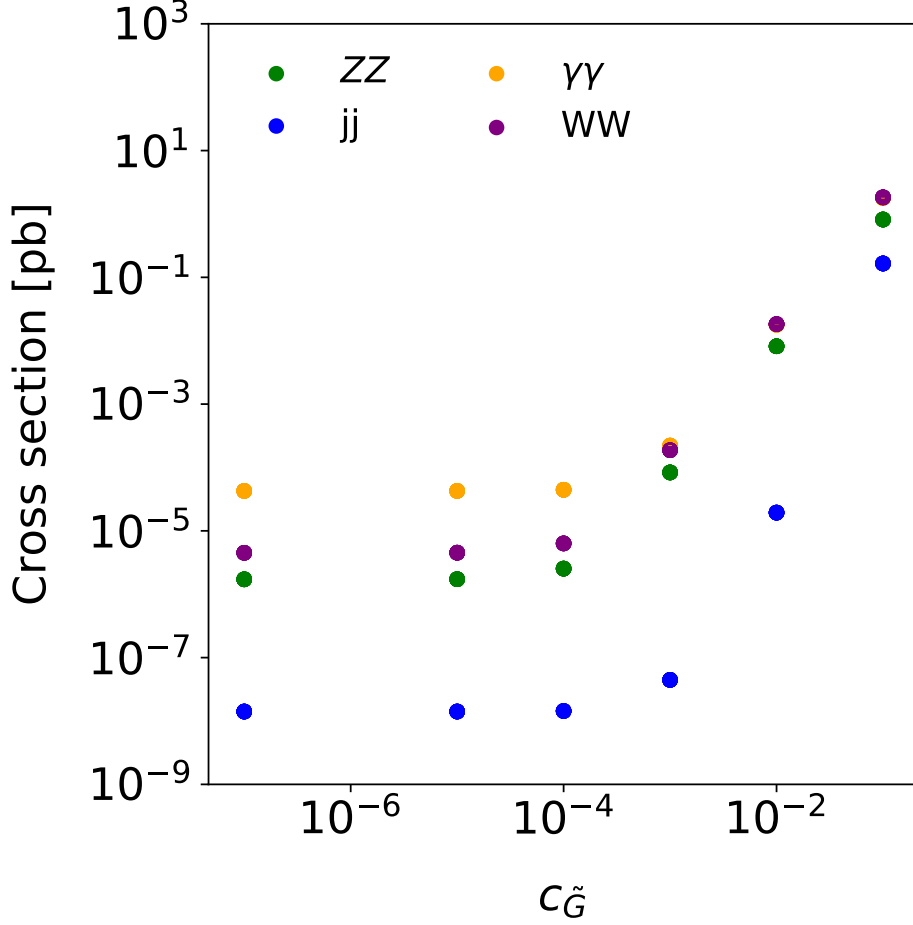


Figure 6.4: Cross-section obtained from MadGraph5 simulation for the processes $pp \rightarrow \text{ALP} \rightarrow XX$ with X being either a Z boson, W boson, photon or jet, as a function of the coupling constant $c_{\tilde{G}}$. The parameters are chosen as follow: $m_a = 1 \times 10^{-3} \text{ MeV}$, $f_a = 1 \text{ TeV}$, $c_{\tilde{W}} = c_{\tilde{B}} = c_{a\Phi} = 1$.

The covariance matrix C is defined as:

$$C_{ij} = \sum_{k \in \text{corr}} e(k)_i e(k)_j + \delta_{ij} \sum_{k \in \text{uncorr}} e(k)_i e(k)_j, \quad (6.6)$$

where corr (uncorr) denote the correlated (uncorrelated) source of uncertainties and δ_{ij} the Kronecker delta. The covariance matrix is the sum of the data and MC covariance matrix:

$$C = C_{\text{data}} + C_{MC}. \quad (6.7)$$

For the data and SM, there is a set of different sources of uncertainties that can be found in HEPData. For the ALPs, the uncertainties are given by the MadGraph5 generation and can be recovered after the RIVET routine. They are statistical uncertainties only and are therefore uncorrelated.

Once $\mu_{95\%}$ is estimated, the boundaries on the ALP diboson coupling constant is deduced from Eq. (6.3):

$$|g_{aZZ} g_{agg}|_{\text{lim}} = \sqrt{\mu} |g_{aZZ} g_{agg}|_{\text{gen}}, \quad (6.8)$$

where g_{aXX} are the coupling constants with "lim" standing for the limit (at 95 % CL) and "gen" for the coupling constant used for the MC ALP signal generation defined in Section 6.3.

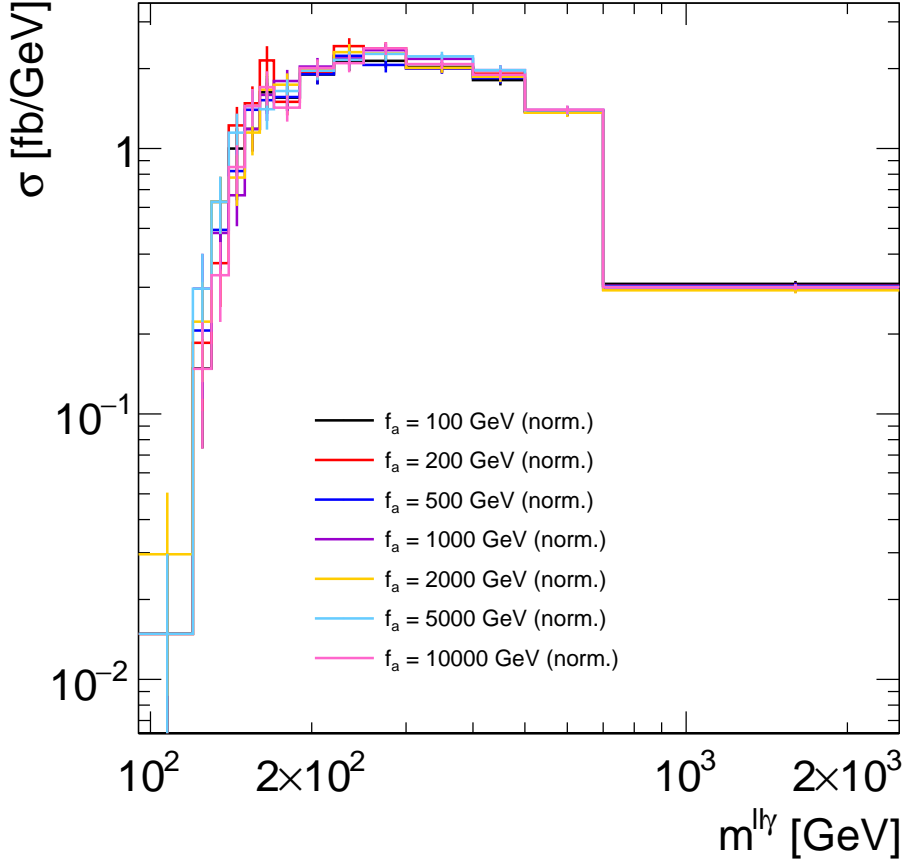


Figure 6.5: ALP signal along the observable $m_{\ell\ell\gamma}$ depending on the scale parameter f_a . The distributions have been normalized to match the $f_a = 1 \text{ TeV}$ cross-section by applying a factor $(f_a/1 \text{ TeV})^4$.

6.5 Results

The first step of the limit setting is to find the observable whose distribution is the most sensitive to a possible ALP signal. For the $Z\gamma$ process, this is found to be p_T^γ . This is determined by fitting the "expected" value for $\mu_{95\%}$ with an Asimov dataset. This means that the data values are replaced by the SM predictions but keeping the data uncertainties. In these conditions, the limit expected for μ in the p_T^γ distribution is $\mu_{95\%}^{exp} = 7.6 \times 10^{-3}$. Applying Eq. (6.8), the expected limit computed for the coupling constants is $|g_{aZ\gamma}g_{agg}|_{exp,lim} = 0.29 \text{ TeV}^{-2}$.

The observed limits are computed with the data and give the experimental boundaries on the ALPs. The observed limit with 95 % confidence is obtained with $\mu_{95\%} = 1.2 \times 10^{-2}$. This is greater than the expected limit but the order of magnitude remains similar. Applying Eq. (6.8), the limit on the coupling constants is set as $|g_{aZ\gamma}g_{agg}|_{lim} = 0.37 \text{ TeV}^{-2}$ (see Fig. 6.6).

The limit on the coupling constants is set for the whole range of $m_a < 100 \text{ GeV}$. On Fig. 6.7, the limit imposed on the $g_{aZ\gamma}$ by the off-shell search is compared to other experiments. This figure is plotted for $g_{aZ\gamma}/g_{agg}$ fixed to the ratio $\alpha_{Z\gamma}/\alpha_s$ (with $\alpha_{EM} = \alpha_{WW} \sin(\theta_W) = \alpha_{Z\gamma} \sin(\theta_W) \cos(\theta_W)$). For each experiment, the limit reacts differently to the change of a parameter. For the set consid-

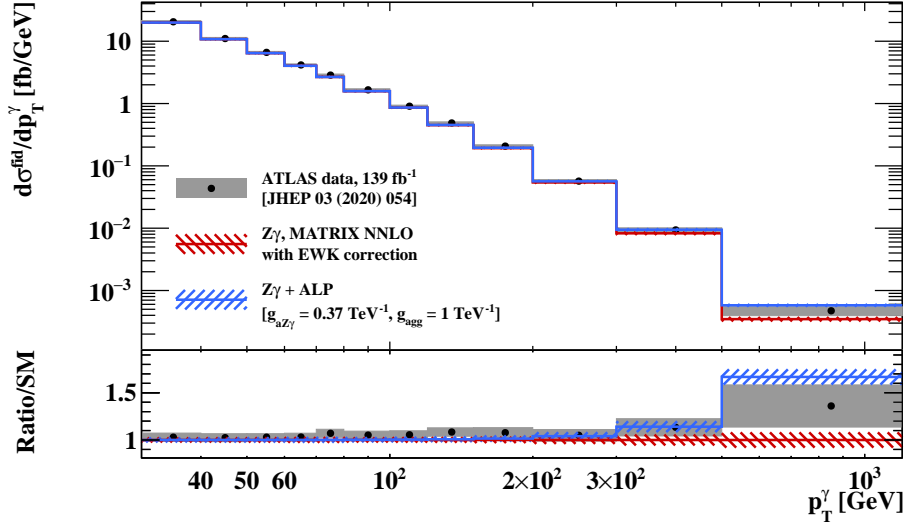


Figure 6.6: Comparison between data, SM estimate and SM+ALP (with an ALP signal strength corresponding to 95 % CL) in the p_T^γ distribution used to set $\mu_{95\%}$.

ered here, the off-shell method can fix boundaries corresponding to an improvement of the $g_{aZ\gamma}$ limits compared to other experiments.

The same procedure has been applied on WW channel based on the data from Ref. [60] and [62]. This was done in parallel to the $Z\gamma$ and with the exact same method. The result on the coupling constants gives the limit $|g_{aWW}g_{\text{agg}}|_{\text{lim}} = 0.62 \text{ TeV}^{-2}$.

In Ref. [131] the limits on the ZZ and $\gamma\gamma$ channel are measured, with a similar method (off-shell search), using CMS data. The boundaries set are $|g_{aZZ}g_{\text{agg}}|_{\text{lim}} = 0.99 \text{ TeV}^{-2}$ and $|g_{a\gamma\gamma}g_{\text{agg}}|_{\text{lim}} = 0.08 \text{ TeV}^{-2}$.

In order to compare the result obtained on different diboson couplings, Eq. (2.22) is considered. All the diboson couplings (except the gluon one) are related to only 3 parameters: f_a , $c_{\tilde{W}}$ and $c_{\tilde{B}}$. To compare the different coupling constants, one has to choose a set of parameters (g_{agg} , f_a) and to plot the bidimensional dependance of $c_{\tilde{W}}$ and $c_{\tilde{B}}$. The result is shown on Fig. 6.8 for the set ($g_{\text{agg}} = 1 \text{ TeV}^{-1}$, $f_a = 1 \text{ TeV}$), which shows that the different channels provide complementary limits on $c_{\tilde{W}}$ and $c_{\tilde{B}}$. This figure must be read as follows: only the band between two lines of the same colour is permitted, all the rest being excluded. This means that the yellow square in the middle is the only solution that has not been excluded by the different measurements. There are two lines for each process since the experimental setup accesses only $g_{aV_1V_2}^2$. This means that the coupling constant can be either positive or negative, hence the two lines.

One might wonder about the changes on the limit on $c_{\tilde{W}}$ and $c_{\tilde{B}}$, if either f_a or g_{agg} is varied. If a variation is applied on f_a , keeping g_{agg} constant, the diboson coupling constant $g_{aV_1V_2}$ is not changed (Eq. (6.3)). However, all the coupling constants depend on a factor $1/f_a$ meaning that the parameters $c_{\tilde{W}}$ and $c_{\tilde{B}}$ will increase by the same factor as f_a . Graphically, the plot will remain the same in shape but with the x- and y-range which will change by the factor applied on f_a . The same reasoning can be applied to the change on g_{agg} , but, this time, the range will decrease proportionally to the increase of the axion-gluon coupling constant. In any case, the different limits all change the same way, meaning that the $Z\gamma$ and $\gamma\gamma$ results will always be the tightest ones.

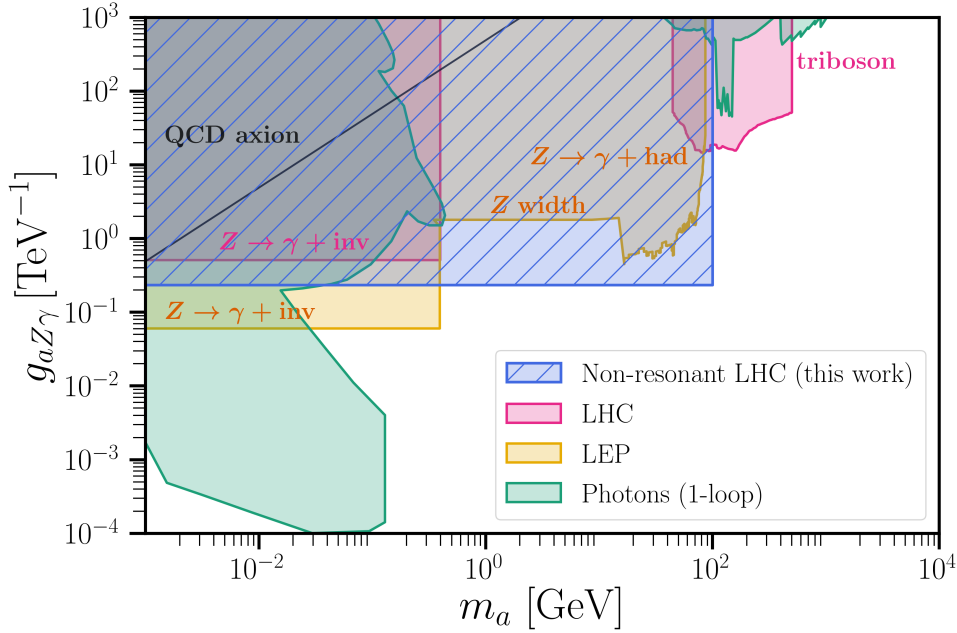


Figure 6.7: Comparison on the 95 % CL boundaries on the coupling $g_{aZ\gamma}$, with the condition $g_{aZ\gamma}/g_{agg} = \alpha_{Z\gamma}/\alpha_s$. The label "LHC" refers to the results from Ref. [127], LEP are from studies of the Z width, and "Photons" are from beam dump experiments, supernova SN1987a observation and LHC results (see Ref. [103] for more information). Figure taken from Ref. [134].

6.6 Discussion

The off-shell search for ALPs is a powerful tool to set limits on the axion coupling to dibosons. Its results are complementary to the limits set by other experiments. In the following, possible improvements to the study are listed.

First, Eq. (6.1) does not contain interference between the SM and the ALPs. Although the interference term might be small (and negligible), this would be interesting to study. The limit $\mu_{95\%} = 1.2 \times 10^{-2}$ imposes that the cross-section of the ALP signal is smaller than $\mu_{95\%} \sigma_{\text{ALP}} = 1.2 \text{ fb}$, which must be compared to the gluon-gluon SM contribution to the $Z\gamma$ process, given by MATRIX NNLO as $\sigma_{SM}^{gg} \approx 9 \text{ fb}$. The term $\mathcal{M}_{SM} \mathcal{M}_{\text{ALP}}^*$, neglected for this search, might become greater than the pure ALP signal, in the $\mu_{95\%}$ value considered here. By design, this study could not take into account such a contribution although it might be interesting to investigate. The contribution of this interference might improve or deteriorate the limit set on the coupling constant, depending if it is a constructive or destructive interference.

Another assumption in this study is the use of the phase-space region $m_a^2 \ll \hat{s} \ll f_a^2$. Although this assumption is true for the QCD axions, there are no global limits on the ALPs mass and decay constant. Therefore, if the scale parameter f_a was in the range or smaller than the LHC typical collision energy, the limit set on Fig. 6.7 would not hold since the model used would be inaccurate in this phase-space.

The last assumption in the work presented is the neglect the axion-quark coupling constant. As it was mentioned before, this contribution is negligible compared to the gluon one, as long as $c_{\tilde{G}} \sim c_{a\Phi}$. But theoretically, nothing prevents the coupling from being $c_{\tilde{G}} \ll c_{a\Phi}$ for ALPs and

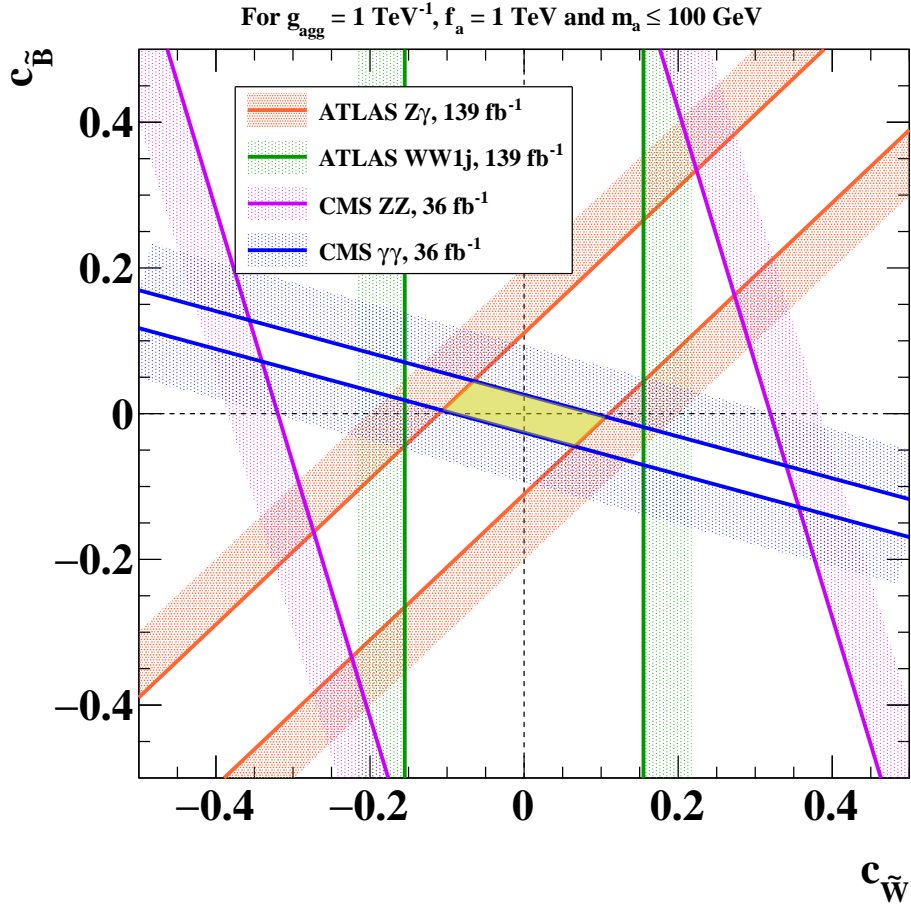


Figure 6.8: Constraints on $c_{\tilde{W}}$ and $c_{\tilde{B}}$ with a 95 % CL based on the search of off-shell ALPs in $Z\gamma$ and WW channels in ATLAS, as well as ZZ and $\gamma\gamma$ channels in CMS from Ref. [131].

therefore the previous analysis from giving inexact results. The axion-quark coupling could play a role in this process but the interference term in this situation would be more likely to be dominant. A proper signal+ALP MC simulation would be required to set limits on the axion couplings.

7 | Conclusion

When data is collected in particle accelerators, the results are compared to what is expected from the SM. This prediction is done using MC generators or calculations, which are based on different assumptions and on the knowledge acquired on the SM. To improve the accuracy of the SM predictions and to search for physics BSM, predictions and data must be compared in precision measurements.

This thesis presents a precision measurement of the $Z\gamma$ +jets process. The data used for this study come from the ATLAS Run 2 data taking from 2015 to 2018, with an integrated luminosity of 139 fb^{-1} . The $Z\gamma$ channel has the advantage to have many events passing the selection criteria, with a relatively low background. The goal of the search was to study jets in order to gain insight of the QCD modelling with different generators and calculations. To do so, a set of observables was chosen with a focus on variables sensitive to jet activities. The background was estimated using mainly data-driven methods, especially for the Z +jets contribution, where a sideband method was used. The use of a data-driven estimate allows for a lower dependency on the MC background simulations. The inclusive uncertainty on the SM prediction is around 4%. A comparison of the unfolded data with several predictions showed globally a good agreement, but with some inaccuracies. The use of data with a higher luminosity would not improve dramatically the results shown as the statistical uncertainties are, in most histograms, smaller than the systematics uncertainties. This search will be useful to help improving generators and calculations, for example by providing input to electroweak precision fits for extracting SM parameters. The HEPData [225] and Rivet routine published with this analysis will be useful for the future improvements of the predictions.

A search for a class of Dark Matter candidates, ALPs, was also introduced in this thesis. The relatively low uncertainties on the $Z\gamma$ and WW channels allowed to set strong constraints on the ALPs coupling constants. This study was the first to use ALPs as off-shell mediator of the diboson creation in proton–proton collisions in ATLAS. The off-shell regime is interesting because the accessible ALPs mass range (here $m_a < 100 \text{ GeV}$) is lower than the mass investigated with a resonance search, whilst the shape of the ALPs signal remains different from the SM. This search used the data from the ATLAS Run 2 dataset and SM expectation as given by the ATLAS collaboration. The ALPs signal was generated using MadGraph5 and, in the absence of signal, its strength was constrained by a statistical treatment using a likelihood method. New limits were set on the coupling constants of the ALPs with gluons and a photon and Z boson pair, with a value $|g_{aZ\gamma}g_{agg}| < 0.37 \text{ TeV}^{-2}$. This limit competes with limits set by other experiments using accelerator physics or astrophysical sources, in the low mass range. When comparing the different limits set by the off-shell search for the coupling constants of the ALPs with W bosons, Z bosons and photons, the $Z\gamma$ channel set one of the strongest boundaries. Further improvement could be done in the future on the off-shell searches. For example, the search for axion could be done on the WW or $\gamma\gamma$ channel from the vector boson scattering, hence removing the assumption on the gluon coupling constant.

A | Spontaneous symmetry breaking

To understand the spontaneous symmetry breaking, let's use a simple model and suppose a scalar field (spin-0) ϕ , whose Lagrangian is invariant under U(1) transformation. The Lagrangian of the field is:

$$\mathcal{L} = [(\partial_\mu - iqA_\mu) \phi^*][(\partial^\mu + iqA^\mu) \phi] - V(\phi) - \frac{1}{4}F_{\mu\nu}F^{\mu\nu}, \quad (\text{A.1})$$

where A_μ the field associated to the gauge invariance and $V(\phi)$ the potential.

In general, a renormalizable SU(2) \times U(1) symmetry potential is written as:

$$V(\phi) = \mu^2 \phi^* \phi + \lambda (\phi^* \phi)^2, \quad (\text{A.2})$$

where μ and λ are two parameters. If the term $\mu^2 > 0$, this is a mass term and the Lagrangian is already written around the ground state. In the Higgs potential, the term μ^2 is negative. This does not mean that the mass is imaginary, but that the field ϕ does not correspond to the physical particle since it is not in the ground state, located in:

$$\langle |\phi| \rangle = v = \sqrt{\frac{-\mu^2}{2\lambda}}. \quad (\text{A.3})$$

To compute the ground state particles, the field must be written as a real and an imaginary part:

$$\phi = (\phi_1 + i\phi_2)/\sqrt{2}. \quad (\text{A.4})$$

The gauge invariance then let the freedom to choose ϕ as a real scalar field. Moreover, the field must be expressed around the field ground state, meaning that the field ϕ_1 is redefined. The previous transformations can be summarized as:

$$\phi_1 = \sqrt{2}v + h(x), \quad \phi_2 = 0. \quad (\text{A.5})$$

Rewriting Eq. (A.1) and applying the transformations cited above, the Lagrangian becomes:

$$\begin{aligned} \mathcal{L} = & \frac{1}{2} [(\partial_\mu h) (\partial^\mu h) - m_h^2 h^2] \\ & - \frac{1}{4} F_{\mu\nu} F^{\mu\nu} + \frac{1}{2} m_A^2 A_\mu A^\mu \\ & - \sqrt{\frac{\lambda}{2}} m_h h^3 - \frac{\lambda}{4} h^4 + q^2 \frac{m_h}{\sqrt{2\lambda}} A_\mu A^\mu h + \frac{q^2}{2} A_\mu A^\mu h^2, \end{aligned} \quad (\text{A.6})$$

with $m_h = \sqrt{-2\mu} = 2\sqrt{\lambda}v$ and $m_A = |q|m_h/\sqrt{2\lambda}$.

The first line denote the Higgs boson equation and introduces its mass m_h . The strength of this equation is to provide a mass term to the initially massless vector field, as shown on the second line. The third line contains the coupling of the Higgs boson with itself and the vector field.

The Higgs mechanism is very similar to this simplified case. The field in the Higgs mechanism is a doublet $\phi = (\phi_a \ \phi_b)$ and is invariant under $SU(2) \times U(1)$. This implies that the gauge bosons (3 W and one B) will mix to give the 4 physical bosons: 2 W , 1 Z and 1 γ . The masses of the bosons, rising analogously to Eq. (A.6), share relations between the bosons:

$$m_\gamma = 0, \quad \frac{m_W}{m_Z} = \cos(\theta_W), \quad (\text{A.7})$$

where θ_W is the Weinberg angle (or weak mixing angle) measured to be $\sin^2(\theta_W) = 0.23$.

B | Kinematic parameters

Special relativity is a theory developed by Albert Einstein in 1905 in the article "Zur Elektrodynamik bewegter Körper" [226], which replaced Newton's laws of motion. One of the main features of the theory is that the speed of light cannot be exceeded.

Here, we focus on the energy contribution in special relativity. Each particle can be described as a four-vector,

$$E_\mu = \begin{pmatrix} E \\ p_x \\ p_y \\ p_z \end{pmatrix}, \quad (\text{B.1})$$

where $E = \gamma m$, $\vec{p} = \gamma m \vec{v} = p_x \vec{u}_x + p_y \vec{u}_y + p_z \vec{u}_z$, $\gamma = 1/\sqrt{1-v^2}$ and v the velocity of the particle.

This four-vector has two arithmetic properties. First, when several particles are added, each component is simply added, which means,

$$\sum_i E_{\mu,i} = \begin{pmatrix} \sum_i E_i \\ \sum_i p_{x,i} \\ \sum_i p_{y,i} \\ \sum_i p_{z,i} \end{pmatrix}. \quad (\text{B.2})$$

Concerning the scalar product, we use a Minkowski space with a $(+ - - -)$ metric, which means,

$$E_{\mu,1} \cdot E_{\mu,2} = E_1 E_2 - \vec{p}_1 \cdot \vec{p}_2 = E_1 E_2 - p_{x,1} p_{x,2} - p_{y,1} p_{y,2} - p_{z,1} p_{z,2}. \quad (\text{B.3})$$

It is also worth to mention that the invariant mass of a particle is given by the norm defined as

$$m^2 = |E_\mu|^2 = E_\mu \cdot E_\mu = E^2 - \vec{p}^2. \quad (\text{B.4})$$

Collider physics In the case of 2 particles colliding in the center-of-mass frame, we have, by definition of the center-of-mass,

$$\vec{p}_1 + \vec{p}_2 = \vec{0}. \quad (\text{B.5})$$

Therefore, the center-of-mass energy defined by $\sqrt{s} = \sqrt{|E_{\mu,1} + E_{\mu,2}|^2}$ can be expressed as,

$$\sqrt{s} = E_1 + E_2. \quad (\text{B.6})$$

Fixed target experiment The fixed target experiments are defined as having particle 2 at rest in the lab frame, leading to

$$E_{\mu,2} = \begin{pmatrix} m_2 \\ 0 \\ 0 \\ 0 \end{pmatrix}. \quad (\text{B.7})$$

This leads to a center-of-mass energy

$$\sqrt{s} = \sqrt{m_1^2 + m_2^2 + 2E_1 m_2} \underset{E_1 \gg m_1, m_2}{\approx} \sqrt{2E_1 m_2}. \quad (\text{B.8})$$

Final state The center-of-mass energy is often used in final states with the name "invariant mass". This value is very useful in the decaying processes since the invariant mass of all the final particles is equal to the mass of the decaying particle.

$$M_{\text{mother}} = \sqrt{\left| \sum_{\text{daughter}} E_{\mu, \text{daughter}} \right|^2}. \quad (\text{B.9})$$

C | Sanity checks on the correlation factor

In Section 5.4.1, the Z + jets method relies on an estimate of the correlation factor R . Since the correlation factor ($R = 1.30 \pm 0.24$) is estimated in MC to be greater than 1, it seems like there is a correlation between identification and isolation. This could have a physical origin, but this could also come from a bias in the Z + jets MC sample which needs to be excluded to ensure the validity of the Z + jets estimate.

C.1 Using data in non-isolated control region

The MC correlation factor estimate should be cross-checked in data. To do so for the Z + jets while reducing the effect of the signal, new control regions A', B', C' and D' are defined in the region where the photon fails the isolation requirement ($E_T^{cone20} > 0.065 p_T^\gamma + E_{\text{gap}}$). Such a division is shown in Fig. C.1 and the different regions are described below.

- Region A': Photon fulfils the isolation criteria $0.065 p_T^\gamma + 2 \text{ GeV} < E_T^{cone20} < 0.065 p_T^\gamma + 4 \text{ GeV}$ and passes the Tight identification.
- Region B': Photon fulfils the isolation criteria $E_T^{cone20} > 0.065 p_T^\gamma + 4 \text{ GeV}$ and passes the Tight identification.
- Region C': Photon fulfils the isolation criteria $0.065 p_T^\gamma + 2 \text{ GeV} < E_T^{cone20} < 0.065 p_T^\gamma + 4 \text{ GeV}$ and fails the Tight identification.
- Region D': Photon fulfils the isolation criteria $E_T^{cone20} > 0.065 p_T^\gamma + 4 \text{ GeV}$ and fails the Tight identification.

The "new" correlation factor is then defined as:

$$R' = \frac{N_{A'}^{Z+\text{jets}} N_{D'}^{Z+\text{jets}}}{N_{B'}^{Z+\text{jets}} N_{C'}^{Z+\text{jets}}}, \quad (\text{C.1})$$

Even in the non-isolated region, the $Z\gamma$ contribution can not be neglected. The $Z\gamma$ estimate by Sherpa 2.2.11 is subtracted from the data to remove that dependence and create a sample enriched in Z + jets events:

$$N_X^{\text{data, corr}} = N_X^{\text{data}} - N_X^{Z\gamma}, \quad (\text{C.2})$$

where X stands for region A', B', C' or D'.

The resulting correlation factors estimated with data and simulation with statistical uncertainties are given in Table C.1. The value of the correlation factor of the $Z\gamma$ -corrected data and POWHEG are matching within uncertainties, meaning that the generator is reliable in this region. However, the values of the different R' are not matching the correlation factors R used to estimate the Z + jets contribution in the signal region. This is not unexpected since they are estimated in separate regions. However, it emphasizes the need of a check in regions closer to the correlation factor.

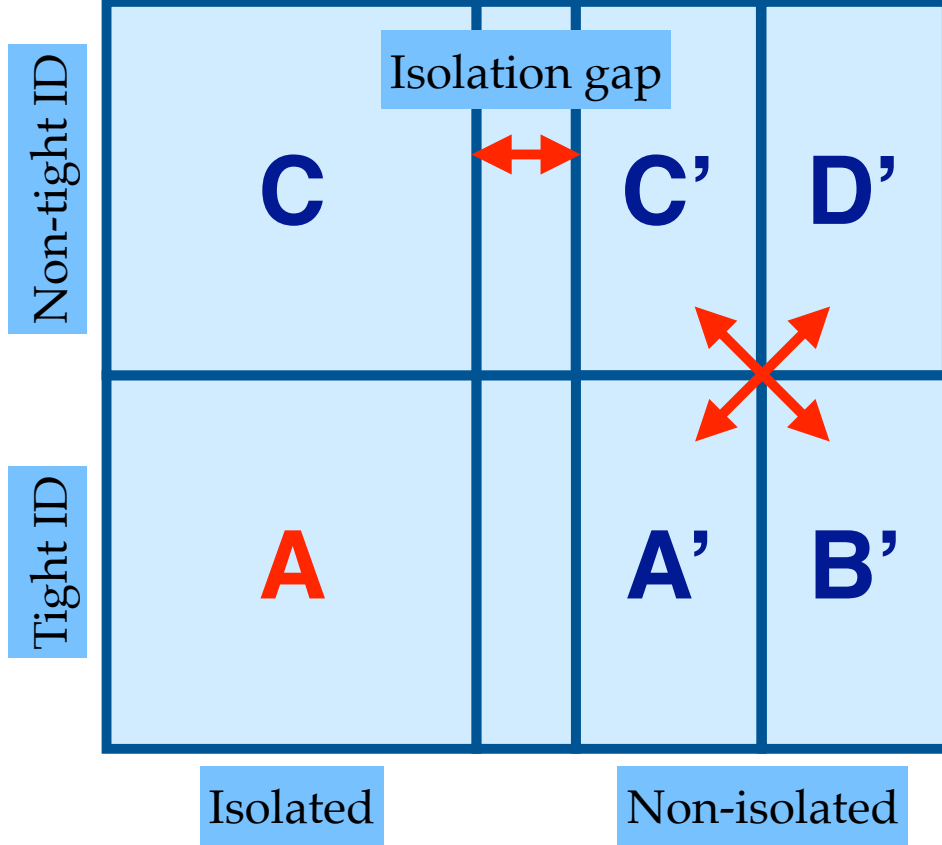


Figure C.1: Representation of the different regions in the sideband method used in the non-isolated region.

C.2 Using events failing the track isolation

Another background enriched region, suited for the computation of the correlation factor in the data, is the region where photons fail the track isolation. In the $Z\gamma$ +jets, to compute the correlation factor, photons are separated depending on their calorimeter isolation and their identification. But they are all required to pass the track isolation criteria $p_T^{cone20} < 0.05 p_T^\gamma$. The region where photons fail the track isolation can then be used as a control region. In this CR, photons are separated in 4 regions A, B, C and D, based on the exact same criteria as in the analysis presented in Section 5.4.1.

Variable	Value
R	1.30 ± 0.04
R'_{POWHEG}	1.08 ± 0.05
R'_{data}	1.19 ± 0.06
$R'_{\text{data, corr}}$	1.00 ± 0.06

Table C.1: Values measured for the correlation factors in the signal region and in the non-isolated control region. The uncertainties indicated here correspond to the statistical uncertainties.

Variable	Value
R	1.30 ± 0.04
$R_{\text{POWHEG}}^{\text{FailTrackIso}}$	1.20 ± 0.02
$R_{\text{data}}^{\text{FailTrackIso}}$	1.46 ± 0.02
$R_{\text{data, corr}}^{\text{FailTrackIso}}$	1.29 ± 0.02

Table C.2: Values measured for the correlation factors in the signal region and in the fail track isolation control region. The uncertainties indicated here correspond to the statistical uncertainties.

Variable	Value
R_{ee}^{POWHEG}	1.27 ± 0.04
R_{ee}^{Sherpa}	1.01 ± 0.28

Table C.3: Values measured for the correlation factors using POWHEG and Sherpa 2.2.1 in the $Z(\rightarrow ee)\gamma$ channel. The uncertainties indicated here correspond to the statistical uncertainties.

Like in the non-isolated control region, the correlation factor can be computed with the data, but is also corrected for the signal leakage in that region (see Eq. (C.2)). The value of the different correlation factors estimated in the baseline region and in the fail track isolation control region are given in Table C.2. Although the results for the corrected data value and the MC estimate in the control region are not perfectly matching, they remain close. More importantly, both are greater than 1, thus favoring the isolation and identification dependency hypothesis over a generator mismodelling.

C.3 Using other generators

If the generator used to estimate the correlation factor for the Z + jets events introduces a bias, it is possible that other generators might not have the same bias. In this case, the correlation factor would be diverging between different generators. The alternative generator Sherpa 2.2.1 was therefore used in the $Z(\rightarrow ee)\gamma$ channel and the results are given in Table C.3. The main issue is the low amount of Z + jets events in Sherpa 2.2.1 leading to a high uncertainty. A definitive interpretation can not be drawn from it, even though the values of the two generators match within uncertainties.

In summary, the different checks give similar values for the MC generator and the data (or a different MC) for the region considered. Moreover, it can be emphasized that the different results for different phase-spaces are different if the statistical uncertainties only are given. Considering the systematic uncertainties on R introduced in Table 5.7 for the POWHEG estimate, even correlation factors from different regions would match with the one used in the Z + jets estimate.

D | Additional plots for the $Z\gamma$ + jets data/SM results

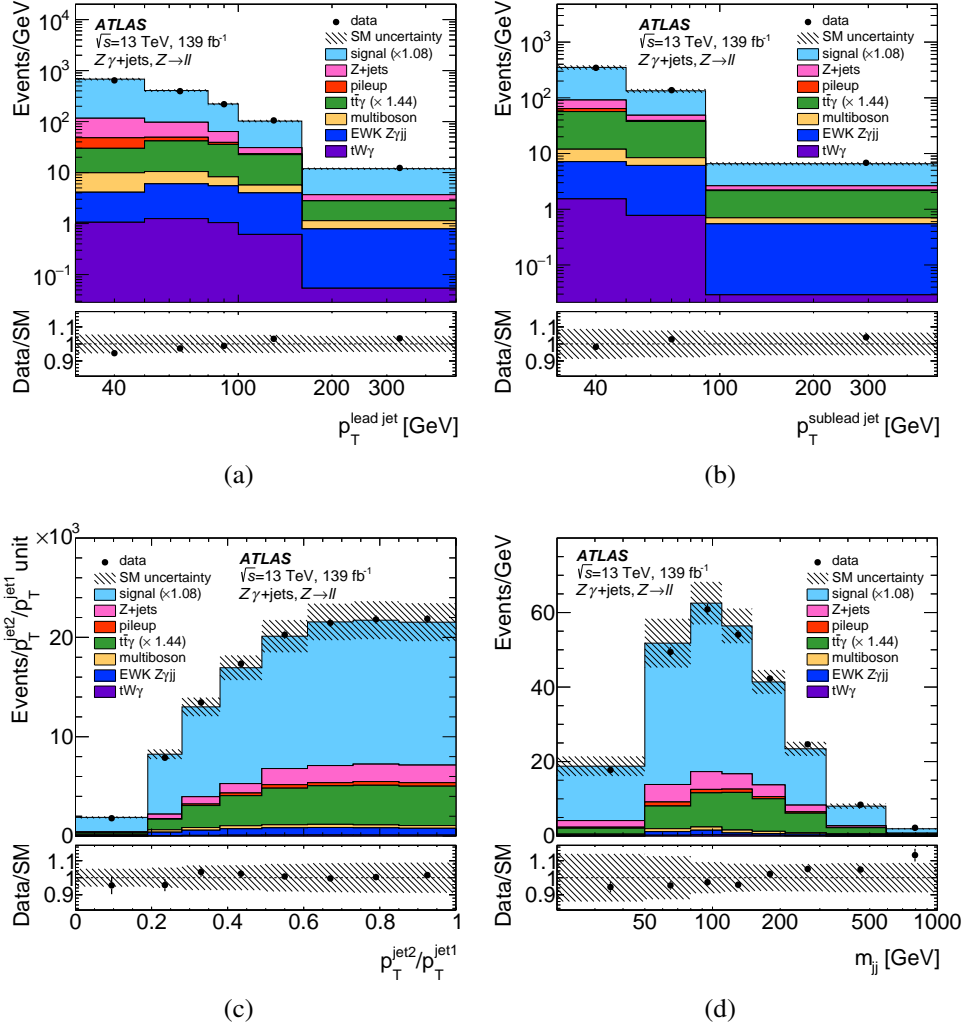


Figure D.1: The measured p_T^{jet1} (a), p_T^{jet2} (b), $p_T^{\text{jet2}}/p_T^{\text{jet1}}$ (c), and m_{jj} (d) yield distributions (dots) in the signal region. The error bars (not visible for most points) represent the data statistical uncertainty. The MC simulation of the signal from Sherpa 2.2.11 (blue histograms) and the estimates of various backgrounds (coloured histograms) are also included. For $tW\gamma$, diboson and $t\bar{t}\gamma$ the background uncertainties are included. The Z+jets systematic uncertainties contain the propagation of the background uncertainties, the E_{gap} and anti-tight criteria, and the generator uncertainty. For the signal, the experimental uncertainties are considered. The lower part of each figure shows the ratio of the data to the expected total SM distribution. The hatched band represents the statistical and systematic uncertainties of the SM background yields added in quadrature.

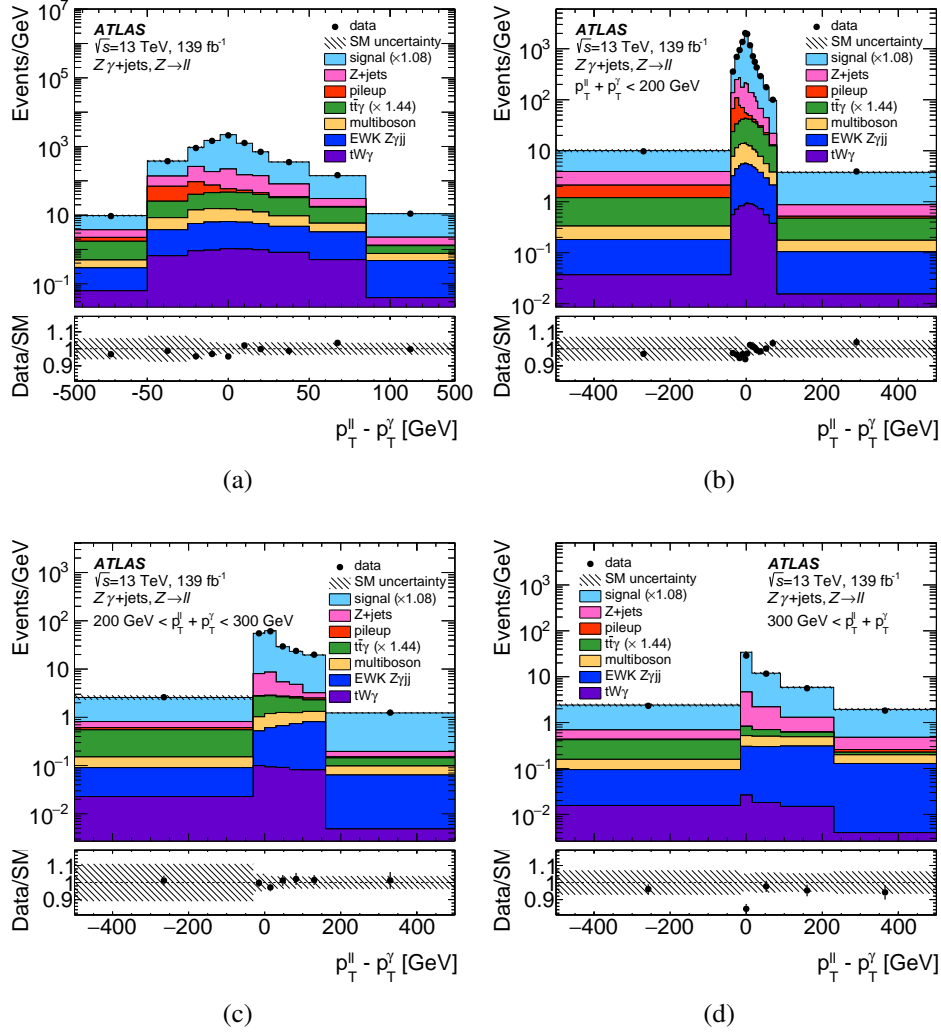


Figure D.2: The measured $p_T^{\ell\ell} - p_T^\gamma$ yield distributions (dots) for the whole $p_T^{\ell\ell} + p_T^\gamma$ range (a), $p_T^{\ell\ell} + p_T^\gamma < 200$ GeV (b), $200 \text{ GeV} < p_T^{\ell\ell} + p_T^\gamma < 300$ GeV (c), and $p_T^{\ell\ell} + p_T^\gamma > 300$ GeV (d) in the signal region. The error bars (not visible for most points) represent the data statistical uncertainty. The MC simulation of the signal from Sherpa 2.2.11 (blue histograms) and the estimates of various backgrounds (coloured histograms) are also included. For $t\bar{t}\gamma$, diboson and $t\bar{t}\gamma$ the background uncertainties are included. The Z + jets systematic uncertainties contain the propagation of the background uncertainties, the E_{gap} and anti-tight criteria, and the generator uncertainty. For the signal, the experimental uncertainties are considered. The lower part of each figure shows the ratio of the data to the expected total SM distribution. The hatched band represents the statistical and systematic uncertainties of the SM background yields added in quadrature.

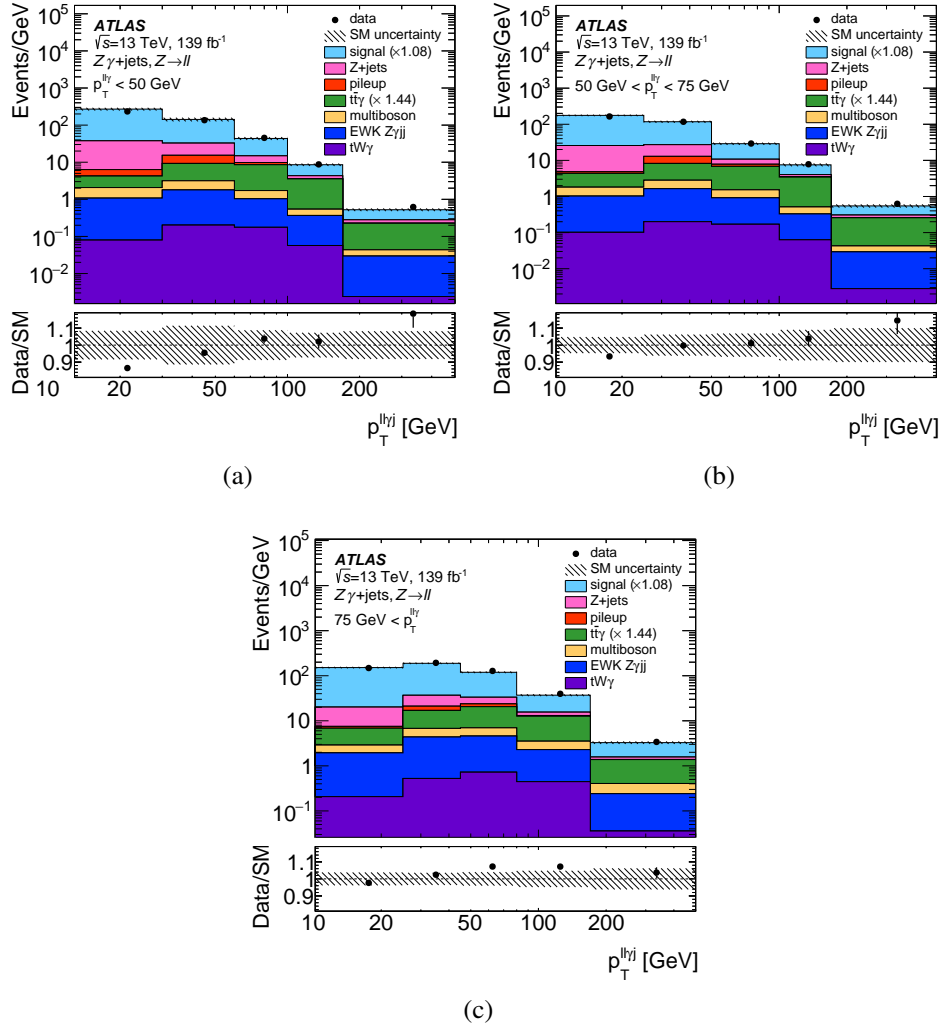


Figure D.3: The measured $p_T^{\ell\ell\gamma j}$ yield distributions (dots) for $p_T^{\ell\ell\gamma} < 50\text{ GeV}$ (a), $50\text{ GeV} < p_T^{\ell\ell\gamma} < 75\text{ GeV}$ (b), and $p_T^{\ell\ell\gamma} > 75\text{ GeV}$ (c) in the signal region. The error bars (not visible for most points) represent the data statistical uncertainty. The MC simulation of the signal from Sherpa 2.2.11 (blue histograms) and the estimates of various backgrounds (coloured histograms) are also included. For $tW\gamma$, diboson and $t\bar{t}\gamma$ the background uncertainties are included. The Z +jets systematic uncertainties contain the propagation of the background uncertainties, the E_{gap} and anti-tight criteria, and the generator uncertainty. For the signal, the experimental uncertainties are considered. The lower part of each figure shows the ratio of the data to the expected total SM distribution. The hatched band represents the statistical and systematic uncertainties of the SM background yields added in quadrature.

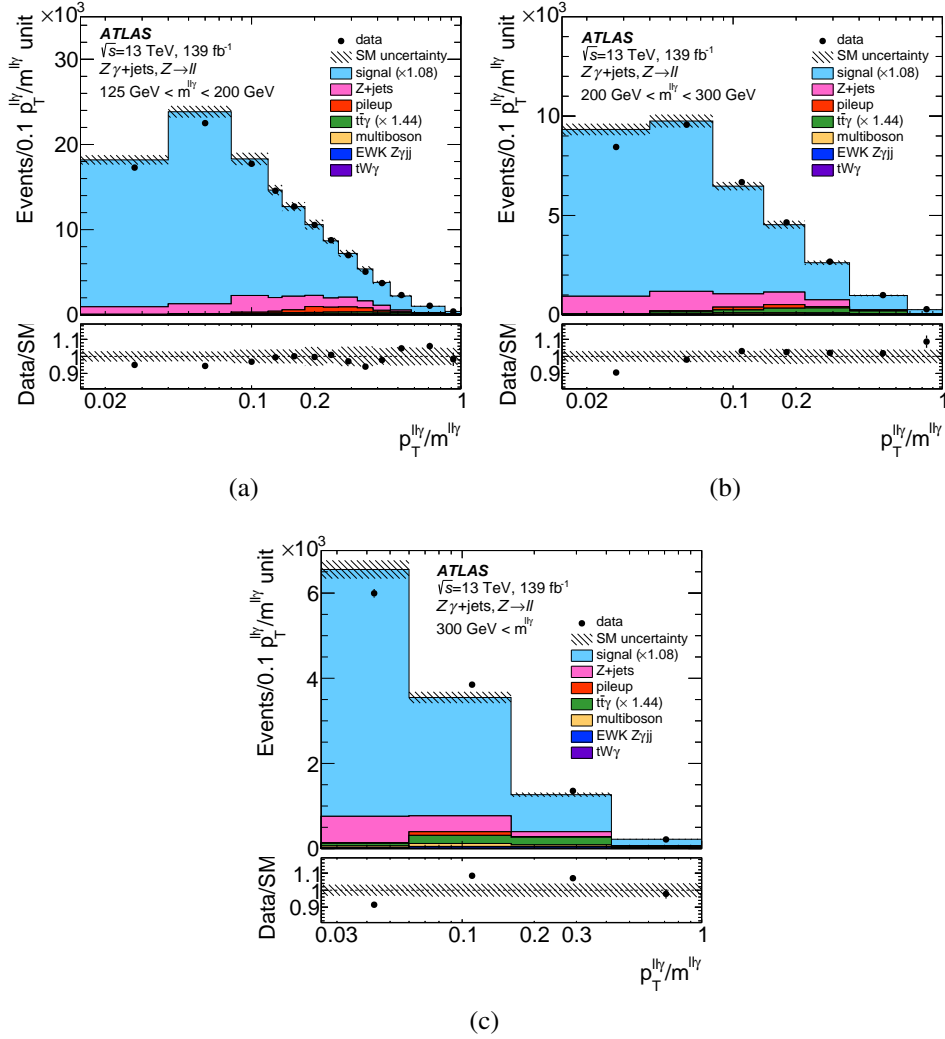


Figure D.4: The measured $p_T^{ll\gamma}/m_{ll\gamma}$ yield distributions (dots) for $125 \text{ GeV} < m_{ll\gamma} < 200 \text{ GeV}$ (a), $200 \text{ GeV} < m_{ll\gamma} < 300 \text{ GeV}$ (b), and $m_{ll\gamma} > 300 \text{ GeV}$ (c) in the signal region. The error bars (not visible for most points) represent the data statistical uncertainty. The MC simulation of the signal from Sherpa 2.2.11 (blue histograms) and the estimates of various backgrounds (coloured histograms) are also included. For $tW\gamma$, diboson and $t\bar{t}\gamma$ the background uncertainties are included. The Z + jets systematic uncertainties contain the propagation of the background uncertainties, the E_{gap} and anti-tight criteria, and the generator uncertainty. For the signal, the experimental uncertainties are considered. The lower part of each figure shows the ratio of the data to the expected total SM distribution. The hatched band represents the statistical and systematic uncertainties of the SM background yields added in quadrature.

E | Additional plots for the unfolded $Z\gamma + \text{jets}$ results

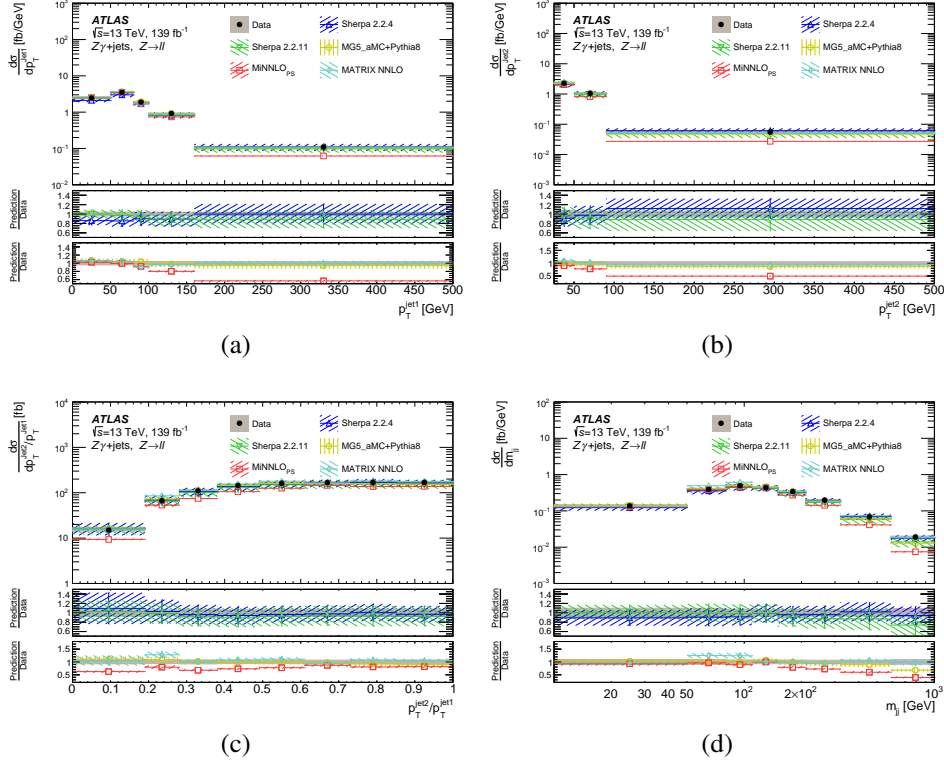


Figure E.1: Measured differential cross-sections (black data points) as a function of the observables $p_T^{\text{jet}1}$ (a), $p_T^{\text{jet}2}$ (b), $p_T^{\text{jet}2}/p_T^{\text{jet}1}$ (c), and m_{jj} (d). Error bars (not visible for most points) on the data points show the statistical uncertainty, while the grey area shows the total uncertainty in the unfolded result. SM predictions include: Sherpa 2.2.4, Sherpa 2.2.11, MadGraph5 (MG5_aMC+Pythia8 in the legend), MiNNLO_{PS}, and MATRIX. Dashed bands represent the statistical uncertainty and theoretical uncertainty on the signal predictions (PDF and scale variations). The bottom panels show the ratio of the SM prediction to the measured cross-sections.

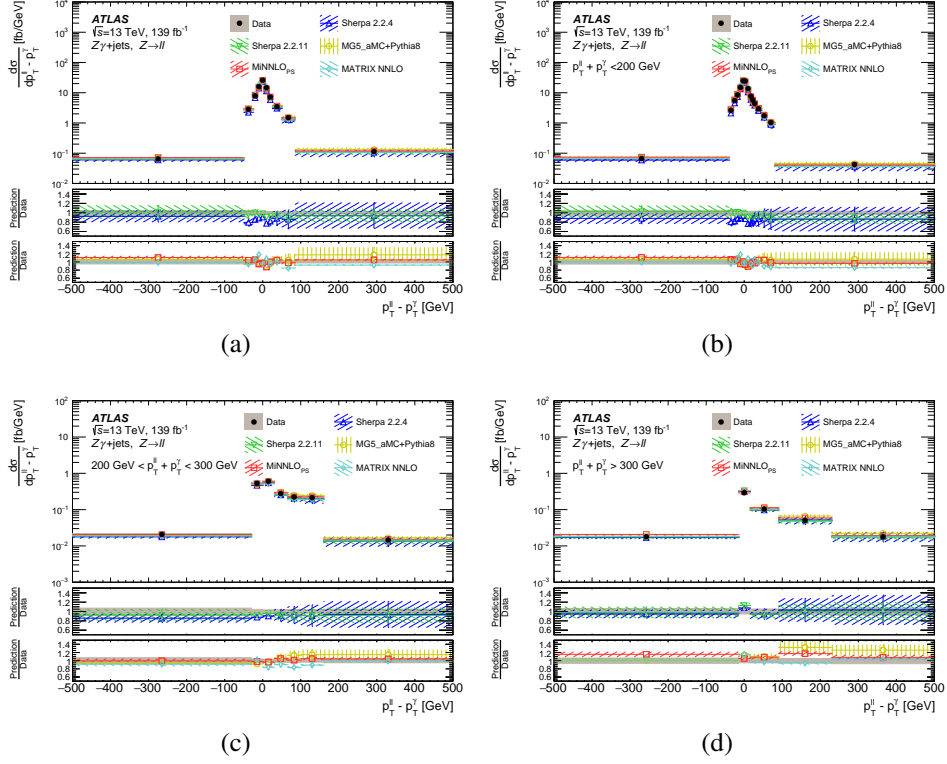


Figure E.2: Measured differential cross-sections (black data points) as a function of the observable $p_T^{\ell\ell} - p_T^{\gamma}$ for the whole $p_T^{\ell\ell} + p_T^{\gamma}$ range (a), $p_T^{\ell\ell} + p_T^{\gamma} < 200\text{ GeV}$ (b), $200\text{ GeV} < p_T^{\ell\ell} + p_T^{\gamma} < 300\text{ GeV}$ (c), and $p_T^{\ell\ell} + p_T^{\gamma} > 300\text{ GeV}$ (d). Error bars (not visible for most points) on the data points show the statistical uncertainty, while the grey area shows the total uncertainty in the unfolded result. SM predictions include: Sherpa 2.2.4, Sherpa 2.2.11, MadGraph5 (MG5_aMC+Pythia8 in the legend), MiNNLO_{PS}, and MATRIX. Dashed bands represent the statistical uncertainty and theoretical uncertainty on the signal predictions (PDF and scale variations). The bottom panels show the ratio of the SM prediction to the measured cross-sections.

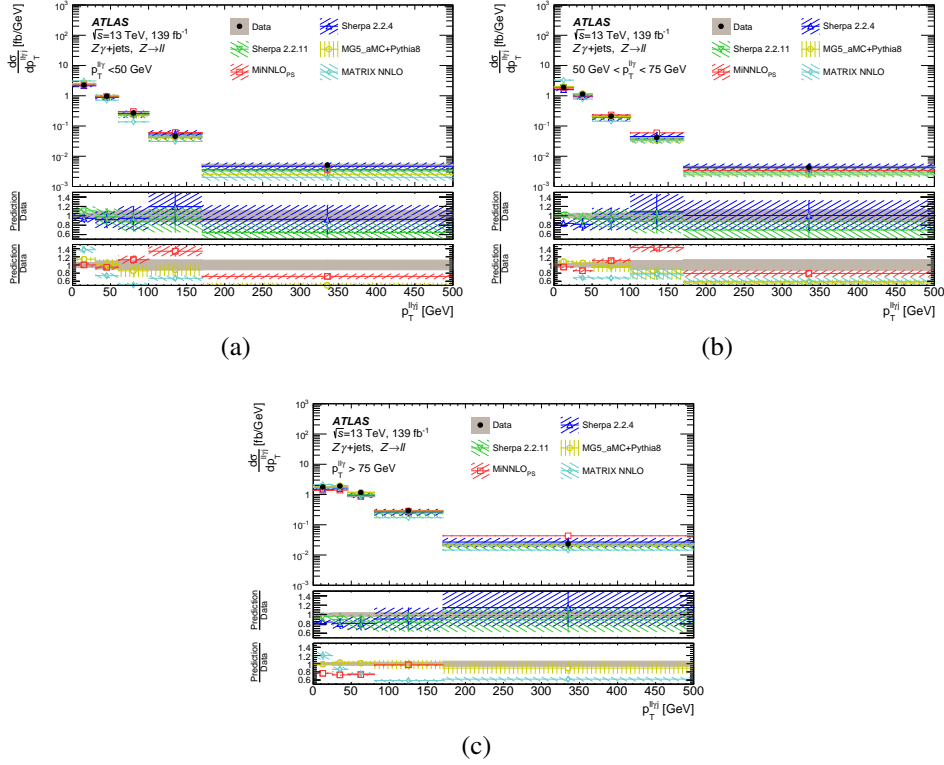


Figure E.3: Measured differential cross-sections (black data points) as a function of the observable $p_T^{\ell\ell\gamma j}$ for $p_T^{\ell\ell\gamma} < 50\text{ GeV}$ (a), $50\text{ GeV} < p_T^{\ell\ell\gamma} < 75\text{ GeV}$ (b), and $p_T^{\ell\ell\gamma} > 75\text{ GeV}$ (c). Error bars (not visible for most points) on the data points show the statistical uncertainty, while the grey area shows the total uncertainty in the unfolded result. SM predictions include: Sherpa 2.2.4, Sherpa 2.2.11, MadGraph5 (MG5_aMC+Pythia8 in the legend), MiNNLO_{PS}, and MATRIX. Dashed bands represent the statistical uncertainty and theoretical uncertainty on the signal predictions (PDF and scale variations). The bottom panels show the ratio of the SM prediction to the measured cross-sections.

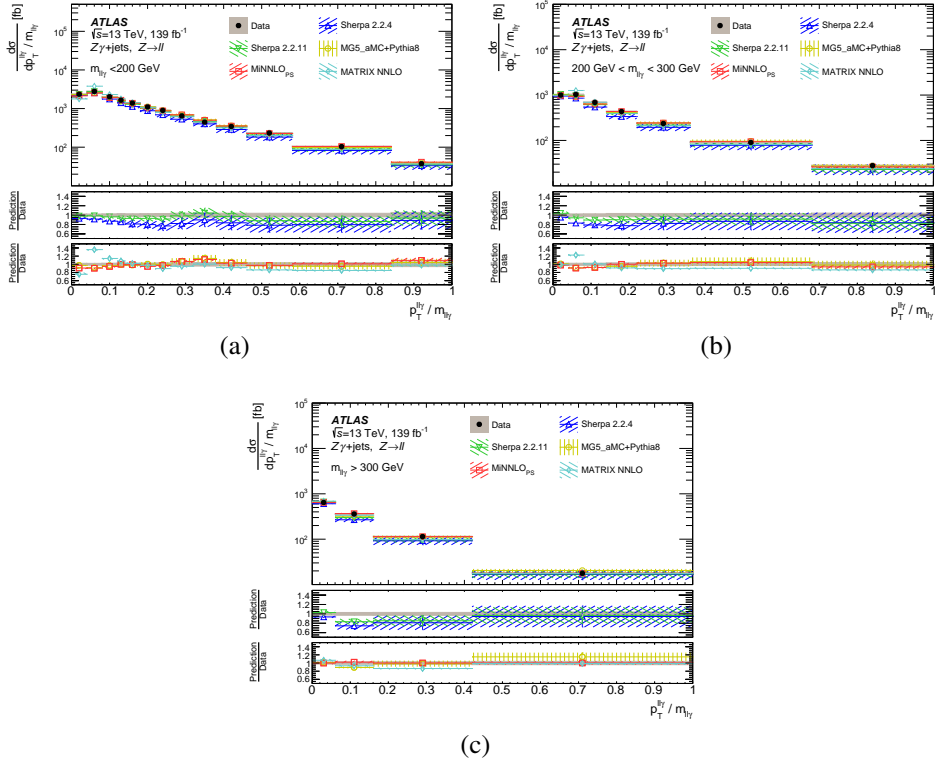


Figure E.4: Measured differential cross-sections (black data points) as a function of the observable $p_T^{ll\gamma}/m_{ll\gamma}$ for $125 \text{ GeV} < m_{ll\gamma} < 200 \text{ GeV}$ (a), $200 \text{ GeV} < m_{ll\gamma} < 300 \text{ GeV}$ (b), and $m_{ll\gamma} > 300 \text{ GeV}$ (c). Error bars (not visible for most points) on the data points show the statistical uncertainty, while the grey area shows the total uncertainty in the unfolded result. SM predictions include: Sherpa 2.2.4, Sherpa 2.2.11, MadGraph5 (MG5_aMC+Pythia8 in the legend), MiNNLO_{PS}, and MATRIX. Dashed bands represent the statistical uncertainty and theoretical uncertainty on the signal predictions (PDF and scale variations). The bottom panels show the ratio of the SM prediction to the measured cross-sections.

Bibliography

- [1] C.C.W.T. Taylor. *The Atomists, Leucippus and Democritus: Fragments : a Text and Translation with a Commentary*. University of Toronto Press, 1999. ISBN: 9780802043900.
- [2] A. Einstein. *Über die von der molekularkinetischen Theorie der Wärme geforderte Bewegung von in ruhenden Flüssigkeiten suspendierten Teilchen*. In: *Annalen der Physik* 322.8 (1905), pp. 549–560. DOI: 10.1002/andp.19053220806.
- [3] Jean Perrin. *Mouvement brownien et grandeurs moléculaires*. In: *Radium (Paris)* 6.12 (1909), pp. 353–360.
- [4] J. J. Thomson. *Cathode rays*. In: *Phil. Mag. Ser. 5* 44 (1897), pp. 293–316. DOI: 10.1080/14786449708621070.
- [5] CMS Collaboration. *Observation of a new boson at a mass of 125 GeV with the CMS experiment at the LHC*. In: *Phys. Lett. B* 716 (2012), p. 30. DOI: 10.1016/j.physletb.2012.08.021. arXiv: 1207.7235 [hep-ex].
- [6] ATLAS Collaboration. *Observation of a new particle in the search for the Standard Model Higgs boson with the ATLAS detector at the LHC*. In: *Phys. Lett. B* 716 (2012), p. 1. DOI: 10.1016/j.physletb.2012.08.020. arXiv: 1207.7214 [hep-ex].
- [7] Planck Collaboration. *Planck 2018 results. VI. Cosmological parameters*. In: *Astron. Astrophys.* 641 (2020). [Erratum: *Astron. Astrophys.* 652, C4 (2021)], A6. DOI: 10.1051/0004-6361/201833910. arXiv: 1807.06209 [astro-ph.CO].
- [8] Michael E. Peskin and Daniel V. Schroeder. *An Introduction to quantum field theory*. Addison-Wesley, 1995. ISBN: 978-0-201-50397-5.
- [9] David Griffiths. *Introduction to elementary particles*. 2008. ISBN: 978-3-527-40601-2.
- [10] Paul Langacker. *The Standard Model and Beyond*. Taylor & Francis, 2017. ISBN: 978-1-4987-6322-6, 978-1-4987-6321-9, 978-0-367-57344-7, 978-1-315-17062-6. DOI: 10.1201/b22175.
- [11] Paul A. M. Dirac. *The quantum theory of the electron*. In: *Proc. Roy. Soc. Lond. A* 117 (1928), pp. 610–624. DOI: 10.1098/rspa.1928.0023.
- [12] F. Englert and R. Brout. *Broken Symmetry and the Mass of Gauge Vector Mesons*. In: *Phys. Rev. Lett.* 13 (1964), pp. 321–323. DOI: 10.1103/PhysRevLett.13.321.
- [13] Peter W. Higgs. *Broken Symmetries and the Masses of Gauge Bosons*. In: *Phys. Rev. Lett.* 13 (1964), pp. 508–509. DOI: 10.1103/PhysRevLett.13.508.
- [14] G. S. Guralnik, C. R. Hagen, and T. W. B. Kibble. *Global Conservation Laws and Massless Particles*. In: *Phys. Rev. Lett.* 13 (1964), pp. 585–587. DOI: 10.1103/PhysRevLett.13.585.
- [15] Chen-Ning Yang and Robert L. Mills. *Conservation of Isotopic Spin and Isotopic Gauge Invariance*. In: *Phys. Rev.* 96 (1954), pp. 191–195. DOI: 10.1103/PhysRev.96.191.

- [16] Oskar Klein. *Quantum Theory and Five-Dimensional Theory of Relativity*. (In German and English). In: *Z. Phys.* 37 (1926), pp. 895–906. DOI: 10.1007/BF01397481.
- [17] Walter Gordon. *Der Comptoneffekt nach der Schrödingerschen Theorie*. In: *Zeitschrift für Physik* 40 (1926), pp. 117–133.
- [18] Alexandru Proca. *Sur la theorie ondulatoire des electrons positifs et negatifs*. In: *J. Phys. Radium* 7 (1936), pp. 347–353. DOI: 10.1051/jphysrad:0193600708034700.
- [19] R. P. Feynman. *The Theory of positrons*. In: *Phys. Rev.* 76 (1949), pp. 749–759. DOI: 10.1103/PhysRev.76.749.
- [20] R. P. Feynman. *Space - time approach to quantum electrodynamics*. In: *Phys. Rev.* 76 (1949), pp. 769–789. DOI: 10.1103/PhysRev.76.769.
- [21] Particle Data Group. *Review of Particle Physics*. In: *PTEP* 2022 (2022), p. 083C01. DOI: 10.1093/ptep/ptac097.
- [22] Cush, Public domain, via Wikimedia Commons. *Standard Model of Elementary Particles*. [Online; accessed 24-March-2022]. 2021. URL: https://commons.wikimedia.org/wiki/File:Standard_Model_of_Elementary_Particles.svg.
- [23] S. H. Neddermeyer and C. D. Anderson. *Note on the Nature of Cosmic Ray Particles*. In: *Phys. Rev.* 51 (1937), pp. 884–886. DOI: 10.1103/PhysRev.51.884.
- [24] J. C. Street and E. C. Stevenson. *New Evidence for the Existence of a Particle of Mass Intermediate Between the Proton and Electron*. In: *Phys. Rev.* 52 (1937), pp. 1003–1004. DOI: 10.1103/PhysRev.52.1003.
- [25] Martin L. Perl et al. *Evidence for Anomalous Lepton Production in $e^+ - e^-$ Annihilation*. In: *Phys. Rev. Lett.* 35 (1975), pp. 1489–1492. DOI: 10.1103/PhysRevLett.35.1489.
- [26] W. Pauli. *Dear radioactive ladies and gentlemen*. In: *Phys. Today* 31N9 (1978), p. 27.
- [27] C. L. Cowan et al. *Detection of the free neutrino: A Confirmation*. In: *Science* 124 (1956), pp. 103–104. DOI: 10.1126/science.124.3212.103.
- [28] G. Danby et al. *Observation of High-Energy Neutrino Reactions and the Existence of Two Kinds of Neutrinos*. In: *Phys. Rev. Lett.* 9 (1962), pp. 36–44. DOI: 10.1103/PhysRevLett.9.36.
- [29] DONUT Collaboration. *Observation of tau neutrino interactions*. In: *Phys. Lett. B* 504 (2001), pp. 218–224. DOI: 10.1016/S0370-2693(01)00307-0. arXiv: hep-ex/0012035.
- [30] Raymond Davis Jr., Don S. Harmer, and Kenneth C. Hoffman. *Search for neutrinos from the sun*. In: *Phys. Rev. Lett.* 20 (1968), pp. 1205–1209. DOI: 10.1103/PhysRevLett.20.1205.
- [31] John N. Bahcall, Neta A. Bahcall, and G. Shaviv. *Present status of the theoretical predictions for the Cl-36 solar neutrino experiment*. In: *Phys. Rev. Lett.* 20 (1968), pp. 1209–1212. DOI: 10.1103/PhysRevLett.20.1209.
- [32] Super-Kamiokande Collaboration. *Evidence for oscillation of atmospheric neutrinos*. In: *Phys. Rev. Lett.* 81 (1998), pp. 1562–1567. DOI: 10.1103/PhysRevLett.81.1562. arXiv: hep-ex/9807003.

- [33] SNO Collaboration. *Direct evidence for neutrino flavor transformation from neutral current interactions in the Sudbury Neutrino Observatory*. In: *Phys. Rev. Lett.* 89 (2002), p. 011301. DOI: 10.1103/PhysRevLett.89.011301. arXiv: nucl-ex/0204008.
- [34] KATRIN Collaboration. *Direct neutrino-mass measurement with sub-electronvolt sensitivity*. In: *Nature Phys.* 18.2 (2022), pp. 160–166. DOI: 10.1038/s41567-021-01463-1. arXiv: 2105.08533 [hep-ex].
- [35] Eleonora Di Valentino and Alessandro Melchiorri. *Neutrino Mass Bounds in the Era of Tension Cosmology*. In: *Astrophys. J. Lett.* 931.2 (2022), p. L18. DOI: 10.3847/2041-8213/ac6ef5. arXiv: 2112.02993 [astro-ph.CO].
- [36] J. R. Oppenheimer et al. *Theoretical interpretation of new particles*. In: *6th Annual Rochester Conference on High energy nuclear physics*. 1956, pp. VIII.1–36.
- [37] Murray Gell-Mann. *The Eightfold Way: A Theory of strong interaction symmetry*. In: (1961). DOI: 10.2172/4008239.
- [38] Murray Gell-Mann. *A Schematic Model of Baryons and Mesons*. In: *Phys. Lett.* 8 (1964), pp. 214–215. DOI: 10.1016/S0031-9163(64)92001-3.
- [39] G. Zweig. *An SU(3) model for strong interaction symmetry and its breaking. Version 1*. In: (1964).
- [40] G. Zweig. *An SU(3) model for strong interaction symmetry and its breaking. Version 2*. In: *DEVELOPMENTS IN THE QUARK THEORY OF HADRONS. VOL. 1. 1964 - 1978*. Ed. by D. B. Lichtenberg and Simon Peter Rosen. 1964, pp. 22–101.
- [41] Elliott D. Bloom et al. *High-Energy Inelastic $e p$ Scattering at 6-Degrees and 10-Degrees*. In: *Phys. Rev. Lett.* 23 (1969), pp. 930–934. DOI: 10.1103/PhysRevLett.23.930.
- [42] Martin Breidenbach et al. *Observed behavior of highly inelastic electron-proton scattering*. In: *Phys. Rev. Lett.* 23 (1969), pp. 935–939. DOI: 10.1103/PhysRevLett.23.935.
- [43] E598 Collaboration. *Experimental Observation of a Heavy Particle J*. In: *Phys. Rev. Lett.* 33 (1974), pp. 1404–1406. DOI: 10.1103/PhysRevLett.33.1404.
- [44] SLAC-SP-017 Collaboration. *Discovery of a Narrow Resonance in e^+e^- Annihilation*. In: *Phys. Rev. Lett.* 33 (1974), pp. 1406–1408. DOI: 10.1103/PhysRevLett.33.1406.
- [45] E. Eichten et al. *Charmonium: The Model*. In: *Phys. Rev. D* 17 (1978). [Erratum: *Phys.Rev.D* 21, 313 (1980)], p. 3090. DOI: 10.1103/PhysRevD.17.3090.
- [46] E288 Collaboration. *Observation of a Dimuon Resonance at 9.5-GeV in 400-GeV Proton-Nucleus Collisions*. In: *Phys. Rev. Lett.* 39 (1977), pp. 252–255. DOI: 10.1103/PhysRevLett.39.252.
- [47] CDF Collaboration. *Observation of top quark production in $\bar{p}p$ collisions*. In: *Phys. Rev. Lett.* 74 (1995), pp. 2626–2631. DOI: 10.1103/PhysRevLett.74.2626. arXiv: hep-ex/9503002.
- [48] D0 Collaboration. *Observation of the top quark*. In: *Phys. Rev. Lett.* 74 (1995), pp. 2632–2637. DOI: 10.1103/PhysRevLett.74.2632. arXiv: hep-ex/9503003.
- [49] Max Planck. *On the Law of Distribution of Energy in the Normal Spectrum*. In: *Annalen Phys.* 4 (1901), p. 553.

- [50] Albert Einstein. *Concerning an heuristic point of view toward the emission and transformation of light*. In: *Annalen Phys.* 17 (1905), pp. 132–148.
- [51] Steven Weinberg. *A Model of Leptons*. In: *Phys. Rev. Lett.* 19 (1967), pp. 1264–1266. DOI: 10.1103/PhysRevLett.19.1264.
- [52] Nicola Cabibbo. *Unitary Symmetry and Leptonic Decays*. In: *Phys. Rev. Lett.* 10 (1963), pp. 531–533. DOI: 10.1103/PhysRevLett.10.531.
- [53] Makoto Kobayashi and Toshihide Maskawa. *CP Violation in the Renormalizable Theory of Weak Interaction*. In: *Prog. Theor. Phys.* 49 (1973), pp. 652–657. DOI: 10.1143/PTP.49.652.
- [54] A. I. Alikhanov et al. *Measuring of the Chirality of the μ Meson*. In: *J. Exp. Theor. Phys.* 38 (1960), pp. 1918–1920.
- [55] G. Backenstoss et al. *Helicity of μ^- Mesons from π -Meson Decay*. In: *Phys. Rev. Lett.* 6 (1961), pp. 415–416. DOI: 10.1103/PhysRevLett.6.415.
- [56] PLUTO Collaboration. *Evidence for Gluon Bremsstrahlung in e^+e^- Annihilations at High-Energies*. In: *Phys. Lett. B* 86 (1979), pp. 418–425. DOI: 10.1016/0370-2693(79)90869-4.
- [57] Dmitri Denisov and Costas Vellidis. *Tevatron greatest hits*. In: *Rept. Prog. Phys.* 85.11 (2022), p. 116201. DOI: 10.1088/1361-6633/ac8e81. arXiv: 2210.13565 [hep-ex].
- [58] ALEPH-DELPHI-L3-OPAL-LEP Electroweak Working Group. *A Combination of preliminary electroweak measurements and constraints on the standard model*. In: (2006). arXiv: hep-ex/0612034.
- [59] ATLAS Collaboration. *Measurement of the W^+W^- production cross section in pp collisions at a centre-of-mass energy of $\sqrt{s} = 13$ TeV with the ATLAS experiment*. In: *Phys. Lett. B* 773 (2017), p. 354. DOI: 10.1016/j.physletb.2017.08.047. arXiv: 1702.04519 [hep-ex].
- [60] ATLAS Collaboration. *Measurement of fiducial and differential W^+W^- production cross-sections at $\sqrt{s} = 13$ TeV with the ATLAS detector*. In: *Eur. Phys. J. C* 79 (2019), p. 884. DOI: 10.1140/epjc/s10052-019-7371-6. arXiv: 1905.04242 [hep-ex].
- [61] ATLAS Collaboration. *Observation of Electroweak Production of a Same-Sign W Boson Pair in Association with Two Jets in pp Collisions at $\sqrt{s} = 13$ TeV with the ATLAS Detector*. In: *Phys. Rev. Lett.* 123 (2019), p. 161801. DOI: 10.1103/PhysRevLett.123.161801. arXiv: 1906.03203 [hep-ex].
- [62] ATLAS Collaboration. *Measurements of $W^+W^- + \geq 1$ jet production cross-sections in pp collisions at $\sqrt{s} = 13$ TeV with the ATLAS detector*. In: *JHEP* 06 (2021), p. 003. DOI: 10.1007/JHEP06(2021)003. arXiv: 2103.10319 [hep-ex].
- [63] ATLAS Collaboration. *Observation of photon-induced W^+W^- production in pp collisions at $\sqrt{s} = 13$ TeV using the ATLAS detector*. In: *Phys. Lett. B* 816 (2021), p. 136190. DOI: 10.1016/j.physletb.2021.136190. arXiv: 2010.04019 [hep-ex].
- [64] ATLAS Collaboration. *Measurement of the ZZ Production Cross Section in pp Collisions at $\sqrt{s} = 13$ TeV with the ATLAS Detector*. In: *Phys. Rev. Lett.* 116 (2016), p. 101801. DOI: 10.1103/PhysRevLett.116.101801. arXiv: 1512.05314 [hep-ex].

- [65] ATLAS Collaboration. *ZZ* $\rightarrow \ell^+ \ell^- \ell'^+ \ell'^-$ cross-section measurements and search for anomalous triple gauge couplings in 13 TeV pp collisions with the ATLAS detector. In: *Phys. Rev. D* 97 (2018), p. 032005. DOI: 10.1103/PhysRevD.97.032005. arXiv: 1709.07703 [hep-ex].
- [66] ATLAS Collaboration. *Measurement of ZZ production in the $\ell\ell\nu\nu$ final state with the ATLAS detector in pp collisions at $\sqrt{s} = 13$ TeV.* In: *JHEP* 10 (2019), p. 127. DOI: 10.1007/JHEP10(2019)127. arXiv: 1905.07163 [hep-ex].
- [67] ATLAS Collaboration. *Observation of electroweak production of two jets and a Z-boson pair.* In: *Nature Phys.* 19 (2023), pp. 237–253. DOI: 10.1038/s41567-022-01757-y. arXiv: 2004.10612 [hep-ex].
- [68] ATLAS Collaboration. *Measurement of the $W^\pm Z$ boson pair-production cross section in pp collisions at $\sqrt{s} = 13$ TeV with the ATLAS Detector.* In: *Phys. Lett. B* 762 (2016), p. 1. DOI: 10.1016/j.physletb.2016.08.052. arXiv: 1606.04017 [hep-ex].
- [69] ATLAS Collaboration. *Observation of electroweak $W^\pm Z$ boson pair production in association with two jets in pp collisions at $\sqrt{s} = 13$ TeV with the ATLAS detector.* In: *Phys. Lett. B* 793 (2019), p. 469. DOI: 10.1016/j.physletb.2019.05.012. arXiv: 1812.09740 [hep-ex].
- [70] ATLAS Collaboration. *Measurement of $W^\pm Z$ production cross sections and gauge boson polarisation in pp collisions at $\sqrt{s} = 13$ TeV with the ATLAS detector.* In: *Eur. Phys. J. C* 79 (2019), p. 535. DOI: 10.1140/epjc/s10052-019-7027-6. arXiv: 1902.05759 [hep-ex].
- [71] ATLAS Collaboration. *Measurement of the $Z\gamma \rightarrow \nu\bar{\nu}\gamma$ production cross section in pp collisions at $\sqrt{s} = 13$ TeV with the ATLAS detector and limits on anomalous triple gauge-boson couplings.* In: *JHEP* 12 (2018), p. 010. DOI: 10.1007/JHEP12(2018)010. arXiv: 1810.04995 [hep-ex].
- [72] ATLAS Collaboration. *Measurement of the $Z(\rightarrow \ell^+ \ell^-)\gamma$ production cross-section in pp collisions at $\sqrt{s} = 13$ TeV with the ATLAS detector.* In: *JHEP* 03 (2020), p. 054. DOI: 10.1007/JHEP03(2020)054. arXiv: 1911.04813 [hep-ex].
- [73] ATLAS Collaboration. *Evidence for electroweak production of two jets in association with a $Z\gamma$ pair in pp collisions at $\sqrt{s} = 13$ TeV with the ATLAS detector.* In: *Phys. Lett. B* 803 (2020), p. 135341. DOI: 10.1016/j.physletb.2020.135341. arXiv: 1910.09503 [hep-ex].
- [74] ATLAS Collaboration. *Measurement of the jet mass in high transverse momentum $Z(\rightarrow b\bar{b})\gamma$ production at $\sqrt{s} = 13$ TeV using the ATLAS detector.* In: *Phys. Lett. B* 812 (2021), p. 135991. DOI: 10.1016/j.physletb.2020.135991. arXiv: 1907.07093 [hep-ex].
- [75] ATLAS Collaboration. *Search for the electroweak diboson production in association with a high-mass dijet system in semileptonic final states in pp collisions at $\sqrt{s} = 13$ TeV with the ATLAS detector.* In: *Phys. Rev. D* 100 (2019), p. 032007. DOI: 10.1103/PhysRevD.100.032007. arXiv: 1905.07714 [hep-ex].
- [76] ATLAS Collaboration. *Standard Model Summary Plots February 2022.* In: (2022).
- [77] Yee Chinn Yap. *Recent observation and measurements of diboson processes from the ATLAS experiment.* In: *Mod. Phys. Lett. A* 35.28 (2020), p. 2030013. DOI: 10.1142/S021773232030013X. arXiv: 2006.08285 [hep-ex].

- [78] CMS Collaboration. *Measurement of WW production rate*. Tech. rep. 2012. URL: <https://cds.cern.ch/record/1460099>.
- [79] ATLAS Collaboration. *Measurement of total and differential W^+W^- production cross sections in proton–proton collisions at $\sqrt{s} = 8\text{ TeV}$ with the ATLAS detector and limits on anomalous triple-gauge-boson couplings*. In: *JHEP* 09 (2016), p. 029. DOI: 10.1007/JHEP09(2016)029. arXiv: 1603.01702 [hep-ex].
- [80] T. Gehrmann et al. *W^+W^- Production at Hadron Colliders in Next to Next to Leading Order QCD*. In: *Phys. Rev. Lett.* 113.21 (2014), p. 212001. DOI: 10.1103/PhysRevLett.113.212001. arXiv: 1408.5243 [hep-ph].
- [81] U. Baur and David L. Rainwater. *Probing neutral gauge boson selfinteractions in ZZ production at hadron colliders*. In: *Phys. Rev. D* 62 (2000), p. 113011. DOI: 10.1103/PhysRevD.62.113011. arXiv: hep-ph/0008063.
- [82] G. J. Gounaris, J. Layssac, and F. M. Renard. *New and standard physics contributions to anomalous Z and gamma selfcouplings*. In: *Phys. Rev. D* 62 (2000), p. 073013. DOI: 10.1103/PhysRevD.62.073013. arXiv: hep-ph/0003143.
- [83] CMS Collaboration. *A measurement of the Higgs boson mass in the diphoton decay channel*. In: *Phys. Lett. B* 805 (2020), p. 135425. DOI: 10.1016/j.physletb.2020.135425. arXiv: 2002.06398 [hep-ex].
- [84] ATLAS Collaboration. *Measurement of the Higgs boson mass in the $H \rightarrow ZZ^* \rightarrow 4\ell$ and $H \rightarrow \gamma\gamma$ channels with $\sqrt{s} = 13\text{ TeV}$ pp collisions using the ATLAS detector*. In: *Phys. Lett. B* 784 (2018), p. 345. DOI: 10.1016/j.physletb.2018.07.050. arXiv: 1806.00242 [hep-ex].
- [85] Benjamin W. Lee, C. Quigg, and H. B. Thacker. *The Strength of Weak Interactions at Very High-Energies and the Higgs Boson Mass*. In: *Phys. Rev. Lett.* 38 (1977), pp. 883–885. DOI: 10.1103/PhysRevLett.38.883.
- [86] K. Becker, M. Becker, and J. H. Schwarz. *String theory and M-theory: A modern introduction*. Cambridge University Press, 2006. ISBN: 978-0-511-25486-4, 978-0-521-86069-7, 978-0-511-81608-6. DOI: 10.1017/CBO9780511816086.
- [87] Rodolfo Gambini and Jorge Pullin. *A first course in loop quantum gravity*. 2011.
- [88] Stephen P. Martin. *A Supersymmetry primer*. In: *Adv. Ser. Direct. High Energy Phys.* 18 (1998), pp. 1–98. DOI: 10.1142/9789812839657_0001. arXiv: hep-ph/9709356.
- [89] Gianfranco Bertone and Dan Hooper. *History of dark matter*. In: *Rev. Mod. Phys.* 90.4 (2018), p. 045002. DOI: 10.1103/RevModPhys.90.045002. arXiv: 1605.04909 [astro-ph.CO].
- [90] Supernova Search Team. *Observational evidence from supernovae for an accelerating universe and a cosmological constant*. In: *Astron. J.* 116 (1998), pp. 1009–1038. DOI: 10.1086/300499. arXiv: astro-ph/9805201.
- [91] Supernova Cosmology Project. *Measurements of Ω and Λ from 42 high redshift supernovae*. In: *Astrophys. J.* 517 (1999), pp. 565–586. DOI: 10.1086/307221. arXiv: astro-ph/9812133.
- [92] Joshua Frieman, Michael Turner, and Dragan Huterer. *Dark Energy and the Accelerating Universe*. In: *Ann. Rev. Astron. Astrophys.* 46 (2008), pp. 385–432. DOI: 10.1146/annurev.astro.46.060407.145243. arXiv: 0803.0982 [astro-ph].

- [93] Muon g-2 Collaboration. *Measurement of the Positive Muon Anomalous Magnetic Moment to 0.46 ppm*. In: *Phys. Rev. Lett.* 126.14 (2021), p. 141801. DOI: 10.1103/PhysRevLett.126.141801. arXiv: 2104.03281 [hep-ex].
- [94] Sz. Borsanyi et al. *Leading hadronic contribution to the muon magnetic moment from lattice QCD*. In: *Nature* 593.7857 (2021), pp. 51–55. DOI: 10.1038/s41586-021-03418-1. arXiv: 2002.12347 [hep-lat].
- [95] Muon g-2 Collaboration. *Final Report of the Muon E821 Anomalous Magnetic Moment Measurement at BNL*. In: *Phys. Rev. D* 73 (2006), p. 072003. DOI: 10.1103/PhysRevD.73.072003. arXiv: hep-ex/0602035.
- [96] T. Aoyama et al. *The anomalous magnetic moment of the muon in the Standard Model*. In: *Phys. Rept.* 887 (2020), pp. 1–166. DOI: 10.1016/j.physrep.2020.07.006. arXiv: 2006.04822 [hep-ph].
- [97] MUonE Collaboration. *Status of the MUonE experiment*. In: *PoS EPS-HEP2021* (2022), p. 642. DOI: 10.22323/1.398.0642.
- [98] Gerard 't Hooft. *Symmetry Breaking Through Bell-Jackiw Anomalies*. In: *Phys. Rev. Lett.* 37 (1976), pp. 8–11. DOI: 10.1103/PhysRevLett.37.8.
- [99] Maxim Pospelov and Adam Ritz. *Theta vacua, QCD sum rules, and the neutron electric dipole moment*. In: *Nucl. Phys. B* 573 (2000), pp. 177–200. DOI: 10.1016/S0550-3213(99)00817-2. arXiv: hep-ph/9908508.
- [100] C. Abel et al. *Measurement of the Permanent Electric Dipole Moment of the Neutron*. In: *Phys. Rev. Lett.* 124.8 (2020), p. 081803. DOI: 10.1103/PhysRevLett.124.081803. arXiv: 2001.11966 [hep-ex].
- [101] R. D. Peccei and Helen R. Quinn. *CP Conservation in the Presence of Instantons*. In: *Phys. Rev. Lett.* 38 (1977), pp. 1440–1443. DOI: 10.1103/PhysRevLett.38.1440.
- [102] R. D. Peccei and Helen R. Quinn. *Constraints Imposed by CP Conservation in the Presence of Instantons*. In: *Phys. Rev. D* 16 (1977), pp. 1791–1797. DOI: 10.1103/PhysRevD.16.1791.
- [103] G. Alonso-Álvarez, M. B. Gavela, and P. Quilez. *Axion couplings to electroweak gauge bosons*. In: *Eur. Phys. J. C* 79.3 (2019), p. 223. DOI: 10.1140/epjc/s10052-019-6732-5. arXiv: 1811.05466 [hep-ph].
- [104] Giovanni Grilli di Cortona et al. *The QCD axion, precisely*. In: *JHEP* 01 (2016), p. 034. DOI: 10.1007/JHEP01(2016)034. arXiv: 1511.02867 [hep-ph].
- [105] Michael Dine, Willy Fischler, and Mark Srednicki. *A Simple Solution to the Strong CP Problem with a Harmless Axion*. In: *Phys. Lett. B* 104 (1981), pp. 199–202. DOI: 10.1016/0370-2693(81)90590-6.
- [106] A. R. Zhitnitsky. *On Possible Suppression of the Axion Hadron Interactions. (In Russian)*. In: *Sov. J. Nucl. Phys.* 31 (1980), p. 260.
- [107] Jihn E. Kim. *Weak Interaction Singlet and Strong CP Invariance*. In: *Phys. Rev. Lett.* 43 (1979), p. 103. DOI: 10.1103/PhysRevLett.43.103.
- [108] Mikhail A. Shifman, A. I. Vainshtein, and Valentin I. Zakharov. *Can Confinement Ensure Natural CP Invariance of Strong Interactions?* In: *Nucl. Phys. B* 166 (1980), pp. 493–506. DOI: 10.1016/0550-3213(80)90209-6.

- [109] Luca Di Luzio et al. *The landscape of QCD axion models*. In: *Phys. Rept.* 870 (2020), pp. 1–117. DOI: 10.1016/j.physrep.2020.06.002. arXiv: 2003.01100 [hep-ph].
- [110] Joerg Jaeckel and Andreas Ringwald. *The Low-Energy Frontier of Particle Physics*. In: *Ann. Rev. Nucl. Part. Sci.* 60 (2010), pp. 405–437. DOI: 10.1146/annurev.nucl.012809.104433. arXiv: 1002.0329 [hep-ph].
- [111] Malte Buschmann, Joshua W. Foster, and Benjamin R. Safdi. *Early-Universe Simulations of the Cosmological Axion*. In: *Phys. Rev. Lett.* 124.16 (2020), p. 161103. DOI: 10.1103/PhysRevLett.124.161103. arXiv: 1906.00967 [astro-ph.CO].
- [112] L. Visinelli and P. Gondolo. *Axion cold dark matter in view of BICEP2 results*. In: *Phys. Rev. Lett.* 113 (2014), p. 011802. DOI: 10.1103/PhysRevLett.113.011802. arXiv: 1403.4594 [hep-ph].
- [113] Adrian Ayala et al. *Revisiting the bound on axion-photon coupling from Globular Clusters*. In: *Phys. Rev. Lett.* 113.19 (2014), p. 191302. DOI: 10.1103/PhysRevLett.113.191302. arXiv: 1406.6053 [astro-ph.SR].
- [114] Yifan Chen et al. *Stringent axion constraints with Event Horizon Telescope polarimetric measurements of M87**. In: *Nature Astron.* 6.5 (2022), pp. 592–598. DOI: 10.1038/s41550-022-01620-3. arXiv: 2105.04572 [hep-ph].
- [115] Daniel Heuchel, Axel Lindner, and Isabella Oceano. *The DESY axion search program*. In: *Workshop on Feebly-Interacting Particles*. 2023. arXiv: 2302.11934 [hep-ex].
- [116] Robin Bähre et al. *Any light particle search II —Technical Design Report*. In: *JINST* 8 (2013), T09001. DOI: 10.1088/1748-0221/8/09/T09001. arXiv: 1302.5647 [physics.ins-det].
- [117] IAXO Collaboration. *Conceptual design of BabyIAXO, the intermediate stage towards the International Axion Observatory*. In: *JHEP* 05 (2021), p. 137. DOI: 10.1007/JHEP05(2021)137. arXiv: 2010.12076 [physics.ins-det].
- [118] E. Armengaud et al. *Conceptual Design of the International Axion Observatory (IAXO)*. In: *JINST* 9 (2014), T05002. DOI: 10.1088/1748-0221/9/05/T05002. arXiv: 1401.3233 [physics.ins-det].
- [119] MADMAX Working Group. *Dielectric Haloscopes: A New Way to Detect Axion Dark Matter*. In: *Phys. Rev. Lett.* 118.9 (2017), p. 091801. DOI: 10.1103/PhysRevLett.118.091801. arXiv: 1611.05865 [physics.ins-det].
- [120] MADMAX Collaboration. *A new experimental approach to probe QCD axion dark matter in the mass range above 40 μeV* . In: *Eur. Phys. J. C* 79.3 (2019), p. 186. DOI: 10.1140/epjc/s10052-019-6683-x. arXiv: 1901.07401 [physics.ins-det].
- [121] ATLAS-CMS-TOTEM Collaborations. *Searches for Axion Like Particles at the LHC*. In: *PoS LHCP2021* (2021), p. 005. DOI: 10.22323/1.397.0005.
- [122] ATLAS Collaboration. *Measurement of light-by-light scattering and search for axion-like particles with 2.2nb^{-1} of Pb+Pb data with the ATLAS detector*. In: *JHEP* 03 (2021), p. 243. DOI: 10.1007/JHEP03(2021)243. arXiv: 2008.05355 [hep-ex]. Erratum: in: *JHEP* 11 (2021), p. 050. DOI: 10.1007/JHEP11(2021)050.

- [123] CMS Collaboration. *Evidence for light-by-light scattering and searches for axion-like particles in ultraperipheral PbPb collisions at $\sqrt{s_{NN}} = 5.02\text{ TeV}$* . In: *Phys. Lett. B* 797 (2019), p. 134826. DOI: 10.1016/j.physletb.2019.134826. arXiv: 1810.04602 [hep-ex].
- [124] ATLAS Collaboration. *Search for Higgs boson decays into a pair of pseudoscalar particles in the $bb\mu\mu$ final state with the ATLAS detector in pp collisions at $\sqrt{s} = 13\text{ TeV}$* . In: *Phys. Rev. D* 105 (2021), p. 012006. DOI: 10.1103/PhysRevD.105.012006. arXiv: 2110.00313 [hep-ex].
- [125] ATLAS Collaboration. *Search for Higgs Boson Decays into a Z Boson and a Light Hadronically Decaying Resonance Using 13 TeV pp Collision Data from the ATLAS Detector*. In: *Phys. Rev. Lett.* 125 (2020), p. 221802. DOI: 10.1103/PhysRevLett.125.221802. arXiv: 2004.01678 [hep-ex].
- [126] CMS Collaboration. *Search for an exotic decay of the Higgs boson to a pair of light pseudoscalars in the final state with two muons and two b quarks in pp collisions at 13 TeV*. In: *Phys. Lett. B* 795 (2019), p. 398. DOI: 10.1016/j.physletb.2019.06.021. arXiv: 1812.06359 [hep-ex].
- [127] ATLAS Collaboration. *Search for dark matter in association with an energetic photon in pp collisions at $\sqrt{s} = 13\text{ TeV}$ with the ATLAS detector*. In: *JHEP* 02 (2021), p. 226. DOI: 10.1007/JHEP02(2021)226. arXiv: 2011.05259 [hep-ex].
- [128] ATLAS Collaboration. *Search for new phenomena in events with an energetic jet and missing transverse momentum in pp collisions at $\sqrt{s} = 13\text{ TeV}$ with the ATLAS detector*. In: *Phys. Rev. D* 103 (2021), p. 112006. DOI: 10.1103/PhysRevD.103.112006. arXiv: 2102.10874 [hep-ex].
- [129] CMS Collaboration. *Search for dark matter produced in association with a leptonically decaying Z boson in proton–proton collisions at $\sqrt{s} = 13\text{ TeV}$* . In: *Eur. Phys. J. C* 81 (2021), p. 13. DOI: 10.1140/epjc/s10052-020-08739-5. arXiv: 2008.04735 [hep-ex].
- [130] Babette Döbrich, Joerg Jaeckel, and Tommaso Spadaro. *Light in the beam dump - ALP production from decay photons in proton beam-dumps*. In: *JHEP* 05 (2019). [Erratum: *JHEP* 10, 046 (2020)], p. 213. DOI: 10.1007/JHEP05(2019)213. arXiv: 1904.02091 [hep-ph].
- [131] M. B. Gavela et al. *Nonresonant Searches for Axionlike Particles at the LHC*. In: *Phys. Rev. Lett.* 124.5 (2020), p. 051802. DOI: 10.1103/PhysRevLett.124.051802. arXiv: 1905.12953 [hep-ph].
- [132] Particle Data Group. *Review of Particle Physics*. In: *Phys. Rev. D* 98.3 (2018), p. 030001. DOI: 10.1103/PhysRevD.98.030001.
- [133] Ciaran O’Hare. *cajohare/AxionLimits: AxionLimits*. 2020. DOI: 10.5281/zenodo.3932430. URL: <https://cajohare.github.io/AxionLimits/>.
- [134] Sonia Carra et al. *Constraining off-shell production of axionlike particles with $Z\gamma$ and WW differential cross-section measurements*. In: *Phys. Rev. D* 104.9 (2021), p. 092005. DOI: 10.1103/PhysRevD.104.092005. arXiv: 2106.10085 [hep-ex].
- [135] John C. Collins, Davison E. Soper, and George F. Sterman. *Factorization of Hard Processes in QCD*. In: *Adv. Ser. Direct. High Energy Phys.* 5 (1989), pp. 1–91. DOI: 10.1142/9789814503266_0001. arXiv: hep-ph/0409313.

- [136] Andy Buckley, Christopher White, and Martin White. *Practical Collider Physics*. IOP, 2021. ISBN: 978-0-7503-2444-1, 978-0-7503-2443-4, 978-0-7503-2442-7. DOI: 10.1088/978-0-7503-2444-1.
- [137] Particle Data Group. *Review of Particle Physics*. In: *PTEP* 2020.8 (2020), p. 083C01. DOI: 10.1093/ptep/ptaa104.
- [138] NNPDF Collaboration. *Parton distributions for the LHC Run II*. In: *JHEP* 04 (2015), p. 040. DOI: 10.1007/JHEP04(2015)040. arXiv: 1410.8849 [hep-ph].
- [139] Massimiliano Grazzini, Stefan Kallweit, and Marius Wiesemann. *Fully differential NNLO computations with MATRIX*. In: *Eur. Phys. J. C* 78.7 (2018), p. 537. DOI: 10.1140/epjc/s10052-018-5771-7. arXiv: 1711.06631 [hep-ph].
- [140] Georgios Billis, Frank J. Tackmann, and Jim Talbert. *Higher-Order Sudakov Resummation in Coupled Gauge Theories*. In: *JHEP* 03 (2020), p. 182. DOI: 10.1007/JHEP03(2020)182. arXiv: 1907.02971 [hep-ph].
- [141] Bo Andersson et al. *Parton Fragmentation and String Dynamics*. In: *Phys. Rept.* 97 (1983), pp. 31–145. DOI: 10.1016/0370-1573(83)90080-7.
- [142] B. R. Webber. *A QCD Model for Jet Fragmentation Including Soft Gluon Interference*. In: *Nucl. Phys. B* 238 (1984), pp. 492–528. DOI: 10.1016/0550-3213(84)90333-X.
- [143] GEANT4 Collaboration. *GEANT4—a simulation toolkit*. In: *Nucl. Instrum. Meth. A* 506 (2003), pp. 250–303. DOI: 10.1016/S0168-9002(03)01368-8.
- [144] Lyndon Evans and Philip Bryant. *LHC Machine*. In: *JINST* 3 (2008), S08001. DOI: 10.1088/1748-0221/3/08/S08001.
- [145] Daniel Dominguez. *3D cut of the LHC dipole*. In: (2014). URL: <https://cds.cern.ch/record/1741036>.
- [146] Esma Mobs. *The CERN accelerator complex*. In: (July 2019). URL: <https://cds.cern.ch/record/2684277>.
- [147] Jorg Wenninger. *Operation and Configuration of the LHC in Run 2*. In: (2019). URL: <https://cds.cern.ch/record/2668326>.
- [148] D. Nisbet. *Cycle with Beam: Analysis and improvements*. In: *7th Evian Workshop on LHC beam operation*. 2017, pp. 41–44.
- [149] Jonathan L. Feng et al. *ForwArD Search Experiment at the LHC*. In: *Phys. Rev. D* 97.3 (2018), p. 035001. DOI: 10.1103/PhysRevD.97.035001. eprint: 1708.09389.
- [150] SHiP Collaboration. *SND@LHC*. Tech. rep. 2020. eprint: 2002.08722. URL: <https://cds.cern.ch/record/2709550>.
- [151] LHCf Collaboration. *The LHCf detector at the CERN Large Hadron Collider*. In: *JINST* 3 (2008), S08006. DOI: 10.1088/1748-0221/3/08/S08006.
- [152] TOTEM Collaboration. *The TOTEM experiment at the CERN Large Hadron Collider*. In: *JINST* 3 (2008), S08007. DOI: 10.1088/1748-0221/3/08/S08007.
- [153] MoEDAL Collaboration. *Technical Design Report of the MoEDAL Experiment*. In: (2009). URL: <https://cds.cern.ch/record/1181486>.
- [154] Michaela Schaumann et al. *First Xenon-Xenon Collisions in the LHC*. In: *9th International Particle Accelerator Conference*. 2018. DOI: 10.18429/JACoW-IPAC2018-MOPMF039.

- [155] P. J. Bryant. *INTRODUCTION TO TRANSFER LINES AND CIRCULAR MACHINES*. In: (1984). DOI: 10.5170/CERN-1984-004.
- [156] ATLAS Collaboration. *Online Luminosity Summary Plots over Multiple Years including full Run 2*. 2019. URL: <https://twiki.cern.ch/twiki/bin/view/AtlasPublic/LuminosityPublicResultsRun2>.
- [157] Zachary Marshall and the ATLAS Collaboration. *Simulation of Pile-up in the ATLAS Experiment*. In: *Journal of Physics: Conference Series* 513.2 (2014), p. 022024. DOI: 10.1088/1742-6596/513/2/022024.
- [158] CERN. *The HL-LHC project*. [Online; accessed 07-September-2022]. 2022. URL: <https://hilumilhc.web.cern.ch/content/hl-lhc-project>.
- [159] R Alemany-Fernandez et al. *Operation and Configuration of the LHC in Run 1*. In: (2013). URL: <https://cds.cern.ch/record/1631030>.
- [160] ATLAS Collaboration. *Luminosity determination in pp collisions at $\sqrt{s} = 8\text{ TeV}$ using the ATLAS detector at the LHC*. In: *Eur. Phys. J. C* 76 (2016), p. 653. DOI: 10.1140/epjc/s10052-016-4466-1. arXiv: 1608.03953 [hep-ex].
- [161] Frederick Bordry et al. *The First Long Shutdown (LS1) for the LHC*. In: *4th International Particle Accelerator Conference*. 2013, MOZB202.
- [162] Rende Steerenberg et al. *Operation and performance of the CERN Large Hadron Collider during proton Run 2*. In: *10th International Particle Accelerator Conference*. 2019, MOPMP031. DOI: 10.18429/JACoW-IPAC2019-MOPMP031.
- [163] ATLAS Collaboration. *Luminosity determination in pp collisions at $\sqrt{s} = 13\text{ TeV}$ using the ATLAS detector at the LHC*. ATLAS-CONF-2019-021. 2019. URL: <https://cds.cern.ch/record/2677054>.
- [164] ATLAS Collaboration. *ATLAS data quality operations and performance for 2015–2018 data-taking*. In: *JINST* 15 (2020), P04003. DOI: 10.1088/1748-0221/15/04/P04003. arXiv: 1911.04632 [physics.ins-det].
- [165] Stephane Fartoukh et al. *LHC Configuration and Operational Scenario for Run 3*. Tech. rep. 2021. URL: <https://cds.cern.ch/record/2790409>.
- [166] I. Zurbano Fernandez et al. *High-Luminosity Large Hadron Collider (HL-LHC): Technical design report*. In: *CERN Yellow Reports: Monographs* 10/2020 (2020). Ed. by I. Béjar Alonso et al. DOI: 10.23731/CYRM-2020-0010.
- [167] ATLAS Collaboration. *The ATLAS Experiment at the CERN Large Hadron Collider*. In: *JINST* 3 (2008), S08003. DOI: 10.1088/1748-0221/3/08/S08003.
- [168] Joao Pequeno. *Computer generated image of the whole ATLAS detector*. 2008. URL: <https://cds.cern.ch/record/1095924>.
- [169] Joao Pequeno. *Computer generated image of the ATLAS inner detector*. 2008. URL: <https://cds.cern.ch/record/1095926>.
- [170] ATLAS Collaboration. *Alignment of the ATLAS Inner Detector in Run-2*. In: *Eur. Phys. J. C* 80 (2020), p. 1194. DOI: 10.1140/epjc/s10052-020-08700-6. arXiv: 2007.07624 [hep-ex].
- [171] ATLAS Collaboration. *ATLAS Detector and Physics Performance: Technical Design Report, Volume 1*. ATLAS-TDR-14; CERN-LHCC-99-014. 1999. URL: <https://cds.cern.ch/record/391176>.

- [172] ATLAS Collaboration. *Study of the material of the ATLAS inner detector for Run 2 of the LHC*. In: *JINST* 12 (2017), P12009. DOI: 10.1088/1748-0221/12/12/P12009. arXiv: 1707.02826 [hep-ex].
- [173] ATLAS Collaboration. *ATLAS Insertable B-Layer: Technical Design Report*. ATLAS-TDR-19; CERN-LHCC-2010-013. 2010. URL: <https://cds.cern.ch/record/1291633>. Addendum: ATLAS-TDR-19-ADD-1; CERN-LHCC-2012-009. 2012. URL: <https://cds.cern.ch/record/1451888>.
- [174] ATLAS Collaboration. *Performance of the ATLAS Transition Radiation Tracker in Run 1 of the LHC: tracker properties*. In: *JINST* 12 (2017), P05002. DOI: 10.1088/1748-0221/12/05/P05002. arXiv: 1702.06473 [hep-ex].
- [175] Joao Pequenao. *Computer Generated image of the ATLAS calorimeter*. 2008. URL: <https://cds.cern.ch/record/1095927>.
- [176] ATLAS Collaboration. *Drift Time Measurement in the ATLAS Liquid Argon Electromagnetic Calorimeter using Cosmic Muons*. In: *Eur. Phys. J. C* 70 (2010), p. 755. DOI: 10.1140/epjc/s10052-010-1403-6. arXiv: 1002.4189 [hep-ex].
- [177] Joao Pequenao. *Computer generated image of the ATLAS Muons subsystem*. 2008. URL: <https://cds.cern.ch/record/1095929>.
- [178] ATLAS Collaboration. *Performance of the ATLAS trigger system in 2015*. In: *Eur. Phys. J. C* 77 (2017), p. 317. DOI: 10.1140/epjc/s10052-017-4852-3. arXiv: 1611.09661 [hep-ex].
- [179] ATLAS Collaboration. *Operation of the ATLAS trigger system in Run 2*. In: *JINST* 15 (2020), P10004. DOI: 10.1088/1748-0221/15/10/P10004. arXiv: 2007.12539 [hep-ex].
- [180] ATLAS Collaboration. *ATLAS TDAQ System Phase-I Upgrade: Technical Design Report*. ATLAS-TDR-023; CERN-LHCC-2013-018. 2013. URL: <https://cds.cern.ch/record/1602235>.
- [181] ATLAS Collaboration. *ATLAS Liquid Argon Calorimeter Phase-I Upgrade: Technical Design Report*. ATLAS-TDR-022; CERN-LHCC-2013-017. 2013. URL: <https://cds.cern.ch/record/1602230>.
- [182] ATLAS Collaboration. *ATLAS New Small Wheel: Technical Design Report*. ATLAS-TDR-020; CERN-LHCC-2013-006. 2013. URL: <https://cds.cern.ch/record/1552862>.
- [183] ATLAS Collaboration. *Trigger Menu in 2018*. ATL-DAQ-PUB-2019-001. 2019. URL: <https://cds.cern.ch/record/2693402>.
- [184] Joao Pequenao and Paul Schaffner. *How ATLAS detects particles: diagram of particle paths in the detector*. 2013. URL: <https://cds.cern.ch/record/1505342>.
- [185] ATLAS Collaboration. *Electron reconstruction and identification in the ATLAS experiment using the 2015 and 2016 LHC proton–proton collision data at $\sqrt{s} = 13$ TeV*. In: *Eur. Phys. J. C* 79 (2019), p. 639. DOI: 10.1140/epjc/s10052-019-7140-6. arXiv: 1902.04655 [hep-ex].
- [186] ATLAS Collaboration. *Electron and photon performance measurements with the ATLAS detector using the 2015–2017 LHC proton–proton collision data*. In: *JINST* 14 (2019), P12006. DOI: 10.1088/1748-0221/14/12/P12006. arXiv: 1908.00005 [hep-ex].

- [187] T. Cornelissen et al. *Concepts, Design and Implementation of the ATLAS New Tracking (NEWT)*. Tech. rep. 2007. URL: <http://cds.cern.ch/record/1020106>.
- [188] ATLAS Collaboration. *Improved electron reconstruction in ATLAS using the Gaussian Sum Filter-based model for bremsstrahlung*. ATLAS-CONF-2012-047. 2012. URL: <https://cds.cern.ch/record/1449796>.
- [189] ATLAS Collaboration. *Electron and photon energy calibration with the ATLAS detector using 2015–2016 LHC proton–proton collision data*. In: *JINST* 14 (2019), P03017. DOI: 10.1088/1748-0221/14/03/P03017. arXiv: 1812.03848 [hep-ex].
- [190] ATLAS Collaboration. *Electron efficiency measurements with the ATLAS detector using the 2015 LHC proton–proton collision data*. ATLAS-CONF-2016-024. 2016. URL: <https://cds.cern.ch/record/2157687>.
- [191] ATLAS Collaboration. *Performance of electron and photon triggers in ATLAS during LHC Run 2*. In: *Eur. Phys. J. C* 80 (2020), p. 47. DOI: 10.1140/epjc/s10052-019-7500-2. arXiv: 1909.00761 [hep-ex].
- [192] ATLAS Collaboration. *Muon reconstruction and identification efficiency in ATLAS using the full Run 2 pp collision data set at $\sqrt{s} = 13$ TeV*. In: *Eur. Phys. J. C* 81 (2021), p. 578. DOI: 10.1140/epjc/s10052-021-09233-2. arXiv: 2012.00578 [hep-ex].
- [193] ATLAS Collaboration. *Measurement of the tau lepton reconstruction and identification performance in the ATLAS experiment using pp collisions at $\sqrt{s} = 13$ TeV*. ATLAS-CONF-2017-029. 2017. URL: <https://cds.cern.ch/record/2261772>.
- [194] ATLAS Electron and Photon Performance Group. *Electron efficiency with full Run2*. 2022. URL: <https://atlas.web.cern.ch/Atlas/GROUPS/PHYSICS/PLOTS/EGAM-2022-02>.
- [195] ATLAS Collaboration. *Muon reconstruction performance of the ATLAS detector in proton–proton collision data at $\sqrt{s} = 13$ TeV*. In: *Eur. Phys. J. C* 76 (2016), p. 292. DOI: 10.1140/epjc/s10052-016-4120-y. arXiv: 1603.05598 [hep-ex].
- [196] ATLAS Collaboration. *Jet energy measurement with the ATLAS detector in proton–proton collisions at $\sqrt{s} = 7$ TeV*. In: *Eur. Phys. J. C* 73 (2013), p. 2304. DOI: 10.1140/epjc/s10052-013-2304-2. arXiv: 1112.6426 [hep-ex].
- [197] ATLAS Collaboration. *Jet reconstruction and performance using particle flow with the ATLAS Detector*. In: *Eur. Phys. J. C* 77 (2017), p. 466. DOI: 10.1140/epjc/s10052-017-5031-2. arXiv: 1703.10485 [hep-ex].
- [198] Matteo Cacciari, Gavin P. Salam, and Gregory Soyez. *The anti- k_t jet clustering algorithm*. In: *JHEP* 04 (2008), p. 063. DOI: 10.1088/1126-6708/2008/04/063. arXiv: 0802.1189 [hep-ph].
- [199] Gavin P. Salam and Gregory Soyez. *A Practical Seedless Infrared-Safe Cone jet algorithm*. In: *JHEP* 05 (2007), p. 086. DOI: 10.1088/1126-6708/2007/05/086. arXiv: 0704.0292 [hep-ph].
- [200] ATLAS Collaboration. *Performance of pile-up mitigation techniques for jets in pp collisions at $\sqrt{s} = 8$ TeV using the ATLAS detector*. In: *Eur. Phys. J. C* 76 (2016), p. 581. DOI: 10.1140/epjc/s10052-016-4395-z. arXiv: 1510.03823 [hep-ex].
- [201] ATLAS Collaboration. *Jet energy scale and resolution measured in proton–proton collisions at $\sqrt{s} = 13$ TeV with the ATLAS detector*. In: *Eur. Phys. J. C* 81 (2020), p. 689. DOI: 10.1140/epjc/s10052-021-09402-3. arXiv: 2007.02645 [hep-ex].

- [202] ATLAS Collaboration. *Measurements of $Z\gamma$ +jets differential cross sections in pp collisions at $\sqrt{s} = 13\text{ TeV}$ with the ATLAS detector*. In: (2022). arXiv: 2212.07184 [hep-ex].
- [203] ATLAS Collaboration. *Measurements of $Z\gamma$ + jets differential cross sections in pp collisions at $\sqrt{s} = 13\text{ TeV}$ with the ATLAS detector*. ATLAS-CONF-2022-047. 2022. URL: <https://cds.cern.ch/record/2816327>.
- [204] ATLAS Collaboration. *A search for the $Z\gamma$ decay mode of the Higgs boson in pp collisions at $\sqrt{s} = 13\text{ TeV}$ with the ATLAS detector*. In: *Phys. Lett. B* 809 (2020), p. 135754. DOI: 10.1016/j.physletb.2020.135754. arXiv: 2005.05382 [hep-ex].
- [205] Jorge Sabater Iglesias et al. *Estimating ZZ production with $Z\gamma$ events at the LHC: cross-section ratio and uncertainties*. In: (2021). arXiv: 2106.01268 [hep-ph].
- [206] ATLAS Collaboration. *Measurements of $W\gamma$ and $Z\gamma$ production in pp collisions at $\sqrt{s} = 7\text{ TeV}$ with the ATLAS detector at the LHC*. In: *Phys. Rev. D* 87 (2013), p. 112003. DOI: 10.1103/PhysRevD.87.112003. arXiv: 1302.1283 [hep-ex]. Erratum: in: *Phys. Rev. D* 91 (2015), p. 119901. DOI: 10.1103/PhysRevD.91.119901.
- [207] ATLAS Collaboration. *Measurements of $Z\gamma$ and $Z\gamma\gamma$ production in pp collisions at $\sqrt{s} = 8\text{ TeV}$ with the ATLAS detector*. In: *Phys. Rev. D* 93 (2016), p. 112002. DOI: 10.1103/PhysRevD.93.112002. arXiv: 1604.05232 [hep-ex].
- [208] Sherpa Collaboration. *Event Generation with Sherpa 2.2*. In: *SciPost Phys.* 7.3 (2019), p. 034. DOI: 10.21468/SciPostPhys.7.3.034. arXiv: 1905.09127 [hep-ph].
- [209] J. Alwall et al. *The automated computation of tree-level and next-to-leading order differential cross sections, and their matching to parton shower simulations*. In: *JHEP* 07 (2014), p. 079. DOI: 10.1007/JHEP07(2014)079. arXiv: 1405.0301 [hep-ph].
- [210] Pier Francesco Monni et al. *MiNNLO_{PS}: a new method to match NNLO QCD to parton showers*. In: *JHEP* 05 (2020). [Erratum: *JHEP* 02, 031 (2022)], p. 143. DOI: 10.1007/JHEP05(2020)143. arXiv: 1908.06987 [hep-ph].
- [211] Daniele Lombardi, Marius Wiesemann, and Giulia Zanderighi. *Advancing MiNNLO_{PS} to diboson processes: $Z\gamma$ production at NNLO+PS*. In: *JHEP* 06 (2021), p. 095. DOI: 10.1007/JHEP06(2021)095. arXiv: 2010.10478 [hep-ph].
- [212] Stefano Frixione. *Isolated photons in perturbative QCD*. In: *Phys. Lett. B* 429 (1998), pp. 369–374. DOI: 10.1016/S0370-2693(98)00454-7. arXiv: hep-ph/9801442.
- [213] Stefan Höche et al. *QCD matrix elements and truncated showers*. In: *JHEP* 05 (2009), p. 053. DOI: 10.1088/1126-6708/2009/05/053. arXiv: 0903.1219 [hep-ph].
- [214] Torbjörn Sjöstrand et al. *An introduction to PYTHIA 8.2*. In: *Comput. Phys. Commun.* 191 (2015), pp. 159–177. DOI: 10.1016/j.cpc.2015.01.024. arXiv: 1410.3012 [hep-ph].
- [215] ATLAS Collaboration. *Measurements of inclusive and differential fiducial cross-sections of $t\bar{t}\gamma$ production in leptonic final states at $\sqrt{s} = 13\text{ TeV}$ in ATLAS*. In: *Eur. Phys. J. C* 79 (2019), p. 382. DOI: 10.1140/epjc/s10052-019-6849-6. arXiv: 1812.01697 [hep-ex].
- [216] G. D’Agostini. *A Multidimensional unfolding method based on Bayes’ theorem*. In: *Nucl. Instrum. Meth. A* 362 (1995), pp. 487–498. DOI: 10.1016/0168-9002(95)00274-X.

- [217] Jon Butterworth et al. *PDF4LHC recommendations for LHC Run II*. In: *J. Phys. G* 43 (2016), p. 023001. DOI: 10.1088/0954-3899/43/2/023001. arXiv: 1510.03865 [hep-ph].
- [218] ATLAS Collaboration. *Measurement of the $Z(\rightarrow \ell^+\ell^-)\gamma$ production cross-section in pp collisions at $\sqrt{s} = 13$ TeV with the ATLAS detector*. In: *HEPData* (2020). DOI: 10.17182/hepdata.89875.
- [219] ATLAS Collaboration. *Measurement of fiducial and differential W^+W^- production cross-sections at $\sqrt{s} = 13$ TeV with the ATLAS detector*. In: *HEPData* (2019). DOI: 10.17182/hepdata.89225.
- [220] ATLAS Collaboration. *Measurements of $W^+W^- + \geq 1$ jet production cross-sections in pp collisions at $\sqrt{s} = 13$ TeV with the ATLAS detector*. In: *HEPData* (2021). DOI: 10.17182/hepdata.100511.
- [221] Celine Degrande et al. *UFO - The Universal FeynRules Output*. In: *Comput. Phys. Commun.* 183 (2012), pp. 1201–1214. DOI: 10.1016/j.cpc.2012.01.022. arXiv: 1108.2040 [hep-ph].
- [222] Christian Bierlich et al. *Robust Independent Validation of Experiment and Theory: Rivet version 3*. In: *SciPost Phys.* 8 (2020), p. 026. DOI: 10.21468/SciPostPhys.8.2.026. arXiv: 1912.05451 [hep-ph].
- [223] Prasanta Chandra Mahalanobis. *On the generalized distance in statistics*. In: *Proceedings of the National Institute of Sciences (Calcutta)* 2 (1936), pp. 49–55.
- [224] Glen Cowan et al. *Asymptotic formulae for likelihood-based tests of new physics*. In: *Eur. Phys. J. C* 71 (2011). [Erratum: *Eur.Phys.J.C* 73, 2501 (2013)], p. 1554. DOI: 10.1140/epjc/s10052-011-1554-0. arXiv: 1007.1727 [physics.data-an].
- [225] ATLAS Collaboration. *Measurements of $Z\gamma$ +jets differential cross sections in pp collisions at $\sqrt{s} = 13$ TeV with the ATLAS detector*. In: *HEPData* (2022). DOI: 10.17182/hepdata.135460.
- [226] A. Einstein. *Zur Elektrodynamik bewegter Körper*. In: *Annalen der Physik* 322.10 (1905), pp. 891–921. DOI: <https://doi.org/10.1002/andp.19053221004>.